Visualizing the electronic structure of small molecules with rovibronic photon emission spectroscopy

Dissertation

zur Erlangung des akademischen Grades eines Doktors der Naturwissenschaften (Dr. rer. nat.)

vorgelegt im Fachbereich 10 - Mathematik & Naturwissenschaften der Universität Kassel

vorgelegt von: Dipl. Phys. Philipp Schmidt

Gutachter: Prof. Dr. Arno Ehresmann
Prof. Dr. Thomas Giesen

Prüfer: Prof. Dr. Philipp V. Demekhin
Dr. Michael Meyer

Kassel, Juli 2018

UNIKASSEL
VERSITÄT

Contents

Chapter 1

Introduction

A key in understanding the fundamental structure of atoms and molecules has been their absorption and emission of electromagnetic radiation across all spectral ranges. The observation of discrete line spectra contributed to the development of core concepts in quantum mechanics and thus the modern picture of physical processes occuring at small scales. The ongoing refinement of both experimental and theoretical methods in spectroscopy allows to deal with succeedingly more complex systems in different interactions to an ever increasing degree of precision. Still, as this frontier is moved further and further, even the simplest molecules continue to capture the attention of researchers to understand new details of their extraordinary rich spectra.

The first among the primary prototype systems is molecular hydrogen, the smallest neutral molecule. Here, theoretical models are benchmarked with experimental data first and their relevance can go far beyond the field of molecular physics [RA17]. Its nature as the most abundant molecule in the universe forms the very basis of countless astrophysical processes. Further examples include the significantly heavier carbon monoxide, the second most abundant neutral molecule in the universe, which exhibits vastly different properties due to its heteronuclear composition. Naturally, these species alongside other diatomic and triatomic molecules serve as the basic models in elementary lectures and textbooks to introduce the concepts of molecular physics. In such places however, many of their characterics like rovibronic transitions, dissociation or ionization are commonly illustrated in a disparate way, even though they are closely interlinked.

This work aims to revisit these small molecular systems and apply the improved ca-

pabilities of modern experimental methods to visualize their electronic structure in a particular holistic approach. For this purpose, the spectrally dispersed recording of spontaneous photon emissions is coupled with the high tunability and small bandwidth of synchrotron radiation. The selection of specific upper states with a well defined exciting photon energy allows to record the subsequent photon emissions discriminated by this upper state. If this is performed over the entire range of accessible transitions and sufficient resolution to separate its features in excitation and emission, the underlying electronic structure of the target is mapped in detail. These transitions of interest occur primarily in the near to vaccum ultraviolet spectral region with photon energies in the range of several electronvolts. In the case of molecular hydrogen and its system of singly excited electronic states, this equates to between 11 and 18 eV in excitation and resulting emissions as low as 6 eV. Its rotational levels hereby mandate a primary bandwidth of less than 5 meV and at least a corresponding secondary resolution to isolate them.
These kinds of photon-in-photon-out mapping techniques are typically limited by their fluence requirements to obtain a large number of full spectra in a reasonable amount of time. Previous studies were hence restricted to select regions of interest or reduced resolution, e.g. to trace several fragmentation channels above the ionization threshold in CO [EMU95] or water vapor [HKS15]. In other spectral regions such as the soft X-ray at photon energies of several hundred electronvolts, spectrometers with enough transmission have only recently become available [WFF09] to enable this method, here termed RIXS $h\nu^2$ mapping, across multiple excited states.
In this work, an existing set-up for dispersed luminescence spectroscopy at synchrotron radiation facilities is improved to achieve the necessary degree of fluence, resolution and automation to obtain large-scale emission maps in the near to vacuum ultraviolet spectral range. The measurements on the diatomic molecules hydrogen, one of its isotopologues and carbon monoxide are complemented by a basic computational method to simulate these emission maps on at least a qualitative level.
Following this introduction, the quantum mechanical description of atomic and molecular systems is summarized in Chapter 2. The experimental and computational methods are detailed in Chapter 3 and 4, respectively. A guide of the visual features appearing on rovibronic emission maps of small molecules in general is provided in Chapter 5, while the actual results for each included species are discussed in Chapter 6. The appendix presents the software framework developed over the course of this work as well as an early report of a characterization method for free-electron lasers.

Chapter 2

Fundamental background

The discovery and spectroscopy of spectral lines marks one of the earliest beginnings of atomic physics. The pioneering work of Joseph von Fraunhofer and Gustav Kirchhoff in the 19th century culminated in Bohr's atom model and later the birth of quantum mechanics. Its modern formulation and contemporary experimental methods have advanced this field further to encompass the description of molecules and more complex systems.
This chapter summarizes this development and serves as a framework for the methods and results presented in this work. It focuses on the description of the hydrogen atom and later hydrogen molecule, which form the most basic objects of investigation in these fields in general and in this work in particular. While the quantum mechanical formulation of the atom is sketched briefly, it is followed by an extensive discussion of molecules. An emphasis is put here on the Born-Oppenheimer approximation, which serves as an excellent example that enables the mathematical treatment of a system based on well funded physical assumptions with remarkable success. Finally, the interaction of matter with light is discussed to model the rovibronic photon excitation of small molecules and their subsequent photon emissions.

2.1 Atomic structure

The most fundamental unit of observation in atomic and molecular physics is the hydrogen atom, the system consisting of a single proton and a single electron bound by

an energy of 13.6 eV. The initially empirical suggestion from Niels Bohr, that such an ensemble may not exist in states of arbitrary energy but rather those of discrete energy, was later verified by its quantum mechanical description. This is usually done for the stationary case by the time-independent Schrödinger equation $\hat{H}\psi = E\psi$ for an electron moving at a distance r in the central potential $V(r) \propto r^{-1}$ of the proton. It may be expressed in the atom's center of mass with the reduced mass μ of proton and electron, the elementary charge e and the fundamentals constants $\hbar, \varepsilon_0$ by:

$$\left(-\frac{\hbar^2}{2\mu}\nabla^2 - \frac{e^2}{4\pi\varepsilon_0 r}\right)\psi = E\,\psi \tag{2.1}$$

This two-body problem can still be solved analytically and is readily found in the literature including its implications discussed below, e.g. [FLS65, Dem06, HW04, BJ06, HS15a, Her44]. It yields for the electron's wavefunction ψ in spherical coordinates r, ϑ, φ with the reduced Bohr Radius a_0 as an abbreviation the general solution:

$$\psi_{nlm}(r,\vartheta,\varphi) = N_{nl} \cdot \exp\left(-\frac{r}{na_0}\right) \cdot L_{n-l-1}^{2l+1}\left(\frac{2r}{na_0}\right) \cdot Y_{lm}(\vartheta,\varphi) \tag{2.2}$$

The generalized Laguerre polynomials L_{n-l-1}^{2l+1} and spherical harmonics Y_{lm} are families of functions, which commonly occur as solutions for specific differential equations and may be found in literature. The factor N_{nl} allows normalization of the radial components to unity, which is already included for the angular component in the spherical harmonics. The corresponding energy values of these states are found to be

$$E_n = \frac{\mu e^4}{8\varepsilon_0^2 h^2 n^2} = \frac{hcR_\infty}{n^2} = \frac{\mu c^2 \alpha^2}{2n^2} \tag{2.3}$$

with the fundamental constants h, c, α and Rydberg constant R_∞. This result for the electron energies in the hydrogen atom is remarkably identical to that of the classical and empirical approach taken in Bohr's atom model, when the electron's discretized radius or shell is used for n.

At first, the integers n, l, m arise as arbitrary parameters for these solutions. Their values are however restricted by the physical boundary conditions of the system. These acceptable ranges enumerate the physical solutions to the Schrödinger equation in (2.1) and therefore the discrete states it may reside in. In this form, they represent

quantities conserved in the dynamics of a state and are termed quantum numbers. The corresponding wavefunction ψ_{nlm} to each combination is typically referred to as an orbital in reference to the classical orbits in Bohr's model.

- The principal quantum number n may only take positive values starting with 1, i.e. $n \geq 1$, and correlates with the shell or electron radius in the classical Bohr's model. A higher n will increase the time the electrons spends farther away from the nucleus and its energy according to (2.3).

- The (orbital) angular momentum quantum number or azimuthal quantum number l contains the amount of angular momentum $\mathbf{l}$ in the (classical) orbital motion around the nucleus. It conforms to the range $0 \leq l < n$ and relates to the physical value by the relation $|\mathbf{l}| = \sqrt{l(l+1)}\hbar$. While n determines the size of an orbital in terms of probability density, the shape is described by l. As such, its values are typically denoted by the letters **s**harp ($l = 0$), **p**rincipal ($l = 1$), **d**iffuse ($l = 2$), **f**undamental ($l = 3$), g, h, ... based on their appearance.

- The magnetic quantum number m or m_l takes values between $-l$ and $+l$ and is the projection of $\mathbf{l}$ onto a particular chosen axis, typically called the z-axis. Within the orbital's shape determined by l, the projection specifies its orientation in space.

The lowest state in the hydrogen atom carries the quantum numbers $n = 1, l = m = 0$ and is called 1s. The next orbitals in order are then 2s, 2p and 3s. It is of note that in this initial model based on (2.1), all states with the same n, but different l, m are energetically degenerated. This accidental degeneracy is a property of its purely central potential and easily broken by the inclusion of further interactions [Pau26, Foc35].
An additional property of the electron emerges in some circumstances, e.g. when the atom is exposed to an external magnetic field. Here a splitting of its energy level occurs (Zeeman effect), which cannot be fully explained by the previously introduced set of quantum numbers n, l, m. This led to the introduction of the spin $\mathbf{s}$, an instrinsic property of the electron, that can be represented mathematically as an angular momentum. It is accompanied by the quantum number s analog to l, i.e. $|\mathbf{s}| = \sqrt{s(s+1)}\hbar$. Its value for an electron is always $s = 1/2$ in units of $\hbar$, which for this reason is classified as a fermion. In the bound context of the hydrogen atom, it may have the projections $m_s = \pm 1/2$ onto a chosen axis. Here, the secondary spin quantum number or spin projection number m_s is commonly referred to as the fourth quantum number s. The complete wavefunction

ψ_{nlms} is obtained by the product of the spatial wavefunction ψ_{nlm} obtained earlier and a spin function $\chi(s)$. Following this phenomenological adoption of the electron spin, it was described formally by the Dirac equation, of which the Schrödinger equation can be considered the non-relativistic limit.
A number of terms may now be added to (2.1) to address the simplifications in its ansatz. These are usually grouped into the fine structure (spin-orbit coupling and relativistic corrections) in the order of meV and hyperfine structure (interaction between electrons and nucleus) in the order of µeV. In addition, the effect of external electric (Stark effect) and magnetic fields (Zeeman effect for weak fields or Paschen-Back effect for strong fields) can be examined. All these extensions will usually reduce the high degree of degeneracy of E_n in (2.3) and split the energy levels as a function of the other quantum numbers as well as external parameters like field strengths. The spin-orbit coupling, for example, defines a new quantum number j of the coupled orbital and spin angular momentum $\mathbf{j} = \mathbf{l} + \mathbf{s}$ with $|\mathbf{j}| = \sqrt{j(j+1)}\hbar$. This results [Dem06] for the energy levels including fine structure, i.e. with spin-orbit coupling and relativistic corrections to the kinetic energy, to:

$$E_{nj} = \frac{\mu c^2 \alpha^2}{2n^2} + \frac{\mu c^2 \alpha^4}{8n^4}\left(3 - \frac{8n}{2j+1}\right) = E_n\left(1 + \frac{\alpha^2}{4n^2}\left(3 - \frac{8n}{2j+1}\right)\right) \tag{2.4}$$

The relative difference to E_n is therefore on the order of $\alpha^2 n^{-2} < 10^{-4}$. Further details on each of these contributions and further considerations are found in the commonly available literature.
The hydrogen atom with its single proton and electron is the only atomic system, where the Schrödinger equation may be solved analytically for the elementary formulation shown above. The next entry in the periodic table, helium, with just two protons and two electrons already loses the spherical symmetry of its potential due to the interaction between the electrons and makes an exact treatment impossible. Nevertheless, a number of properties can be described accurately on the basis of hydrogen-like single electrons in an effective (shielded) potential of remaining electrons and the nucleus. The Pauli exclusion principle then allows to populate the orbitals based on the quantum numbers n, l, m, s. As it states that fermions (in this case, electrons) may not occupy the same quantum state, expressed by their quantum numbers, in a quantum system, it yields a build-up principle for the elements in the periodic table. Depending upon the specific

coupling between the angular momenta in the atom, the overall electronic configuration can then be described as a whole by a term symbol. For lighter atoms, the orbital angular momenta **l** and spins **s** of each electron couple to the angular momenta **L** and **S**, which are then added to form the total angular momentum **J**. This case of so called LS-coupling then defines the term symbol with the corresponding quantum numbers to these total angular momenta as:

$$^{2S+1}L_J \tag{2.5}$$

The values of L are written with the same letter abbreviations as for the quantum number l of a single electron, but upper case. The ground state can be found using Hund's rules [Her44], e.g. $^2S_{1/2}$ for hydrogen, $^1S_0$ for helium (as well as all other noble gases), $^2P_{1/2}$ for boron and $^4S_{3/2}$ for nitrogen.

2.2 Molecular structure

The bond of two or more atoms through the interaction of their electrons is called a molecule. The smallest neutral molecule, formed by two hydrogen atoms, is the hydrogen molecule H_2. As with the atom itself, this molecule as well as its cation H_2^+ serve as the fundamental prototype systems in the theoretical treatment and general understanding of molecular structure.
With the significantly increased number of degrees of freedom, a number of additional approaches are required for their description. This section introduces the separation of electronic and nuclear motion in the adiabatic approximation and the molecular potential energy surface resulting from the Born-Oppenheimer approximation. These allow the concept of an electronic, vibrational and rotational molecular state. In the end, the limits of the performed approximations and assumptions as well as possible improvements are discussed.

2.2.1 Separation of electronic and nuclear motion

In general, a molecule consists of any number of nuclei and electrons. Throughout this section, the properties of the nuclei are denoted with upper case letters and enumeration index i, while lower case letters and the index j are used for electrons. Each nucleus with

mass M_i and charge $Z_i \cdot e$ resides at position $\mathbf{R}_i$, whereas each electron of mass m and charge $-e$ is found at $\mathbf{r}_j$. The positions of all nuclei and electrons are combined in $\mathbf{R}$ and $\mathbf{r}$, respectively. The rest frame of the molecule is also chosen as the frame of reference. An ansatz analog to the hydrogen atom in (2.1) then consists of a kinetic energy operator $\hat{T}$ and potential energy operator $\hat{V}$ to form the time-independent Schrödinger equation $(\hat{T} + \hat{V})\psi = \hat{H}\psi = E\psi$. Again, the influence of any spin interaction is neglected at this point. The kinetic energy operator $\hat{T} = \hat{T}_\mathrm{N} + \hat{T}_\mathrm{e}$ is simply the sum of kinetic energy contributions from all nuclei and electrons:

$$\left(-\frac{\hbar^2}{2} \sum_i \frac{1}{M_i} \nabla_i^2 - \frac{\hbar^2}{2m} \sum_j \nabla_j^2 + \hat{V} \right) \psi(\mathbf{r}, \mathbf{R}) = E\, \psi(\mathbf{r}, \mathbf{R}) \tag{2.6}$$

The laplacians ∇_i^2 and ∇_j^2 act on the respective nuclear and electronic coordinates in this case. The potential energy operator consists of the Coulomb interactions between all the nuclei, all the electrons and each combination of nucleus and electron:

$$\begin{aligned} \hat{V} &= \hat{V}_\mathrm{N,N} + \hat{V}_\mathrm{e,e} + \hat{V}_\mathrm{N,e} \\ &= \frac{e^2}{4\pi\varepsilon_0} \left(\sum_{i>i'} \sum_i \frac{Z_i Z_{i'}}{|\mathbf{R}_i - \mathbf{R}_{i'}|} + \sum_{j>j'} \sum_j \frac{1}{\left|\mathbf{r}_j - \mathbf{r}_{j'}\right|} - \sum_i \sum_j \frac{Z_i}{\left|\mathbf{R}_i - \mathbf{r}_j\right|} \right) \end{aligned} \tag{2.7}$$

In this form, even for the simplest molecule H_2^+ with just two nuclei and a single electron, the equation is a complex multi-body problem without sufficient symmetry to be solved analytically. It is therefore essential to reduce this complexity by choosing a suitable approximation.

As the mass of the nuclei is always much larger than for the electrons, it may be assumed that they move on a significantly slower timescale. The light electrons are then able to almost instantaneously adapt to a new nuclear configuration and perceive it as nearly fixed in space. The nuclei in turn observe the electrons only as an average over $\mathbf{r}$ for each of their positions $\mathbf{R}$. The nuclear coordinates are thus assumed constant in the electronic wavefunction and only a parametric dependence. It is important to not mistake this as an *independence* of electrons and nuclei. The parameter $\mathbf{R}$ should rather be interpreted as a dependence of the electronic wavefunction on the nuclear *positions*, but not their respective *velocities*. For each $\mathbf{R}$, there is a well defined electron distribution and it follows any changes to these positions adiabatically. This model is hence also called the adiabatic

or clamped-nuclei approximation.
Mathematically, this approximation can be described with a pertubation ansatz. When the nuclei are considered fixed in space, their kinetic energy vanishes. It may therefore be considered small compared to the electron's kinetic energy and their kinetic energy operator $\hat{T}_\mathrm{N}$ only a perturbation term. The Hamiltonian $\hat{H}$ in such an approach consists of the sum of unperturbed $\hat{H}_0$ and its small perturbation $\hat{H}'$ with:

$$\hat{H}_0 = \hat{T}_\mathrm{e} + \hat{V} \tag{2.8}$$

$$\hat{H}' = \hat{T}_\mathrm{N} \tag{2.9}$$

The unperturbed Schrödinger equation becomes a pure electronic equation according to

$$\hat{H}_0\,\phi(\mathbf{r};\mathbf{R}) = U(\mathbf{R})\,\phi(\mathbf{r};\mathbf{R}) \tag{2.10}$$

for the electronic wavefunction ϕ as a function of $\mathbf{r}$ and the parameter $\mathbf{R}$, denoted by the semicolon. This ϕ contains the electron distribution mentioned above for any, but fixed $\mathbf{R}$. Its corresponding eigenvalues U retain this parametric dependence in the same way. If the solutions to (2.10) are chosen as a complete orthonormal basis, the original wavefunction ψ for the full molecule described with (2.6) can be expressed as an infinite sum of these ϕ_k:

$$\psi(\mathbf{r},\mathbf{R}) = \sum_k \Phi_k(\mathbf{R})\,\phi_k(\mathbf{r};\mathbf{R}) \tag{2.11}$$

The expansion coefficients $\Phi_k(\mathbf{R})$ again depend parametrically on the nuclear coordinate $\mathbf{R}$, for which the electronic wavefunctions ϕ_k were obtained in (2.10). When this ψ is inserted into (2.6), these coefficients turn out to represent the nuclear wavefunctions. It results [Dem05] into a corresponding Schrödinger equation for the perturbed Hamiltonian:

$$\left(\hat{H}' + U_n(\mathbf{R})\right)\Phi_n(\mathbf{R}) + \sum_k c_{nk}\Phi_k(\mathbf{R}) = E\,\Phi_n(\mathbf{R}) \tag{2.12}$$

Both indices n,k enumerate the set of solutions of (2.10) (and due to the perturbation ansatz those of (2.12) as well) and represent its unperturbed electronic eigenstates.
The coupled equations (2.10) for the electronic and (2.12) for the nuclear wavefunction

together describe the molecule in an equivalent way to the total wavefunction ψ in (2.6). In the first equation, the electronic component is obtained for a particular fixed nuclear configuration $\mathbf{R}$. The second equation in turn describes the nuclear motion under an average of the electron's influence in the form of $U(\mathbf{R})$. This is in line with the central assumption of the adiabatic approximation in that the nuclei move significantly slower than the electrons. The sum term in (2.12) and its coefficients c_{nk} then again couple these individual states k and n in an potentially infinite sum to compensate for these approximations. However, this formulation allows to include further assumptions regarding these c_{nk}, which are discussed in the following sections.

2.2.2 Born-Oppenheimer approximation

The most accessible approach to the remaining coupling terms between electronic and nuclear motion in (2.12) is to neglect all coefficients completely, i.e.

$$c_{nk} \stackrel{!}{=} 0 \; \forall n, k \tag{2.13}$$

This is commonly called the Born-Oppenheimer approximation, but sometimes used interchangeably with the adiabatic approximation discussed in the previous section. Both concepts were originally introduced in [BO27]. A different, but equivalent formulation of this approximation is the ansatz for the total molecular wavefunction ψ as a product of the electronic wavefunction ϕ and the nuclear wavefunction Φ in the form of

$$\psi(\mathbf{r}, \mathbf{R}) = \phi(\mathbf{r}; \mathbf{R})\, \Phi(\mathbf{R}) \tag{2.14}$$

as the expansion in (2.11) is reduced to only one term.
The most fundamental consequence of this approximation are the fully decoupled Schrödinger equations originating from (2.10) and (2.12). As the sum in the nuclear component vanishes, it is reduced to just

$$\left(\hat{T}_\mathrm{N} + U(\mathbf{R})\right) \Phi(\mathbf{R}) = E\, \Phi(\mathbf{R}) \tag{2.15}$$

The electronic eigenvalue $U_n(\mathbf{R})$, which was obtained for the electrons' eigenstate n at a fixed nuclear configuration $\mathbf{R}$, acts here as a potential energy for the nuclei to move in. It contains an average of the electron's kinetic energy and all interaction potentials

expressed by (2.7) and is called the potential energy surface (PES) of the molecule in the electronic state n. For each value of n, the nuclear wavefunction in turn features its own spectrum of eigenvalues E_k. These are identified with the nuclear motion and designated the nuclear state k in the electronic state n. This distinct separation of electronic and nuclear states is only possible within the Born-Oppenheimer approximation, because it completely neglects any interaction between their movement to allow the product ansatz shown in (2.14). For the total energy, a product of wavefunctions leads to a sum of energy contributions. Using this and (2.15), one obtains

$$E_{\text{total}} = U^{(n)}(\mathbf{R}) + T_{\text{K}}(\mathbf{R}) = E_{\text{electronic}} + E_{\text{nuclear}} = \text{const} \tag{2.16}$$

As it may no longer depend on either coordinates $\mathbf{r}$ or $\mathbf{R}$ and is constant for a particular state, the same amount of energy must be distributed in a particular molecular state between the electronic potential energy and the nuclei's kinetic energy for each nuclear configuration $\mathbf{R}$. As this configuration changes, it may therefore be continuously converted from one to the other.

The potential energy surface becomes a potential energy curve for diatomic molecules, as the nuclear configuration $\mathbf{R}$ may be reduced to the scalar internuclear distance R in a suitable frame of reference. Figure 2.1 shows the potential energy curves of molecular hydrogen H_2 for several electronic states, particular the ones relevant in photon excitation or emission processes of this work. These are all bound states, in that they form some kind of potential well with an energy minimum T_{e} at a internuclear distance R, then called the equilibrium distance R_{e}. Here the molecule is stable and forms a chemical bond, as its total energy can be smaller at these finite R within the potential well than as separate atoms at $R \to \infty$. Repulsive states on the other hand follow some form of R^{-x} trend with $x \geq 1$ and lead to dissociation, as they do not have an energy minimum for any value of R.

The curve shape of bound states in these molecular species can typically be approximated well by a Morse potential of the form

$$U(R) = T_{\text{e}} + D_{\text{e}}(1 - e^{-a\,(R-R_{\text{e}})})^2 \tag{2.17}$$

with the well depth D_{e} and width parameter a. The nuclear states now live within each of these potential energy curves at specific energetic positions above T_{e}, as they are their

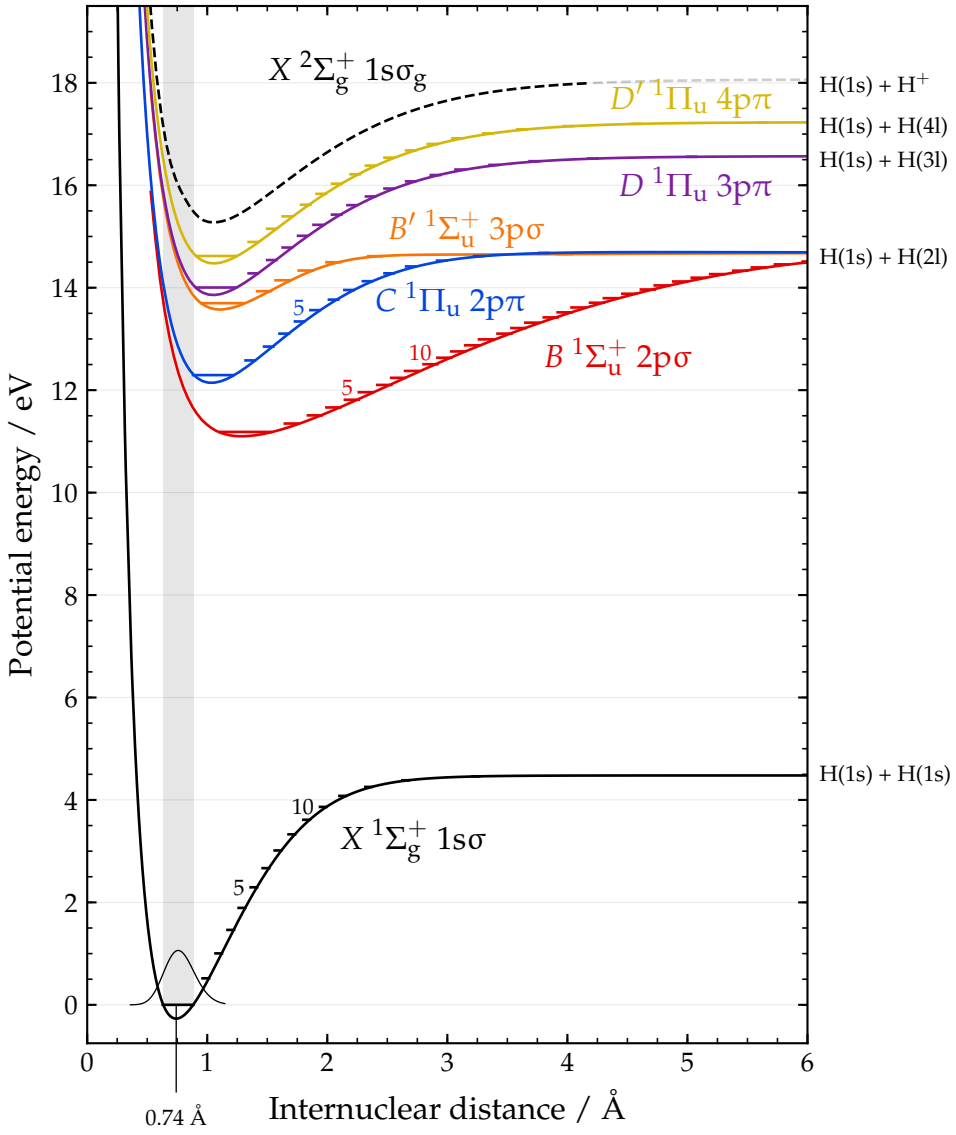

Fig. 2.1: *The Born-Oppenheimer potential energy curves of the hydrogen molecule's ground state $X\ ^1\Sigma_g^+$ (solid line) and of the cation $X\ ^2\Sigma_g^+$ (dashed line) is shown in black, while the most relevant electronically excited states, which are optically accessible, are included in other colors. For each state, the vibrational levels and atomic excitations the states converge towards at large internuclear distances are annotated. For all neutral states, an additional 1sσ electron is omitted in the configuration. The data for the potential energy curves is taken from [Wol93, SW02, WS03b].*

eigenvalues according to (2.15). Analog to the quantum harmonic oscillator, these states are referred to as vibrational levels and designated with the quantum number v starting with $v = 0$. Each electronic state possesses only a finite amount of bound vibrational levels between its energy minimum T_e and limit $T_e + D_e$ at large internuclear distances. Beyond this limit, the vibrational states are continuous and dissocative, as the nuclei are no longer confined to the potential well. The value D_e, or more correctly $D_0 = D_e - E_0$ corrected for the zero-point energy E_0 of the lowest vibrational state, is hence called the dissociation energy of the respective electronic state. The nuclear vibration (and rotation) is covered in more detail in Section 2.2.4.
The electronic state lowest in energy is called the electronic ground state, while those above are electronically excited. An introduction into transitions (involving the absorption or emission of photons) of molecules follows in Section 2.3.

2.2.3 Electron configuration of molecular orbitals

The electronic states introduced in the previous section as part of the Born-Oppenheimer approximation contain a particular configuration of the molecules' electrons. It should be possible to reduce this configuration to a set of quantum numbers, which are conserved in the dynamics of this state. As with the atomic orbitals in Section 2.1, these may then be used to completely describe each electronic state. Since atoms with several electrons are build up by hydrogen-like solutions consisting of only a single electron, a similar approach is suitable for molecules to define molecular orbitals.
The hydrogen cation H_2^+ is the molecular equivalent of the hydrogen atom. While the full Hamiltonian in (2.6) may not be solved analytically, it is possible for the electronic wavefunction with fixed nuclei in the Born-Oppenheimer approximation. The electronic Schrödinger equation for this species with the distance $r_i = |\mathbf{r} - \mathbf{R}_i|$ between the electron and each nucleus becomes:

$$\left(-\frac{\hbar^2}{2m}\nabla^2 + \frac{e^2}{4\pi\varepsilon_0}\left(\frac{1}{R} - \frac{1}{r_1} - \frac{1}{r_2}\right)\right)\phi(\mathbf{r};R) = U(R)\,\phi(\mathbf{r};R) \tag{2.18}$$

This grants its potential energy operator $\hat{V}$ a cylindrical symmetry, which may be calculated in elliptical coordinates.
Its solution, found in [Dem05] for example, yields for the electron the known principal

quantum number n in addition to a new one, which describes the projection of its orbital angular momentum $\mathbf{l}$ on the internuclear axis. It is usually denoted λ and may take any value up to the quantum number for the orbital angular momentum, l, which in turn is limited to be smaller than n, i.e. $\lambda \leq l < n$. The actual value of l, however, is no longer a suitable quantum number, as the missing potential's spherical symmetry causes the value of l to change as it precedes around the internuclear symmetry axis. It is nevertheless common to denote a molecular orbital by the three values n, l and λ. While λ specifies a projection onto a chosen axis similar to m in the hydrogen atom, $\pm\lambda$ is energetically degenerated for a fixed nuclear frame. It is usually considered positive and its sign is ignored. As a general notation rule, the symbols of atomic quantities are changed to greek letters when viewed in a molecular context. Beginning with λ for the molecular projection of l, its values are also characterized by the corresponding greek version of the orbital letter codes, i.e. σ for $\lambda = 0$ and π for $\lambda = 1$.

In the move to diatomic molecules with several electrons, it is again useful to consider the total angular momenta resulting from the addition of the electron's individual ones. As l is no longer a viable quantum number, its sum L is neither. However, its projection λ on the intermolecular axis is conserved. For sufficiently light atoms, a case similar to LS-coupling in atoms appears. The total orbital angular momentum $\mathbf{L}$ is coupled stronger to the internuclear axis than to the total spin $\mathbf{S}$. The conservation applies then to the projection M_L of the total orbital angular momentum $\mathbf{L}$ as well and its absolute value may be used as a quantum number Λ in the style of L for the atomic case:

$$\Lambda = |M_L| = 0, 1, 2, ..., L \tag{2.19}$$

The naming custom for the different values of angular momentum applies here again with greek upper case letters, i.e. Σ denotes a state with $\Lambda = 0$, while $\Lambda = 1$ is called a Π-state. The total spin $\mathbf{S}$ is treated in the same way and the quantum number Σ carries its projection M_S in a molecular system accordingly:

$$\Sigma = M_S = -S, -S + 1, ..., S \tag{2.20}$$

Finally, as both $\mathbf{L}$ and $\mathbf{S}$ precede around the internuclear axis on their own, they form a total angular momentum $\mathbf{J} = \mathbf{L} + \mathbf{S}$ with the same motion. Its projection Ω is then a

preserved quantity as well and used a quantum number. It is obtained by the absolute value of the sum

$$\Omega = |\Lambda + \Sigma| \tag{2.21}$$

An additional important property of electronic states in diatomic molecule is their symmetry. The electronic wavefunction ϕ may be reflected along an arbitrary plane containing the internuclear axis by the operator $\hat{P}$. As the repeated application of this operator $\hat{P}^2\psi = \psi$ must produce the original result, its eigenvalues are ± 1. A particular molecular state may therefore be of either positive parity or negative parity, denoted by the exponent + or -, by fulfilling either condition of

$$\hat{P}\phi^+ = +\phi^+ \qquad\qquad \hat{P}\phi^- = -\phi^- \tag{2.22}$$

In a homopolar or homonuclear molecule with equal charge for both nuclei, the inversion of all coordinates in the center of mass by the operator $\hat{I}$ is another possible symmetry operation. It features the same spectrum as the reflection $\hat{P}$ and therefore separates the states into gerade states, which do not change their sign, and ungerade states, which do. These are usually expressed by an index:

$$\hat{I}\phi_\mathrm{g} = +\phi_\mathrm{g} \qquad\qquad \hat{I}\phi_\mathrm{u} = -\phi_\mathrm{u} \tag{2.23}$$

With all these properties taken into account, the molecular term symbol to describe the overall electronic configuration is written as:

$$(X)\ {}^{2S+1}\Lambda^{(+/-)}_{\Omega(,\mathrm{g/u})} \tag{2.24}$$

A single latin letter X is often prepended as the name of a state. The letter X itself is always used for the ground state, while the excited states follow in roughly energetic order beginning with A. If an excited states has a different multiplicity $2S + 1$ than the ground state, a lower case letter will be used. The parity $+/-$ is often omitted for states with $\Lambda > 0$, as they are energetically degenerate in a fixed nuclear frame. The inclusion of rotation breaks this degeneracy very slightly, called Λ-doubling. The inversion g/u is only defined for homopolar molecules as discussed above. If the condition concerning the coupling between **L** and **S**, called Hund's case (a), is not fulfilled, Λ and Σ cease to

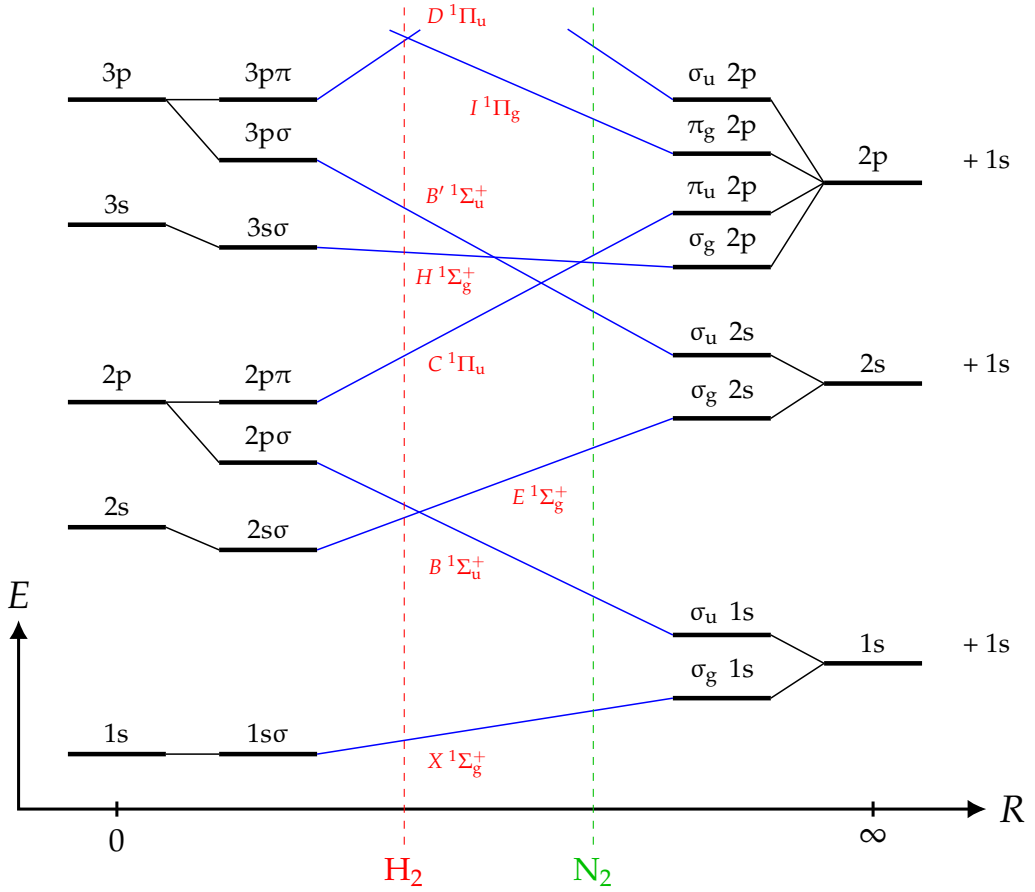

Fig. 2.2: *The correlation diagram of a homonuclear diatomic molecule allows the build-up of its electronic states. The atomic orbitals in the respective limits of the united atom (left) and separated atom (right) approximate the singly excited molecular orbitals. These can be connected taking the conservation of angular momenta and symmetries correctly into account. The states of actual molecules with finite R are then found between these limits with the resulting molecular term symbols annotated for the example of singulet states ($S = 0$) in molecular hydrogen H_2. Both axes are only qualitative and not plotted to scale.*

be viable quantum numbers. Depending upon the electronic configuration, a variety of other couplings can be realized [Her50a]. For the light diatomic molecules in this work, this is in general not the case.

The build-up of these electronic states is typically performed by imagining the molecule in the approximation $R \to 0$, the united atom, and $R \to \infty$, the seperated atoms. In the united atom, the molecule with nuclear charges Z_1 and Z_2 is thought of as an atom with charge $Z_1 + Z_2$ and an equal amount of electrons. The configuration for the resulting atom is known from the periodic table. When the nuclei are now pulled

apart again, the electron's orbital angular momentum **l** may begin to rotate around the intermolecular axis giving rise to its projection λ, as shown for the molecular hydrogen ion. Hence, the same atom allows several molecular configurations with different λ_j. For the separated atoms, the molecule is treated as completely separated atoms with their own atomic orbitals. When the nuclei come closer now, their individual orbitals combine to form the molecular orbitals. In addition to various values for the projection λ onto the intermolecular axis, the resulting electronic wavefunction may have a gerade or ungerade symmetry. This method is called the linear combination of atomic orbitals (LCAO), particular in its use to approximate the electronic wavefunctions to obtain their energies $U(R)$ by solving the Schrödinger equation (2.10).
A correlation diagram now combines both limits to estimate the energetic order of states. For a homonuclear diatomic molecule like H_2 or N_2, this is shown in Figure 2.2 for the excitations of one electron. To correlate the states on each side, the conservation of angular momenta and symmetries must be correctly taken into account to identify valid correlations. In this particular example, this applies to the projection of the orbital angular momentum λ and the inversion symmetry. The principal quantum number n and azimuthal quantum number l on the other hand may change, as they are not an eigenvalue in both limits at the same time. The valid combination with the lowest energies each are then connected repeatedly. As an actual molecule's equilibrium distance is at a finite value of R between these limits, the order of electronic states and their dissociation products can be approximated.
The molecular states included in the potential energy diagram in Figure 2.1 are annotated with their label, molecular term symbol and the united atom configuration. As molecular hydrogen is a rather small molecule with a short equilibrium distance, this approximation more closely resembles the sequence of states, e.g. the $B'\ ^1\Sigma_u^+\ 3p\sigma$ state is found higher in energy than $C\ ^1\Pi_u\ 2p\pi$. This agrees with the energetic order $3p\sigma > 2p\pi$ in the united atom as opposed to $\sigma_u\ 2s < \pi_u\ 2p$ for separated atoms. A larger homonuclear molecule consisting of much heavier nuclei, such as N_2, has a larger equilibrium distance and hence may have a different energetic order as indicated in Figure 2.2.
To obtain the actual electronic energies and thus the potential energy curve $U(R)$, it is still necessary to solve the electronic Schrödinger equation (2.10). While this was shown to be possible for the molecular hydrogen ion H_2^+ under specific circumstances, this is in general not the case for any more complex molecule. Instead, a variety of approximations have been developed to approach this problem, such as LCAO mentioned above in

the model of separated atoms. In addition, $U(R)$ can be written as an expansion of spectroscopically measured term values. Further details are found in the common literature on this topic [Her50a, Dem05, Dem06, HS15b, BJ06, HW04] as well as recent works in general [CSLHXL17] or on specific molecules, e.g. H_2 [Wol93, SW02, WS03b] or CO [DHWTJF13].

2.2.4 Nuclear vibration and rotation

The Born-Oppenheimer approximation enables the definition of a distinct electronic and nuclear state. The electronic energies $U(R)$ of the fixed nuclear frame serve as the potential energy for the nuclear motion. Based on (2.15), the Schrödinger equation for this motion of a diatomic molecule with the reduced nuclear mass $\mu = M_1 M_2 / (M_1 + M_2)$ is then:

$$\left(-\frac{\hbar^2}{2\mu} + U(R) \right) \Phi(\mathbf{R}) = \Phi(\mathbf{R}) \tag{2.25}$$

As the potential $U(R)$ only depends on the radial distance R, it has spherical symmetry and can be separated in the corresponding spherical coordinates $\mathbf{R} = (R, \vartheta, \varphi)$. This situation is similar to the hydrogen atom and its spherical Couloumb potential, but with an arbitrary potential except for its symmetry. Still, the same separation ansatz can be used with the spherical harmonics as the general solution for the angular component of spherical potentials:

$$\Phi(R, \vartheta, \varphi) = S(R) \cdot Y(\vartheta, \varphi) \tag{2.26}$$

The differential equation for the radial component $S(R)$ originates from this ansatz as well. With the definition $\chi(R) = R \cdot S(R)$ and the angular momentum $\mathbf{J}$ with quantum number J, i.e. $|\mathbf{J}| = \sqrt{J(J+1)}\hbar$, it results in [Dem05]

$$\left(-\frac{\hbar^2}{2\mu} \frac{\mathrm{d}^2}{\mathrm{d}R^2} + U(R) - \frac{\hbar^2}{2\mu R^2} J(J+1) \right) \chi(R) = E\, \chi(R) \tag{2.27}$$

This Schrödinger equation describes the radial motion $\chi(R)$ of the nuclei. This can be identified with nuclear vibration, that is the change of internuclear distance. The

additional energy term contains the angular momentum and is hence recognized as the nuclei's rotation. In this formulation, the solutions of equation (2.27) are the vibrational wavefunctions $\chi(R)$ with parametric dependence on the rotational quantum number J. Below the dissociation energy D_e of the respective potential energy curve $U(R)$, these eigenvalues $E < D_e$ are discrete and represent bound states of the molecule with the vibrational quantum number v and energy E_v. For $E \geq D_e$, the spectrum is continuous and called the vibrational continuum. The respective wavefunctions converge towards plane waves of a free particle, are no longer bound and dissociate the molecule. They are typically assigned on the basis of the nuclear momentum expressed by the (also continuous) wavenumber k, e.g. $\chi_k(R)$ and E_k.
The total energy of a molecular state in the Born-Oppenheimer approximation previously obtained as a sum of electronic and nuclear energy in (2.16) can now be further separated into three components:

$$E_{\text{total}} = E_{\text{electronic}} + E_{\text{vibrational}} + E_{\text{rotational}} \tag{2.28}$$

These three components are characterized by the electronic state as discussed in the previous section and the vibrational and rotational quantum numbers v, J. As the nuclei's kinetic energy is treated as a perturbation of the electronic Hamiltonian for this derivation, its proportion needs to be small enough to justiy this ansatz. For a small diatomic molecule, the electronic contribution is on the order of several eV, while the vibrational and rotational energy levels are successively smaller by around two orders of magnitude. In molecular hydrogen for example, the levels of the $B\ ^1\Sigma_u^+$ $2p\sigma$ state are (relative to the ground state):

$$\begin{aligned} E(B\ ^1\Sigma_u^+, v = 0, J = 0) &= 11.19\,\text{eV} = E_0 \\ E(B\ ^1\Sigma_u^+, v = 1, J = 0) &= E_0 + 0.16\,\text{eV} \\ E(B\ ^1\Sigma_u^+, v = 0, J = 1) &= E_0 + 4.9\,\text{meV} \end{aligned}$$

The hydrogen molecule acts here as an upper limit. Due to the μ^{-1} dependencies in (2.27), the vibrational and rotational energies per level are reduced for heavier nuclei. In addition, the number of bound vibrational levels increase with the decreasing gaps between them. This modifies the vibrational and rotational structure for isotopologues, where one or more atoms in the molecule are exchanged by a different isotope, in

particular. Here the nuclear masses are changed, but the potential energy surfaces remain the same in the Born-Oppenheimer approximation.
In Chapter 4, the numerically calculated nuclear wavefunctions $\chi(R)$ for the ground state $X\,^1\Sigma_g^+$ 1sσ of H_2 are plotted in Figure 4.1 for all bound vibrational levels including rotation excitation and an example in the continuum.

2.2.5 Adiabatic and non-adiabatic corrections

The coefficients c_{nk} in (2.12) define the coupling between the electronic and nuclear motion in their separated equations. In the Born-Oppenheimer approximation, these are neglected completely to obtain an uncoupled system with distinct electronic and nuclear states. In a next step, the diagonal elements can be considered while conserving this uncoupled system, as the off-diagonal entries still vanish:

$$c_{nk} \stackrel{!}{=} 0 \; \forall n \neq k \tag{2.29}$$

Under the assumption that the electronic wavefunctions ϕ are normalized for all nuclear configurations $\mathbf{R}$, i.e. $\langle \phi_n | \phi_n \rangle = 1$, these diagonal coefficients can be written [Dem05] as the expectation value of the perturbation $\hat{H}' = \hat{T}_\mathrm{N}$ of these electronic wavefunctions:

$$c_{nn} = \langle \phi_n | \hat{H}' | \phi_n \rangle = \langle \phi_n | \hat{T}_\mathrm{N} | \phi_n \rangle = \frac{\hbar^2}{2} \sum_i \frac{1}{M_i} \int \left(\frac{\partial \phi_n}{\partial \mathbf{R}_i} \right)^2 \mathrm{d}\mathbf{r} \tag{2.30}$$

This set of coefficients is now inserted into the nuclear Schrödinger equation in (2.12) and results in a similar form to the Born-Oppenheimer approximation of

$$\left(\hat{T}_\mathrm{N} + U^{(\mathrm{ad})}(\mathbf{R}) \right) \Phi(\mathbf{R}) = E \, \Phi(\mathbf{R}) \tag{2.31}$$

The modified potential energy surface $U^{(\mathrm{ad})}(\mathbf{R})$ contains the diagonal coeffiecients c_{nn} as the so called adiabatic correction to the Born-Oppenheimer potential:

$$U_n^{(\mathrm{ad})}(\mathbf{R}) = U_n(\mathbf{R}) + \frac{\hbar^2}{2} \sum_i \frac{1}{M_i} \int \left(\frac{\partial \phi_n}{\partial \mathbf{R}_i} \right)^2 \mathrm{d}\mathbf{r} \tag{2.32}$$

It introduces a dependency on the nuclear mass to $U(\mathbf{R})$, which changes the potential slightly for different isotopologues of a molecule. The partial derivative of the electronic

wavefunction after the nuclear coordinates can be interpreted as a correction to the actually non-instantaneous adaption of the electrons to a particular nuclear configuration. Instead, the nuclei at their position $\mathbf{R}$ move in the potential that belongs to a recently past $\mathbf{R}'$. There is still no mixing of different electronic states ϕ_n, ϕ_k, so that the electrons still follow the nuclei adiabatically without changing to another potential energy surface. The separation into individual states facilitated by the Born-Oppenheimer approximation still holds.
The nuclear coordinates $\mathbf{R}$ appear only in the interaction term $\hat{V}_{\mathrm{N,e}}$ of the electron's Hamiltonian, as the internuclear distances in $\hat{V}_{\mathrm{N,N}}$ are considered fixed. The original Born-Oppenheimer potential however contains the derivatives after the electronic coordinates in their kinetic energy. The correction term c_{nn} may therefore scale at most with $T_\mathrm{e} \cdot \sum m/M_i$ in relation to $U(R)$. Even for the lightest molecules such as H_2 with $m_\mathrm{e}/(2m_\mathrm{p}) \approx 3 \cdot 10^{-4}$, the adiabatic correction is therefore only a small contribution.

When all c_{nm} are considered, it is no longer possible to fully separate the electronic and nuclear states. The nuclear motion then mixes different of the former Born-Oppenheimer states ϕ_n to form the total molecular wavefunction ψ, i.e. vibration and rotation may trigger transitions between these states. In the original work that introduced the Born-Oppenheimer approximation [BO27], an estimation for its breakdown conditions is given using a general perturbation ansatz. The Hamiltonian is written in the form

$$\hat{H} = \hat{H}_0 + \hat{T}_\mathrm{N} = \hat{H}_0 + \lambda \cdot \hat{W} \tag{2.33}$$

to express the magnitude of the perturbation $\hat{W}$ with the dimensionless parameter $\lambda < 1$. In that work, $\lambda = \sqrt[4]{m/M}$ was shown to be a convenient choice. The vibrational and rotational terms then appear in orders of λ^2 and λ^4, which corresponds to their approximate relative contributions of 10^{-2} and 10^{-4}, respectively. The non-adiabatic electronic energies $U_n^{(\mathrm{na})}$ can then be expanded in this parameter using the Born-Oppenheimer solutions:

$$U_n^{(\mathrm{na})} = \underbrace{U_n + \langle \phi_n | \hat{T}_\mathrm{N} | \phi_n \rangle}_{U_n^{(\mathrm{ad})}} + \sum_{k \neq n} \frac{\langle \phi_n | \hat{T}_\mathrm{N} | \phi_k \rangle \ \langle \phi_k | \hat{T}_\mathrm{N} | \phi_n \rangle}{U_n - U_k} + \mathcal{O}\left(\lambda^3\right) \tag{2.34}$$

The newly added second order correction term contains the coupling between each combination of the electronic Born-Oppenheimer states ϕ_n and ϕ_k. The matrix element

$\langle \phi_n | \hat{T}_N | \phi_k \rangle$ of the nuclear kinetic energy operator expresses the transition probability from the electronic state n to k due to the nuclear motion. The denominator $U_n - U_k$ is the difference between their respective potential energy curves. The closer these curves therefore are, the larger the whole correction term becomes. When they cross and the difference vanishes, the Born-Oppenheimer approximation hence breaks down completely and the expansion in (2.34) diverges. In the adiabatic picture, an avoided crossing ocurrs at these positions instead and the eigenvalues repel each other. This is a general phenomenon in the adiabatic treatment of perturbed quantum systems whose eigenvalues may become equal [LL81]. They are shifted to prevent them from crossing on at least two coordinates. In a diatomic molecule, the potential energy curves of two states about to cross are bend to form new potential energy curves as illustrated in Figure 2.3 for the $E, F\ ^1\Sigma_g^+$ state in molecular hydrogen. This double-well states is created from the avoided crossing of the singly excited bound state $E\ ^1\Sigma_g^+\ 2s\sigma$ and the doubly excited repulsive state $F\ ^1\Sigma_g^+\ 2p\sigma^2$. At larger internuclear distances, additional avoided crossings with the ion pair potential of $H^+ + H^-$ and $G, K\ ^1\Sigma_g^+$ occur that alter its slope and finally restore the dissociation limit of H(1s) + H(2l).
The general perturbation ansatz in the expansion in (2.34) reveals the Born-Oppenheimer approximation to represent the perturbation in zeroth order, while the adiabatic approximation follows as the first order. Even higher orders couple the electronic states further through other mechanisms such as rotation.

2.3 Interaction of light and matter

A central tool to investigate the structure of atoms and molecules is spectroscopy, the interaction between electromagnetic radiation and matter. For this work, this applies particularly to the absorption and subsequent emission of single photons by transitioning between the states of a quantum mechanical system. A fundamental role in the mathematical formulation of this process is taken by the dipole approximation and its resulting selection rules. Furthermore, the Franck-Condon principle uses the separation of electronic and nuclear motion in the Born-Oppenheimer approximation to characterize rovibronic transitions in molecules. These may change the molecule's **ro**tational, **vib**rational and elect**ronic** state and constitute the bulk of processes explored in this work.

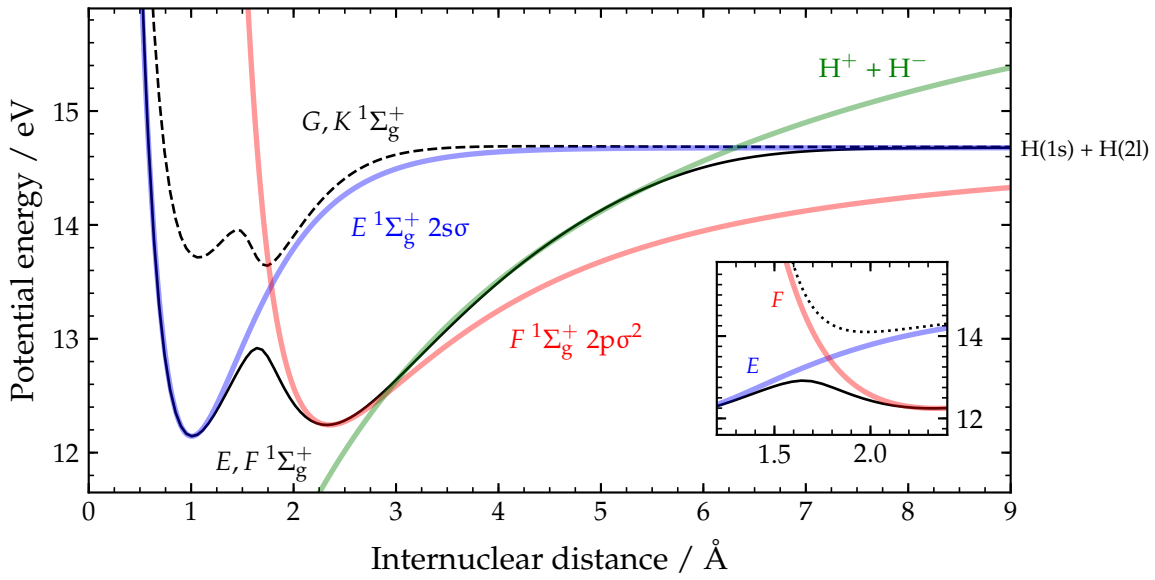

Fig. 2.3: *The potential energy curve of the $E, F\ ^1\Sigma_g^+$ state (black solid) is the result of avoided crossings between $E\ ^1\Sigma_g^+$ 2sσ (blue), $F\ ^1\Sigma_g^+$ 2pσ² (red), the ion pair potential of $H^+ + H^-$ (green) and $G, K\ ^1\Sigma_g^+$ (black dashed). Its double well in particular is formed by the intersection of E and F around $R = 1.8$ Å as shown in the inset in detail. Here, the original state's curves (blue and red) bend away from the intercept point instead of crossing each other (black solid and dotted).*

2.3.1 Einstein coefficients

Radiative transitions between two states n and k may occur either spontaneously or stimulated. In the former case, the initial state n has to be higher in energy for the process to occur, i.e. $E_n > E_k$,. It then decays radiatively to the lower state k via the emission of a photon. The presence of an external photon, on the other hand, may stimulate a transition. This can either be its absorption to change from a lower level to a higher level or the induced emission of another photon to again decay radiatively. The probability per unit time $\mathrm{d}P/\mathrm{d}t$ for these processes involving single photons is typically expressed by the Einstein coefficients A for spontaneous transitions and B for stimulated ones:

$$\left(\frac{\mathrm{d}P}{\mathrm{d}t}\right)_{\text{spon}} = A_{nk} \qquad \left(\frac{\mathrm{d}P}{\mathrm{d}t}\right)_{\text{stim}} = B_{nk}\,\rho(\nu) \tag{2.35}$$

In the stimulated case, the spectral energy density $\rho(\nu)$ represents the external influence. These coefficients therefore describe the rates at which at an atom or molecule will inter-

act with electromagnetic radiation independent of its fluence. They can be interrelated by statistical means in any given system for the same pair of involved states n, k [Dem05]. The Einstein coefficients for stimulated processes, that is for absorption and induced emission between n and k, differ by the ratio of each state's degeneracies g_n, g_k via the relation:

$$B_{nk} = \frac{g_k}{g_n} B_{kn} \tag{2.36}$$

The Einstein coefficient A_{nk} for spontaneous emission in turn relates to the corresponding coefficient B_{nk} for induced emission by

$$A_{nk} = \frac{8\pi}{h^2 c^3} \left(E_n - E_k\right)^3 B_{nk} \tag{2.37}$$

This comparison of induced and spontaneous emission for a transition between the same states emphasizes, that the probability for spontaneous processes increases significantly with the respective energy difference between these states.

2.3.2 Dipole approximation and selection rules

In a general semiclassical picture, the electromagnetic wave is described by its vector potential $\mathbf{A}(\mathbf{r}, t)$ as a function of space and time. Because its wavelength λ in the optical regime, i.e. $\lambda \gg 10\,\text{Å}$, is typically much larger than the atomic and molecular distances of around 1 Å, it may be approximated as a constant field between electrons and nuclei. A multipole expansion of the vector potential can therefore be reduced to its lowest-order term and taken at $\mathbf{A}(0, t)$ in the corresponding frame of reference. The radiative transition between two states n and k, expressed by their wavefunctiosn ψ_n and ψ_k, is then solely described [HW04] by the matrix element d_{nk} of the dipole operator $\hat{d} = q\hat{r}$:

$$d_{nk} = \langle \psi_n | \hat{d} | \psi_k \rangle \tag{2.38}$$

This ansatz is hence called the dipole approximation and the first component of the multipole expansion in (2.38) labeled E1. It holds well under the condition mentioned above, that is until the wavelength is not larger than the target size. In addition, it breaks down for strong fields, e.g. by intense lasers, where the electrons can achieve a high kinetic energy during the electromagnetic pulse. The next terms in an expansion of $\mathbf{A}$ are

the magnetic dipole (M1) and electric quadrupole (E2), named after their proportionality to the magnetic moment and electric quadrupole moment of the target, respectively. These can typically be neglected and are on the order of 10^{-5} or lower [Her50a] in comparison to E1, at least for the processes investigated in this work. Unless stated explicitly otherwise, all radiative transitions are hence assumed to be compatible with the dipole approximation.
The probability per unit time for a radiative transition can be obtained by expressing the Einstein coefficients defined in (2.35) with the dipole matrix element [Dem05]:

$$A_{nk} = \frac{4}{3}\alpha c \left(\frac{E_n - E_k}{\hbar c}\right)^3 \left| \langle \psi_n | \hat{d} | \psi_k \rangle \right|^2 \tag{2.39}$$

The relations (2.37) and (2.36) then yield the corresponding Einstein coefficients for stimulated processes as well:

$$B_{nk} = \frac{2}{3}\alpha c^4 \hbar^2 \left| \langle \psi_n | \hat{d} | \psi_k \rangle \right|^2 \tag{2.40}$$

The initial and final states n, k are identified by their quantum numbers in atomic and molecular systems as determined in the preceding sections. Based on the symmetries of the transition moment in dependence of these quantum numbers, the matrix element may vanish and prevent a transition from taking place. This set of conditions is called selection rules. Physically, they can be motivated by principles of conservation, e.g. for the angular momenta as a photon itself also carries one. In the most fundamental case of the hydrogen atom with its single electron, these are [Dem06]:

$$\Delta l = \pm 1 \qquad \Delta m = 0, \pm 1 \qquad \Delta s = 0 \tag{2.41}$$

For the magnetic quantum number m, the case $\Delta m = 0$ takes effect for linearly polarized light, while $\Delta m = \pm 1$ applies to left or right circularly polarized light, respectively. The aforementioned higher orders of the transition have each their own set of selection rules. For example, an electric quadrupole transition changes the first to $\Delta l = 0, \pm 2$. In atoms with multiple electrons, the quantum numbers for the coupled angular momenta are used instead and yield somewhat analog results. The precise conditions depend on the type of spin-orbit coupling present and may be found readily in literature [Her44].
While in an atom all transitions are electronic, in a molecule they may affect the electronic,

vibrational and rotational components separated in the Born-Oppenheimer approximation individually. A transition may be either purely rotational and alter only the rotational level, rovibrational and include a n additional change in the vibrational level or rovibronic and differ in all three states. The molecular electric dipole operator in the center of mass consists of the charge and location of all electrons and nuclei. With that, it may be split into an electronic and nuclear component:

$$\hat{d} = e\sum_i Z_i \mathbf{R}_i - e\sum_j \mathbf{r}_j = \hat{d}_\mathrm{N} + \hat{d}_\mathrm{e} \tag{2.42}$$

The matrix elements of the dipole operator can then be further evaluated [Dem05] using the product ansatz $\psi(\mathbf{r},\mathbf{R}) = \phi(\mathbf{r};\mathbf{R})\cdot\Phi(\mathbf{R})$ for electronic and nuclear wavefunction made possible by the Born-Oppenheimer approximation. This way, the matrix element can be separated into the contributions defined in (2.42) from the electronic and nuclear dipole operator:

$$\begin{aligned} d_{nk} &= \langle \phi_n\Phi_n|\hat{d}_\mathrm{N}+\hat{d}_\mathrm{e}|\phi_k\Phi_k\rangle = \int \phi_n^*\Phi_n^*(\hat{d}_\mathrm{N}+\hat{d}_\mathrm{e})\phi_k\Phi_k\,\mathrm{d}\mathbf{r}\,\mathrm{d}\mathbf{R} \\ &= \underbrace{\int \Phi_n^*\hat{d}_\mathrm{N}\left(\int \phi_n^*\phi_k\,\mathrm{d}\mathbf{r}\right)\Phi_k\,\mathrm{d}\mathbf{R}}_{\text{Nuclear dipole term}} + \underbrace{\int \Phi_n^*\left(\int \phi_n^*\hat{d}_\mathrm{e}\phi_k\,\mathrm{d}\mathbf{r}\right)\Phi_k\,\mathrm{d}\mathbf{R}}_{\text{Electronic dipole term}} \end{aligned} \tag{2.43}$$

If the initial and final state n,k belong to the same electronic state, their respective electronic wavefunctions are identical $\phi_n = \phi_k$. The integration over the electronic coordinates $\mathbf{r}$ in the second term becomes zero, as its integrand is odd. The matrix element $d_{nk}^{(vJ)}$ for a purely rotational or rovibrational transition reduces in this way to

$$d_{nk}^{(vJ)} = \int \Phi_n^*\hat{d}_\mathrm{N}\Phi_k\,\mathrm{d}\mathbf{R} = \langle\Phi_n|\hat{d}_\mathrm{N}|\Phi_k\rangle \tag{2.44}$$

and is only mediated by the nuclear dipole operator and wavefunctions. For a diatomic molecule, its selection rules [Her50a] for a purely rotational transition amount to $\Delta J = \pm 1$. As part of a rovibrational transition, this is extended by $\Delta J = 0$ depending on the polarization of the exciting or emitted electromagnetic wave. Rotational lines are commonly classified as the R branch ($\Delta J = +1$), P branch ($\Delta J = -1$) and Q branch ($\Delta J = 0$). The vibrational quantum number may also only differ by $\Delta v = \pm 1$ in a rovibrational transition, if the potential energy curve is approximated as strictly harmonic. As the

typical Morse potential becomes increasingly anharmonic for higher vibrational levels, this rule is relaxed to include the higher so called overtones of $\Delta v = \pm 2, \pm 3, ...$, but with decreasing intensity. In a homonuclear molecule, however, the nuclear dipole operator vanishes for all n, k due to the equal charge $Z_1 = Z_2$ and exactly opposite arrangement $\mathbf{R}_1 = -\mathbf{R}_2$ of the nuclei. This prevents any purely rotational or rovibrational transition in these systems.

If the electronic state changes between n and k, the first summand in (2.43) vanishes, because the electronic wavefunctions form an orthonormal set and the inner product is $\langle \phi_n | \phi_k \rangle = 0$. For the selection rules of electronic transitions, its inner product $\langle \phi_n | \hat{d}_\mathrm{e} | \phi_k \rangle$ imposes conditions on the change of electronic quantum numbers. In a diatomic molecule that fulfill Hund's case (a) [Her50a], one obtains for the angular momenta projections similar to the atomic case:

$$\Delta\Lambda = 0, \pm 1 \qquad\qquad \Delta\Sigma = 0 \tag{2.45}$$

In addition to that, the electron wavefunction symmetries defined in Section 2.2.3 are restricted. A state with its parity denoted by $+/-$ combines only with states of the same parity:

$$+ \not\leftrightarrow - \tag{2.46}$$

This is commonly only relevant for Σ-states, as all states with $\Lambda > 0$ are (mostly) energetically degenerate with respect to parity. Next to parity, a homonuclear molecule further possesses an inversion symmetry, which is either *gerade* oder *ungerade*. For a dipole transition, states only combine with states of the opposite inversion symmetry:

$$\mathrm{g} \longleftrightarrow \mathrm{u} \tag{2.47}$$

The vibrational quantum number v may in principle change to any level in the other electroinc state during the transition. In practice, the intensity depends strongly on the particular pair of lower and upper level v, v' and may vanish for some combinations. The Franck-Condon principle allows to quantify these and is investigated in the next section by a closer look at the transition dipole moment d_{nk} for rovibronic transitions. A change in the rotational quantum number remains governed by the same rules of

$\Delta J = 0, \pm 1$ and exhibit corresponding R, Q and P branches for each vibronic transition. But while an R and P branch appears for all vibronic transitions that fulfill the selection rules above, a Q branch may only emerge when the projection Λ of the orbital angular momentum changes, i.e. $\Delta\Lambda = \pm 1$.

2.3.3 Franck-Condon principle

The transition dipole moment for a rovibronic transition between different electronic states is reduced from (2.43) to only the second summand, the electric dipole term, as the nuclear dipole term vanishes in this case:

$$d_{nk} = \int \Phi_n^* \left(\int \phi_n^* \hat{d}_\mathrm{e} \phi_k \, \mathrm{d}\mathbf{r} \right) \Phi_k \, \mathrm{d}\mathbf{R} = \langle \Phi_n \phi_n | \hat{d}_\mathrm{e} | \Phi_k \phi_k \rangle \tag{2.48}$$

The nuclear coordinates $\mathbf{R}$ are only a parametric dependence in the electronic wavefunctions ϕ and the same applies then to the inner matrix element $\langle \phi_n | \hat{d}_\mathrm{e} | \phi_k \rangle$. It can be evaluated first and yields a function of the internuclear coordinate:

$$d_{nk}^{(\mathrm{e})}(\mathbf{R}) = \int \phi_n^* \hat{d}_\mathrm{e} \phi_k \, \mathrm{d}\mathbf{r} = \langle \phi_n | \hat{d}_\mathrm{e} | \phi_k \rangle \tag{2.49}$$

which is often called the electronic transition moment or transition dipole surface for the electronic state transition $n \to k$. It describes the coupling between n, k at different internuclear distances and contains solely the selection rules for the general transition between them as outlined in (2.45), (2.46) and (2.47) for diatomic molecules, for example. It does not depend on the vibrational or rotational state either before or after the transition. Its dependence on the internuclear distance is typically rather smooth and rather weak, so that it can be neglected. Instead, a constant averaged value $\left\langle d_{nk}^{(\mathrm{e})} \right\rangle$ is used. This is called the Condon approximation and reduces the matrix element of the dipole operator finally to:

$$d_{nk} = \langle \Phi_n | d_{nk}^{(\mathrm{e})} | \Phi_k \rangle \approx \left\langle d_{nk}^{(\mathrm{e})} \right\rangle \langle \Phi_n | \Phi_k \rangle \tag{2.50}$$

In this form, the transition dipole moment is only proportional to the overlap between the nuclear wavefunctions of the respective rovibronic level. As the probability is given by the square of this matrix element, it directly influences the observed intensity in

absorption and emission. In a semiclassical interpretation, the nuclear configuration in the final state must be compatible with that of the initial state. Alternatively, the rovibronic transition can be considered instantaneous on the nuclear timescale without any possibility of adaption of their motion. This is called the Franck-Condon principle introduced in [Con26, Con28], while the square of the rovibrational overlap is known as Franck-Condon factor.

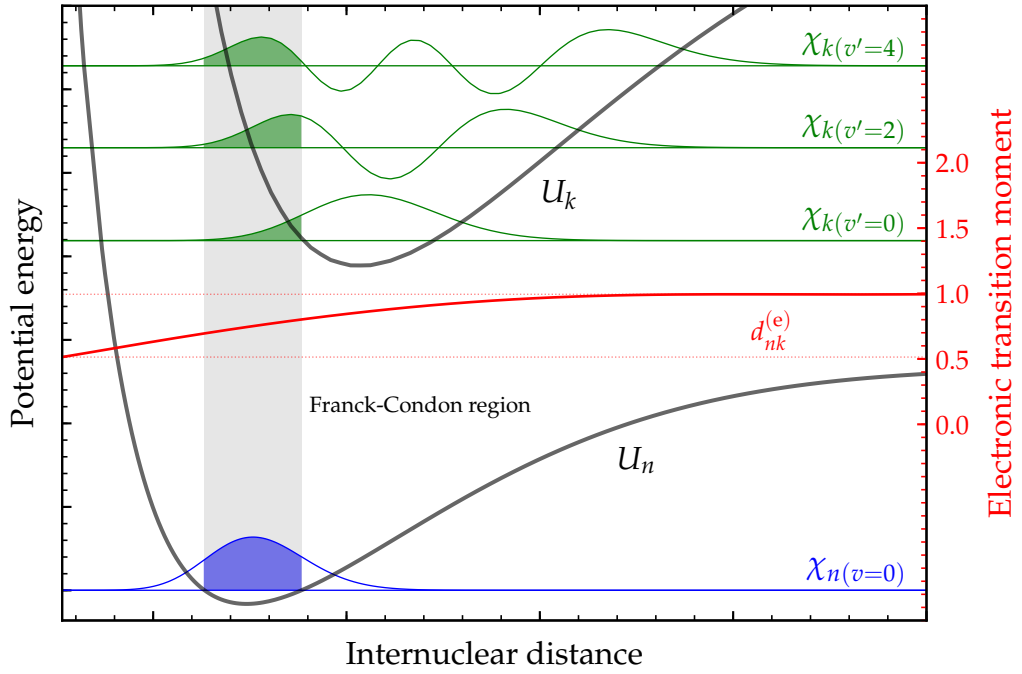

Fig. 2.4: *The probability for a rovibronic transition according to the Franck-Condon principle is primarily governed by the overlap between the vibrational wavefunctions χ_n, χ_k in the initial state n (blue) and final state k (green). The electronic transition moment (red) modulates this overlap slightly, but may be approximated as constant. Several vibrational levels for the upper state k are shown and each features a different overlap with the initial state. For transitions from the electronic and vibrational ground state, the interval of classically allowed internuclear distances is labeled the Franck-Condon region (grey).*

For a diatomic molecule, the wavefunction product in (2.50) can be separated further. The nuclear motion Φ is here a product of the radial component χ and spherical harmonics Y for the angular component as shown in (2.26) and (2.27). The electronic wavefunctions are defined in a fixed nuclear frame of cylindrical symmetry and thus will depend only on the internuclear distance R and not the angles ϑ, φ of the nuclear coordinates. The same hence applies to the electronic dipole operator and allows a corresponding

separation of the transition dipole moment into a product of these components. Then, the Condon approximation can be applied again to take an averaged electronic transition moment and simplify the matrix element to the radial overlap:

$$d_{nk} = \langle \chi_n | \hat{d}^{(\mathrm{e})}_{nk} | \chi_k \rangle \langle Y_n | Y_k \rangle \approx \left\langle d^{(\mathrm{e})}_{nk} \right\rangle \langle \chi_n | \chi_k \rangle \langle Y_n | Y_k \rangle \tag{2.51}$$

The angular component $\langle Y_n | Y_k \rangle$ depends actually just on the rotation quantum number J and its projection M as Y_{MJ}. When the term is integrated over all combinations of the latter and squared, it results [Dem05] in the Hönl-London formulae $S_{J_n J_k}$, which contain the initial and final rotational quantum number J_n and J_k as well as the change $\Delta\Lambda$ between the electronic states. The squared transition dipole moment for a rovibronic transition in diatomic molecules is then:

$$|d_{nk}|^2 = \left| \langle \chi_n | d^{(\mathrm{e})}_{nk} | \chi_k \rangle \right|^2 S_{J_n J_k} \approx \left\langle d^{(\mathrm{e})}_{nk} \right\rangle^2 |\langle \chi_n | \chi_k \rangle|^2 S_{J_n J_k} \tag{2.52}$$

The compatibility of nuclear configuration in a diatomic molecule represents a vertical transition in the potential energy diagram, as the internuclear distance R remains unchanged. The internuclear distances covered by the electronic and vibrational ground state are called the Franck-Condon region. The molecule may transition from this state only to vibrational levels in electronically excited states, which have a finite amplitude in this region. The Franck-Condon principle is illustrated for a diatomic molecule in Figure 2.4. The potential energy curves, nuclear wavefunctions and electronic transition moments are examples from the $X\ ^1\Sigma^+_\mathrm{g}$ and $C\ ^1\Pi_\mathrm{u}$ state of molecular hydrogen. Here, the Franck-Condon region is typically defined by the classically allowed internuclear distances within the potential energy curve, even though the wavefunction extends into this forbidden part. It covers about 68% or one standard deviation of the probability density of the ground state in this molecule.

Chapter 3

Experimental method

The set-up to map the excitation-energy dependent far and vacuum ultraviolet emissions of gaseous species is based on a set of experimental techniques collectively called Photon Induced Fluorescence Spectroscopy (PIFS). It allows a flexible configuration on target delivery and spectroscopic detection schemes using synchrotron radiation as the excitation source [HSH18, HOS17, GMJV17, OJS16, HKS15]. A number of developments upon this method were performed in this work to achieve high secondary resolution combined with sufficient luminance for rapid data acquisition, so a large interval of measurement points can be covered efficiently.
After an introduction into synchrotron radiation sources in general, the particular HZB facility and the U125/2 10m-NIM beamline used there as well as the common characteristics of PIFS are described in this chapter. This is followed by the specific set-up used and its required adaptions. Lastly, the analysis procedures are illustrated to construct the final results from the recorded raw data.

3.1 Synchrotron radiation source and beamline

The electromagnetic radiation emitted by radially accelerated charged particles at relativistic energies is called synchrotron radiation after its first observation at synchrotron accelerators [EGL47]. While the particle still emits like a dipole in its own rest frame, the relativistic Lorentz transformation at such velocities causes a strong collimation in the laboratory frame [Sch49]. The resulting brilliance in conjunction with the ability to

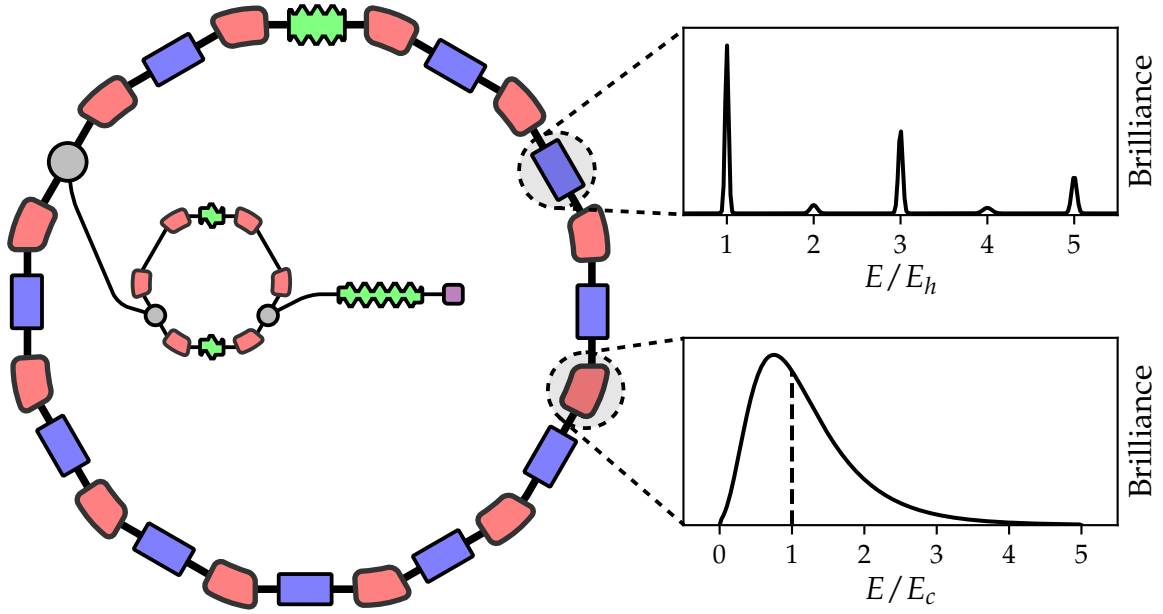

Fig. 3.1: *A synchrotron radiation source consists of a large storage ring, where bending magnets (red) and undulators (blue) generate electromagnetic radiation from relativistic charged particles. These are prepared by a series of acceleration elements (green) and a smaller booster synchrotron after their creation at the source (purple), while the storage ring only preserves their energy. The emission spectra of the source devices are characterized by the critical energy E_c for bending magnets and fundamental or harmonic energy E_h for undulators.*

manipulate parameters like the polarization and photon energy continiously over large ranges is used at synchrotron radiation sources for scientific experiments across many disciplines.

A facility as sketched in Figure 3.1 uses a storage ring to maintain a beam of relativistic charged particles, which are either electrons or positrons due to a m^{-4} scaling of radiated power. The light generating devices consist of the bending magnets sustaining the circular orbit and specific insertion devices called undulators installed at straight sections of the storage ring, that form a periodic lattice of alternating magnetic fields. Here the electrons are forced into an undulating motion and concentrate their radiated power around a fundamental energy E_h and its multiples, which is determined by the magnetic field geometry [Motz51]. The bending magnet exhibits a broad spectrum divided into equal halfs by the critical energy E_c. It is mainly dependent upon the fixed ring curvature (and hence the required magnetic field) and beam energy.

The Helmholtz-Zentrum Berlin (HZB) in Berlin, Germany houses the BESSY II storage

ring (**B**erliner **E**lektronen**s**peicher**sy**nchrotron), a synchrotron radiation source operating since 1998 at an electron energy of 1.7 GeV with over 50 beamlines ranging from terahertz radiation to hard X-rays. In its primary hybrid operation mode, it features a 300 mA beam current that is kept constant by frequent injections (TopUp mode) divided into individual bunches between 2 and 20 ns apart.
The U125/2 10m-NIM beamline is dedicated to the energy range between 5 and 40 eV or wavelength range between 250 and 30 nm covering the near to vacuum ultraviolet spectral ranges. The U125/2 undulator [BFG01] is built up by 32 periods of 125 mm permanent magnets in a quasi-periodic manner to suppress the higher harmonics, while its planar design restricts the polarization to linear horizontal. The monochromator of this beamline [RBS01] is constructed in a normal incidence geometry with 10 m arm length on a off-Rowland circle mounting, thus reducing the amount of optical aberrations considerably. This achieves a primary resolution of up to $E/\Delta E = 85000$ with a grating at 1200 mm^{-1} line density and 10 µm slit sizes [Hel16]. In addition, gratings with densities of 300 mm^{-1} and 4800 mm^{-1} are available depending on the need for photon flux or even higher resolution.
The energy range provided by this instrument allows access to the valence region of many atomic and molecular systems, which covers several physical processes that have been investigated using PIFS such as [HKS15, ORK15, GMJV17, GMJS10]. In the case of molecular hydrogen and its isotopes in particular, it covers the range of molecular singly and doubly excited states completely and enables a study without gaps.

3.2 Common elements of PIFS

The primary hardware components common to all its applications consist of the modular interaction chamber mounted on top of a vertical grating spectrometer, which is in turn attached to a mobile and adjustable frame. This is depicted in its basic configuration without any components tailored for a specific application in Figure 3.2. The measurement of dispersed luminescence after excitation by photons provided by a synchrotron radiation source is therefore the core functionality provided with the explicit option to record a multitude of additional quantities. The specific arrangement used for this work is described in Section 3.3.3, while here the function of its common components is introduced.

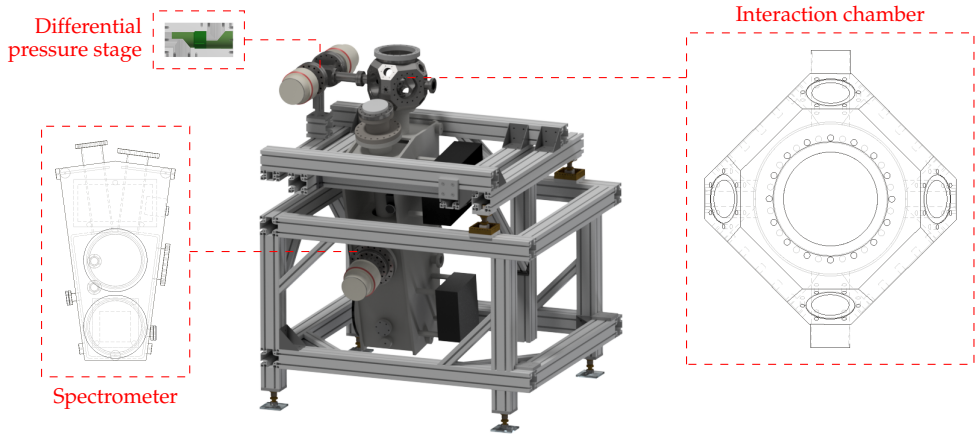

Fig. 3.2: *The basic configuration of PIFS consists of the interaction chamber mounted on top of the vertical luminescence spectrometer, which is in turn attached to a mobile and adjustable frame. The interaction chamber itself features a hexagonal shape and may be rotated depending upon the needs for a particular experiment. The spectrometer is configurable for a wide array of spectral ranges through the choice of window materials, gratings and detectors. A number of differential pressure stages with replaceable apertures can be used in sequence to separate the vacuum conditions inside the interaction chamber from any facility equipment.*

3.2.1 Interaction chamber

The interaction chamber features a wide array of flanges to place experimental equipment in line of sight of the central interaction region with the already mentioned grating spectrometer always using the bottom flange. Here, either detection devices such as cameras, mass spectrometers or single particle detectors can be placed or accessories like electrical feedthroughs and vacuum pumps. Different means of target delivery methods have been developed for this chamber:

- **Static pressure cell** [GMJV17, OJS16, ORK15, HKS15, GMJS13b, GMJS10]
  An enclosed smaller chamber is mounted inside the interaction chamber with apertures and windows to allow synchrotron radiation to enter and luminescence to leave. It is able to reach high and especially well defined target densities over a long duration. An advanced version of such a cell was developed for this work and is described in more detail in Section 3.3.1.

- **Heatable liquid cluster source** [Han18]
  This supersonic jet source is capable of creating clusters of materials, which are liquids at room temperature and ambient pressure. They are stored in an internal

reservoir and the cluster generation can be further supported by the capability of seeding as well as heating. In conjunction with luminescence experiments, it is optimized for running at high and stable target densities.

- **Cryogenic gas cluster source** [HSH18, HLF17]
  Clusters of gaseous targets can be generated by this cluster source, which is regulated by cooling down to cryogenic temperatures and high inlet pressures. Both liquid nitrogen and helium may be used as a coolant depending upon the boiling point of the used substance. It features two independent nozzles allowing vastly different cluster conditions without the need to vent and disassemble.

- **Liquid microjet** [HOS17]
  A stream of liquid target in a laminar flow is transported over a short distance into a vacuum vessel by this technique using thin nozzles. In particular, this allows the in-situ investigation of biological samples with synchrotron radiation in their natural environment dissolved in water.

The interaction chamber is connected to the beamline port at a synchrotron radiation source through a number of differential pressure stage modules to separate the respective vacua. Each module features a long exchangeable aperture unit with two parabolic reflectors directed at a turbomolecular pump each. The amount required depends on the vacuum conditions in the interaction chamber imposed by the the target delivery with each module generating a pressure differential of approximately 10^3.

3.2.2 Grating spectrometer

The photon spectrometer located below the interaction chamber is a commercial *McPherson Type 225 spectrometer* in normal incidence geometry as outlined in Figure 3.3. It features a small opening angle of 15°, where the optical aberrations due to a single optical element are still small. A special translation mount for the spherical reflection grating allows the entrance and exit flange to stay on its Rowland circle across the whole accessible wavelength range and hence retain the focus conditions. Through the use of different combinations of grating and detector systems, it can operate from the edge of the near infrared at 900 nm down to the vacuum ultraviolet spectral range at 40 nm.
Its entrance arm usually begins with an entrance slit to reduce the amount of scattered light entering and optionally define the projected image on the focusing grating. It can be

integrated into all previously mentioned target delivery methods and has a configurable width ranging from 100 µm to 2 mm, which trades off between resolution and luminance. The spherical surface of the ruled grating projects a sharp image of the entrance slit in both the zeroth order, the direct reflection, as well as the higher dispersion orders. Its grooves are blazed to optimize the reflectivity under a certain angle, which equates to an increased reflectivity for a wavelength interval in dispersion at these particular angles. On its exit arm, a position sensitive detector is mounted to record a spatial portion of the dispersed spectrum. The spectral width covered by a single detector image is determined by the detector geometry and grating dispersion and is typically in the range of several tens of nanometers. For example, a grating with a line density of 1200 mm^{-1} coupled with a 50 mm detector in the far ultraviolet (300 nm to 115 nm) is able to image about 30 nm at a time.

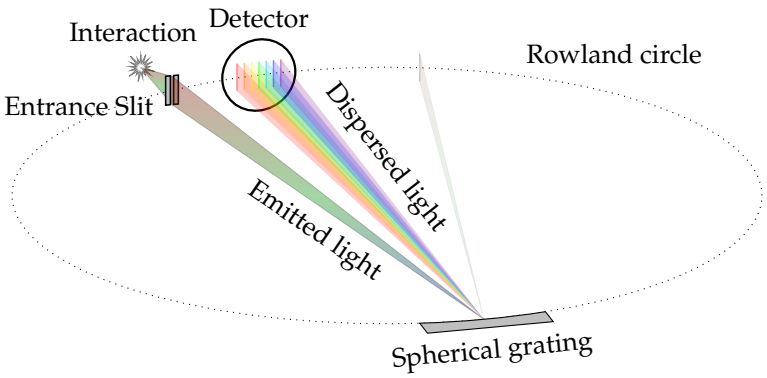

Fig. 3.3: *The spectrometer in normal incidence geometry is characterized by the Rowland circle, on which the spherical grating, the entrance slit and detector are positioned. The slit guides the luminescence emitted during a target interaction into the spectrometer and is projected both in zeroth order as well as dispersed orders onto the detector. Its spatial resolution allows to record a portion of the dispersed spectrum at once.*

The detection devices in use for the emitted photons are usually single particle counting devices based on micro channel plates (MCPs). These amplify the photoionisation caused by a single impact to be detected individually. This results in an improved signal-to-noise ratio for gas-phase experiments at a synchrotron radiation facility compared to CCD systems due to the combination of a low target density and the light source's high repetition rate. Each individual excitation has only a low probability by itself to cause a event that can be detected, but a significant amount occurs when integrated over time. The time between two events is hence highly statistical and requires long exposures with

mostly noise for a camera to capture. For longer wavelengths above 120 nm, several photocathode materials are used to greatly enhance the photoelectron yield, while below this limit the MCP surface itself is sufficient [HSO18].

3.3 Excitation-energy dependent luminescence mapping

For the measurements presented in this work, dispersed luminescence spectra at far and vacuum ultraviolet wavelengths have to be recorded for a large number of excitation energies (up to 2801 positions in the case of hydrogen in the vacuum ultraviolet) due to the comparably small bandwidth. At each of these energies, the spectrum covers two distinctive detector systems with three and four grating positions, respectively. This results in up to 20.000 individual recordings for a complete luminescence map of a hydrogen isotope. A number of requirements arise from these conditions:

1. The luminance has to be sufficient across the complete map to record a spectral section (i.e. a detector image) in less than 60 s to finalize it in a resonable amount of measuring time.

2. High secondary spectrometer resolution is required to resolve the rotational transitions, which for hydrogen amounts to $\Delta\lambda < 0.5\,\mathrm{nm}$ or $\lambda/\Delta\lambda > 300$.

3. For each measuring point, the experiment has to be configured rapidly, record data from several sources at the same time and continue with the next point with a high degree of automation.

These specifications were achieved through a number of developments added to the PIFS toolkit. The luminance is provided through a new differentially pumped static pressure cell described in detail in Section 3.3.1, which allowed the necessary target density while still maintaining high vacuum conditions. In addition, this density can be produced reliably and kept stable to ease normalization between different regions on the map. Proper optical alignment of this cell in combination with an optimized set-up of the detector electronics enable the resolution of individual transitions in emission. The specific detector configuration and the means of data acquisition are illustrated in Section 3.3.2. Finally, a newly developed software framework *Metro* allows computer-based control of all experimental parameters and equipment. It performs a predetermined

measurement plan autonomously and is configurable to a wide array of experimental specifics. The hard- and software implementation as used for this work can be found in Section 3.3.3, while a more general introduction of the development, concepts and features of *Metro* is given in Appendix A.

3.3.1 Octagon interaction cell

A closed interaction cell allows to maintain a relatively high static pressure in comparison to the surrounding chamber vacuum while still allowing synchrotron radiation to pass through small apertures. In addition, the target density in the enclosed volume can be well defined and controlled over the course of a measurement. This combination of features is ideally suited for this work to achieve sufficient luminance across a wide range of excitation energies and sustain these conditions as precisely as possible for the huge number of individual measurements.
The interaction chamber presented in Section 3.2.1 has an octagonal shape in the plane of the exciting synchrotron beam where the majority of flanges for detection devices are situated. A new gas cell was developed that imitates this general shape by corresponding surfaces with an opening to allow each of these flanges to have a clear view of the interaction region. Its general design, inner layout and several common plates are depicted in Figure 3.4.
The plates allows customization of the ten openings around the cell - eight in the octagonal plane and one on the top and bottom, respectively. While the threading is compatible for all these ports, they feature slightly different geometries to accomodate different plate requirements:

- The majority of openings (six in the central plane, one on the top/bottom) provide a notch a window or filter material up to a thickness of 1 mm to install in addition to gaskets. A typical application of this is the window plate featuring a central opening to mount a luminescence detector on a side flage of the interaction chamber.

- One opening on the top/bottom has a deeper notch to install thicker window materials up to 3 mm, which may withstand the pressure difference between the (coarse) vacuum in the cell and air. When a properly sealed adapter is used to mount the cell, this allows to not pump the luminescence spectrometer, for example.

- Two openings in the central plane have a maximal inner diameter without any notch. This is commonly used to install the long entrance/exit apertures.

Apart from plates, which allow the synchrotron radiation or any emitted luminescence to pass, a number of other plates exist for special purposes. The gas inlet plate has a central threading to allow connection to typical pipe flange systems such as Swagelok. This enables both a robust and flexible delivery method for a variety of targets and their requirements. The measurement of ionization yields is possible through ion apertures mounted electrically isolated on a feedthrough plate. A variable slit is able to improve the spectrometer resolution by limiting the amount of scattered light or acting as the focal point of the spherical grating. Lastly, any opening not in use may be covered by a blind plate to ensure minimal target leakage.

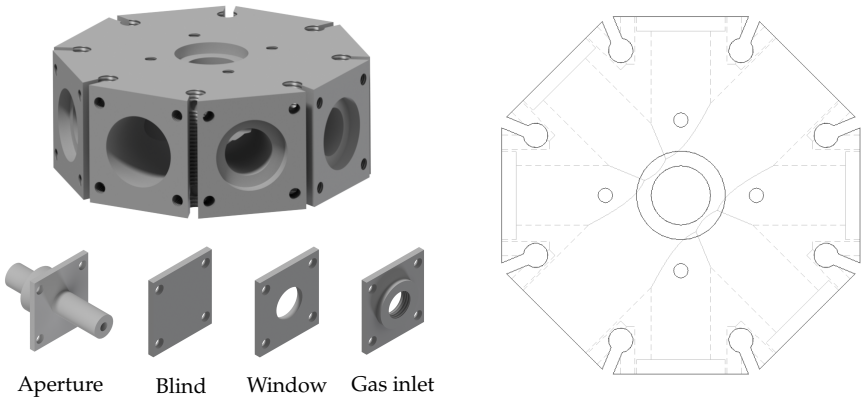

Fig. 3.4: *The developed gas cell has an octagonal shape corresponding with the outer surfaces of the interaction chamber as seen in a rendered picture in the upper left and the wireframe from the top/bottom on the right. All ten connection flanges (one each of the top and bottom as well as eight along its octagonal plane) use compatible threading with different inner diameters depending on the requirements. A multitude of plates can be mounted on these with a few common ones shown in the lower left. The cell itself can be mounted through the eight vertical threadings at its perimeter.*

The cell is mounted through eight vertical and open threadigs at its perimeter, which may be tailored to the specific interaction chamber or orientation it is used in. The adapter developed for this work is a short pipe, which connects through standard CF flanges located in the standard interaction chamber in Section 3.2.1 on one side and to the outer threadings on the cell side. This allows a seal against air in combination with the deep notch mentioned above to make the evacuation of the spectrometer optional.

3.3.2 Dispersed UV photon detection

Two different detector systems were used to cover the wavelength range between 75 nm and 180 nm in emission. Each consisted of a combination of reflective grating and actual detector device with its data acquisition electronics. In both cases, the gratings were ruled with a line density of 1200 mm^{-1}:

- **Vacuum ultraviolet** (VUV) below 130 nm
  A grating blazed at 80 nm was used in conjunction with an open-face MCP stack (i.e. no photocathode) in front of a wedge and stripe anode for position detection.

- **Far ultraviolet** (FUV) above 115 nm
  With a blaze wavelength of 150 nm the grating dispersed here onto an image amplifier using a magnesium fluoride window and caesium telluride photocathode with a delay line anode for position detection.

To combine the results of both detectors into a single dataset during the analysis, the overlap region between 115 and 130 nm is essential.
The principle of a wedge and stripe anode as used for the detector in the VUV regime is shown in Figure 3.5. It separates the incoming charge cloud into three isolated components: wedges, stripes and the meander in between. Following the depicted orientation, the wedges are aligned vertically and thus vary in width along this axis. The portion of the total charge hitting this electrode therefore gives the vertical coordinate, while the increasing thickness of the vertical stripes from left to right then yields the horizontal coordinate with the same approach. The meander fills the space between wedges and stripes and receives the remaining charge. For each electrode, it is measured as a voltage over the typical 50 Ω termination with two amplification stages, an inverting preamplifier and an integrating amplifier. For the resulting signals, an analog-to-digital converter allows determination of the peak height to compute the position for the given event.
In the FUV, the employed image intensifier and delay line anode is depicted in Figure 3.6. In contrast to an open detector like in the VUV, the image intensifier houses the MCP stack in a sealed enclosure. On the forward side, a magnesium fluoride window transmits photons with a wavelength down to 115 nm, which are converted to electrons up to a wavelengths of 300 nm by a caesium telluride film deposited on the inside. After amplification by the MCPs, a resistive screen transfers the charge onto the anode outside

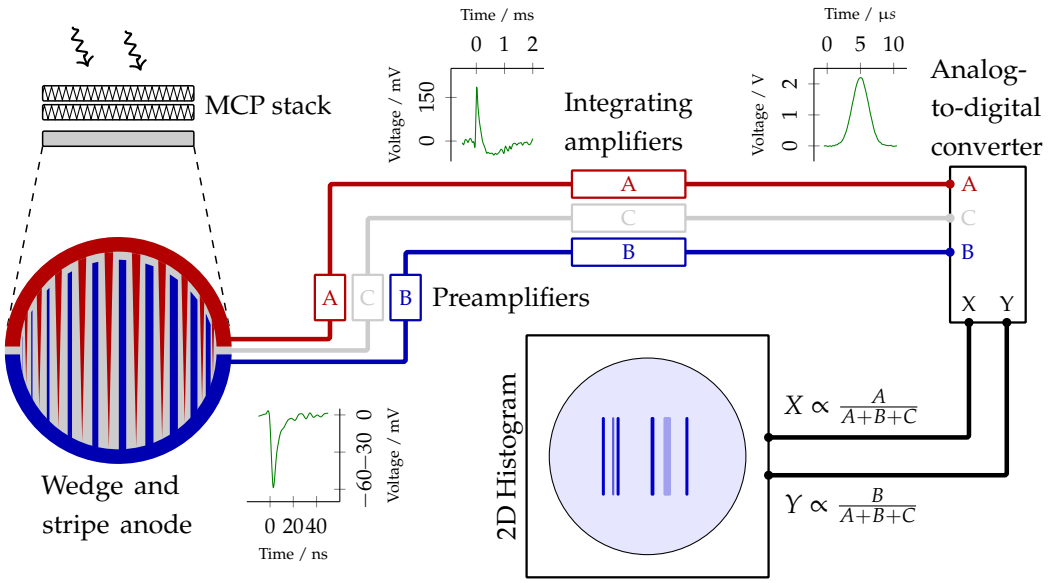

Fig. 3.5: *Photons impinging upon the first MCP of the VUV detector trigger the emission of photoelectrons, which are multiplied through the stack. The anode's separation into stripes and wedges allows the location of this charge cloud. After amplification in two stages, the relative charge distribution for wedge, stripe and underlying meander is measured.*

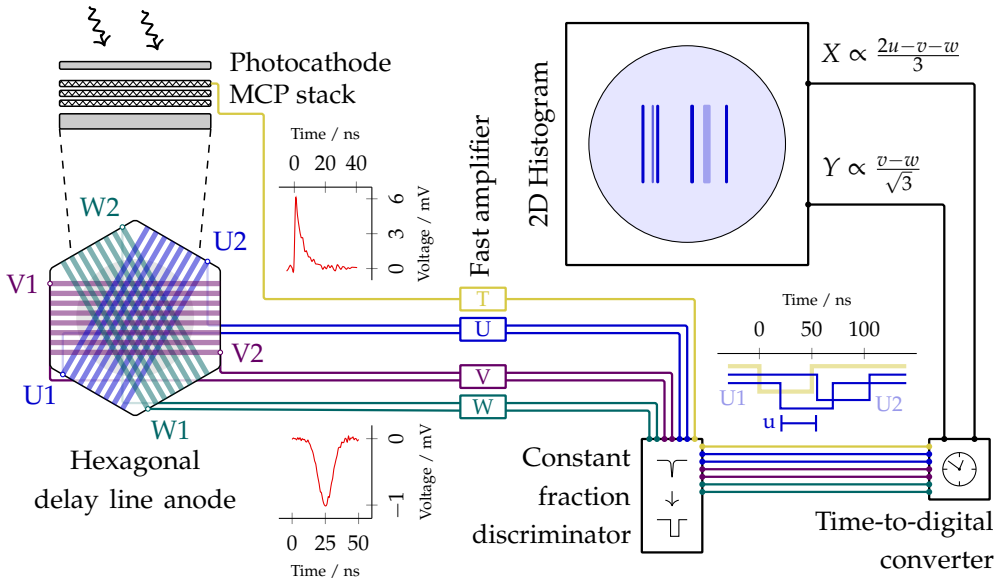

Fig. 3.6: *The photocathode in front of the FUV detector's MCPs enhances the emission of photoelectrons at longer wavelength for multiplication in the stack. The charges then reach three wires mounted in a hexagonal pattern. The arrival times at their respective ends together with the initial time signal caused by electron impactare measured by a TDC after amplification and digitization in a CFD.*

of the intensifier, which consists of three wires placed in a hexagonal pattern. Here the charge travels as a current to both ends of these three delay lines. The difference in arrival times between the ends can be used to locate the impact. This is done by converting the analog signal for each end after amplification of its voltage over a termination of 50 Ω to digital pulses using constant fraction discriminators (CFDs). In addition to these six anode signals, this is also performed for the small voltage drop across the first MCP when the initial electron from the cathode hit, called the MCP signal or time signal. For the resulting seven digital signals, a time-to-digital converter (TDC) measures the time differences using the MCP signal as a common trigger, which in turn can be used to compute the position.

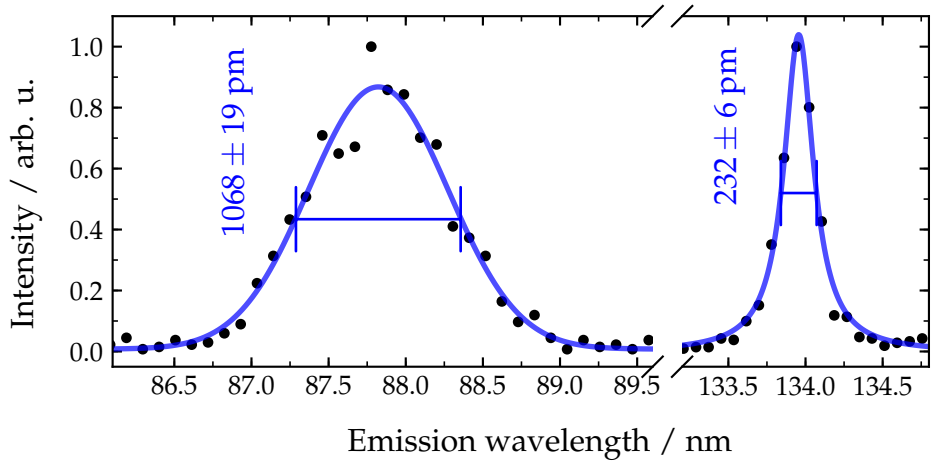

Fig. 3.7: *A small spectral portion in the VUV (left) and FUV (right) demonstrates the achieved resolution with the respective detection systems. The emission lines used here are molecular band transitions of hydrogen with natural linewidths in the range of several fm and a Doppler broadening of < 1 pm. The drawn blue lines are Gaussian (left) and Lorentzian (right) line profiles fitted for the best possible agreement to obtain the annotated FWHM.*

The resolution achieved with these detector systems in conjuction with the spectrometer set-up described in Section 3.2.2 is evaluated in Figure 3.7 for two exemplary lines in each spectral region. The FWHM of fits to their respective line profiles yields:

$$\left(\frac{\lambda}{\Delta\lambda}\right)_{\mathrm{FUV}} \approx 570 \qquad \left(\frac{\lambda}{\Delta\lambda}\right)_{\mathrm{VUV}} \approx 80$$

The utilized transitions to compare these devices belong to molecular band transitions, which allows to neglect both the natural linewidth for fluorescence lifetimes below 1 ns

[AL15] and the Doppler broadening at room temperature. The FUV detector reached a significantly higher resolution as compared to the VUV and a rotational resolution in emission could therefore only be achieved in the FUV spectral region based on a delay line anode. Here it is limited by the horizontal dimensions of the exciting synchrotron radiation beam that passed through the interaction cell, which is reported to be between 200 and 300 µm. For the VUV detector, the broader line profiles are assumed to be caused either by the general anode geometry or the subsequent amplification stages. The electronic readout at 12 bit is capable of relative resolutions of $\lambda/\Delta\lambda > 2000$, while the luminescing column is the same as in the FUV.

3.3.3 Set-up overview and configuration

An overview of the specific experimental configuration used to map the rovibronic emissions of gaseous species is sketched in Figure 3.8. In the center of the interaction chamber, the gas cell presented in Section 3.3.1 is installed. Through the use of long and small apertures for the entrance and exit opening, a high target density within the cell of up to 1 mbar can be reached. The target gas is inserted through a pipe mounted on a side opening of the cell. This density is kept as constant as possible by measuring the pressure within the inlet system measured with a capacitance manometer and controlling a magnetically opened gas valve connected to the backing supply. Isolated circular metal plates are affixed perpendicular to the synchrotron beam passing through the cell. While one plate is set to a positive potential, the current against ground of the other one is measured as a signal proportional to the amount of ionization in the target. On the bottom port of the cell directed towards the spectrometer, a slit with an opening of 500 µm is situated to limit the scattered light. The detector systems introduced in Section 3.3.2 are used on its exit arm. At the downstream end of the interaction chamber, a Faraday cup measures the amount of synchrotron radiation transmitted through the gas cell. This value is used on conjuction with the photocurrent of the last refocusing mirror on the facility side for an estimation of the incoming photon flux I_0.
The developed software framework and application *Metro* controls both the experimental environment parameters such as beamline energy or target pressure and facilitates the readout of all detection devices. It executes a previously programmed measurement plan autonomously to achieve the large number of individually measured points required for a complete emission map in as little time as possible, while still collecting all data

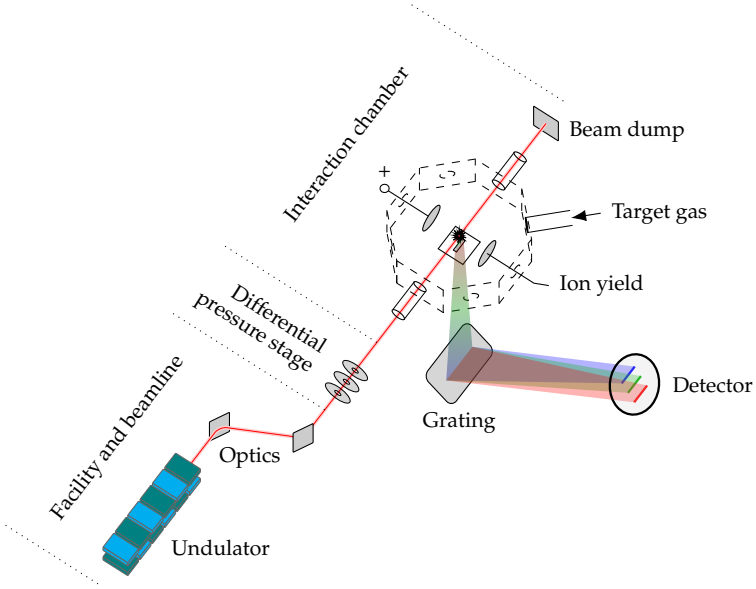

Fig. 3.8: *The complete experiment consists of the components provided by the facility and beamline, the beam transfer through differential pressure stages and the actual interaction chamber. This transfer section separates the facility vacuum from the experimental conditions in the gas cell, which is installed around the radiation's focal point. Through a side port the target gas is introduced, while ion apertures perendicular to the beam axis allow the measurement of ion yields. A slit below the cell projects the emitted luminescence on the grating, which in turns disperses it onto a position-sensitive detector.*

necessary for normalization and calibration. For a typical recording, this includes:

- Photon detector image
- Target ion current
- Beam dump photocurrent
- Refocusing mirror photocurrent
- Capacitance pressure as an analog voltage
- Coil current for magnetically opened target valve
- Beamline energy
- Storage ring current

In addition, the power distribution for the vacuum system is controlled and its current parameters are logged to ensure the facility requirements are fufilled at all times.

3.4 Data analysis

A map of rovibronic emissions consists of a multitude of individual measurements, each covering a small spectral portion for a specific excitation energy. After the spectral reconstruction of a singular measurement, the composition of these along the axis of excitation energy and of emission wavelength is performed. Finally, these axes are calibrated to their respective physical quantities across the complete map.

3.4.1 Singular detector image

For each energy and grating position, the detection devices introduced in Section 3.3.2 collect a number of photons impinging upon the detector. The impact location of each event is inferred by the underlying anode principles shown in Figure 3.5 and Figure 3.6, respectively. This results in an arbitrary point $\mathbf{p} = (x, y)$ that is transformed as $\mathbf{p}'$ into a standardized coordinate system centering the complete detector image within $[0, 1]$ through:

$$\mathbf{p}' = R_\beta \, S \, R_\alpha \, (\mathbf{p} + S\mathbf{t} - \mathbf{a}) + \mathbf{a} \tag{3.1}$$

First, a custom translation $\mathbf{t} = (t_x, t_y)$ is used to center the image. The scaling matrix S allows this quantity to act on the image space of $[0, 1]$ rather than the original signal. Through the use of $\mathbf{a} = (0.5, 0.5)$, the following rotations are applied around the center of the image interval rather than the origin. The matrices R_α, R_β and S here are defined by:

$$R_\alpha = \begin{pmatrix} \cos\alpha & -\sin\alpha \\ \sin\alpha & \cos\alpha \end{pmatrix} \qquad\qquad S = \begin{pmatrix} s_x & 0 \\ 0 & s_y \end{pmatrix}$$

The initial rotation by α aligns the image in such a way that the scaling operation S may correct shape deformations in addition to fitting the image into the target space, while the final rotation by β ensures the dispersion axis is parallel to an axis of the coordinate system, usually the x-axis. These transformed points are projected on a discrete grid on both spatial axes of 512 channels for the interval $[0, 1]$. A two-dimensional histogram of these positions then constitutes the detector image for this measurement. This detector image reveals the dispersed emissions as vertical lines, which are projections of the

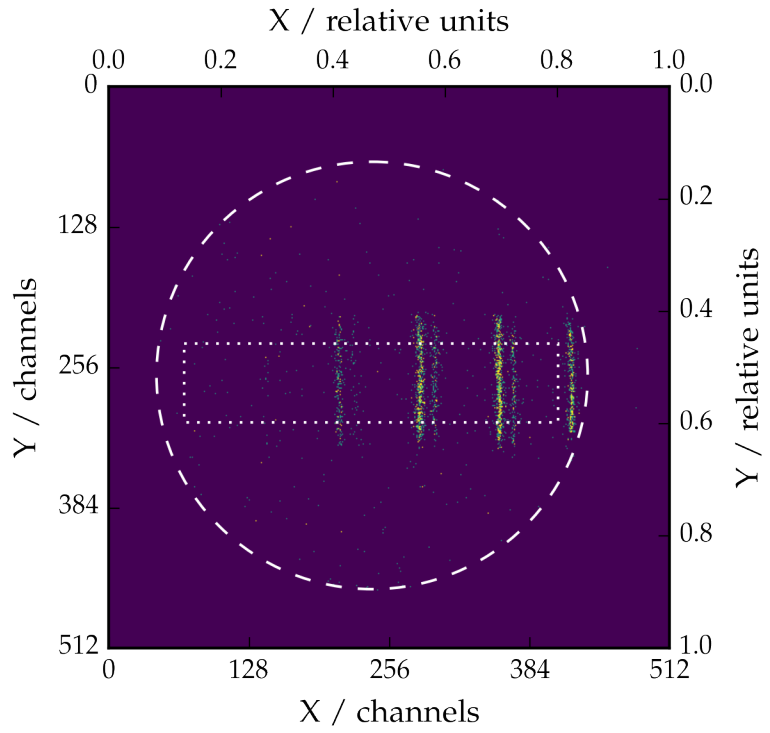

Fig. 3.9: *The detector image is calculated as a two-dimensional histogram of individual photon events on the FUV detector. The grating was positioned for a central wavelength of* $\lambda \approx 125\,\mathrm{nm}$ *with the recorded emissions of molecular hydrogen excited at an incoming photon energy of 11.17 eV. The applied transformation projects the image into the interval* $[0, 1]$*, which in turn is scaled to 512 channels. The dashed circle marks the edge of the detector's active area while the dotted rectangle indicates the region-of-interest used for further analysis.*

entrance slit. In order to reduce the effect of non-linearities towards the edge of the anodes as well as the slit, only a region-of-interest (ROI) around the center is taken. An example is given in Figure 3.9 for a grating position of $\lambda_{\mathrm{center}} \approx 125\,\mathrm{nm}$.

3.4.2 Emission spectra

The measured emission spectrum $R_\theta(l)$ for a grating position θ as a function of the horizontal detector position l is now the result of binning the detector image vertically within its region-of-interest such as in the left plot of Figure 3.10. Due to the proper alignment in the previous step, the original dispersion axis is parallel to the horizontal image axis and represents physically a wavelength scale. The vertical summation adds up all hits at a certain wavelength and thus represents the respective intensity. This

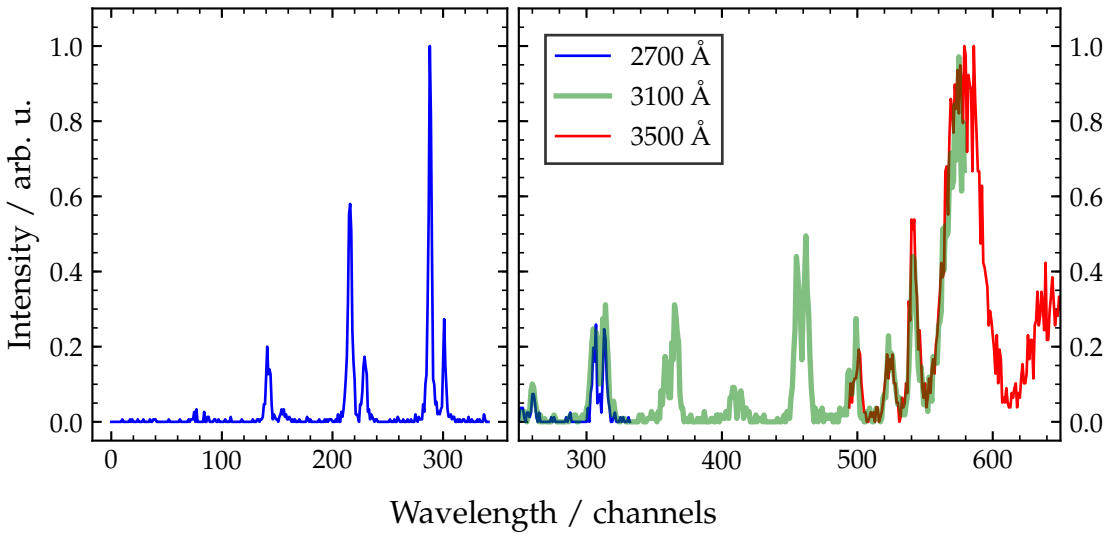

Fig. 3.10: *A partial emission spectrum is shown in the left plot created from the detector image in Figure 3.9 prior to normalization. It resulted from molecular hydrogen excited with a photon energy of 11.17 eV at a central wavelength of* $\lambda \approx 125\,\mathrm{nm}$ *(grating position 2700 Å). The right plot demonstrates the overlap between the partial emission spectra of different grating positions in blue, green and red, respectively. The excitation occured here at a photon energy of 12.5 eV.*

intensity is then normalized to the experimental conditions by the measurement time τ, target density ϱ and incoming photon flux I_0 as well as a correction $Q_0(l)$ to account for properties specific to the experiment, e.g. spatial quantum efficiency on the active detector area. The final result is a partial emission spectrum $I_\theta(l)$ consistent within the data set in relative units:

$$I_\theta(l) = \frac{R_\theta(l)}{\tau \varrho I_0 \, Q_0(l)} \tag{3.2}$$

These normalized partial spectra are obtained once per energy step across the excitation energy range and for each grating position required to cover the relevant spectral range. In the case of hydrogen, this spans the energy range of 11 to 18 eV and the grating positions 1800 Å, 2000 Å, 2200 Å in the VUV and 2700 Å, 3100 Å and 3500 Å in the FUV. These are then composed to a full emission spectrum for the VUV and FUV through overlapping of the spectral sections of each grating position. An example for such a spectral overlap is shown in the right plot of Figure 3.10. Each partial spectrum is translated on the wavelength axis by an amount corresponding to the grating position

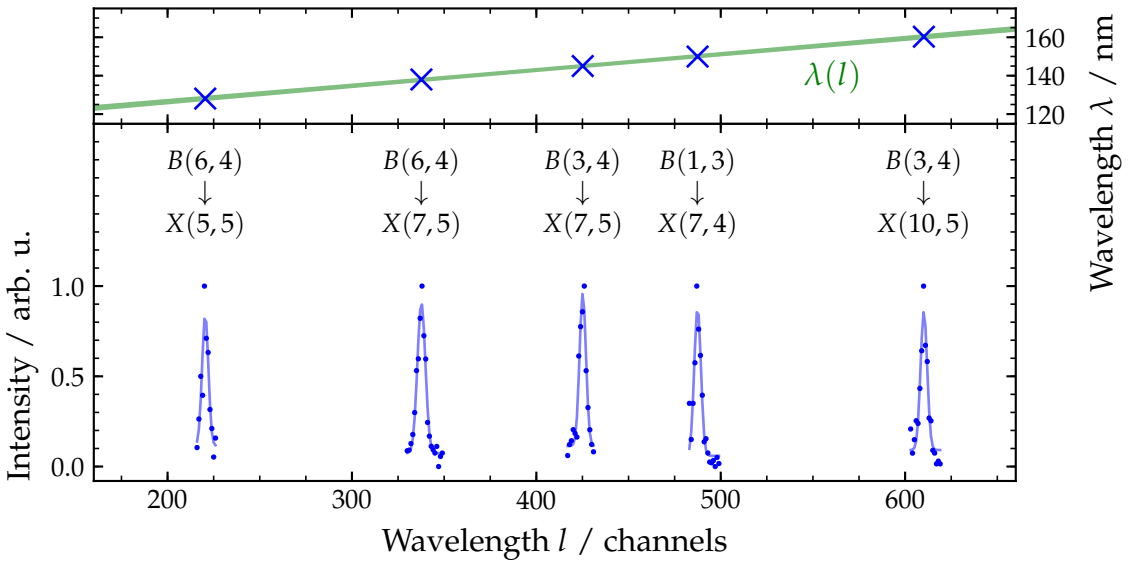

Fig. 3.11: *The wavelength scale is calibrated from the arbitrary channels as an expression of horizontal detector position to the physical quantity by fitting known spectral lines (blue, bottom) and performing a polynomial regression (green) with literature values for the emission (top). This sample shows several of these calibration points in the FUV in the $B\,{}^1\Sigma_u^+$ molecular bands for hydrogen, which originate from measurement at different excitation energies. The uncertainty in the peak position is well below a single channel in all cases, while the fitted plot's linewidth is equivalent to one standard deviation at each point.*

difference and within the overlap region of two spectra, the average of both is taken. The wavelength scale at this point is still expressed by the horizontal detector position, a value dependant on the arbitrary signal levels and the transformation applied in (3.1) followed by a projection onto a chosen number of pixels. The calibration $\lambda(l)$ to calculate the actual wavelength of the incoming photons is obtained for the composite spectra $I_{\mathrm{VUV}}(l)$ and $I_{\mathrm{FUV}}(l)$ of each spectral region independently. A set of spectral lines is identified and their position l is correlated with their known emission wavelength λ from literature or calculations. Figure 3.11 illustrates this process for the FUV of molecular hydrogen with several features in the Lyman band. Since each grating position was kept constant while scanning over the complete interval of excitation energies, the results from any of these excitations may be used for this method. The calibration is performed to wavelength rather than photon energy, since it is the native quantity measured by the spectrometer through dispersion. The inverse relation $E \propto \lambda^{-1}$ between these quantities causes the approximately constant resolution in wavelength to vary

significantly in photon energy. In addition, the results would require interpolation for a linear energy scale. Hence the emission spectra in this work are mostly expressed as a function of wavelength rather than energy or wavenumber. Finally, after the calibration a second correction term $Q_1(\lambda)$ is applied to account for the spectral quantum efficieny of the detection system as a whole, e.g. by the grating's reflectivity or the cathode's photoionization cross section.

3.4.3 Composition along excitation energy and spectral regions

In general, the excitation energy positions assigned to each spectrum may require slight corrections by comparison with literature values for known features in similar manner as the wavelength axis. In the case of the measurements performed in this work, the feedback provided by the beamline facilities were sufficiently precise though as shown in Figure 3.12.

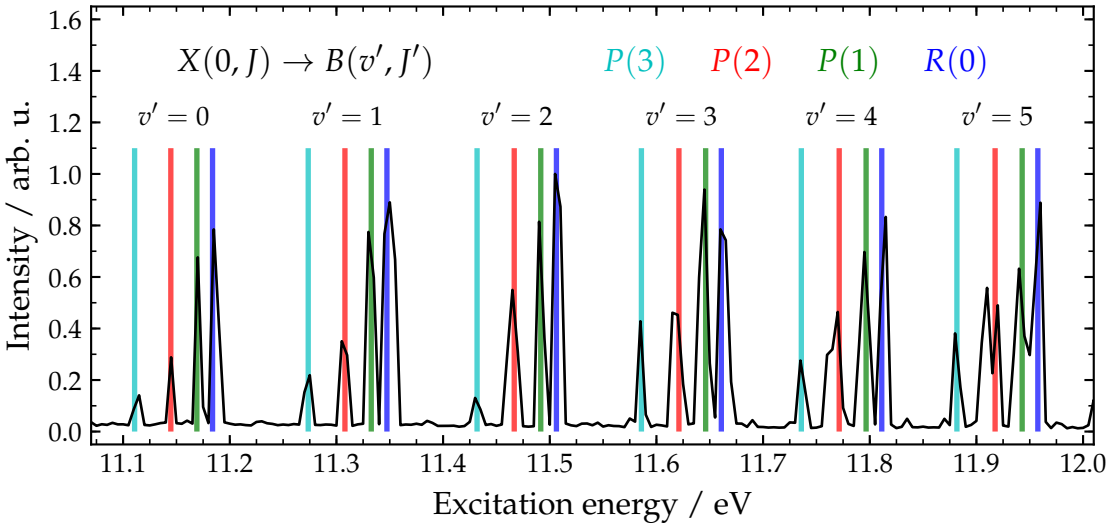

Fig. 3.12: *The energy positions in the excitation function for FUV emissions obtained as a sum over all spectral features is in full agreement with literature values for the Lyman band absorption of molecular hydrogen. The excitation energy axis is taken here from the feedback provided by the beamline without any further calibration.*

In addition to the dispersed luminescence data, the ion yield was measured by installing ion apertures in the gas cell. The generated current at each excitation energy is normalized to the target density ϱ and incoming photon flux I_0 analog to the emission spectra in (3.2), thus yielding the excitation function for ionization of the target gas.

The individual spectra can then be plotted side-by-side as a shaded matrix with the excitation energy varying along the horizontal axis and emission wavelength as the vertical axis. Both spectral regions yield such an emission map individually as shown in Figure 3.13 for molecular hydrogen with both axes fully calibrated. The intensity in such a representation is encoded by a colormap, which has to be chosen carefully for a uniform and authentic description of intensity. The recently developed colormap *viridis* is particularly suited for this application [SvdW15].

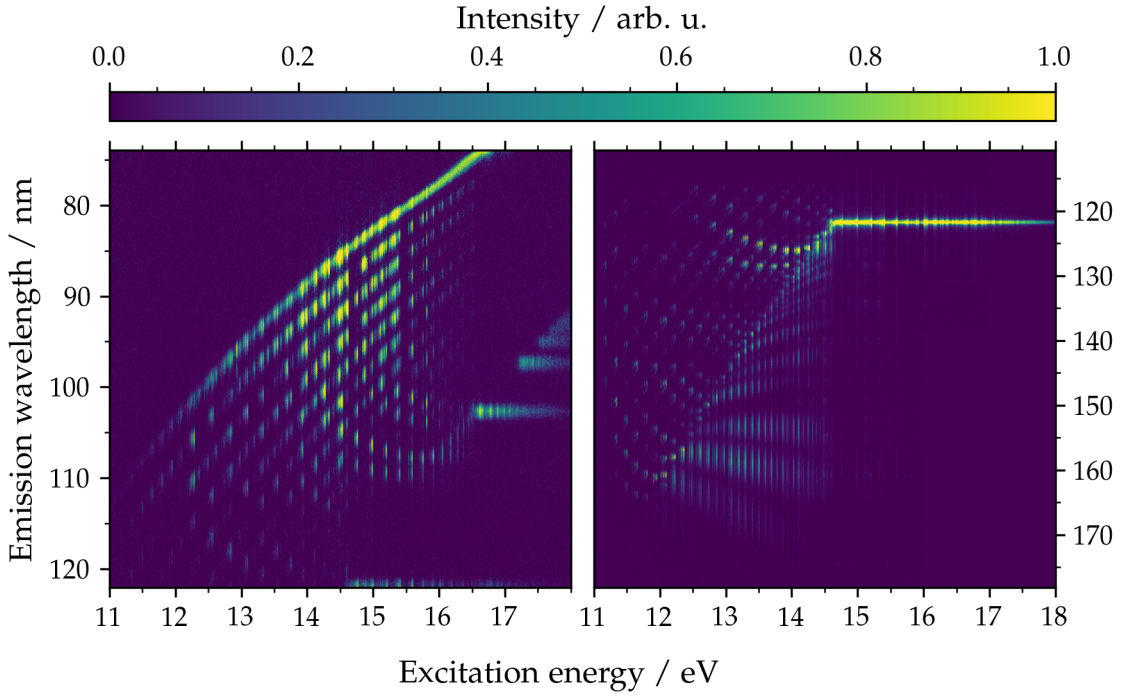

Fig. 3.13: *Emission map of molecular hydrogen in the VUV (left) and FUV (right) individually. The excitation energy axis consists of 2801 measured emission spectra covering the interval in steps of 2.5 meV. A non-linear transformation is applied to the encoded intensities of the colormap to increase the contrast as detailed in* (3.3) *with* $a_{\mathrm{VUV}} = 20$ *and* $a_{\mathrm{FUV}} = 85$.

The dynamic range between very intense emissions (e.g. the Lyman-α line of atomic hydrogen fragments) and the majority of features however is still too large for a singular presentation. The intensity $I(E, \lambda)$ for the emission wavelength λ after an excitation with a photon energy E is hence scaled by a non-linear transformation to I' in order to emphasize dynamics at lower intensities and reduce them at higher ones, where saturation is reached quickly. The emission maps shown in this work use a bounded exponential distribution with a single scaling parameter a to this effect. With the actual

relative intensity $F = I / I_{\max}$ and the scaled relative intensity $F' = I' / I'_{\max}$ after applying the transformation, it is defined by:

$$F' = 1 - \exp(-a\,F) \tag{3.3}$$

This relation is illustrated in the left plot of Figure 3.14 for different values of the scaling parameters a. It causes the scaled relative intensity F' to appear at an actual relative intensity $F = -\ln(1 - F')/a$. For the sample maps in Figure 3.13 with $a_{\mathrm{VUV}} = 20$ and $a_{\mathrm{FUV}} = 85$, an apparent intensity of $F' = 0.99$ is already reached for $F = 0.23$ in the VUV and $F = 0.05$ in the FUV. For lower values of F however, the transformation still preserves an approximately linear behaviour.

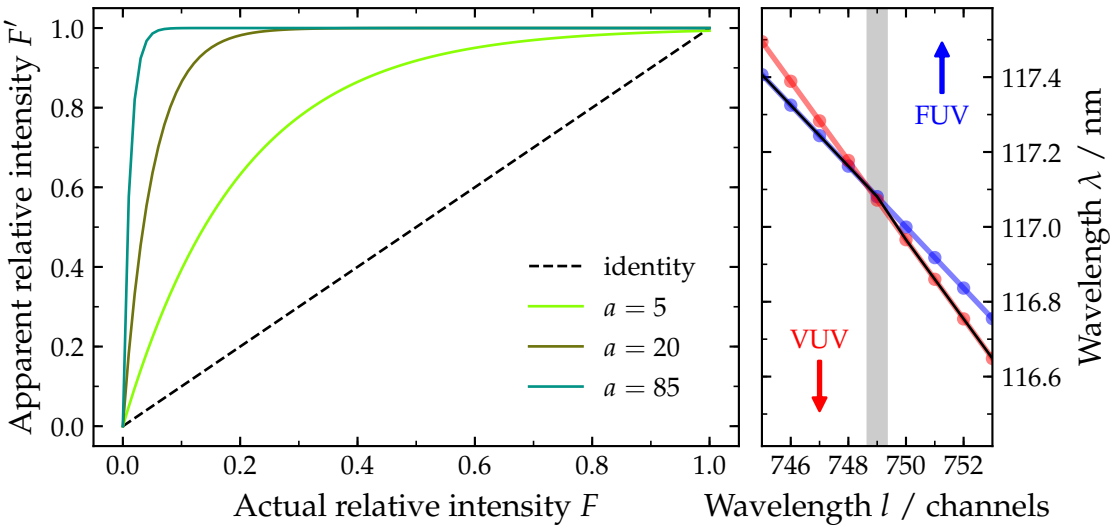

Fig. 3.14: *The non-linear scaling applied to the intensity on the displayed emission maps is shown in the left plot for different parameters a in comparison with the identiy. It projects the dynamic range into a small interval at lower intensities to increase their contrast at the cost of reduced details for intense emissions. The right plot details the intersection between the wavelength calibration in the VUV (red) and FUV (blue) with the grey bar representing the channel offset used between the two spectral regions. The resulting calibration for the composed map is added as a black line.*

In the final step to obtain the complete emission map, the two spectral regions are combined to a single data set. While the general method is the same as for the partial spectra joined earlier (e.g. in the right plot of Figure 3.10), the transition between the wavelength calibrations $\lambda(l)$ of FUV and VUV has to be taken into account, which may

not be continuous. Due to the readily available calibration points in this case, the overlap coincides well with the intersection between the calibration curves as shown in the right plot of Figure 3.14.
A completed result for the emission map is found in Figure 3.15 for molecular hydrogen. An introduction into its visual features is given in Chapter 5. A computational model to obtain such a representation from theoretical means is introduced in the follwing Chapter 4, while a further discussion follows in Chapter 6.

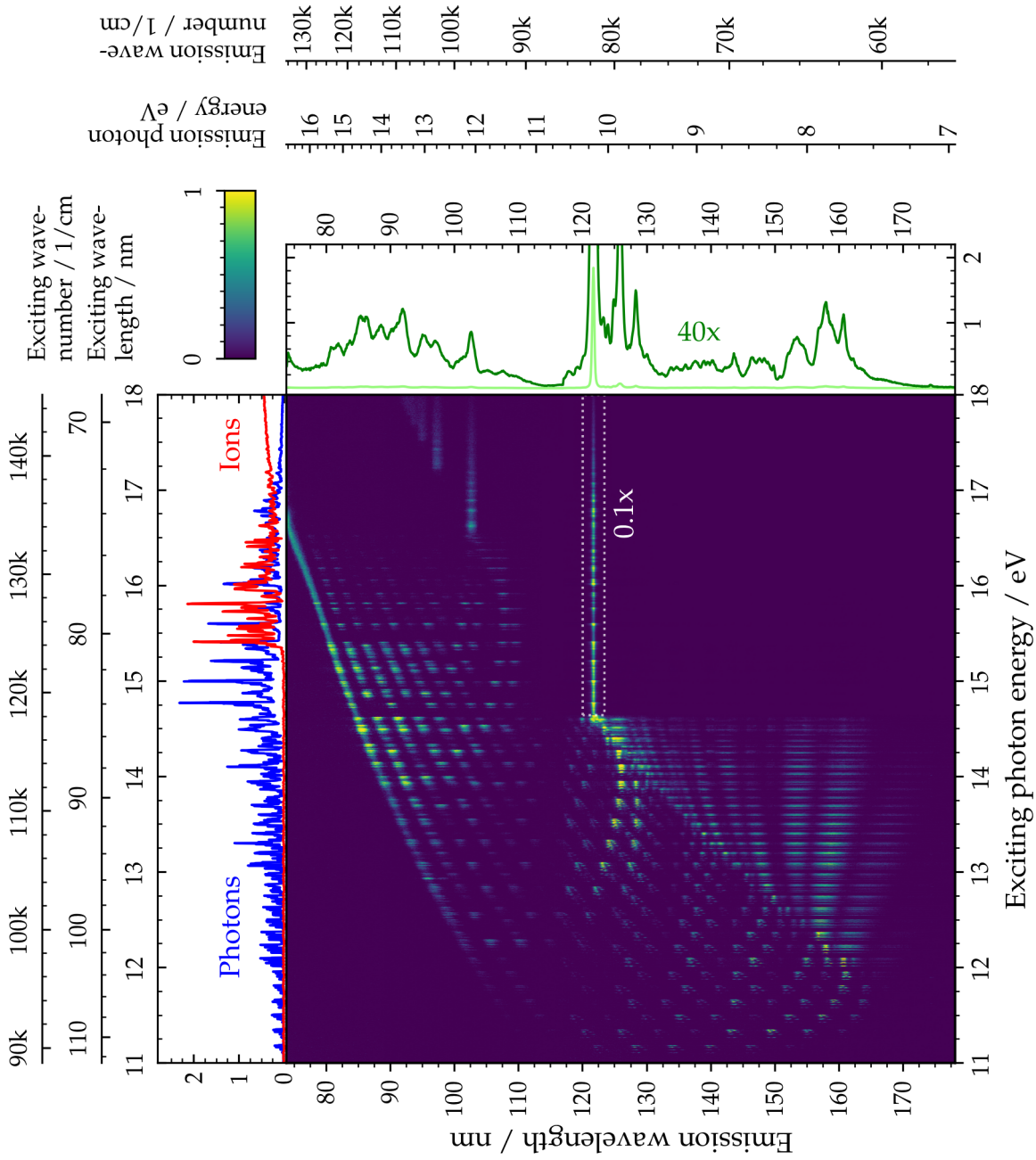

Fig. 3.15: *The complete rovibronic emission map of molecular hydrogen covering all singly excited electronic states. The excitation function for photon emission as a sum in vertical direction (blue) and for ionization (red) is plotted above, while the integrated emission spectrum (green) as a sum in horizontal direction is shown to the right. The Lyman-α line is reduced in intensity before a non-linear intensity scaling with $a = 15$ is used.*

Chapter 4

Computational method

Based on the experimental results, the emission map can be analyzed and understood by the subsequent identification of all the individual components it is comprised of. A complementary approach is to calculate the transitions expected for the involved states and processes and compose these to a simulated emission map. This differential perspective on each of the visible features by themselves helps significantly when navigating emissions maps for the first time.
This chapter describes basic computational methods used to model the emission spectra of diatomic molecules and then simulate the complete emission map. After solving the time-independent Schrödinger equation numerically, the nuclear wavefunctions in the Born-Oppenheimer approximation of all electronic states are applied to estimate the various spontaneous emissions following a single-photon excitation. Several decay mechanisms are then presented and expressed in this framework.

4.1 Solutions to the time-independent Schrödinger equation

As introduced in Section 2.2.4, the radial motion χ of the nuclei describes the separated vibrational and rotational motion in a diatomic molecule. With an alternative formulation of the nuclear kinetic energy operator $\hat{T}_{\mathrm{N}} = \hat{p}^2/2\mu$ as a function of the momentum

operator $\hat{p}$, it can be expressed analog to (2.27) as:

$$\left(\frac{\hat{p}^2}{2\mu} + U(R) - \frac{\hbar^2}{2\mu R^2} J(J+1)\right) \chi(R) = E\,\chi(R) \tag{4.1}$$

The potential energy curves $U(R)$ for the electronic states are obtained from experimental term values or calculations in literature, which may take a variety of corrections into account to increase the accuracy of the Born-Oppenheimer approximation (e.g. [Wol93] for H_2). With these, equation (4.1) is solved numerically by expressing its Hamilton operator $\hat{H}$ as a discrete matrix H on a finite grid and solving the resulting eigenvalue problem

$$H\mathbf{v} = E\mathbf{v} \tag{4.2}$$

to obtain the eigenvalues E as energy levels and eigenvectors $\mathbf{v}$ as a numerical approximation of the respective wavefunction $\chi(R)$. The grid is chosen to discretize the nuclear coordinate R in its domain $[R_{\min}, R_{\max}]$ into N equidistant points of distance ΔR between R_1 and R_N:

$$\Delta R = \frac{R_{\max} - R_{\min}}{N-1} \tag{4.3}$$

$$R_n = R_{\min} + (n-1) \cdot \Delta R \tag{4.4}$$

The boundaries of the internuclear distance depend on the particular geometry of the potential well in each potential energy curve. It typically starts at around $R_{\min} = R_1 \approx a_0/2$ and ends at $R_{\max} = R_N \geq 20a_0$.
In general, the individual matrix elements H_{nm} for an operator $\hat{H}$ can be obtained using a given basis set φ_k with:

$$H_{nm} = \langle \varphi_n | \hat{H} | \varphi_m \rangle \tag{4.5}$$

These are now determined for the chosen and discretized grid. For this purpose, the hamilton operator is separated into three components $H = H_{\text{kin}} + H_{\text{pot}} + H_{\text{rot}}$ analog to its summands in (4.1).
The latter two terms are trivial, as they can be expressed as a diagonal matrix in position space using the base set $\phi_{r'}(r) = \delta_{rr'}$ of the position operator. For the potential energy

operator, these diagonal elements are equal to the potential $V(R)$ evaluated on each point of the grid:

$$H_{\text{pot}} = \begin{pmatrix} V(R_1) & & 0 \\ & \ddots & \\ 0 & & V(R_N) \end{pmatrix} \tag{4.6}$$

For the rotational component, the rotational quantum number J is treated as a parameter and then yields correspondingly:

$$H_{\text{rot}} = \frac{\hbar^2}{2\mu} J(J+1) \begin{pmatrix} R_1^{-2} & & 0 \\ & \ddots & \\ 0 & & R_N^{-2} \end{pmatrix} \tag{4.7}$$

The momentum operator $\hat{p}$ used in the kinetic component H_{kin}, however, has the representation $\hat{p} = -i\hbar\,\partial/\partial r$ in position space. As the basic vectors here are not eigenfunctions of this operator, it cannot be represented as a diagonal matrix in the same way. But in momentum space, this operator is reduced to $\hat{p} = p$ and the basic vectors there are its eigenfunctions again. This approach of solving the kinetic component H_{kin} in momentum space is often called the Fourier grid Hamiltonian (FGH) method and described originally in [MBK89]. Using the de-Broglie relation $p = \hbar k$, the momentum is given by the wavenumber k. This in turn can be modelled numerically in this grid by the set of integer ratios the total internuclear distance is defined in:

$$A_n = -\frac{N}{2} + 1, \ldots, \frac{N}{2} \tag{4.8}$$

$$k_n = A_n \cdot \frac{2\pi}{R_N - R_1} \tag{4.9}$$

Since this representation has been performed in momentum space, while (4.2) is to be solved in position space, the basis for the momentum operator is represented in terms of plane waves $\phi_k(r) = (2\pi)^{-1/2} \exp(ikr)$. The position r is modelled in this case by:

$$r_n = \frac{n}{N} \cdot (R_N - R_1) \tag{4.10}$$

A useful form of this basis set for its later application in H_{kin} is as a matrix ϕ, where k and r vary along its columns and rows using their quantizations in (4.9) and (4.10), respectively:

$$\phi = \frac{1}{\sqrt{2\pi}} \begin{pmatrix} \exp\left(2\pi i \, A_1 \, \frac{1}{N}\right) & \dots & \exp\left(2\pi i \, A_N \, \frac{1}{N}\right) \\ \vdots & \ddots & \vdots \\ \exp\left(2\pi i \, A_1 \, \frac{N}{N}\right) & \dots & \exp\left(2\pi i \, A_N \, \frac{N}{N}\right) \end{pmatrix} \tag{4.11}$$

The calculation of the individual matrix elements for the kinetic energy component of $\hat{H}$ are then just matrix operations between ϕ and the vector $\mathbf{A}$ defined in (4.8):

$$H_{\text{kin}} = \frac{p^2}{2\mu} = \frac{\hbar^2}{2\mu} (R_N - R_1)^{-2} \, \phi^* \mathbf{A}^{\mathrm{T}} \mathbf{A} \, \phi \tag{4.12}$$

The eigenvalues E and -vectors $\mathbf{v}$ for the final matrix H are determined using the QR algorithm [GG97] for Hermitian matrices in LAPACK [ABB99]. Each element in the eigensystem represents a vibrational level of the molecule in a specific electronic state (expressed by its potential $V(R)$) and rotational quantum number J.
The result set contains both the bound vibrational levels up to the dissociation limit as well as unbound continuum levels beyond it. Due to the nature of this approach, the latter are also discrete. This can be interpreted physically as them being sampled at regular intervals on the potential energy scale above the limit at a particular E_k with continuous interpolation between them. The highest continuum energy within the result set of the computation as well as the energy spacings between the levels are determined by the grid's geometry. The discretization of the internuclear distance defines a smallest expressable wavelength and hence a highest energy. The potential energy axis in turn is divided into finite elements between the ground state and this maximal energy level and yields the spacing between the levels. With the squared grid sizes and equidistant approach used in this work, these two values are correlated. In cases where a smaller spacing is required, an interpolation is used instead to obtain continuous solutions to an arbitrary degree.
An exemplary result is shown in Figure 4.1 for the ground state of hydrogen for all bound vibrational levels, a continuum level as well as the finer rotational structure. The continuum included here is the result with index $v = 60$ and lies at $E_k = 0.46\,\text{eV}$, while

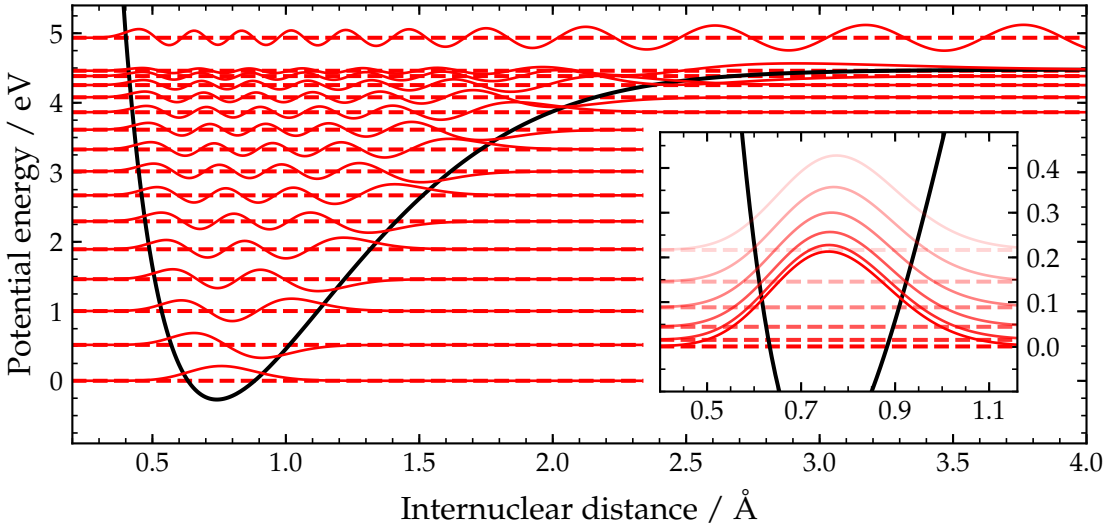

Fig. 4.1: *The nuclear wavefunctions (red solid) of the* $X\ ^1\Sigma_g^+$ *state of molecular hydrogen as a function of the internuclear distance is shown in the electronic potential of this state (black) at their respective energy level (red dashed). The 15 bound vibrational levels as well as a continuum level at* $E_{k''} = 0.46\,\mathrm{eV}$ *(*$v = 60$ *in the numerical discretization) are included. For each vibrational level, only the rotational ground state is shown while the small inset in the lower right compares the lowest rotational excitations for the* $v = 0$ *state.*

the highest bound level is $v = 14$. In the following Section 4.2, these continuum levels are referred to by their discretized vibrational level v as a direct extension of the bound states for the purpose of calculations. The lowest of these continuum levels just above the highest bound state is designated v_{limit}. Therefore all levels $v < v_{\mathrm{limit}}$ represent bound states and all $v \geq v_{\mathrm{limit}}$ lie in the vibrational continuum.
The wavefunctions $\chi(R)$, obtained from the eigenvectors $\mathbf{v}$, are normalized to satisfy the condition:

$$\int_{-\infty}^{\infty} |\chi(R)|^2 \,\mathrm{d}R = 1 \tag{4.13}$$

For the equidistant grid as defined above, the discretization changes the integral to a sum over all grid elements and this normalization can be performed by:

$$\chi(R) = \zeta(\mathbf{v}) \frac{\mathbf{v}}{\sqrt{\sum_i v_i \,\Delta R}} \tag{4.14}$$

The term $\zeta(\mathbf{v})$ takes the values 1 or -1 to correct the phase's sign, which is left undefined by the algorithm applied above to solve the eigenwert problem. While not of relevance to compute square integrals for transition probabilities, it is necessary for the sign to be consistent in the complete eigensystem for the later interpolation of continuum states. For this work, it is always chosen in such a way to conform with a positive amplitude of the rovibrational ground state $v = 0, J = 0$.
The normalization condition in (4.13) assumes unity over the numerical grid and all bound wavefunctions completely vanish there. However, this does not apply to the discretized wavefunctions of continuum states $v \geq v_{\text{limit}}$, whose probability density extends to $R \to \infty$ with nonnegligible values. Instead, if those eigenvalues grow exponentially with their vibrational quantum number v, i.e. they follow an exponential function with parameters E_0, K, γ in the form

$$E_v = E_0 + Ke^{\gamma v} \tag{4.15}$$

the normalization may be performed on the basis of a density of eigenstates $\rho(E_v)$ around any eigenvalue E_v in the continuum [MMR88]. The properly normalized wavefunction $\chi(r)$ of a discretized continuum state can then be obtained from the wavefunction $\tilde{\chi}(R)$ normalized to unity by $\chi(R) = \sqrt{\rho(E_v)}\,\tilde{\chi}(R)$. For $\gamma < 2$, that is for small energetic spacings between the sampled energies, the density may be approximated by:

$$\rho(E_v) \approx \frac{2}{E_{v+1} - E_{v-1}} \tag{4.16}$$

These conditions are both easily fulfilled for the solutions obtained in this work for molecules and grid sizes $N \geq 1024$. An example is found in Figure 4.2 for the ground state $X\ ^1\Sigma_g^+$ of H_2. Following the region of bound levels, the sample spacing increases exponentially here. Typical values for γ with $N = 2048$ for this species range from $\gamma_{B'} = 0.002$ for the $B'\ ^1\Sigma_u^+$ state to $\gamma_B = 0.03$ for $B\ ^1\Sigma_u^+$.

4.2 Calculation of emission spectra

The emission spectra recorded with the PIFS method as outlined in Chapter 3 are the result of an excitation using synchrotron radiation from the ground state q into an excited state q', which then decays via various mechanisms involving a photon emission to a

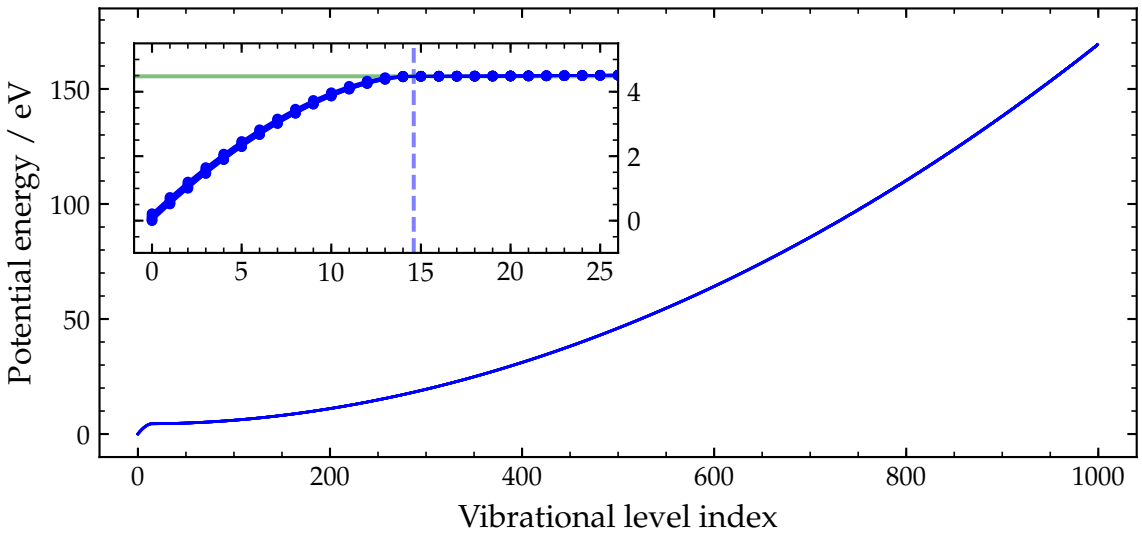

Fig. 4.2: *The energy position of vibrational levels as obtained by solving the Schrödinger equation numerically for the electronic ground state of molecular hydrogen with $J = 0$. The levels $v < v_{\mathrm{limit}} = 15$ are bound states, while $v \geq v_{\mathrm{limit}}$ describe the discretized levels in the dissociation continuum. This boundary (blue dashed line) is apparent by a change in gradient (small inset) and at the dissociation limit of the ground state potential (green solid line). The energetic spacing between the continuum levels grows exponentially with the vibrational quantum number v.*

relaxed state q''. The bandwidth of the incoming radiation is small with regards to the differences between energy levels in the molecular systems, yet large compared to the line broadenings at the experimental conditions. To simulate its results, a Gaussian spectral shape may be used for the exciting pulse $G_{h\nu}$ with photon energy $h\nu$ and bandwidth $\Delta E_{h\nu}$ and for the luminescence R emitting at E_{rlx} with width ΔE_{det}:

$$G_{h\nu}(E) = \frac{1}{\sigma_{h\nu}} \exp\left(-\frac{1}{2}\left(\frac{E - h\nu}{\sigma_{h\nu}}\right)^2\right) \tag{4.17}$$

$$R(E, E_{\mathrm{rlx}}) = \frac{1}{\sigma_{\mathrm{det}}} \exp\left(-\frac{1}{2}\left(\frac{E - E_{\mathrm{rlx}}}{\sigma_{\mathrm{det}}}\right)^2\right) \tag{4.18}$$

The excitation bandwidth $\Delta E_{h\nu}$ as well as the detector resolution ΔE_{det} is meant as a full width at half maximum and connected to the standard deviation parameter used in these definitions by $\Delta E_x = 2\sqrt{2\ln 2}\,\sigma_x$. As discussed in Section 3.3.2, the linewidth ΔE_{det} is completely dominated by the detector resolution and allows to neglect the

natural linewidth and Doppler broadening. Hence the spectral intensity distribution $I(E)$ emitted after such an excitation is

$$I(E) = \sum_{q',q''} B_{qq'}\, G_{h\nu}(E_{q'} - E_q)\, A_{q'q''}\, R(E, E_{q'} - E_{q''}) \tag{4.19}$$

with the Einstein coefficients $B_{qq'}$ for the excitation via absorption of a photon and $A_{q'q''}$ for the subsequent spotaneous emission as defined in Section 2.3.1 to express the respective transition rates.
In a diatomic molecule, this may be understood in excitation as a transition between rovibronic states, that is a transition

$$q(v, J) \to q'(v', J') \tag{4.20}$$

between two different electronic states q, q' including a possible change in their respective vibrational level v and rotational level J. As derived in (2.39) and (2.40), the Einstein coefficients for these processes are given by the matrix elements of the dipole operator d_{qq}. In the Born-Oppenheimer approximation, these can be expressed by the Franck-Condon factor, i.e. the squared overlap of the nuclear wavefunctions χ, χ' (in the respective vibrational rotational level) weighted with the electronic transition moment $d^{(\mathrm{e})}_{qq'}(R)$ and the Hönl-London formulae $S_{JJ'}$ as:

$$B_{qq'} \propto S_{JJ'} \left| \int \chi' \chi\, d^{(\mathrm{e})}_{qq'}(R)\, \mathrm{d}R \right|^2 \tag{4.21}$$

$$A_{q'q''} \propto \left(E_{q'} - E_{q''}\right)^3 B_{q'q''} \tag{4.22}$$

With the computations performed in Section 4.1, the nuclear wavefunctions are available for all electronic states to be expected in emission including their vibrational and rotational excitations. The transition moments $d^{(\mathrm{e})}_{qq'}(R)$ contain the dependance of the electronic matrix element on the nuclear coordinate and are, similar to the potential energy curves, taken from accurate calculations available in literature [WS03a, WS03b], if available. As this dependence is usually rather smooth, it may be approximated as constant in all other cases (called the Condon approximation) [Her50a]. This slightly shifts the ratio between individual v, v' bands, but does not change their trend in general. The Hönl-London formulae only depend on the change of the orbital momentum

and rotational quantum number and are independent of the actual molecular species [Her50a].
Among the decay mechanisms that govern the process $q' \rightarrow q''$, the most prominent ones within the scope of this work are molecular bands, continuum emissions and luminescence from fragments. They each require a slightly different approach in order to use the developed formalism based on (4.21) and (4.22) as well as its numerical solutions. In particular, this involves the interaction with the discretized vibrational continuum and coupling between electronic states in the latter two cases.
Common among all decay paths is the initial ground state q, which in the case of molecular hydrogen is $X\,{}^1\Sigma_g^+$ with a thermal distribution of its vibrational and rotational levels. This population N_i of any rovibrational state i with energy E_i and degeneracy g_i in the thermodynamic equilibrium at temperature T can be modelled in general by a Maxwell-Boltzmann distribution:

$$N_i = \frac{N}{Z} g_i \exp\left(-\frac{E_i}{k_\mathrm{B} T}\right) \tag{4.23}$$

The factor N/Z with the total number of particles N and partition function Z serves to normalize this distribution to $\sum N_i = N$. At room temperature, all species investigated in this work remain limited to $v = 0$ in their ground state due to

$$E(v = 1) \gg k_\mathrm{B} \cdot 300\,\mathrm{K} \approx 13\,\mathrm{meV} \geq E(J = 1)$$

The rotational excitation however is already significant and exceeds $J = 0$ in all cases. Using (4.23), the relative rotational population for any level J can be obtained by using the degeneracy $g_J = (2J + 1)$ and the normalization constant A to ensure $\sum N_J/N = 1$:

$$\frac{N_J}{N} = \frac{(2J+1)}{A} \exp\left(-\frac{E_J}{k_\mathrm{B} T}\right) \tag{4.24}$$

For molecular hydrogen, this results for $J \leq 3$ to a relative population of 0.13, 0.66, 0.12, 0.09, respectively. All higher levels $J \geq 4$ contribute with less than 0.01 combined.
Exemplary results for the spectral intensity distribution $I(E)$ based on (4.19) are shown in Figure 4.3 for two different excitation energies with different emission features appearing. The excitation of molecular hydrogen at 14.03 eV populates almost exclusively the $v' = 24$ level of $B\,{}^1\Sigma_u^+$ leading to both molecular bands into bound levels of the ground state

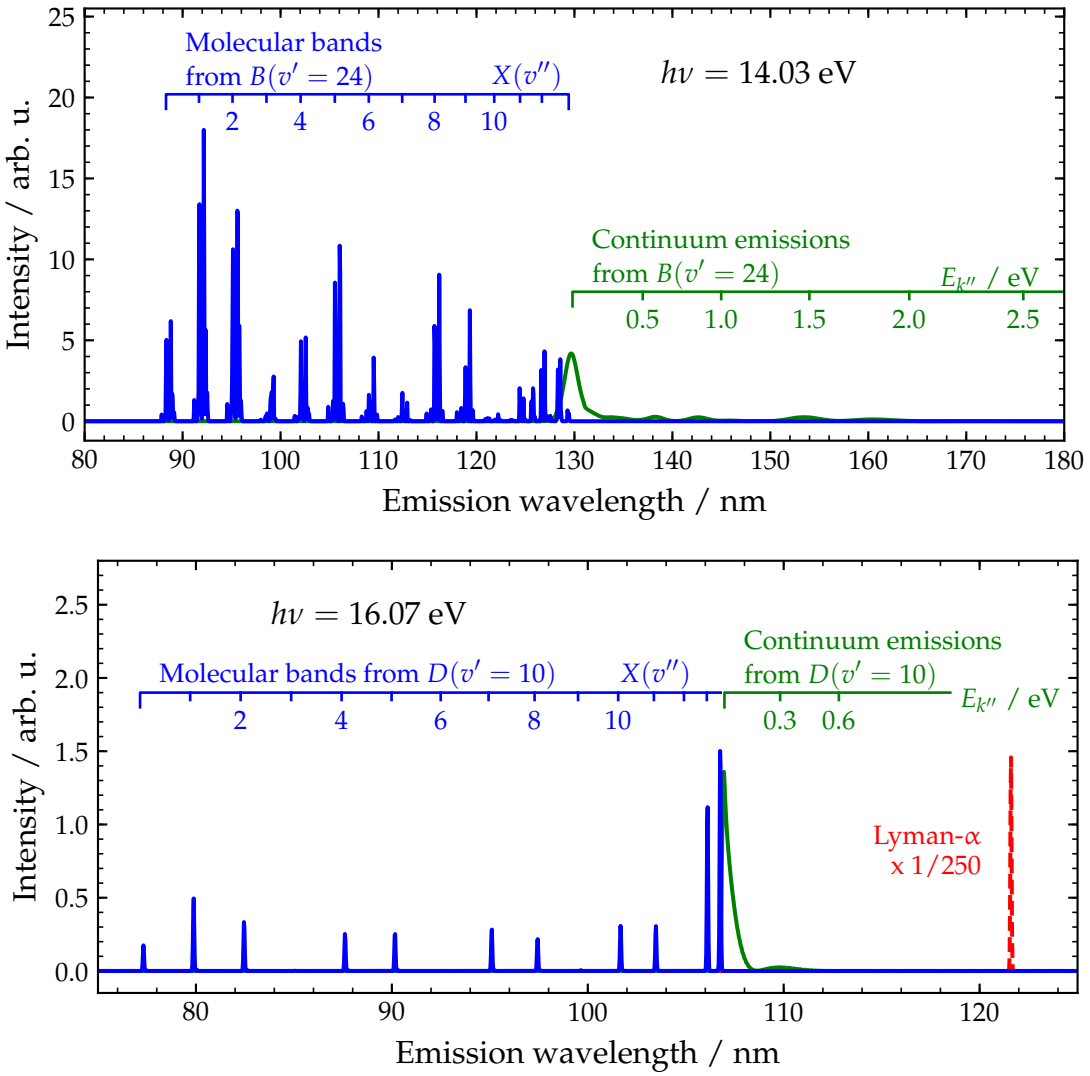

Fig. 4.3: *Two examples for calculated emission spectra of molecular hydrogen after excitation by synchrotron radiation with a photon energy of* $h\nu = 14.03\,\mathrm{eV}$ *(upper) and* $h\nu = 16.07\,\mathrm{eV}$ *(lower). In both cases, the excitation had a bandwidth of* $\Delta E_{h\nu} = 20\,\mathrm{meV}$ *while being recorded at a detector resolution of* $\Delta\lambda_{\mathrm{det}} = 70\,\mathrm{pm}$*. In the upper spectrum, the* $v' = 24$ *level of the* $B\,{}^1\Sigma_u^+$ *state is excited primarily and results into subsequent molecular bands (blue) and continuum emissions (green). In the lower spectrum, strong Lyman-α emissions from H(2p) fragments indicate the dissociation of several electronic states, while weak molecular bands as well as continuum emissions from the higher* $D\,{}^1\Pi_u(v' = 10)$ *state are also visible.*

as well as broad unbound emissions into its continuum. Small contributions from $C\,^1\Pi_u(v'=8)$ and $D\,^1\Pi_u(v'=0)$ are found within the band structure as well. The other depicted excitation at 16.08 eV is beyond the first dissociation threshold and those states converging to H(2p) + H(1s) lead to strong Lyman-α luminescence, the transition H(2p) $\rightarrow$ H(1s) in the hydrogen atom, from their fragments. There are still weak bands and continuum emissions from higher states such as $D\,^1\Pi_u(v'=10)$, but significantly less than the atomic line.

Molecular bands

The band structure of molecules denotes the regular type of transition described in (4.20). After the absorption of a photon, the molecule is excited from the ground state q to a higher electronic state q' with $\Delta v \geq 0$ and $\Delta J = 0, \pm 1$ depending on the particular selection rules (see Section 2.3.2). This state then decays by another transition to a lower electronic state, which for this work is in general the ground state $q'' = X$ with any allowed vibrational and rotational excitation:

$$\begin{aligned} & X(v=0; J=0,1,2,3) \\ \rightarrow\ & q'(0 \leq v' < v'_{\text{limit}}; J' = J, J \pm 1) \\ \rightarrow\ & X(0 \leq v'' < v''_{\text{limit}}; J'' = J', J' \pm 1) \end{aligned}$$

This kind of transition only occurs between bound vibrational levels of each respective electronic state with the highest bound vibrational level obtainable as shown in Figure 4.2. The entirety of the molecular bands can be modelled by inserting all states q' accessible via dipole selection rules with all v' up to their vibrational limit v'_{limit} as well as $0 \leq v'' < 15 = v''_{\text{limit}}$.

Continuum emissions

The hydrogen molecule is capable of radiative transitions into the vibrational continuum of a lower state to form the Condon diffraction bands. For this work, the process from the various electronically excited states q' with bound vibrational level into the continuum

of the ground state is most relevant:

$$\begin{aligned} & X(v=0; J=0,1,2,3) \\ \rightarrow\ & q'(0 \leq v' < v'_{\text{limit}}; J' = J, J \pm 1) \\ \rightarrow\ & X(v'' \geq v''_{\text{limit}}; J'' = J', J' \pm 1) \end{aligned}$$

For pratical purposes, v'' may be restricted to vibrational levels not too far away from the molecular potential well, i.e. somewhat close to the dissociation limit, where the emission intensity does not vanish completely. The spectra calculated in this work therefore confine the relaxed state to $v''_{\text{limit}} \leq v'' \leq 150$ in the case of molecular hydrogen. This kind of treatment of continuum levels with the discrete solutions obtained by (4.2) requires the condition that the energetic spacing between these levels is sufficiently smaller than the assumed detector resolution ΔE_{det}. Depending upon the grid geometry, this is not necessarily fulfilled for all electronic states. Linear interpolation between neighboring continuum levels is used to retrieve the energies $\tilde{E}$ and wavefunctions $\tilde{\chi}$ for arbitrary indices $w \in \mathbb{R}$, which are then akin to the real momentum of an actual continuum level. Using $x = w - \lfloor w \rfloor$, this interpolation is performed by:

$$\begin{aligned} \tilde{E}_w &= (1-x)E_{\lfloor w \rfloor} + xE_{\lceil w \rceil} \\ \tilde{\chi}_w &= (1-x)\chi_{\lfloor w \rfloor} + x\chi_{\lceil w \rceil} \end{aligned}$$

An example of this is shown in Figure 4.4 by interpolating the actually known level $v = 82$ by the discretized level below and above it, i.e. its closest known integer neighbors $\lfloor w \rfloor \equiv v - 1 = \underline{v} = 80$ and $\lceil w \rceil \equiv v + 1 = \overline{v} = 84$. While this approximation behaves poorly for large internuclear distances, even for wide states such as $B\ ^1\Sigma_u^+$ the transitions only occur at distances of $R \leq 8$ Å. The interpolation depends critically on the correct sign of the phase relation between the used wavefunctions to avoid destructive interference, which is ensured by the correction term $\zeta(\mathbf{v})$ in (4.14).

Atomic fragments

An excitation from the ground state into the vibrational continuum of an electronic state will rapidly dissociate the molecule into fragments, in the case of hydrogen these are two hydrogen atoms. Initially, they are in an excited state nl themselves depending upon the

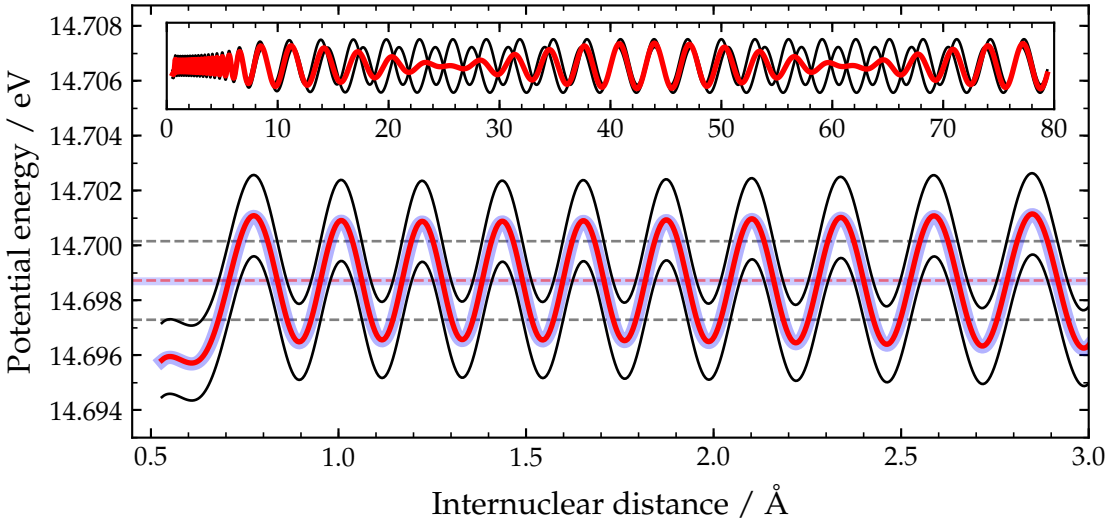

Fig. 4.4: *The energy level and wavefunction for $v = 82$ of the $B\,{}^1\Sigma_u^+$ state has been interpolated (blue) between $\underline{v} = 80$ and $\overline{v} = 84$ (both black) and compared to the result as obtained from the original calculation (red). The agreement is excellent for smaller internuclear distances $R \leq 10\,\text{Å}$ above the potential well and starts to deviate significantly for $R \gg 10\,\text{Å}$ due to a phase mismatch. As all considered transitions occur at $R \leq 8\,\text{Å}$, these differences can be ignored.*

symmetry of the dissociating state, which may then result in a radiative transition into their ground state. For the processes within this work, it is sufficient to assume this may only apply to one of the fragments. Hence the process can be summarized by:

$$\begin{aligned} & X(v = 0; J = 0, 1, 2, 3) \\ \rightarrow\ & q'(v' \geq v'_{\text{limit}}; J' = J, J \pm 1) \\ \rightarrow\ & \text{H}(nl) + \text{H}(1\text{s}) \end{aligned}$$

The transition into the dissociating molecular state q' can still be modeled using (4.22). Under the assumption that this population is identical to that of the forming $\text{H}(nl)$ atoms, their emissions may be obtained using the respective atomic branching ratios. As with the previously discussed continuum emissions, the upper vibrational level v' may be limited for practical purposes, in this case to around $E_{v'} \approx 18\,\text{eV}$ or $v' \approx 1000$. The spacing of the *discrete* vibrational continuum levels must in this case be smaller than the exciting bandwidth $\Delta E_{h\nu}$ and may require an interpolation in the same way.

Limitations of this method

The process described above for the emissions of atomic fragments only covers the direct excitation into vibrational levels in the continuum beyond the dissocation limit. The excitation function for the Lyman series of molecular hydrogen however exhibits a wide range of resonances attributed to predissociation of bound level of higher electronic states, e.g. the $^1\Pi_u^+$ component of D for $v' \geq 3$ through direct or indirect coupling with the continuum of primarily $B'\ ^1\Sigma_u^+$ [LSJ12b]. Due to the purely adiabatic ansatz of this model, it is not able to express this coupling between different electronic states. But as the predissociation yields of most states required for the emission map are well known [GBGM79], they can be approximated by treating excitation into the unstable levels partially as a dissociation with the subsequent emission from the created fragments, i.e. an emission at the respective constant atomic line rather than in the molecular band.
The same issue applies for autoionization beyond ionization threshold of 15.43 eV, because the H_2 molecule and its isotopologues possess the rare property to have several vibrational levels in this energy region that are stable against this process and still emit fluorescence. The competition between these decay mechanisms has been investigated for the majority of states [GMJS10] and found to selectively quench emissions.

4.3 Emission map composition

The spectral intensity distribution $I(E)$ in (4.19) is equivalent to the result of measuring at a single excitation energy in the context of the experimental results. In order to map all the rovibronic emissions, this spectrum is now calculated over a wide range of excitation energies and plotted side-by-side as a shaded matrix of $E_{h\nu}$ and emission energy or wavelength. The result is shown in Figure 4.5 for the complete regime of singly excited electronic states as it was performed in the experiment.
The same non-linear colormap was used as described in Section 3.4.3. An introduction into the visual features arising from this representation is given in the following Chapter 5. The differences between this elementary computation model and the experimental results are discussed in Chapter 6.

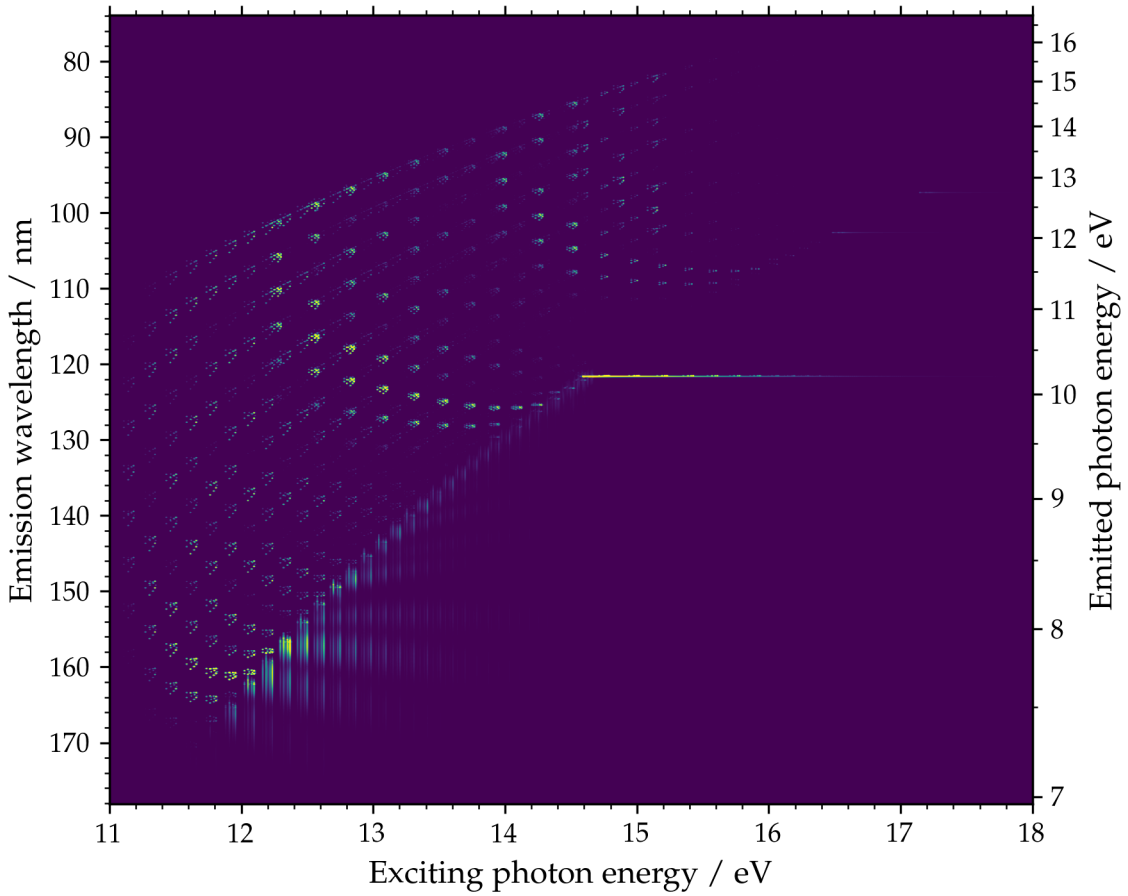

Fig. 4.5: *Emission map of molecular hydrogen based on calculated emission spectra for excitation energies between 11 eV and 18 eV covering all singly excited electronic states. Its visual features are reproduced in agreement with the measured results. A bandwidth of* $\Delta E_{h\nu} = 10\,\mathrm{meV}$ *is used for the excitation, while the spectral detection has a resolution of* $\Delta E_{\mathrm{det}} = 120\,\mathrm{pm}$. *A non-linear intensity scaling with* $a = 35$ *is used as defined by* (3.3).

Chapter 5

Exploration of visual features

While emission maps may provide a unique perspective of the transitions and processes occuring in a bound system, they require an initial understanding of this presentation method for a correct interpretation. This chapter aims to facilitate this perception by guiding through the typical features appearing for molecular hydrogen in the regime of singly excited states and connecting them with the type of transitions they are caused by. All maps shown here are based on the simulated results obtained with the computational method introduced in the preceding Chapter 4. In contrast to the usual convention in this work, the emission maps depict the emitted photon *energy* rather than *wavelength* as a function of excitation energy. This causes arguments related to the conservation of energy to appear as linear relations rather than hyperbolas, which may prove more intuitive to the reader.
This chapter restricts itself to a general introduction of the underlying mechanisms. A more detailed discussion of the results, including the experimental data, other isotopologues of hydrogen as well as different molecular species, can be found in the following Chapter 6.

5.1 General navigation

The emission map is usually presented as a shaded matrix, a rectangular array of numbers rendered as a grid of colored pixels. The colors of each pixel correlate to the numerical value of the corresponding cell based on a colormap relation. Each number of

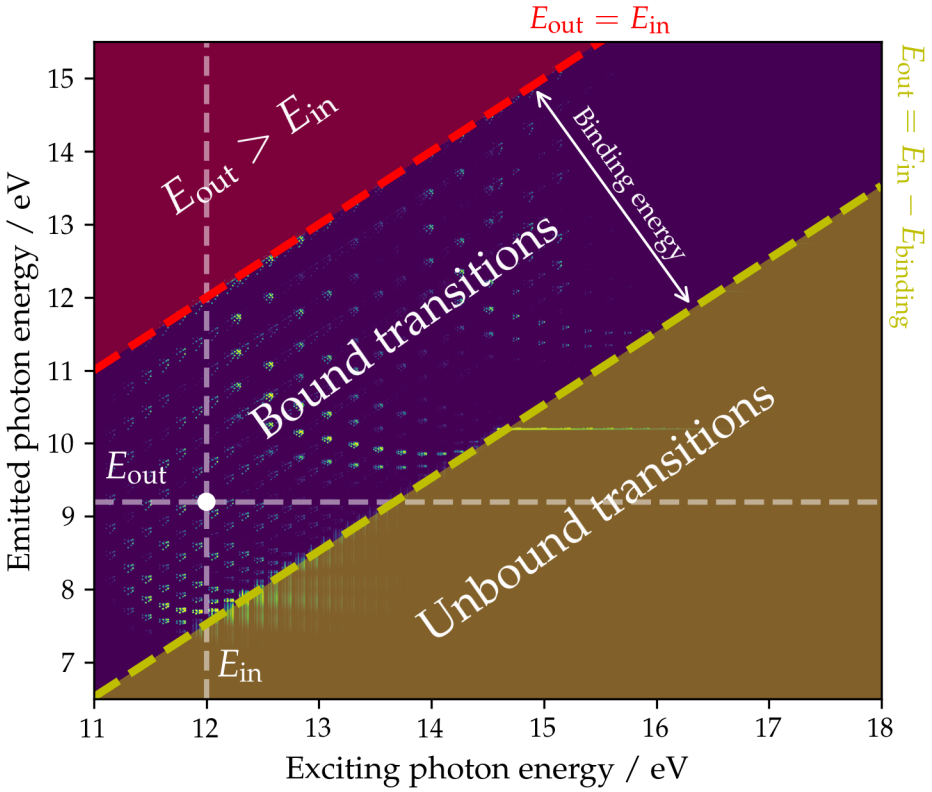

Fig. 5.1: *Each point on the emission map shows the emission probability for a photon of energy E_{out} on the vertical axis after excitation by E_{in} on the horizontal axis. In the context of a resonant excitation and following relaxation, this can be thought of how likely the amount E_{out} is released by the system after internal conversion when introducing E_{in}. The map then divides into three regions of unbound transitions (yellow), bound transitions and a usually forbidden zone (red) beyond elastic scattering.*

this matrix represents physically the probability of emitting a particular photon energy E_{out} after exciting with another particular photon energy E_{in}. During this process, the system transitions first from an initial state q to the excited state q' and then relaxes to the final state q'':

$$q \xrightarrow{E_{in}} q' \xrightarrow{E_{out}} q'' \tag{5.1}$$

The intermediate state q' may actually consist of additional radiationless transitions, which determine the selection of the final state q'' the system will proceed to.
For this work, the horizontal axis is always chosen to be the excitation axis with the

emissions remaining for the vertical axis. Thus, a column of this matrix contains all emissions occuring after excitation at a particular photon energy and is equivalent to an emission spectrum. It can be thought of as selecting a specific excitation, and thus the intermediate state q', to happen and observing its results at different emission positions depending on the internal processes. A row on the other hand corresponds to the excitation function for emitting a particular photon energy.
In the context of a bound system, the relation between E_{in} and E_{out} divides an emission map into three distinct regions in dependence of the system's binding energy E_{binding}. This value is meant here as the highest internal energy $E_{\text{sys}} = E_{\text{in}} - E_{\text{out}}$ the system may possess for a stable configuration. For radiative transitions in small molecules such as molecular hydrogen, it may be assumed that only the electronic ground state $X\ ^1\Sigma_g^+$ fulfills this condition. The binding energy is then its potential energy for large reaction coordinates, e.g. 4.48 eV for H_2 whose regions are illustrated in Figure 5.1. In the context of a Morse potential, this is often called the dissociation energy $D_e - E_0 = D_0$ of X corrected for the molecule's zero point energy E_0. The three regions are:

- The bound transitions occuring for $E_{\text{in}} \geq E_{\text{out}} \geq E_{\text{in}} - E_{\text{binding}}$ or $E_{\text{sys}} \leq E_{\text{binding}}$ where the final state q'' is again a bound state of the system.
- The unbound transitions when more energy than its binding energy remains in the system with $E_{\text{out}} < E_{\text{in}} - E_{\text{binding}}$ or $E_{\text{sys}} > E_{\text{binding}}$. In a molecule, the final state q'' for all emissions in this region will involve its dissociation.
- The forbidden transitions where due to $E_{\text{out}} > E_{\text{in}}$ or $E_{\text{sys}} < 0$ the conservation of energy will not be fulfilled, if the system resides in his ground state in the beginning.

Naturally, the region of bound transitions lies between the forbidden and unbound transition. It is contained by the bisector with $E_{\text{out}} = E_{\text{in}}$ towards higher emission energies and the dissociation line $E_{\text{out}} = E_{\text{in}} - E_{\text{binding}}$ towards lower emission energies. The features emerging in these regions are discussed in the following two sections.

5.2 Bound transitions

The region of transitions involving only bound states of hydrogen is made up completely by the molecular band structure of the various electronically excited states in both excita-

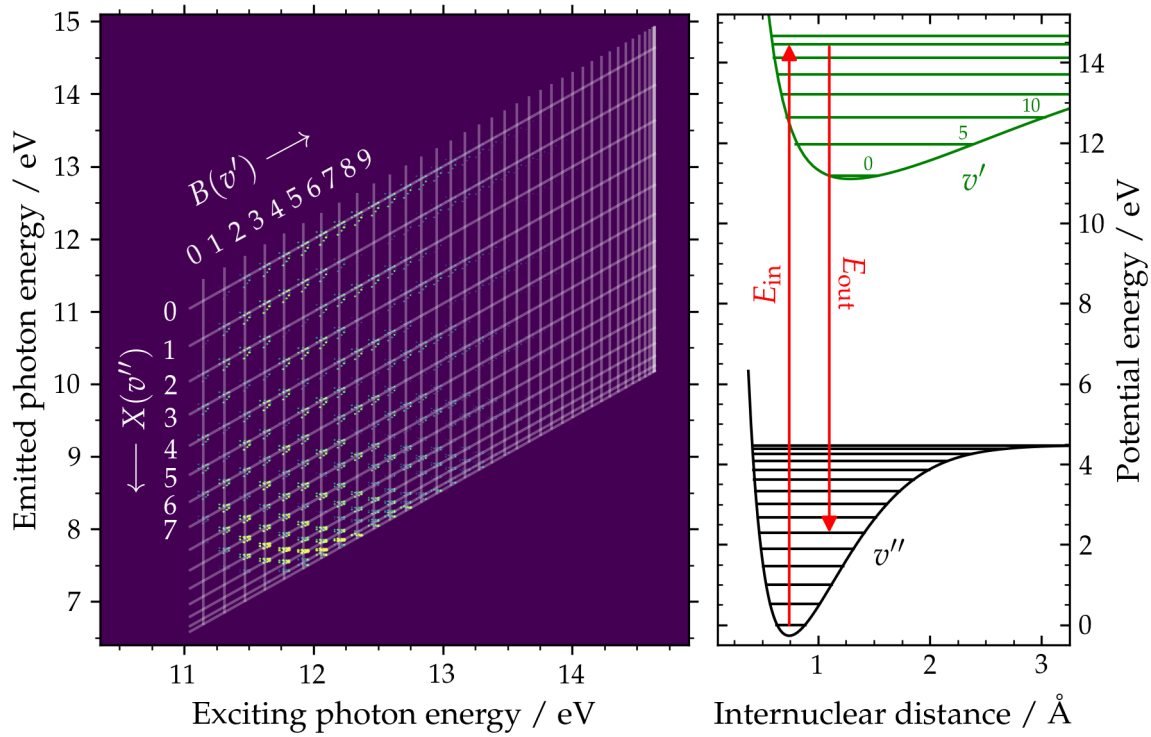

Fig. 5.2: *This partial emission map in the left plot contains only the features generated by the molecular bands of the $B\,{}^1\Sigma_u^+$ state. The upper levels v' are selected by the excitation energy and hence appear as vertical columns, while the relaxed levels v'' remain with an energy difference E_{sys} to the initial state and form parallel lines to the bisector. Such an exemplary process is sketched in the potential energy diagram in the right plot. Each electronic state's bands result in a checkerboard structure in total.*

tion and relaxation. Starting from the electronic ground state $X\,{}^1\Sigma_g^+$ with the thermally populated vibrational and rotational levels $X(v, J)$, it involves all allowed permutations of the upper electronic states $q'(v', J')$ accessible via single-photon excitation and the final relaxed state $X(v'', J'')$.

$$X(v = 0; J = 0, 1, 2, 3) \xrightarrow{E_{in}} q'(v'; J' = J, J \pm 1) \xrightarrow{E_{out}} X(v''; J'' = J', J' \pm 1)$$

The combinations of upper and lower vibrational level v', v'' appear as a rotated large-scale grid structure on the emission map for each electronic state q', which then overlap. The simulated emission map containing only the bound transitions involving the $B\,{}^1\Sigma_u^+$ state are shown in Figure 5.2.
The horizontal position of this grid containing all upper and lower level combinations

is different for each electronically excited state as a function of v', as it represents the excitation into its levels with their specific potential energy. But all electronic states share the same parallel bisector lines for their lower vibrational level v'' after relaxation, as these levels are part of the same ground state X. An overview of the relative positions of the most important electronic states can be found in Section 5.4 of this chapter.
The intensity distribution across this vibrational grid is a direct portrait of the respective Franck-Condon factors (see Section 2.3.3) and thus a two-dimensional illustration of the vibrational wave function overlaps v, v' (with $v \stackrel{!}{=} 0$) and v', v'' as a function of both v' and v''. It visualizes the Condon parabola [Her50a], which gives the set of lower vibrational levels with the highest intensity for any given upper level in emission. As such, the maximum intensity evolves along those excited levels with a particularly large probability density around the equilibrium distance and those relaxed levels overlapping with the upper turning points. This trend converges strikingly with increasing excitation energy towards the point, where the eventual dissociation of the particular upper state occurs by excitation into its continuum. Depending on the upper electronic state, this corresponds to one half of one or more Condon parabolas.

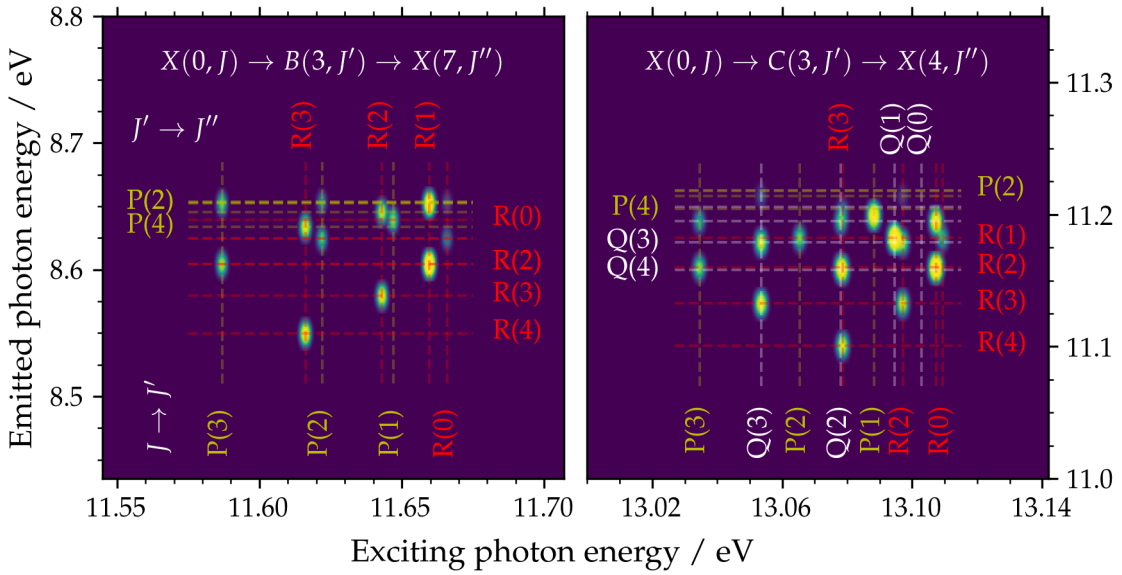

Fig. 5.3: *An emission map section of the rotational substructure for two exemplary bound transitions into the $B\ ^1\Sigma_u^+$ state on the left and the $C\ ^1\Pi_u$ state on the right. The rotational branches for the vertical excitation $J \rightarrow J'$ and horizontal emission $J' \rightarrow J''$ are annotated in yellow for P, white for Q and red for R.*

The rotational levels in turn are visible as a substructure in each of these v', v'' features when examined with sufficient resolution. Figure 5.3 contains a band structure subsection of the $B\ ^1\Sigma_u^+$ and $C\ ^1\Pi_u$ state for a particular combination of v' and v'' each. Each of these subsections is the magnification of a singular node on the grid of Figure 5.2. While all level combinations form a grid similar to vibration, the stricter selection rules of rotation reduce the populated nodes significantly. The relative intensities between the different rotational branches in excitation and emission are governed by the Hönl-London formulae $S_{JJ'}$ defined in (2.52), which depend on the geometry of the involved electronic states. For example, a $\Sigma \to \Sigma$ transition with $\Delta\Lambda = 0$ such as for B is limited to $\Delta J \pm 1$ and hence contains no Q branch with $\Delta J = 0$ at all. A $\Sigma \to \Pi$ process ($\Delta\Lambda = 1$) for the C state on the other hand includes all three branches due to its selection rule $\Delta J = 0, \pm 1$.

5.3 Unbound transitions

For all transitions in the unbound region, the emitted energy E_{out} is less than the difference between the excitation energy E_{in} and the binding energy E_{binding} of the initial state, in the case of molecular hydrogen the ground state's potential energy for $R \to \infty$. Such a process in this system will therefore never reach the ground state as its final state and involves dissociation for the visible radiative features. This is realized by different mechanisms each with different methods of photon emission, which are categorized into three distinct processes here:

- Direct excitation into an unbound vibrational level
- Predissociation by interstate coupling
- Dissociative continuum emissions

In the first case, the transition from the ground state leads directly into a vibrational continuum of the electronically excited state. Each electronic state converges towards a particular atomic excitation state for large internuclear distances that then results from its dissociation. These can decay via luminescence of atomic spectral lines, in particular the Lyman series for H(np) $\to$ H(1s). They appear as continuous horizontal lines on the emission map beginning at the dissociation line, commonly with declining intensity

for higher excitation energies. They are shown exclusively in the matrix of Figure 5.4, while the excitation scheme is sketched in the potential energy diagram for an exemplary continuum level of $C\ ^1\Pi_u$. The remaining energy, the distance $E_{k''}$ of the continuum level to the dissociation limit, is released as kinetic energy of the fragments.

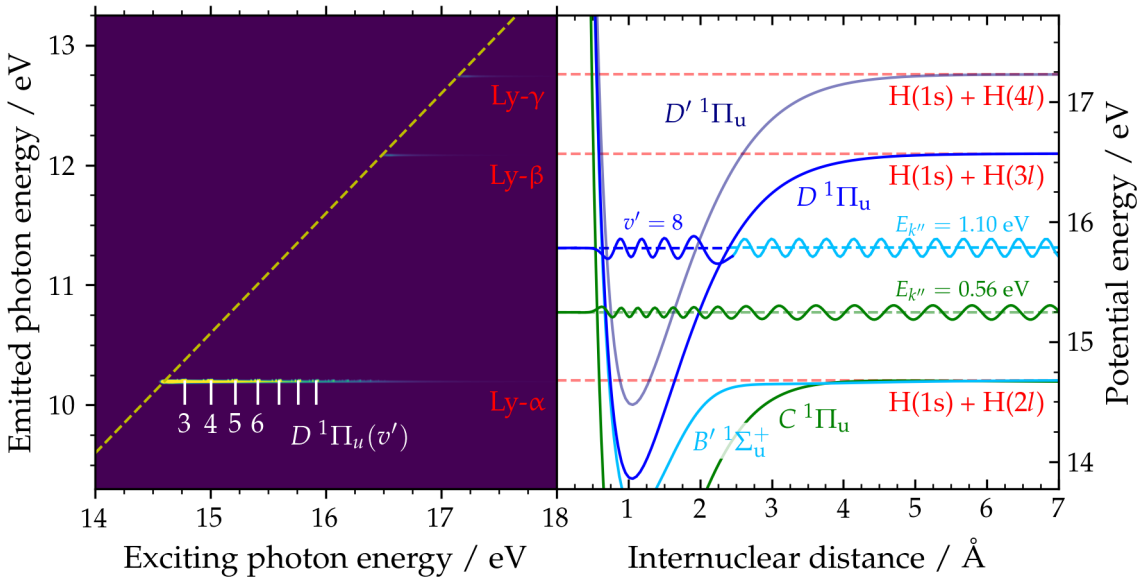

Fig. 5.4: *The partial emission map in the left plot contains only the luminescence from atomic fragments after dissociation. Each electronic state in the potential energy diagram to the right converges for large internuclear distances towards a particular exicitation state of dissociated fragments (red). The excitation can either occur directly into the vibrational continuum of* $C\ ^1\Pi_u$ *or resonantly in predissociating levels of* $D\ ^1\Pi_u$ *coupling to lower states, primarily* B'.

Higher orders of the hydrogen spectral series, such as Balmer with $H(nl) \rightarrow H(2l)$ transitions, will occur as well with sufficient excitation state n in accordance to the branching ratios. While they do not appear within the covered spectral range of molecular transitions, they will usually trigger a subsequent Lyman decay due to their remaining excitation with $n > 1$ and hence appear as a contribution to this emission line.

In general, the predissociation process in the second mechanism occurs, when a system dissociates even though the populated level is normally below the limit of its respective electronic state and therefore bound. In this case, the initial excitation is therefore the same as for a bound transition, but the vibrational level of the electronically excited state is strongly coupled to other electronic states, which are lower in potential energy and possibly already in their respective vibrational continuum. After the transition into

this lower state, the dissociation continues in the same way as in the direct case above. The atomic emissions are hence at the same photon energies of the Lyman series, but in excitation at the resonance positions for the upper vibrational levels that couple. This is also included in Figure 5.4 for the rotational coupling of the $^1\Pi_u^+$ component of D to $B'\,^1\Sigma_u^+$ for $v' \geq 3$.

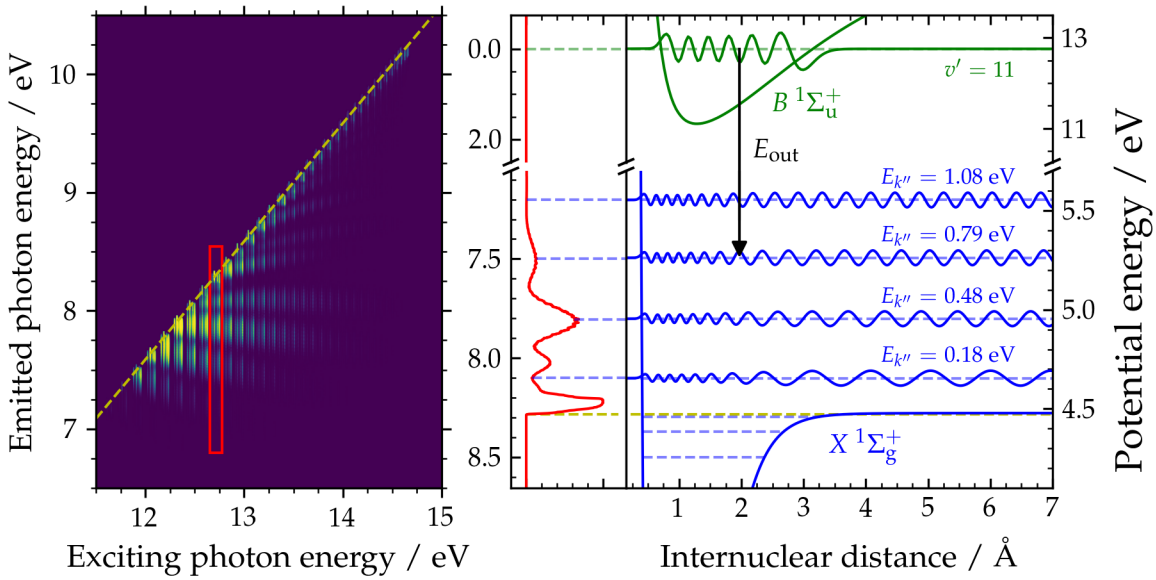

Fig. 5.5: *The partial emission map in the left plot contains only the continuum emissions from the $B\,^1\Sigma_u^+$ state. The spectral distribution for the upper bound level $v' = 11$ (red) is shown on the right alongside the potential energy diagram. Here the continuous bands arise from transitions between the discrete upper state (green) and the vibrational continuum of the ground state (blue) sketched for a selection of energy differences $E_{k''}$ to its limit.*

The relaxation via dissociative continuum emissions in the third case of unbound transitions ends in the vibrational continuum of the ground state after a regular excitation into an upper bound level. While in general possible for all electronically excited states, this decay method is particularly prominent for the Lyman band of molecular hydrogen due to the $B\,^1\Sigma_u^+$ state's wide potential energy curve. It allows a significant probability density at larger internuclear distances, where no suitable bound level of the ground state exists to transition into. The generated spectral distribution is continuous with characteristic variations in intensity. These are caused by the slow variation of the continuum wavefunctions as a function of the distance $E_{k''}$ from the respective dissociation limit, which in turn cause a slow variation of the overlap between this continuum wavefunc-

tion and the upper state. They are called Condon diffraction bands [Con28] as a whole for all upper vibrational levels of a state and featured in Figure 5.5 with a depiction of the process in the potential energy diagram.

5.4 Separating electronic states

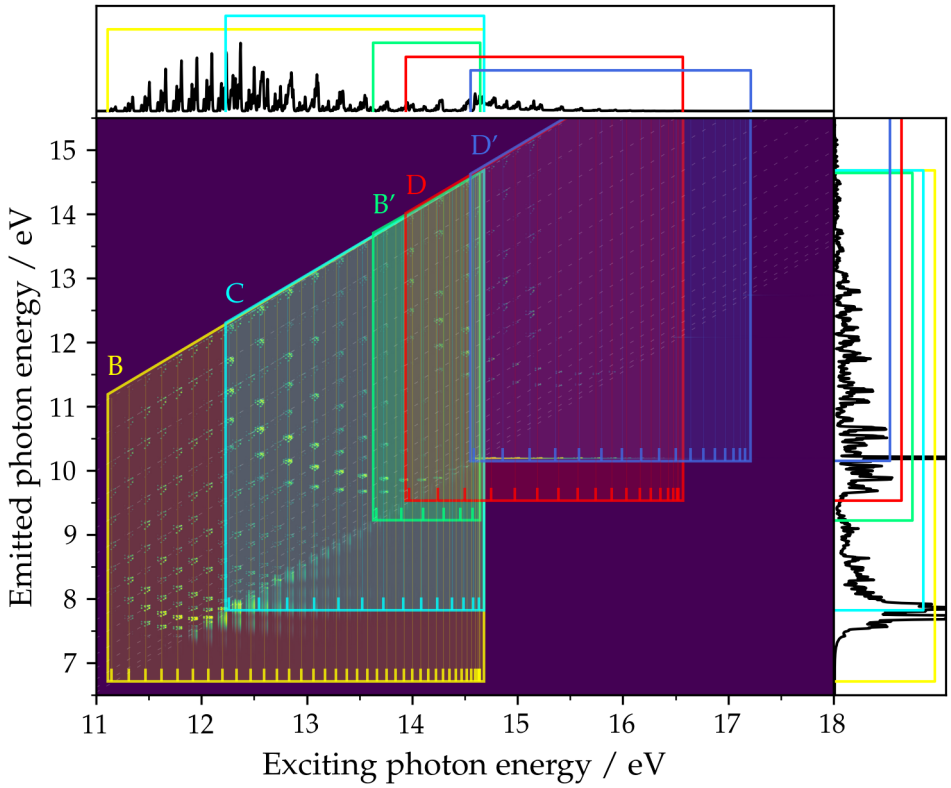

Fig. 5.6: *Each accessible electronically excited state covers a portion on the emission map (center), emission excitation function (top) and integrated emission spectrum (right) corresponding to its range of excitation and subsequent emissions. The most relevant states for molecular hydrogen are shown with B (yellow), C (cyan), B′ (green), D (red) and D′ (blue). For each state on the emission map, the excitations into the vibrational levels are indicated by vertical lines while diagonals lines (dashed white) mark the same levels after relaxation into the ground state by photon emission.*

The bound and unbound transition mechanism introduced in the previous sections may occur to varying degrees for any electronically excited state the system is excited into. As the exciting photon energy, and hence position on the horizontal axis, selects

a particular upper state, the features of all states appear side-by-side on the matrix at the respective level positions. Figure 5.6 illustrates the position of the electronic states in excitation and emission by shading the extent where the respective emissions appear. The included states are those accessible via dipole selection rules that dominate the rovibronic emissions visible on a map of molecular hydrogen.

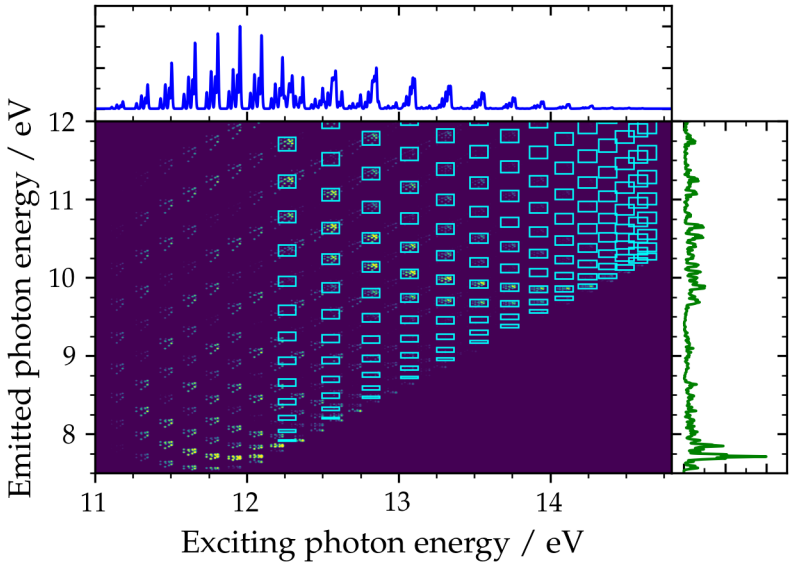

Fig. 5.7: *The partial emission map only contains the bound transitions involving the upper* $B\,{}^1\Sigma_u^+$ *and* $C\,{}^1\Pi_u$ *states together with their excitation function (blue) and integrated emissions (green). Those belonging to the latter are marked with cyan rectangles, while the level combinations of the former state are unmarked.*

A unique advantage of emission maps is now the disentanglement of electronic, vibrational or rotational features that may overlap in absorption or emission. This is particulay prominent for molecular hydrogen, where the structures of different states and levels become heavily intertwined due to their large energetic gaps. The typical progression of bands is no longer consecutive but mixed [GMJV17]. If the emissions are mapped dependent upon the excitation however, the majority of features will unravel again. For the states shown in Figure 5.6, these shaded areas still overlap as a whole, but the features themselves, such as the combinations of excited and relaxed vibrational level for bound transition as introduced in Section 5.2, still appear somewhat separately on the map. It is this distinctiveness, that is lost in the the excitation function or the integrated emission spectrum. This is demonstrated in Figure 5.7 for the relative positions of the

Lyman and Werner bands, which contain the molecular bands from the $B\ ^1\Sigma_u^+$ and $C\ ^1\Pi_u$ state, respectively. In particular their integrated emissions are only distinguishable by fitting the known spectral line positions, but emerge side-by-side for most vibrational level combinations on the emission map.

5.5 Summary of most relevant features

After the discussion of the various visual features, shapes and systematic progressions in this chapter, the annotations in Figure 5.8 summarize all the most relevant details visible on emission maps of molecular hydrogen and its isotopes.

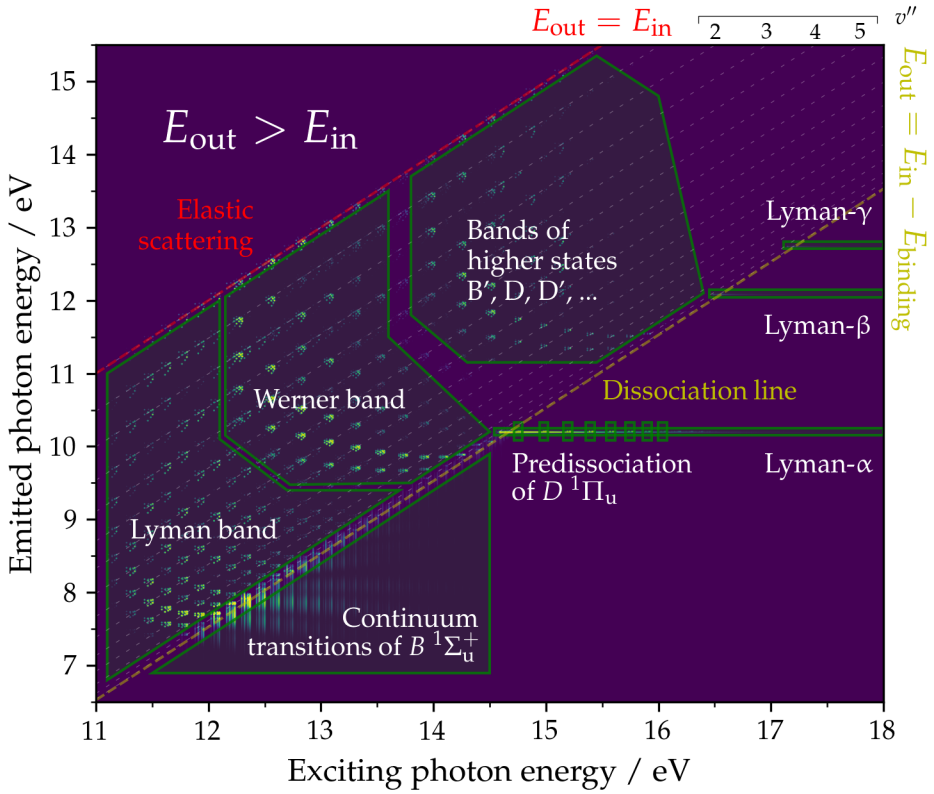

Fig. 5.8: *This computed emission map of molecular hydrogen summarizes the majority of visible features in distinct categories. This includes particularly strong bound transition and unbound transitions, the atomic lines originating from fragments after dissociation and systematics for assigning upper and lower levels.*

Chapter 6

Results for diatomic species

Following a general interpretation of the visual features and systematics typically appearing on rovibronic emission maps of small molecules in the previous Chapter 5, this chapter discusses further spectroscopic conclusions that can be drawn from this technique for a variety of small molecules.
Experimental data has been obtained for hydrogen H_2, its heavier isotopologue deuterium D_2 as well as the heteronuclear carbon monoxide CO and is complemented by computations based on Chapter 4. With the same method, simulated data for the remaining homonuclear hydrogen isotopologue tritium T_2 as well as the asymmetrical hydrogen deuteride HD is shown. The full emissions maps are found at the end of the respective section for each covered species.

6.1 Molecular hydrogen

As the smallest neutral molecule as well as most abundant one in the universe, hydrogen has been researched extensively and in great detail both from a theoretical perspective and in experiments. For this system in particular, the emission map technique presented in this work aims to achieve a new perspective for properties, which can be found in other works individually. A comprehensive overview of studies concerning the absorption structure of H_2 can be found in [GMJS13a]. Using Fourier transform absorption spectroscopy and the PIFS method this work is also based upon, the rovibronic level energies of all accessible states can be measured with a high precision of

up to $\Delta\nu = 0.2\,\mathrm{cm}^{-1}$ or $\Delta E = 25\,\mu\mathrm{eV}$ and compared favourably to multi-channel defect theory (MQDT) calculations. Exclusive ab initio treatments with Born-Oppenheimer potential energy curves corrected for adiabatic couplings and transition moments include [SW02, WS03a, WS03b, WOS06], which are also used by the computational results shown here. Further references are given in the discussion of each state and its visible features on the emission map over the following paragraphs.
The full experimental result for H_2 is shown in Figure 6.12 directly and in Figure 6.13 overlaid with numerous annotations for the most noticeable features and relevant regions. The simulated result follows in Figure 6.14 for the complete matrix and in Figure 6.15 isolated by several of the major states involved. Its emission structure exhibits a large variety of structures in both the bound as well as the unbound region. These stem from its number of accessible electronically exited $n\mathrm{p}\lambda$ Rydberg states, in particular the ${}^1\Sigma_\mathrm{u}^+$ $n\mathrm{p}\sigma$ series B, B' and ${}^1\Pi_\mathrm{u}$ $n\mathrm{p}\pi$ series C, D and D' starting with $n = 2$. For each of these $n\mathrm{p}\lambda$, the respective Lyman series emissions of hydrogen atoms after fragmentation follow up on the bound transitions joined by extensive radiative dissociations.

6.1.1 The $B\ {}^1\Sigma_\mathrm{u}^+\ 2\mathrm{p}\sigma$ state

The absorption spectrum of molecular hydrogen begins with the Lyman band generated for excitation energies between 11.18 and 14.68 eV into the 39 bound vibrational levels of $B\ {}^1\Sigma_\mathrm{u}^+\ 2\mathrm{p}\sigma$, the lowest ${}^1\Sigma_\mathrm{u}$ state and thus the first to be allowed by dipole selection rules. The large number of levels, among other unique properties of this state, is a consequence of its exceptionally wide potential energy curve (see Figure 2.1), which in turn is caused by the highly ionic character of this state, particulary at internuclear distances $2\,\text{Å} \leq R \leq 11\,\text{Å}$. In such a case, it is more likely to encounter both electrons at the same nucleus in a $\mathrm{H}^+\mathrm{H}^- \pm \mathrm{H}^-\mathrm{H}^+$ superposition than at different nuclei (which would be a covalent character) [WKB11].
The resulting shift in the equilibrium distance between $X\ {}^1\Sigma_\mathrm{g}^+$ and $B\ {}^1\Sigma_\mathrm{u}^+$ to $R_e \approx 1.3\,\text{Å}$ distributes the bound transitions of the Lyman band over a wide array of lower vibrational levels in emission, akin to a wide Condon parabola as discussed in Section 5.2. Its vertex is shifted in both the upper and lower vibrational level to higher values due to an negligible overlap of the $v' = 0$ and $v'' = 0$ levels with the other respective state. In addition, it prohibits elastic scattering for this state almost completely. The overall emission band appears therefore quite different on the emission map than the other

states, which feature a more common covalent bond. In contrast to the absorptions of the Lyman band, the emissions have so far been investigated by a lesser degree, especially after selective excitation, with an extensive work found in [ARL93] using pressure discharges and subsequent identification of lines. The basic computational model introduced in Chapter 4 is able to reproduce the bound emissions characteristics for this state well. A detailed look with rotational resolution is shown in Figure 6.1 for a particular vibronic transition process in the Lyman band.

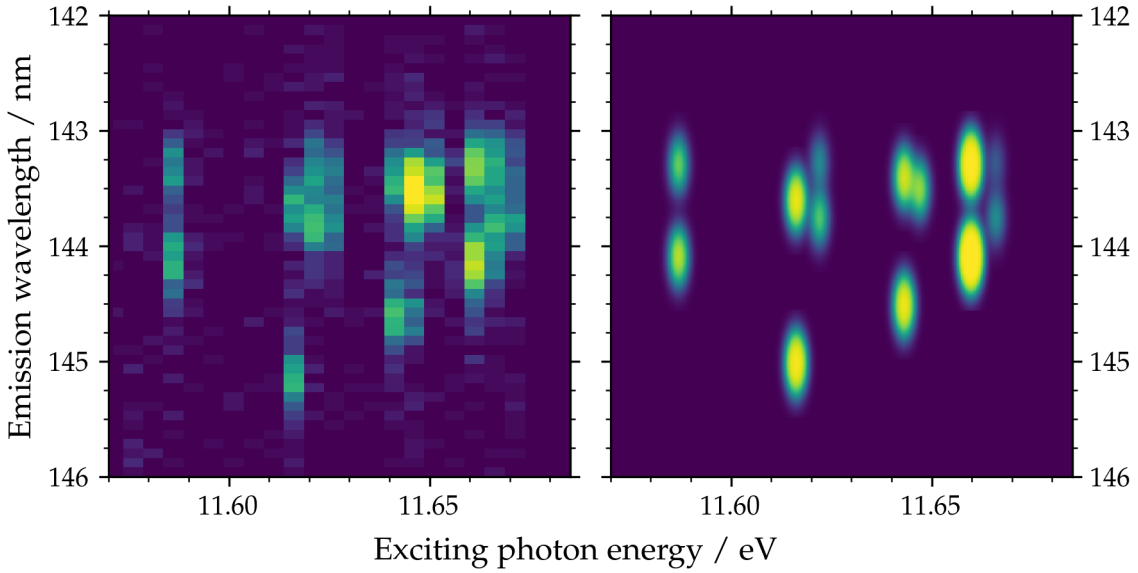

Fig. 6.1: *Detailed comparison of the experimental (left) and simulated data (right) for the particular vibronic process* $X(v = 0, J) \rightarrow B(v' = 3, J') \rightarrow X(v'' = 7, J'')$ *of molecular hydrogen in rotational resolution. Its branches can be identified in the same way as in Figure 5.3.*

The convergence of this state towards the H(1s) + H(2l) limit at a large nuclear separation causes the bands to merge onto the Lyman-α line after excitation into its vibrational continuum beyond 14.68 eV. The simulated and isolated map for this state in Figure 6.15 reveals only a weak transition rate into the vibrational continuum and thus contribution for the atomic luminescence when compared to the bound transitions. This is discussed in more detail in Section 6.1.3 about the $B'\,{}^1\Sigma_u^+$ state.

The most striking feature of this state on the emission map are the rich structures appearing below the dissociation line. These belong to a type of unbound transition from the bound vibrational level of $B\,{}^1\Sigma_u^+$ into the vibrational continuum of the ground state $X\,{}^1\Sigma_g^+$. But in this case, they are expanded significantly by the aforementioned wide

potential curve, which allows these transition to still occur at rather large internuclear distances of $R \geq 2\,\text{Å}$. This point is well beyond the potential well of the ground state and may thus only lead into continuum states. Starting with the prediction of such a mechanism called diffraction bands by Condon in [Con28], there have been only a few studies concerning this phenomenon. The first experimental observation by integrated dispersion measurements of flash discharges was reported in [DHS70] and assigned correctly with the help of a theoretical model in [SD72]. The integrated emissions and idenfication via synthetic spectra have since then been reported with much greater resolution after electron impact in [ARL97]. The selective excitation of individual upper levels using synchrotron radiation isolated the diffraction band in [SZ78, NS87, SNR90] for the first time and thus allowed to investigate the effect of rotation. Studies of the radiative lifetime of these states [SC72] confirmed a comparable lifetime to bound processes in the range of slightly less than 1 ns. The astrophysical relevance of this mechanism has been suggested even before the first measurements as a fundamental destruction path of molecular hydrogen in interstellar clouds, then often called the Solomon process [SW67]. A recent investigation into its relation with direct photodissociation in this context is found in [GAP12].

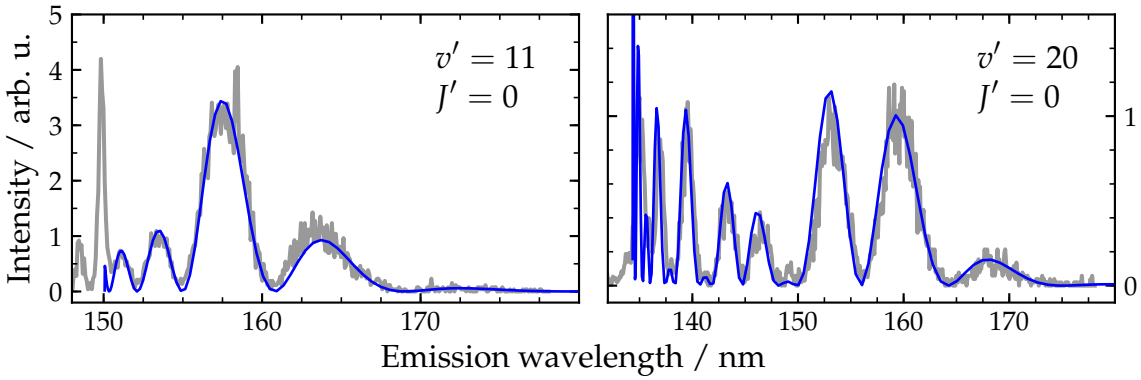

Fig. 6.2: *The measured emission spectrum (grey) of the dissociative process* $B(v', J = 0) \rightarrow \mathrm{H(1s)} + \mathrm{H(1s)} + h\nu$ *after an excitation from* $X(v = 0, J = 1)$ *is in good agreement with the simulation (blue). The latter includes only features arising from the continuum transition and begins at the dissociation limit of the ground state for this upper limit.*

The experimental results obtained from the emission map are in full agreement with these previous works as well as the presented computation method. A comparison for the spectra of two exemplary upper rovibrational level in the Lyman band, which are

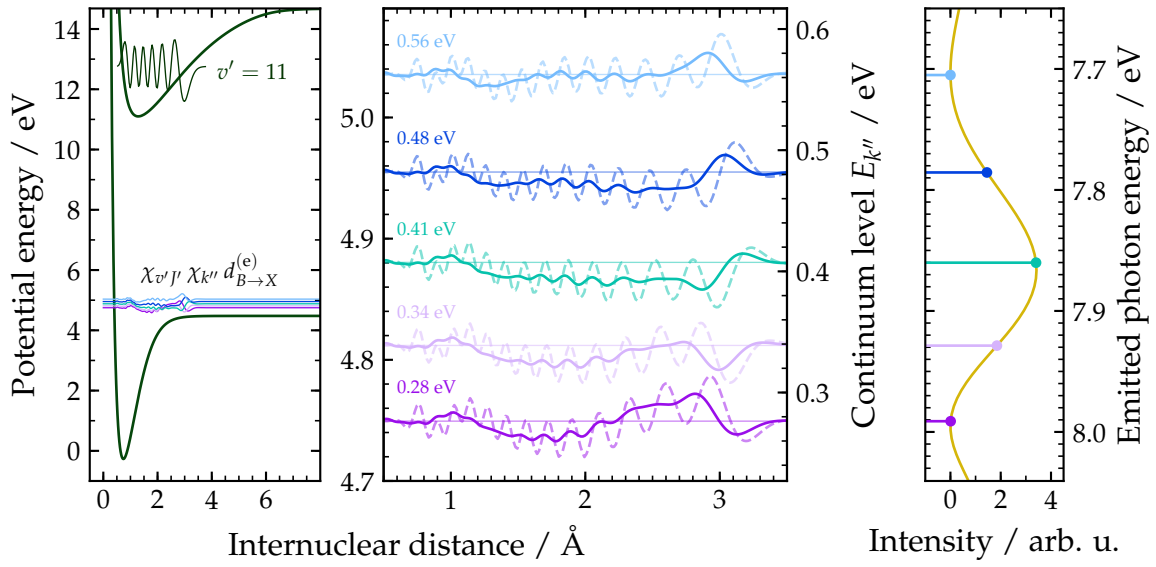

Fig. 6.3: *The wavefunction overlap $\chi_{v'J'}\chi_{k''}$ weighted by the electronic transition moment $d^{(e)}_{B\to X}$ between the upper bound level $v' = 11$, $J' = 1$ of $B\,{}^1\Sigma_u^+$ and several states k'' in the continuum of $X\,{}^1\Sigma_g^+$ is shown in the potential energy diagram to the left (violet to blue). A magnified view of the actual overlap (dashed) and its moving average (solid) to guide the eye is added in the middle. The right axis here depicts the level position $E_{k''}$ relative to the limit rather than the total potential energy. The continuum emission spectrum (yellow) as the squared integral is included to the right with the respective position for each continuum level. It is plotted as a function of emitted photon energy rather than wavelength and to scale with the middle plot.*

singular columns on the map, is shown in Figure 6.2. As introduced in Section 5.3, in general these emissions are the result of transitions between bound vibrational levels and unbound continuous states at distances $E_{k''}$ above the dissociation limit, which is released as the kinetic energy of its fragments. Since the emission intensity reflects the wavefunction overlap between the participating states, this may be considered as probing the continuum of $X\,{}^1\Sigma_g^+$ by the upper level for each particular level. Because the emission map now contains these transition type in its entirety for all vibrational levels of the $B\,{}^1\Sigma_u^+$ state with additional rotational resolution (corresponding to an initial thermal population), this probing can also be performed in the direction of the bound level. This is especially viable for the extensive diffraction bands of the $B\,{}^1\Sigma_u^+$ state in molecular hydrogen and reveals properties, which disappear easily in the integrated spectra after electron impact [ARL97] or selective spectra of only singular levels [NS87]. The spectral fluctuations for the same upper vibrational level, that is vertically, occur by

alternating constructive and destructive interference. As $E_{k''}$ changes along the emission axis, the frequency and phase of the continuum wavefunctions changes and hence the resulting overlap with the same bound wavefunction. Figure 6.3 depicts this overlap for $v' = 11$ and several $E_{k''}$ side-by-side with the emission spectrum. For a maximum in the emission to occur like for $E_{k''} = 0.41\,\mathrm{eV}$, the overlap can be seen to mostly have the same sign as opposed to the situation for 0.28 eV, where large areas cancel out due to an opposite sign. When the emission spectrum is expressed as a function of emitted photon energy, it may be plotted to scale with the potential energy. For any given emitted photon energy in the diffraction bands, the corresponding continuum state is linear to E_{out} and may be expressed as:

$$\begin{aligned} E_{X,\infty} + E_{k''} + E_{\mathrm{out}} &= E_{B,0} + E_{v'J'} \\ E_{k''} &= \underbrace{E_{B,0} - E_{X,\infty}}_{\text{const}} + E_{v'J'} - E_{\mathrm{out}} \end{aligned} \tag{6.1}$$

The symbols used here are summarized in Figure 6.4 both in the context of the emission map as well as the potential energy diagram. $E_{q,0}$ and $E_{q,\infty}$ denote the potential energy of the lowest vibrational level and dissociation limit of the electronic state q, respectively. The energy distance $E_{k''}$ of a particular emission can hence be found with (6.1) and Figure 6.4 on the emission map as the vertical distance to the dissociation line, which by itself is solely determined by the upper level $E_{v'J'}$. This energy is the bound analog to $E_{k''}$ by containing the energy above its respective limit, in this case the lowest state of $B\ ^1\Sigma_u^+$ with $E_{B,0}$, to allow the constant portions to be separated easily. The highest value obtained for this state is $E_{v'=38,J'} \approx 3.5\,\mathrm{eV}$. As the upper level in the excitation scheme of the emission map, $E_{v'J'}$ is selected by the exciting photon energy E_{in} and is therefore also a horizontal coordinate. But in the case of any rotational excitation $J \geq 0$ in the ground state with energy E_0, it will appear at up to three horizontal positions, that is up to three different E_{in}:

$$E_{\mathrm{in}} - E_0 = E_{B,0} + E_{v'J'} \tag{6.2}$$

The number of occurences depends on the P, Q and R branch selection rules of the particular electronic state concerned, with only P and R in the case of $B\ ^1\Sigma_u^+$. The amount of splitting in this work is limited to the first three thermally excited levels $J \geq 1$ of

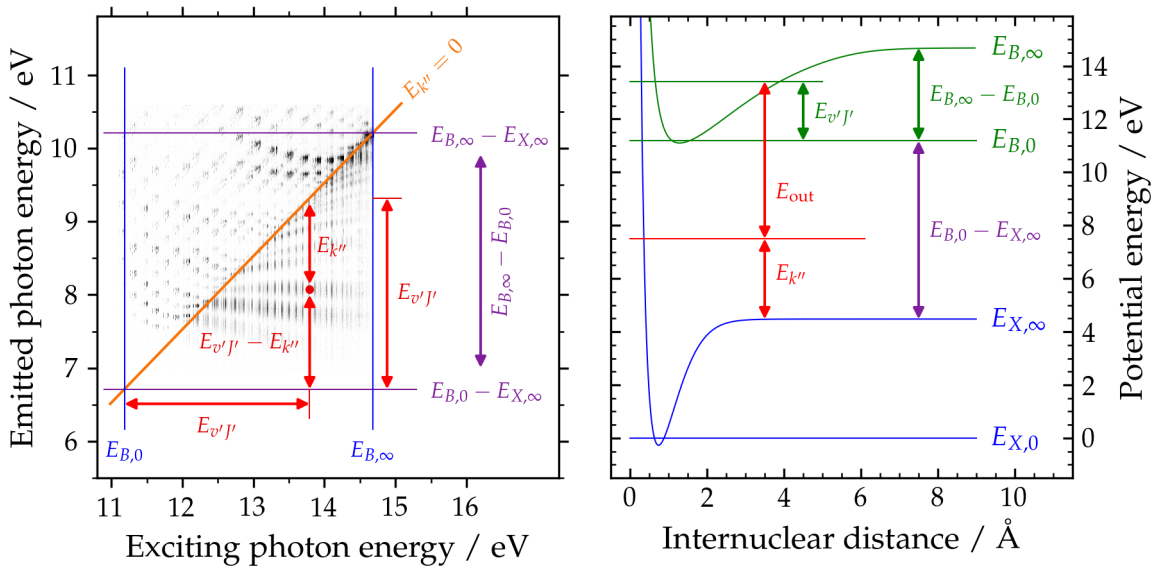

Fig. 6.4: *The symbols relevant for the discussion of continuum emissions in the context of the emission map (left) and the potential energy diagram (right). The exemplary emission (point on the emission map, horizontal level on the potential energy digram) as well as upper vibrational level are chosen arbitrary in both representation for improved readability.*

hydrogen at $v = 0$ at 15, 45 and 88 meV, respectively. For simplicity, the majority of samples shown here use the P(1) excitation with $J' = 0$, which may only be reached from $J = 1$ and are thus unique. The rotational resolution in emission is mostly hidden by the broad emission features.

A particular prominent property of the continuum transitions on the emission map is the characteristic horizontal trend emerging for the peaks of maximum intensity as highlighted in Figure 6.5. Each upper vibrational level by itself possesses a number of maxima, which grows as the level increases. But the positions of these maxima on the emission axis develop in a continuous manner and form several emission arms, which shall be labeled I to VII (with even higher ones emerging). Let the maxima $i = \mathrm{I}, \mathrm{II}, \mathrm{III}, \ldots$ appear at the vertical position $E_{\mathrm{out}}^{(i)}$, then this corresponds with (6.1) and (6.2) to:

$$\begin{aligned} E_{\mathrm{out}}^{(i)} &= E_{B,0} - E_{X,\infty} + E_{v'J'} - E_{k''} \\ &= E_0 - E_{X,\infty} + E_{\mathrm{in}} - E_{k''} \end{aligned}$$

As $E_{\mathrm{v'J'}}$ is a linear function of E_{in}, it may be thought of as the horizontal position on the emission map expressed within the potential energy well of the $B\ ^1\Sigma_{\mathrm{u}}^+$ state. Then $E_{\mathrm{k''}}$

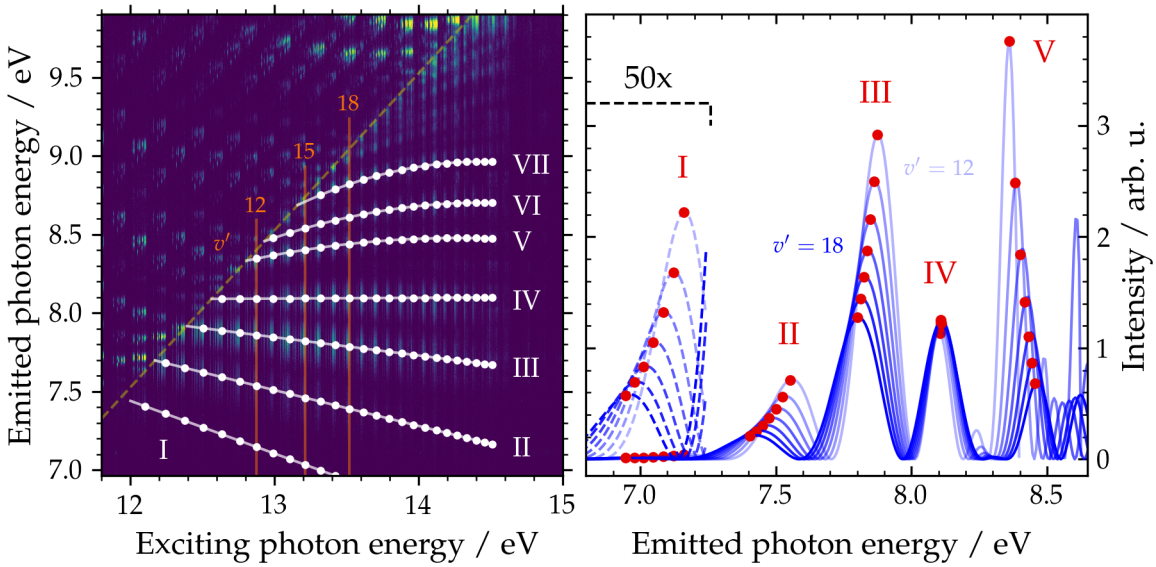

Fig. 6.5: *The emission map on the left centers on the experimental result for continuum emissions in the Lyman band with the trend of several intensity peaks highlighted and labeled I to VII. Its vertical axis depicts the emitted photon energy rather than wavelength here to present the linear/quadratic relation more intuitively. The respective computed emission spectra (blue) for the upper vibrational levels $v' = 12$ to 18 in the dissociative process $B(v', J = 0) \rightarrow \mathrm{H(1s)} + \mathrm{H(1s)} + h\nu$ after an excitation from $X(v = 0, J = 1)$ are shown in the right plot including the fitted intensity peaks in red. In addition, the weak spectral part for $E_{\mathrm{out}} \leq 7.24\,\mathrm{eV}$ is magnified (dashed).*

denotes the vertical position in the same way within the vibrational continuum of $X\,{}^1\Sigma_g^+$. The constants can be abbreviated with $E_{\mathrm{X-B}} = E_{B,0} - E_{X,\infty}$ resulting in:

$$E_{\mathrm{out}}^{(i)} = E_{X-B} + E_{v'J'}^{(i)} - E_{k''}^{(i)} \tag{6.3}$$

The maxima develop for specific correlations between $E_{v'J'}$ and $E_{k''}$, which define how much one must change additionally if the other is changed to maintain the maximum wavefunction overlap. This may be interpreted as the rate at which the two states, the bound level in $B\,{}^1\Sigma_u^+$ and the continuum one in $X\,{}^1\Sigma_g^+$, remain similar expressed by the distance to their limit. The difference $E_{v'J'} - E_{k''}$ for that matter is positive for all continuum emissions observed and annotated in Figure 6.5. For a sufficient overlap to occur, the bound energy may therefore be assumed to always be larger than the unbound one, i.e. $E_{v'J'} > E_{k''}$. On the emission map, these transitions are then restricted to photon energies of at least E_{X-B}, which forms a triangular region together with the dissociation

line and $E_{B,\infty}$ on the excitation axis in Figure 6.4.
If the trend now appears as a function $E_{\text{out}}^{(i)} = f(E_{\text{in}})$ on the emission map, the difference $E_{v'J'}^{(i)} - E_{k''}^{(i)}$ can be obtained with (6.2) by:

$$E_{v'J'}^{(i)} - E_{k''}^{(i)} = f(E_{v'J'} + E_{B,0} + E_0) - E_{X-B} \tag{6.4}$$

For a constant function $f(x) = a$, where the trend is parallel to the excitation axis, this reduces to $E_{v'J'}^{(i)} - E_{k''}^{(i)} = a - E_{X-B}$. Here the overlap develops identically for both states for higher energies offsetted by a constant amount a. A linear function $f(x) = ax + b$ will instead add a small correction term linear in $E_{v'J'}$ with $E_{v'J'}^{(i)} - E_{k''}^{(i)} = aE_{v'J'} + \text{const.}$ A polynomial ansatz for $f(x)$ corresponds to an expansion of the difference in orders of $E_{v'J'}$. This has been performed in Figure 6.5 by polynomials of first (for I, II, III and IV) and second degree (for IV, V and VI).
For trend I to III, the direct fit functions on the emission map in terms of $E_{\text{out}}^{(i)}$ and E_{in} evaluate to:

$$\begin{aligned} E_{\text{out}}^{(\text{I})} &= -0.336\ E_{\text{in}} + 11.5\,\text{eV} \\ E_{\text{out}}^{(\text{II})} &= -0.228\ E_{\text{in}} + 10.5\,\text{eV} \\ E_{\text{out}}^{(\text{III})} &= -0.116\ E_{\text{in}} + 9.36\,\text{eV} \end{aligned}$$

Using (6.4), these may instead be expressed by the resulting energy difference between the upper and lower level as a function of $E_{v'J'}$ for interpretation in the context of (6.3):

$$\begin{aligned} E_{v'J'}^{(\text{I})} - E_{k''}^{(\text{I})} &= -0.336\ E_{v'J'} + 0.996\,\text{eV} \\ E_{v'J'}^{(\text{II})} - E_{k''}^{(\text{II})} &= -0.228\ E_{v'J'} + 1.21\,\text{eV} \\ E_{v'J'}^{(\text{III})} - E_{k''}^{(\text{III})} &= -0.116\ E_{v'J'} + 1.34\,\text{eV} \end{aligned}$$

These three trends follow a negative slope and hence derivative, so the difference is reduced when $E_{v'J'}$ increases. It starts, e.g. for I, at an offset of 0.991 eV and then $E_{k''}$ grows quicker than $E_{v'J'}$ to maintain the maximum overlap and thus emission intensity. As the slopes of I and II are the third and second multiple of III, respectively, the similarity repeats along higher orders consistent with the periodic nature of the wavefunctions with increasing frequency.

For trend IV, the slope almost vanishes and the intensity maxima appear to be at a constant position on the emission axis. The transformed fit result accounts to:

$$E^{(\mathrm{IV})}_{v'J'} - E^{(\mathrm{IV})}_{k''} = 0.00486\; E_{v'J'} + 1.37\,\mathrm{eV}$$

At an energy difference of 1.37 eV with respect to each of their limits, the bound wavefunction of $B\,{}^1\Sigma^+_\mathrm{u}$ and continuous one of $X\,{}^1\Sigma^+_\mathrm{g}$ therefore keep a mostly similar oscillatory structure. A constant function is additionally the natural progression following trends I, II and III as the *zeroth order* of the series.
For trends IV to VI, the linear (or almost constant) expansion is no longer sufficient and a term quadratic in $E_{v'J'}$ needs to be added. The results translated into the potential energy frame are then:

$$\begin{aligned}
E^{(\mathrm{V})}_{v'J'} - E^{(\mathrm{V})}_{k''} &= -0.067\,\mathrm{eV}^{-1}\; E^2_{v'J'} + 0.413\; E_{v'J'} + 1.13\,\mathrm{eV} \\
E^{(\mathrm{VI})}_{v'J'} - E^{(\mathrm{VI})}_{k''} &= -0.107\,\mathrm{eV}^{-1}\; E^2_{v'J'} + 0.692\; E_{v'J'} + 0.867\,\mathrm{eV} \\
E^{(\mathrm{VII})}_{v'J'} - E^{(\mathrm{VII})}_{k''} &= -0.167\,\mathrm{eV}^{-1}\; E^2_{v'J'} + 1.088\; E_{v'J'} + 0.487\,\mathrm{eV}
\end{aligned}$$

The linear term is here positive and always larger than the quadratic one in the domain $E_{v'J'}$ occupies, as the trends are moving to higher emission energies. As opposed to I to III, their derivative is positive and they increase the difference when higher levels are excited with IV constituting the constant case in between. This region of the continuum emissions is created by smaller $E_{k''}$ than the others and the transitions end closer to the dissociation limit of $X\,{}^1\Sigma^+_\mathrm{g}$. The respective wavefunctions there are still influenced more by the potential well of this state. This perturbance can be interpreted as the origin of the quadratic term, which then *bends* the trend away from the ground state again to higher $E_{k''}$ and therefore lower E_out than the linear expression would by itself.
For all the trends discussed so far, only the position of maximum intensity has been taken into account as a measure of how the overlap progresses with increasing $E_{v'J'}$ and $E_{k''}$. The overlap or rather the intensity itself may be analyzed as well within a particular trend, which shall be performed qualitatively here based on the marked peak maxima in Figure 6.5. The particular trend IV, which is constant in its emitted photon energy, also maintains approximately the same intensity over the range of vibrational levels $v' = 12$ to 18. To the left, that is for lower emitted photon energies E_out and correspondingly higher $E_{k''}$, the intensity follows a linear (III) or quadratic (I, II) profile. On the right side

however for higher E_{out} and smaller $E_{k''}$, similar shapes emerge but with the opposite sign of its derivative. In both cases, the intensity decreases for higher upper vibrational level at the same E_{out}, which is a universal behaviour amongst all continuum emissions due to the growing oscillations at large $E_{k''}$.
There are several higher lying trends (in terms of emitted photon energy) that can still be clearly separated, which follow the principles discussed here with even stronger quadratic contributions. They move vertically closer together with significantly smaller widths, since high vibrational excitations of $B\ ^1\Sigma_u^+$ with comparably strong oscillations for a bound level mix with low continuum states with weak oscillations for their part. The density of emission features becomes denser and is harder to isolate. Above 9.5 eV, continuum emissions from the $C\ ^1\Pi_u$ state appear in addition.

6.1.2 The $C\ ^1\Pi_u\ 2p\pi$ state

Starting at 12.29 eV and with the same limit at 14.68 eV, the Werner band joins the Lyman band following an excitation into the 14 bound vibrational levels of $C\ ^1\Pi_u\ 2p\pi$, the lowest $^1\Pi_u$ and second lowest dipole allowed state. It features a much more tightly bound potential well than $B\ ^1\Sigma_u^+$ with an equilibrium distance of $R_e \approx 1.05$ Å comparable to the higher electronically excited states and the ground state $X\ ^2\Sigma_g^+$ of the molecular hydrogen cation.
The emissions from bound states follow a rather narrow Condon parabola, which is significantly more complete than for the Lyman band fluorescence with both the lower and upper arm visible. The transitions into higher levels of $X\ ^1\Sigma_g^+$ are still stronger, but elastic scattering is present and comparable. As a $^1\Pi_u$ state with an orbital angular momentum of $\Lambda = 1$, the rotational branches to the ground state ($\Lambda = 0$) contain a Q branch in addition to P and R due to $\Delta\Lambda = 1$. While technically this Q branch is only allowed for C^-, i.e. the lower component of the Λ-type doublet of $C\ ^1\Pi_u$, and the other two branches for C^+, this splitting is on the order of 1 meV for most levels and could not be resolved on the emission map. The additional features in the rotational structure appearing for this can be identified easily on Figure 5.3 where they are shown side-by-side with a $\Delta\Lambda = 0$ process. Investigations in the literature into the Werner band emissions band usually accompany those of the Lyman band such as [ASY82, ASK84] for electron impact and [ARL93] for pressure discharges.
The bound transitions end at the H(1s) + H($2l$) limit, where excitation into the continuum

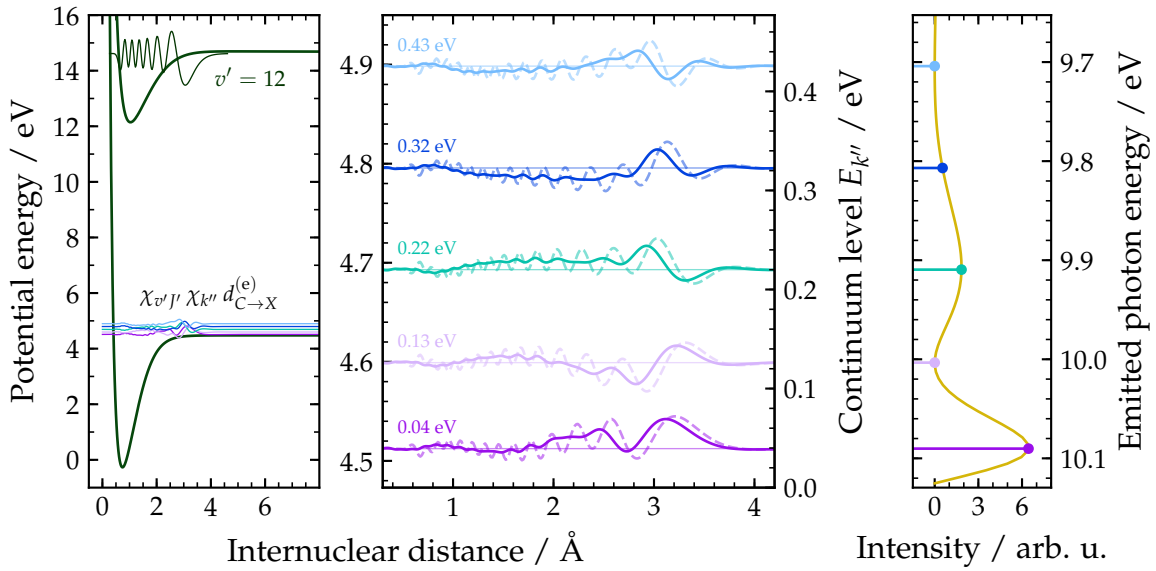

Fig. 6.6: *The wavefunction overlap $\chi_{v'J'}\chi_{k''}$ weighted by the electronic transition moment $d^{(e)}_{C\to X}$ between the upper bound level $v' = 12$, $J' = 1$ of $C\ ^1\Pi_u$ and several states k'' in the continuum of $X\ ^1\Sigma_g^+$ is shown (left) alongside a magnified view of this region (middle) and the resulting emission spectrum (right). The representation is analog to Figure 6.3.*

of $C\ ^1\Pi_u$ leads to dissociation and subsequent emission of the atomic Lyman-α line for $l = 1$ fragments. The contributions are more intense than in the case of $B\ ^1\Sigma_u^+$ and decline exponentially until about 17 eV, where they mostly vanish. This is discussed in more detail in Section 6.1.3 about the $B'\ ^1\Sigma_u^+$ state.

Below the dissociation line in the Werner band, the $C\ ^1\Pi_u$ state generates a small amount of continuum transitions. Its peak intensity is comparable to those in the Lyman band, but it covers vastly less area on the emission map. The much steeper potential energy curve of this state restricts the accessible range of internuclear distances the transition can occur on. Given the very high oscillations of continuum wavefunctions directly above the potential well of $X\ ^1\Sigma_g^+$, the overlap may occur mostly at the outer turning point of the upper bound level. On one hand, this causes only the higher vibrational excitations of $C\ ^1\Pi_u$ with turning points at larger R to cause significant emissions into the continuum. On the other hand, these are limited to much lower values $E_{k''}$ than for $B\ ^1\Sigma_u^+$, where the oscillations are comparable to the few bound states. In summary, the continuum emissions spawn only for larger upper vibrational states at $E_{v'J'}$ and small continuum levels at $E_{k''}$. On the emission map, this translates to a late onset on the horizontal

axis and a small vertical window close to the dissociation line. Figure 6.6 depicts the case analog to $B\ ^1\Sigma_u^+$ in Figure 6.3 for the overlap between bound states of $C\ ^1\Pi_u$ and continuum levels of $X\ ^1\Sigma_g^+$ alongside the emission spectrum. As with the Lyman band, the continuum emissions of $C\ ^1\Pi_u$ can be found in literature both theoretically [SD72], with selective excitation [NS87, SNR90] as well as broadband methods such as electron impact [ARL97]. The close proximity to the vibrational levels of $B\ ^1\Sigma_u^+$ in both excitation and emission is again separated on the emission map.

6.1.3 The $B'\ ^1\Sigma_u^+\ 3p\sigma$ state

Excitations between 13.69 and 14.62 eV may reach the only six vibrational levels of the $B'\ ^1\Sigma_u^+\ 3p\sigma$ state. This state has the shallowest potential well at 0.92 eV comparing to 4.5 eV for the ground state, 3.5 eV for the extraordinary wide $B\ ^1\Sigma_u^+$ and around 2.5 eV in the case of the $^1\Pi_u$ states.

The experimental data lacks any trace of the bound emissions from $B'\ ^1\Sigma_u^+$, which lie within a small part of the Werner band at its high energy limit. The simulated emissions separated by state in Figure 6.15 reveal a significantly weaker intensity for these compared to the preceding $2p\lambda$ states, as they are increased thirty-five times in their intensity to be visible on the same scale in that figure.

The left plot of Figure 6.7 contains a closer look on the bound emission of $B'\ ^1\Sigma_u^+$ on their own scale with annotations for the upper and lower vibrational levels. This separation provided by the emission map exposes the consequences of the low well depth. In general, the features follow a Condon parabola as observed for the other states, but it is distorted significantly to lower v'' with the vertex appearing between $v'' = 2$ and 3. This and the small number of vibrational levels becomes apparent as well after the dissociation limit approaches for $v' > 5$, where the parabola did not converge towards the dissociation line. Instead, the highest v'' are not reached in emission from any upper vibrational level v' but the last. Here the narrow potential well of $B'\ ^1\Sigma_u^+$ never reaches to distances up to the outer reversal point of vibrationally excited levels of $X\ ^1\Sigma_g^+$, where the majority of probability amplitude resides. A peculiar addition is the drop in intensity for $v'' = 10$, which reaches less than 1% of the typical emissions from the single upper level $v' = 4$.

Even though the electron configuration of $B'\ ^1\Sigma_u^+$ is $3p\sigma$ (+ $1s\sigma$) in the united atom configuration, it converges towards the H($2l$) + H(1s) limit for larger internuclear distances. At

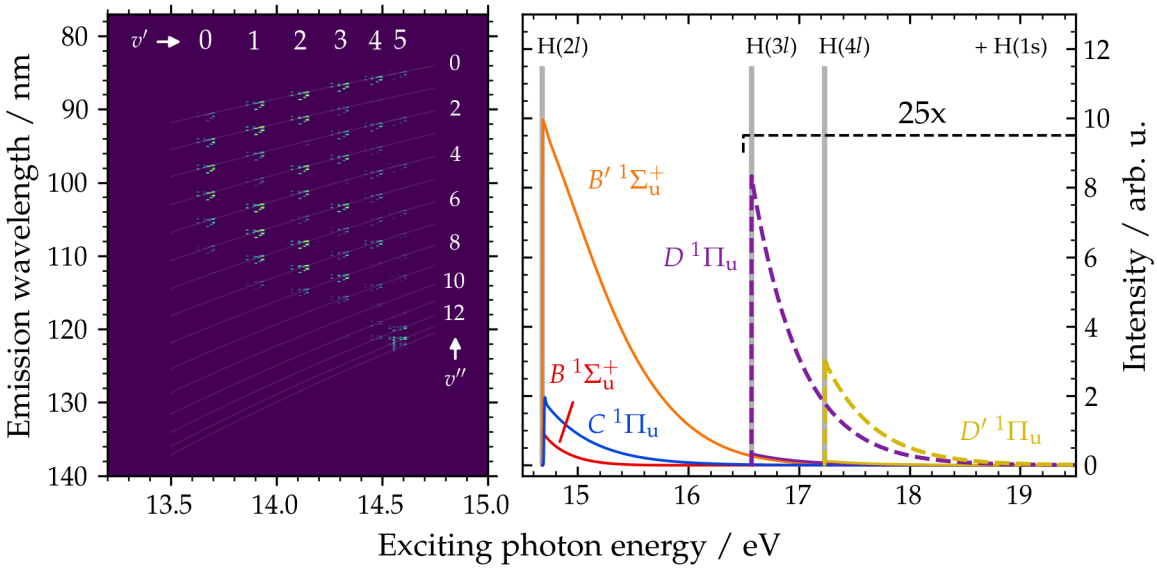

Fig. 6.7: *The partial emission map on the left contains only the bound and continuum emissions from the $B'\,{}^1\Sigma_u^+$ state with annoated upper and lower vibrational level v', v''. The excitation function for transitions into the vibrational continua (solid) leading to dissociation are shown for the commonly investigated states to the right. In addition, the contributions from $D\,{}^1\Pi_u$ and $D'\,{}^1\Pi_u$ are repeated with magnification relative to this scale (dashed).*

this point, it even provides the greatest contribution of direct excitation into continuum states and subsequent Lyman-α emission. The right plot in Figure 6.7 compares this state to the other signifcant ones presented here in terms of this intensity. The shown curves are obtained with the theoretical model of this work, but also exist in literature [LSJ12b]. For the highest upper vibrational level $v' = 5$, a slight amount of dissociative continuum transition appears as well as indicated on the left plot of Figure 6.7. It is created exclusively from the R(3) branch in excitation and then R(4) in emission, a combination of levels which happens to be the only one to exhibit a nonnegligible wavefunction overlap for this state.

6.1.4 The $D\,{}^1\Pi_u$ $3p\pi$ state

This state covers the region between 14.00 and 16.57 eV relative to the ground state of molecular hydrogen with 18 bound vibrational levels. It is the lowest accessible state that lies beyond the H(2l) dissociation limit by converging against H(3l) as well as partially above the ionization threshold of 15.43 eV. At the same, it introduces an additional

decay channel in the form of predissociation, where it may transition radiationless into the continuum of lower electronic states. This process alters the emission structure significantly and becomes even more abundant for the higher $np\lambda$ states following.
For the general trend, the bound emissions have a similar structure as the Werner band of $C\ ^1\Pi_u$ with a narrow Condon parabola and convergence along the dissociation line. However, the vibrational levels $v \geq 3$, the first levels above the H($2l$) limit, undergo a rapid predissociation process for the $^1\Pi_u^+$ component, which quenches any comparably slow molecular fluorescence [GMSJ12]. The $^1\Pi_u^-$ on the other hand remains stable and decays radiatively, because it is forbidden by the same symmetry rules that apply to dipole transitions to directly couple to $B'\ ^1\Sigma_u^+$ [GBGM79], which features strong dissociation via its continuum (see Section 6.1.3). As $^1\Pi_u^-$ is restricted to transitions with $\Delta J = 0$ to $^1\Sigma_g^+$, the bound emissions of $D\ ^1\Pi_u$ for $v \geq 3$ are limited to the rotational Q branch in excitation. The R and P branch is found as resonances in the atomic Lyman-α emissions of fragments formed after the predissociation process. Historically, this occurence of predissociation was discovered due to the larger line widths for the absorption lines of $^1\Pi_u^+$ (via the P, R branches) compared to $^1\Pi_u^-$ (via the Q branch), which hinted at a fast decay process [BDJ35, GMBG79].
These relations are depicted in Figure 6.8 for several rotationally resolved emissions. The left plot shows emissions after excitation into $D(v' = 2)$ below the first dissociation threshold. Both components $^1\Pi_u^+$ and $^1\Pi_u^-$ with their P, R and Q branches occur and lead to emission by bound molecular transitions to various vibrational levels v'' of the ground state. The right plot for the upper level $v' = 10$ is split between bound transitions for the Q branch and Lyman-α luminescence at the resonance position of P and R.
$D\ ^1\Pi_u$ and the electronically excited states with even higher energies belong to the group of superexcited states, because they are above the ionization threshold of the molecule [Pla62]. As these still possess only a single excitation, they are further categorized as superexcited states of the second kind. These states typically behave significantly different in their dynamics and characteristics and signify a molecule, which does not simply ionize once excited sufficiently. The emission of fluorescence in extensive molecular bands as a competitive decay channel in this region is an exceptional property of hydrogen. This was initially discovered in absorption studies after excitation with synchrotron radiation of small bandwidth [BGGM80] and later followed with particular studies focused on the interplay between ionization, dissociation and fluorescence [GMJS10, GMJR10]. The emission map extended by the excitation function for ionization

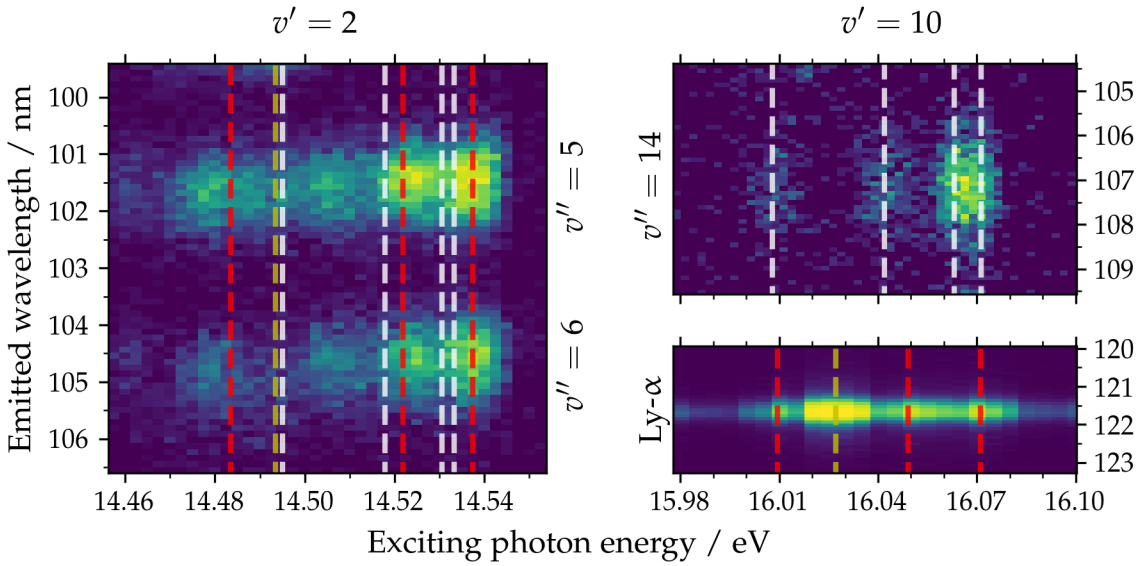

Fig. 6.8: *These partial emission maps isolate features from the $D\ ^1\Pi_u$ state. The left and upper right plot contain bound transitions from $v' = 2$ to $v'' = 5, 6$ and $v' = 10$ to $v'' = 14$, respectively. The lower right plot shows the Lyman-α line in the same range of excitation energies as the upper right. The rotational branches are annotated in excitation for R (red), Q (white) and P (yellow). The P and R branch belong to the Π^+ component, while the Q branch is exclusive to Π^-.*

for each exciting photon energy (as presented in Figure 6.12) contains and visualizes these relations through the region of bound transitions (for the direct fluorescence), the emission from fragments (for dissociation) and the ionization signal. It is automatically sensitive to separate the first two of these pathways through the dispersive measurement while still selecting individual upper levels. Nevertheless, the theoretical model used in this work is not capable of treating these different decay channels ab initio. As discussed in the limitations of the method in Section 4.2, it uses the mentioned literature instead to include them on an empirical basis.

In its limit, the $D\ ^1\Pi_u$ state is the first one to converge towards the $n = 3$ limit. Here it results in the dissociation into H(3p) fragments, which may then emit the Lyman-β line at 102.6 nm visible as a horizontal line on the emission map. In comparison to the lower states at the H($2l$) limit, this excitation into the vibrational continuum is significantly weaker as seen in the right part of Figure 6.7.

Finally, this state contributes a small amount of continuum transitions for several Q branches at high vibrational excitations v'. While weak, they are clearly separated from

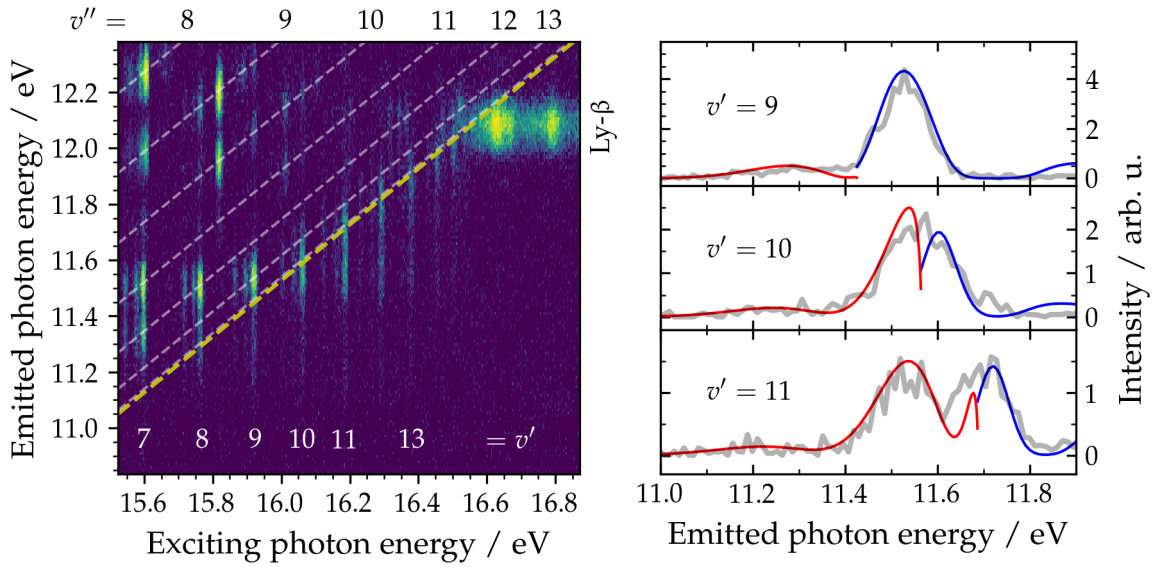

Fig. 6.9: *The partial emission map on the left shows the emissions after excitation of several vibrational levels v' of $D\ ^1\Pi_u$ into both the ground state for higher v'' (grey dashed) as well as the the continuum transitions below the dissociation line (yellow dashed). The experimental emission spectra (grey), plotted as a function of emitted photon energy rather than wavelength, for three particular v' are added on the right with the theoretical emission spectrum for bound (blue) and continuum (red) transitions.*

the bound transitions just below the dissocation line. Figure 6.9 shows this part of the emission map with level annotations and emission spectra from three exemplary upper vibrational levels v'. Here, the contributions from bound and continuum transitions are added based on the theoretical model of this work.

6.1.5 Higher $np\lambda$ states

The $^1\Sigma_u^+$ $np\sigma$ and $^1\Pi_u$ $np\pi$ Rydberg series accessible by dipole selection rules continue for $n \geq 3$ up to the ground state $X\ ^2\Sigma_g^+$ $1s\sigma_g$ of the molecular cation. As the majority of all these states is already beyond the ionization threshold of 15.43 eV, the lowest vibrational level $v = 0$ of $X\ ^2\Sigma_g^+$, the competition of different decay channels occurs in the same way as for $D\ ^1\Pi_u$, albeit unique for the situation of each state [GMJS10, GMJR10].

For $\lambda = 0$, this begins with the $B''\ ^1\Sigma_u^+$ $4p\sigma$ state. Its bound levels lie between 14.49 and 16.57 eV converging to the H($3l$) limit. For even higher $n \geq 5$, the states are usually labeled in order of their appearance in the $^1\Sigma_u^+$ series with B'' as the third one, i.e. $3\ ^1\Sigma_u^+$.

As already observed for $B'\ ^1\Sigma_u^+$ 3pσ and just noted for B'', these states tend towards a dissociation limit of H(1s) + H($(n-1)l$) with reduced principal quantum number [GMJS13b], except in the case $n = 2$ for B. The $B''\ ^1\Sigma_u^+$ state is actually part of the first configuration with ungerade symmetry to have a double well in its potential energy curve due to avoided crossings with $\bar{B}\ ^1\Sigma_u^+$ 2sσ 2pσ that results in the $B''\bar{B}\ ^1\Sigma_u^+$ 4pσ + 2sσ 2pσ state. The inner well of $B''\bar{B}$ has an equilibrium distance of 1.08 Å in line with the other electronically excited states, while the outer well is separated by a barrier at around 3 Å and assumes its minimum value for 5.9 Å. In fact, all $^1\Sigma_u^+$ npσ with $n \geq 4$ are double well states. The $B''\bar{B}$ state itself has been investigated in [GMKW07b, GMKW07a], whereas several higher members of this series are found in [GMJS13b]. The nature of these valence bonds at long-range due to their double wells are the focus of [KdLU03]. Earlier works in this regard concentrated on the $^1\Sigma_g^+$ states such as $E, F\ ^1\Sigma_g^+$, which also feature double wells except in the case of $X\ ^1\Sigma_g^+$ and are discussed in Section 6.1.6 in their role as a relaxation state after emission.

The next state with $\lambda = 1$ is $D'\ ^1\Pi_u$ 4pπ, whose vibrational levels occupy the region starting at 14.62 eV and culminating into H(4l) + H(1s) at 17.23 eV. Apart from $D''\ ^1\Pi_u$ 5pπ for $n = 5$, the succeeding states in this series are usually identified by the principal quantum number n of their excited electron, as they are mixed energetically with different nl states with $l > 1$ but the same $^1\Pi_u$ symmetry. The dissociation limit is decreased by one unit in its principal quantum number for $n \geq 4$ [GMJS13a] similar to the higher npσ states described above. Specific examinations of these states are done particularly on the basis of their absorption structure such as [GMJS13c, GMJS13a].

A commonly used shorthand notation for the Rydberg series of states in molecular hydrogen is the electronic configuration $nl\lambda$ of its excited electron followed by the state label, if applicable, and omitting the molecular term, e.g. 4pπD' for $D'\ ^1\Pi_u$ 4pπ. This assignment to individual electronic states is only meaningful up to $n \approx 7$, as the coupling between electronic state and vibrational-rotational motion breaks down for even higher n with a transition to Hund's coupling case d) [GMJS13c]. At that point, a better representation is the nuclear state of the molecular cation in addition to another excited electron. The features present on the emission map are almost exclusively described with $n \leq 6$, however, and the concept of electronic states with their associated vibrational and rotational structure is still reasonable.

The region on the emission map with features belonging to the higher npλ states, that is the upper right corner with higher excitation energies and lower emission wavelengths, is

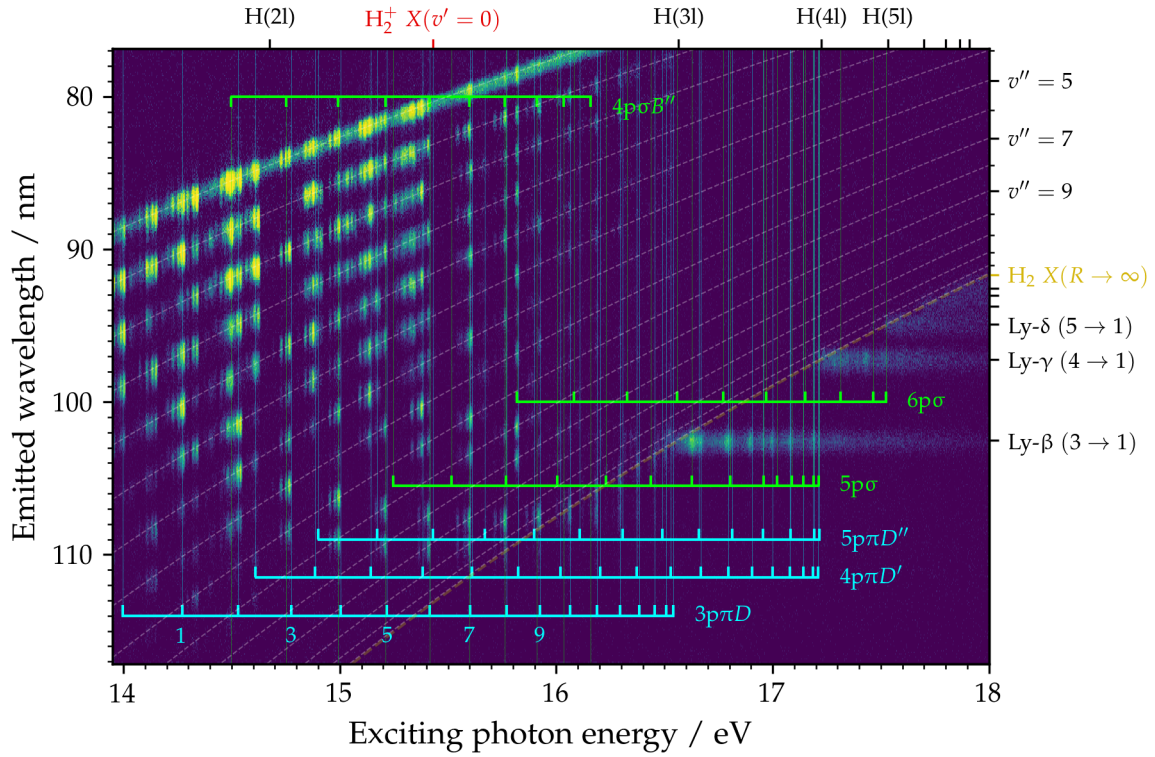

Fig. 6.10: *The partial emission map in the region of higher npλ states of molecular hydrogen. The vibrational levels of several $^1\Sigma_u^+$ npσ states (green) by their R(1) and $^1\Pi_u$ npπ states (blue) by their Q(1) branches are annotated along with the ground state levels in emission (grey dashed) and the dissociation line (yellow). On the top axis, the exciting photon energy required for the respective dissociation limits and ionization threshold (red) is plotted, while the right plot identifies several atomic emission lines and trend lines for lower vibrational level v'' after relaxation.*

shown in Figure 6.10. It is restricted to the upper left by elastic scattering with $E_{in} = E_{out}$, which at these excitation energies is particulary enhanced with a continuos background due to scattered synchrotron radiation. All features of radiative transitions into the 15 bound vibrational levels of $X\ ^1\Sigma_g^+$ after excitation can be attributed to particular upper levels of an $np\lambda$ state. The previously discussed competition of autoionization and predissociation with molecular fluorescence may now be disentangled by examining which combination of v', v'' is found as a bound transition, as a resonance on Lyman emissions from the previous dissociation limit or else as part of the ionization.
For $D\ ^1\Pi_u$, where the $^1\Pi_u^+$ component predissociates for $v \geq 3$ and only the Q branch remains for molecular fluorescence, this has been performed in the preceding Section 6.1.4.

The higher states in this series with D' and D'' participate in fluorescence up to the ionization threshold, but are then dominated by autoionization. The predissociation process (before the H($3l$) limit to $n = 2$) is significantly weaker as the required change in principal quantum number is larger than in the case of just D [GMJS10]. The multitude of overlapping molecular bands up to the ionziation threshold is therefore almost completely quenched with the exception of said Q branches of D and singular, weak contributions of B'', for example.
Below the region of bound transitions consisting of the 15 vibrational levels of $X\ ^1\Sigma_g^+$, the Lyman series is present starting with Lyman-β. Once the H($3l$) threshold is reached, predissociation of several $n \geq 4$ states can be found for Lyman-β and for $n \geq 6$ even on Lyman-γ. The principal quantum number is reduced twice here from the initial molecular configuration $n\mathrm{p}\lambda$ that converges towards the $n' = n - 1$ limit and couples to the continuum of state $n'\mathrm{p}\lambda$, which in turn converges towards $n'' = n' - 1 = n - 2$. As the Q branches of $D\ ^1\Pi_u$ form the highest remaining complete molecular band, Lyman-β is the highest atomic emission line with a Condon parabola converging against it. The higher members of the Lyman series begin at the dissociation line after the excitation is sufficient to reach the respective continuum without any structure coming before. The emission map ends just before the dissociation limit of the ground state $X\ ^2\Sigma_g^+$ of the molecular cation at 18.08 eV, i.e. $H_2^+\ X(R \to \infty)$, which defines the upper limit for any singular excitation of the neutral molecule.

6.1.6 Emissions into the $E, F\ ^1\Sigma_g^+\ 2s\sigma + 2p\sigma^2$ state

The emission maps of molecular hydrogen presented in this work, both experimentally and theoretically, consider only the ground state $X\ ^1\Sigma_g^+$ as the final destination for bound transitions. However, based on the dipole selection rules for diatomic (2.45), (2.46) and homonuclear (2.47) molecules, other transitions may occur after a sufficiently energetic excitation as well. In the case of fluorescence from the $n\mathrm{p}\lambda$ states with $^1\Sigma_u^+$ or $^1\Pi_u$ symmetry excited on the emission map and presented here, this includes the remaining $^1\Sigma_g^+$ states in addition to the ground state.
The first in this series is $E, F\ ^1\Sigma_g^+\ 2s\sigma + 2p\sigma^2$, a double well state generated by an avoided crossing between $E\ ^1\Sigma_g^+\ 2s\sigma$ and the doubly excited state $F\ ^1\Sigma_g^+\ 2p\sigma^2$. Its potential energy curve is plotted in Figure 6.11 along with its vibrational level positions and computed wavefunctions. Well below the energetic barrier separating the two wells at around

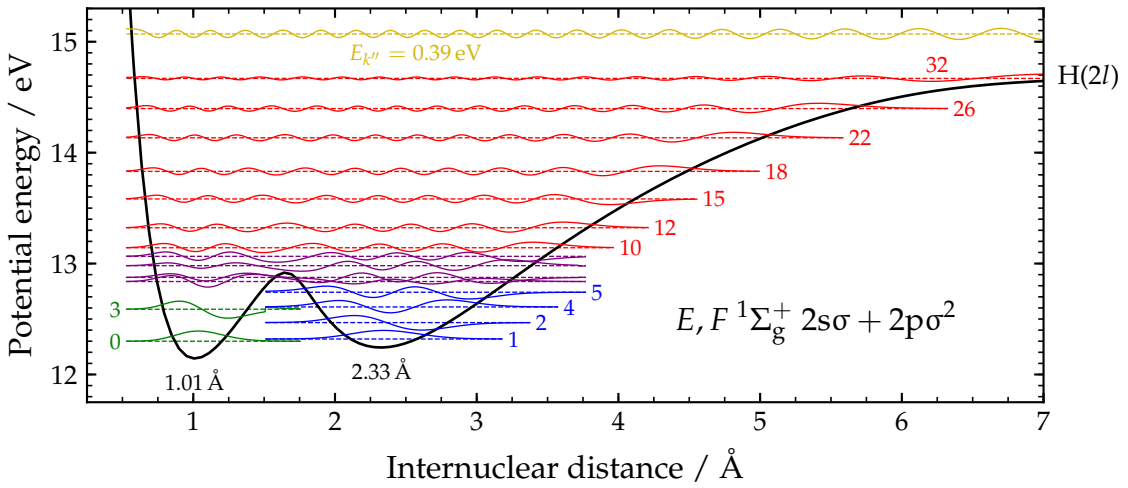

Fig. 6.11: *The potential energy curve of the $E, F\ ^1\Sigma_g^+\ 2s\sigma + 2p\sigma^2$ state of molecular hydrogen from [OSW99] with the vibrational levels and wavefunctions calculated with the model described in Chapter 4. The level split into the inner (green) and outer (blue) well followed by an intermediate region (violet) of tunneling and perturbance by the potential barrier. For $10 \leq v \leq 32$, the levels live within the greater well up to the dissociation continuum (with a exemplary continuum state in yellow) converging to H(1s) + H(2l).*

1.65 Å, these level are restricted to either the inner or the outer well. Close to the barrier at $v \approx 6$, significant amplitude is found in both components through tunneling. The levels $v \geq 10$ are an eigenstate of the greater well up to the last bound level with $v = 32$. For large internuclear distance, the state converges towards the H(1) + H(2l) limit.
As it lies energetically within the other electronically excited states with $n = 2$ discussed here, the emissions into this state occur at much higher wavelengths. The majority is found in the visible regime at around 550 nm and weaker components span the near ultraviolet to near infrared. Compared with the emission maps in the far ultraviolet and vacuum ultraviolet covering the emissions into the ground state, this one is hence shifted considerably along the vertical axis. In literature, this spectral range is typically dominated by continuum transitions between the triplet states $a\ ^3\Sigma_g^+$ and $b\ ^3\Sigma_u^+$ as well as molecular bands from $^1\Sigma_g^+$ states (such as E, F) to $B\ ^1\Sigma_u^+$ following an excitation by electron-impact [JAP98]. As these upper states cannot be reached via electric dipole transitions like selective synchrotron radiation or fluorescence, they cannot be present on an emission map. A previous work with this constraint that selectively excites $np\lambda$ states which subsequently fluoresce into E, F may be found in [ÁEK04] and covers a few specific upper vibrational levels with $n \geq 4$ and emissions between 500 and 600 nm.

The photon emissions were found there to be in agreement with those to the ground state with respect to the expected population of the upper states. While this spectral range was not covered experimentally in this work, the theoretical model introduced in Chapter 4 may be used to simulate the expected result. This is shown in Figure 6.16 for the bound transitions of several $n\mathrm{p}\lambda$ states to $E, F\ ^1\Sigma_g^+$, i.e. the process:

$$\begin{aligned} & X(v=0; J=0,1,2,3) \\ \rightarrow\ & n\mathrm{p}\lambda(0 \leq v' < v'_{\mathrm{limit}}; J' = J, J \pm 1) \\ \rightarrow\ & EF(0 \leq v'' < 33; J'' = J', J' \pm 1) \end{aligned}$$

Compared to the other simulated emission maps, any atomic emissions after dissociation into H($3l$) fragments leading to Balmer lines is omitted. Dissociative continuum emissions are possible but negligible (10^{-5}) in their intensity compared to the bound transitions. For the higher states $n \geq 4$, the constraints on fluorescence due to autoionization and predissociation discussed in the previous sections are taken into account. Because it covers a greater relative range of emissions, it is plotted as a function of emitted photon energy rather than wavelength, as the inverse relation between these two values distorts the otherwise linear trends considerably.

The strongest features found on this emission map in the visible regime are molecular bands from the $3\mathrm{p}\sigma B'$, $3\mathrm{p}\pi D$ and $4\mathrm{p}\pi D'$ states, in particular the latter. This is in excellent agreement with the discussed literature, that places the peak emission around 550 nm. Some amount of overlap with the $2\mathrm{p}\pi C$ state exists, but the spontaneous emissions from this state with photon energies of $\ll 1$ eV is suppressed by the respective Einstein coefficient due to its cubic scaling with the energy difference.

The levels of both the inner and the outer well of $E, F\ ^1\Sigma_g^+$ contribute with comparable intensities and overlap due to their small energetic distance, while the intensity fades when relaxing into its higher vibrational levels. As the potential well depth and position of this state is similar to the other excited states and hence different than the ground state, the characteristic trends of maximum intensity, the Condon parabolae, run almost horizontally.

A few other states satisfy the selection rules for transitions from Rydberg states as well, which includes the higher members in the $^1\Sigma_g^+$ series such as $H\ ^1\Sigma_g^+$ $3\mathrm{s}\sigma$ and $G, K\ ^1\Sigma_g^+$ $3\mathrm{d}\sigma + 2\mathrm{p}\pi^2$ as well as $^1\Pi_g$ stats like $I\ ^1\Pi_g$ $3\mathrm{d}\pi$. As these lie even higher in their

potential energy, their level differences to the Rydberg states are increasingly shifted in the infrared and further. Similar to the transitions $C \rightarrow E, F$ discussed above, the Einstein coefficient for spontaneous emissions suppresses these processes heavily in favor of transitions into $E, F\ ^1\Sigma_g^+$ and particularly $X\ ^1\Sigma_g^+$.

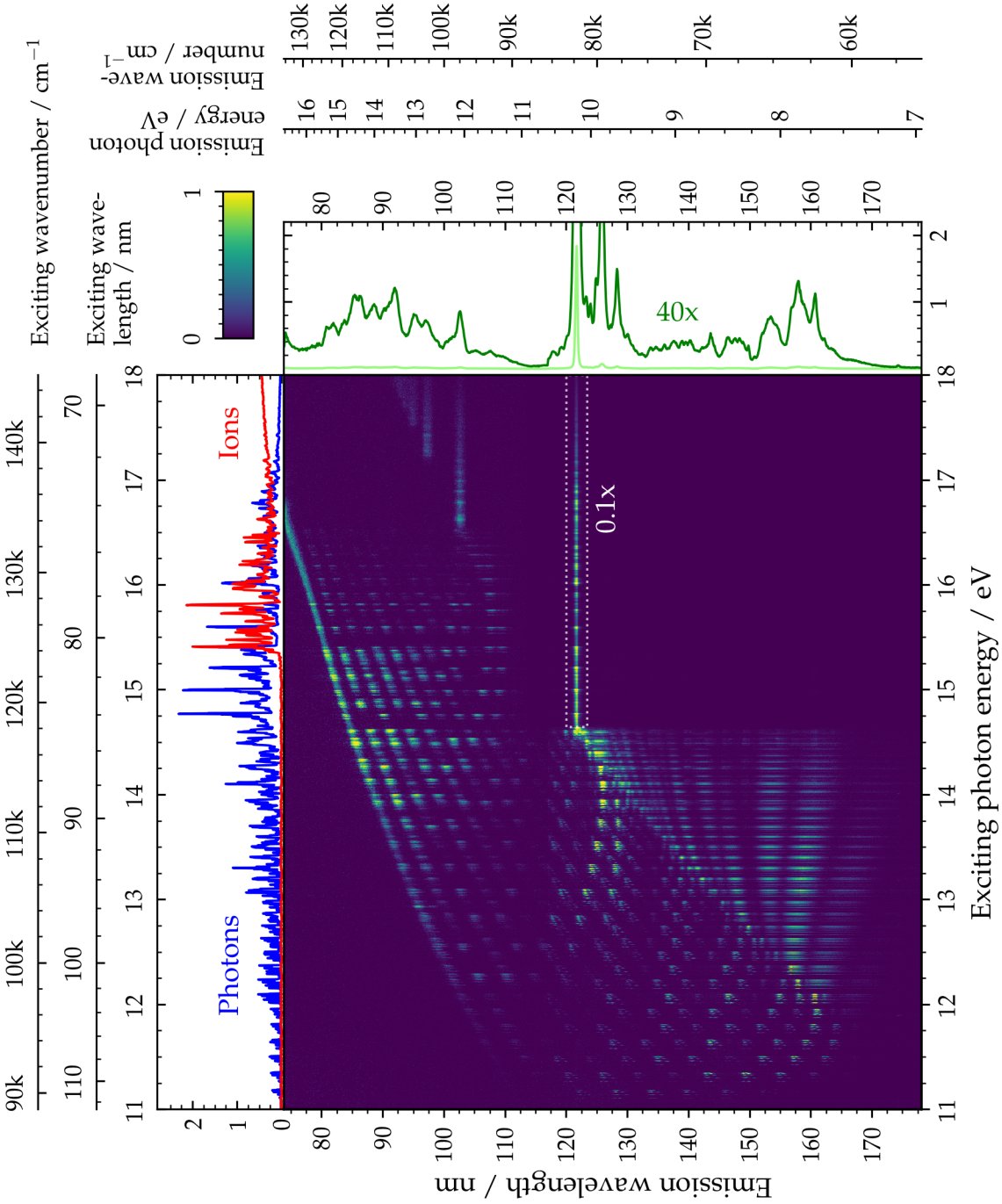

Fig. 6.12: *The complete rovibronic emission map of molecular hydrogen in the regime of singly excited electronic states based on the experimental results. The excitation function for photon emission as a sum in vertical direction in blue, for ionization in red as well as the integrated emission spectrum in green is shown. The Lyman-α line is reduced in intensity before a non-linear intensity scaling with $a = 15$ is used as defined in* (3.3).

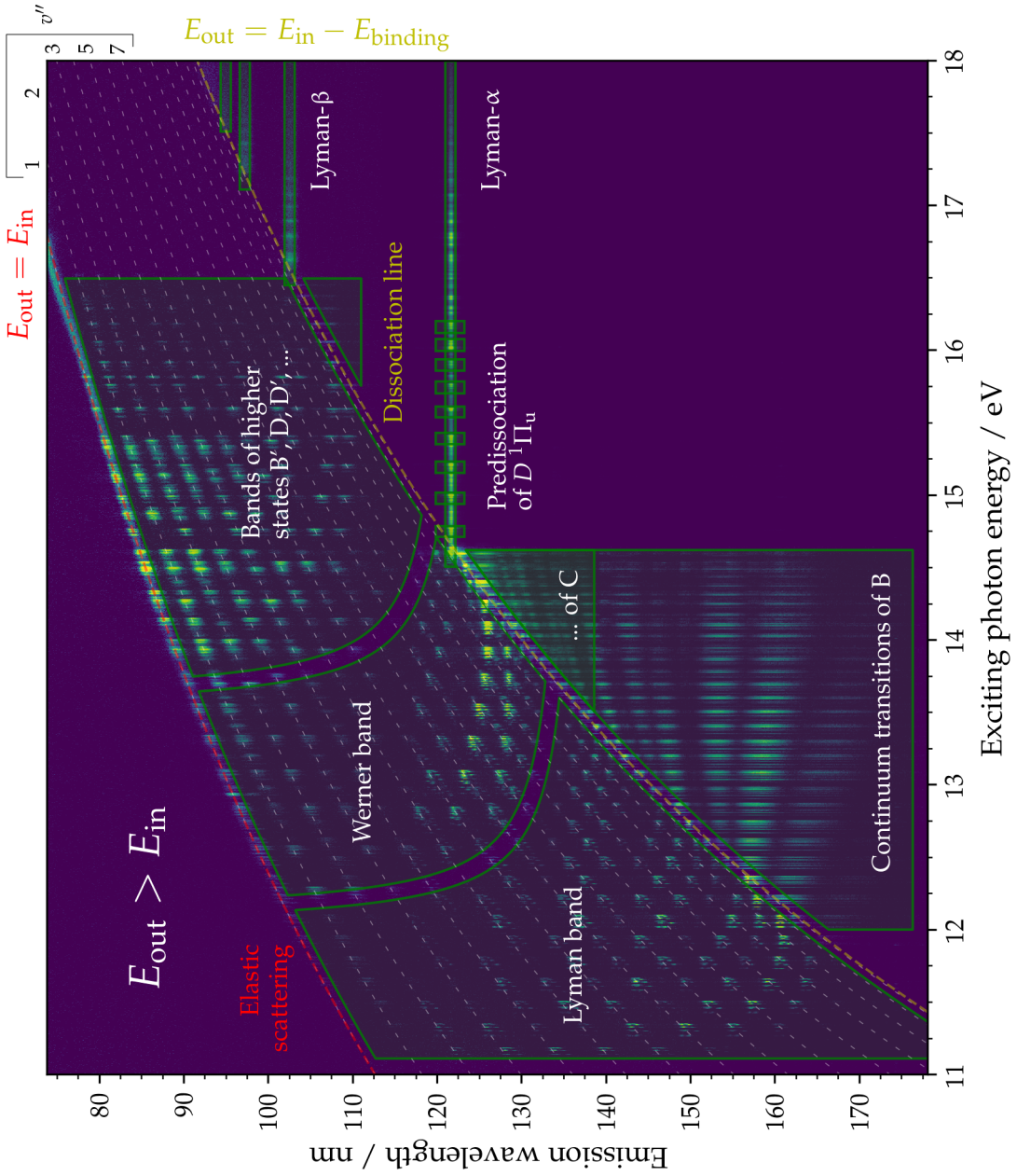

Fig. 6.13: *The complete rovibronic emission map of molecular hydrogen in the regime of singly excited electronic states. The most relevant visible features are summarized categorically, such as different regions of bound transitions or unbound transitions as well emission after dissociation. The same presentation is used as in Figure 6.12.*

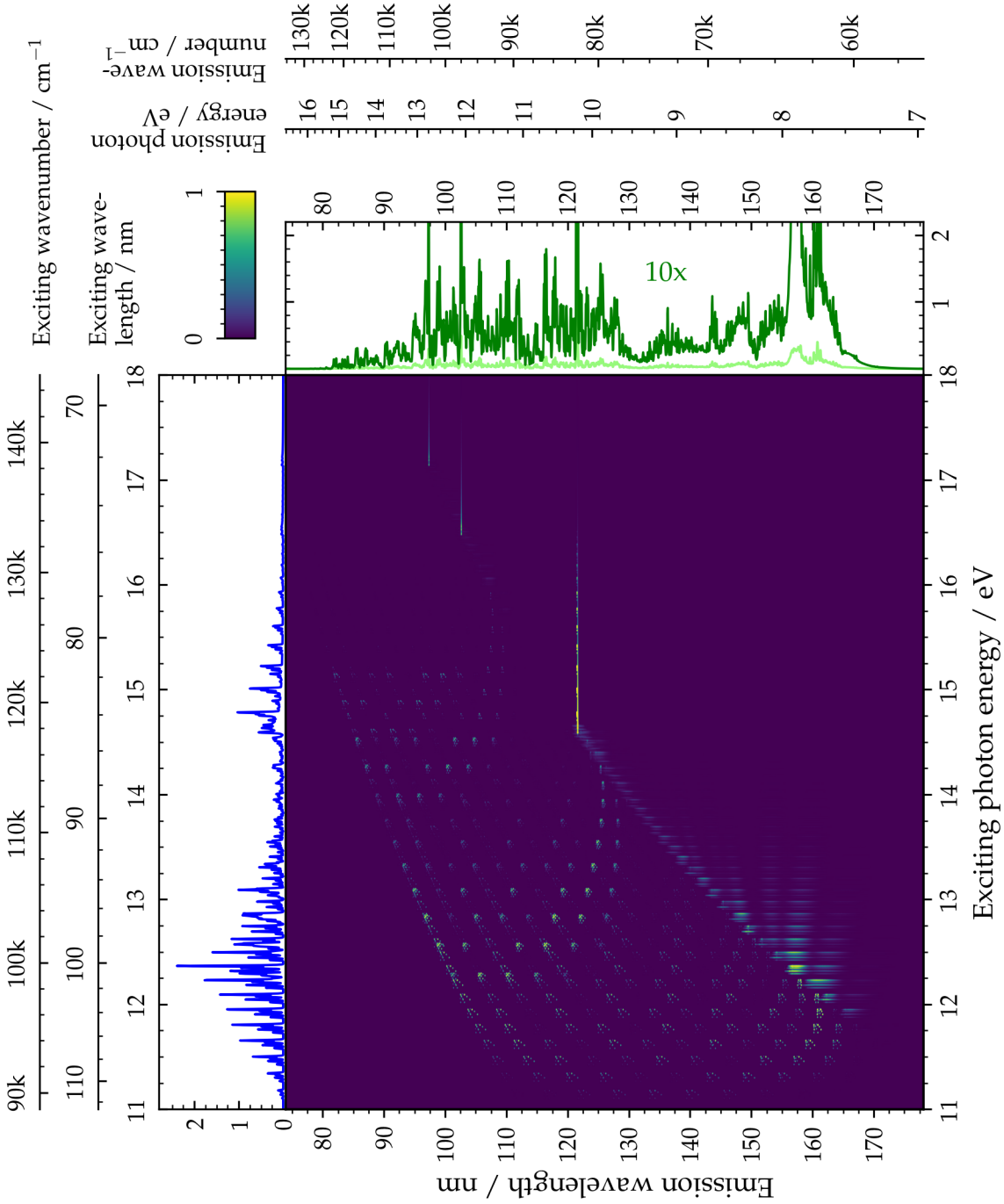

Fig. 6.14: *The complete rovibronic emission map of molecular hydrogen in the regime of singly excited states based on the simulation with a comparable resolution to Figure 6.12. The excitation function for photon emission as a sum in vertical direction in blue as well as the integrated emission spectrum in green is shown. A non-linear intensity scaling with $a = 60$ is used as defined in* (3.3).

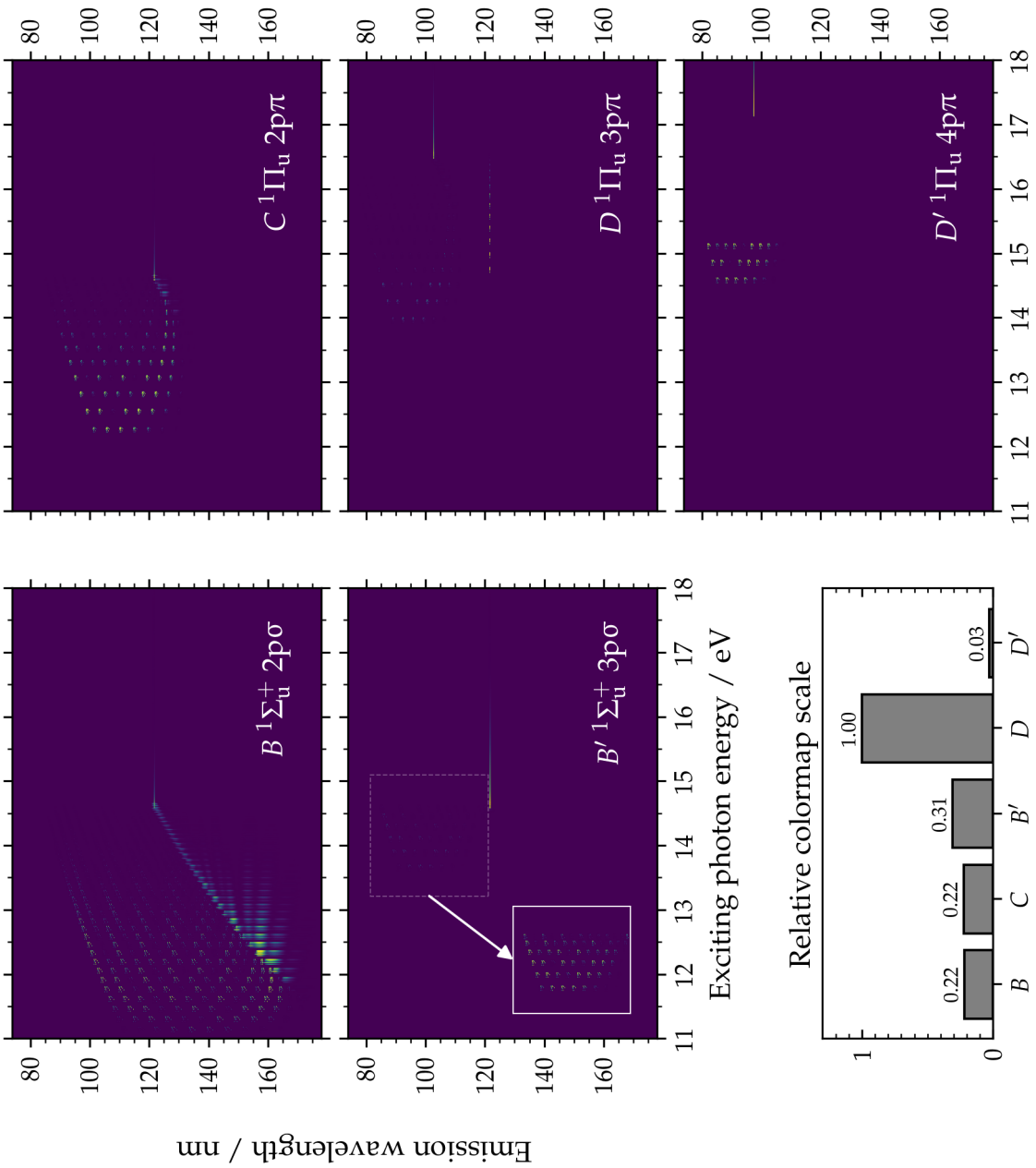

Fig. 6.15: *The separated emission maps of molecular hydrogen based on the simulation for each of the major states involved. Each state is scaled individually to maximize its contrast with* $a = 35$ *as defined in* (3.3)*. The relation between the colormaps is shown in the lower left plot. In addition, the inset for the* $B'\,{}^1\Sigma_u^+$ *state adds the bound transitions again scaled individually, which is around thirty-five times weaker.*

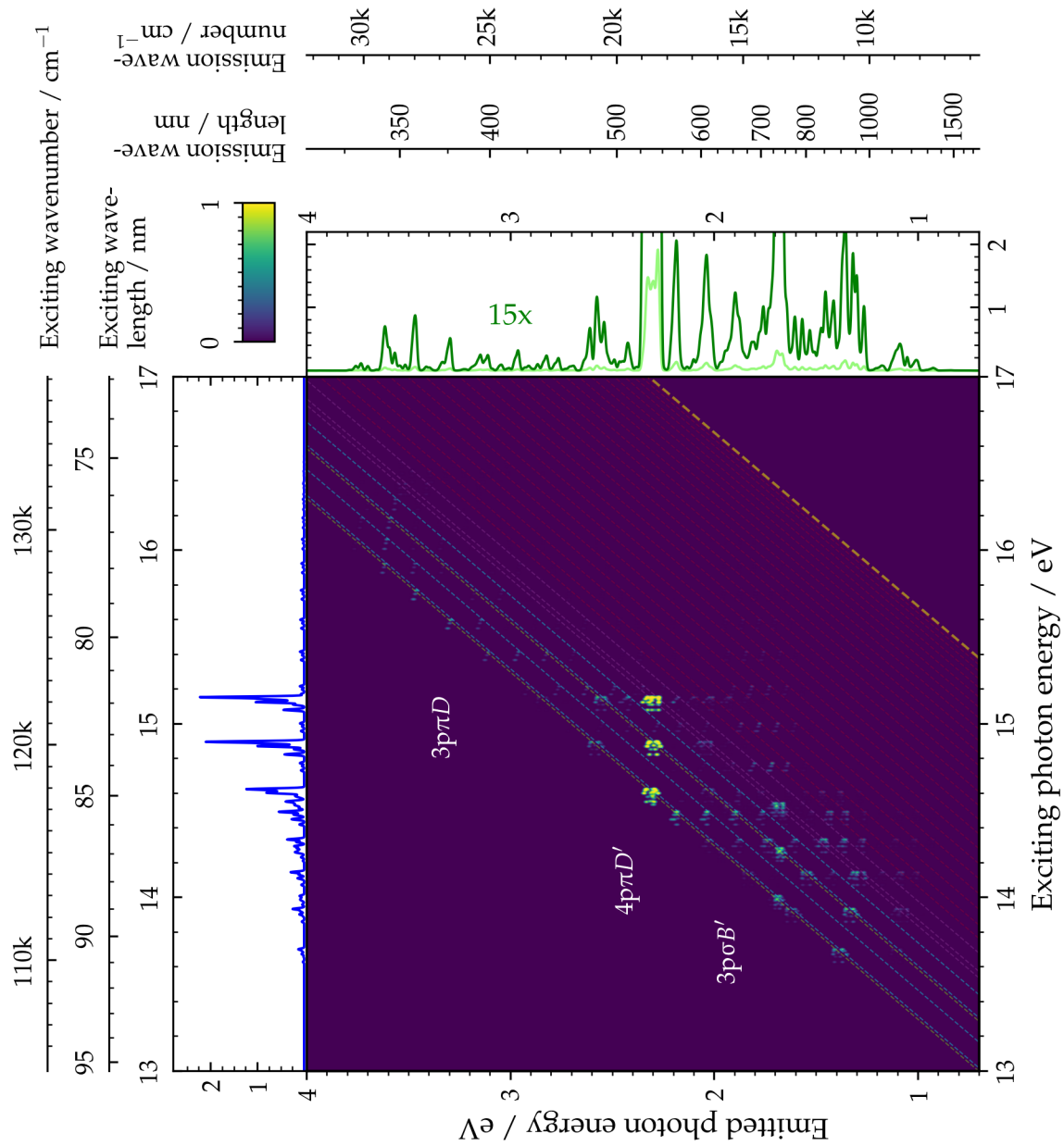

Fig. 6.16: *The rovibronic emission map of molecular hydrogen in the visible spectral range for bound transitions of select singly excited electronic states to $E, F\ ^1\Sigma_g^+\ 2s\sigma + 2p\sigma^2$ based on a simulation. The excitation function for photon emission as a sum in vertical direction in blue and the integrated emission spectrum in green is shown. The vibrational levels of EF after relaxation are annotated for the inner well (green), outer well (blue), transition (violet) and greater well (red). For each relevant feature, the responsible upper state is added. A non-linear intensity scaling is used with $a = 25$ as defined in* (3.3).

6.2 Molecular deuterium

The deuterium molecule D_2 consists of two deuterons, the nuclei of the heaviest stable isotope of hydrogen. As its mass is doubled by the addition of a neutron, this molecule exhibits a rather strong isotopic effect, which makes it comparably accessible to experimental methods. With the hydrogen molecule as one of the most important prototype system in molecular physics in general, the deuterium molecule therefore lends itself to study the particular spectroscopic impact of the nuclear mass. This section explores the influence found on rovibronic emission maps.
An extensive overview of the work on molecular deuterium's state and level structure prior to the advent of laser- and synchrotron-based methods is found in [FSC85]. Further investigations include Fourier transform absorption spectroscopy [dLDS12, DIU11] as well as PIFS [GMSJ12, GMVJ15, GMJD16, GMVJ16, GMJV17]. These are often performed directly in conjunction with molecular hydrogen or analog to the course of action applied to it, mostly related to superexcited states discussed further below.
As with H_2, the full experimental results are available for D_2 and shown in Figure 6.19 in their entirety, while Figure 6.20 annotates the different regions and most important features visible. In addition, the same computational approach was used and yields the simulated results of Figure 6.21 as a composited matrix and of Figure 6.22 with the emissions separated by the upper state. The same potential energy curves and electronic transition moments [Wol93, WS03a, WS03b, OSW99] were used as a starting point. A major change involves the reduced mass μ and mass-corrected Rydberg constant $R_M = R_\infty/(1 + m_e/M)$, which amount in this case to

$$\mu_{H_2} = 0.504\,\mathrm{u} \qquad R_{H_2} = 13.598\,\mathrm{eV}$$
$$\mu_{D_2} = 1.008\,\mathrm{u} \qquad R_{D_2} = 13.602\,\mathrm{eV}$$

These were used to adapt the potential energy curves as part of the adiabatic correction described in (2.32), which are shifted by up to 0.08 eV [SW02]. The difference between the curves is illustrated in the left plot of Figure 6.17 for the ground state $X\,{}^1\Sigma_g^+$. The thermal population of rotational levels at room temperature based on (4.24) results for molecular deuterium in a population of $J \leq 5$ with $0.18, 0.20, 0.38, 0.11, 0.10, 0.01$ for each level starting with $J = 0$, respectively.
The immediate observation when comparing the emission map of these two isotopo-

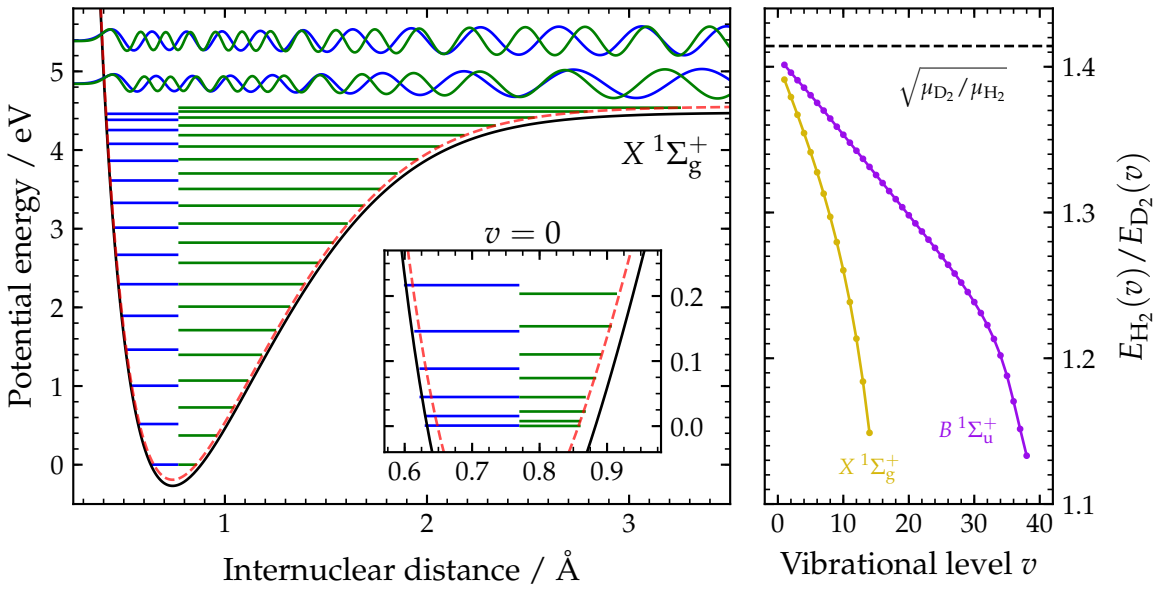

Fig. 6.17: *The bound vibrational levels of the ground state $X\,^1\Sigma_g^+$ of both molecular hydrogen (blue) and deuterium (green) are shown in the left plot in the potential energy curve of H_2 (black) and D_2 (red dashed). In addition, two wavefunctions in the vibrational continuum are included with the same total energy for both isotopologues. The small inset extends this to the rotational levels for $v = 0$. The right plot compares the ratio between the level energies for $X\,^1\Sigma_g^+$ (yellow) and $B\,^1\Sigma_u^+$ (purple) against the expectation value for an harmonic oscillator (black dashed).*

logues is the different number of vibrational levels of each electronic state. The heavier one, D_2, has smaller energy spacings between its levels and significantly more of it. This is shown side-by-side with H_2 in the left plot of Figure 6.17 for both vibration and rotation. As derived in (2.27), the nuclei move in the potential energy curve generated by the electrons. Their rovibrational motion is then described by the stationary states of that potential. At low rovibrational excitations in a sufficient energetic distance from its dissociation energy D_e, this potential may be approximated as harmonic, i.e. $U(R) \propto R^2$. The levels E_v in such a potential with the force constant k and mass m are

$$E_v = \hbar\omega(v + \frac{1}{2}) = \hbar\sqrt{\frac{k}{m}}(v + \frac{1}{2}) \propto \sqrt{\frac{1}{m}} \tag{6.5}$$

As noted above, the potential energy curves differ only very slightly and the force constants $k_{H_2} \approx k_{D_2}$ can be assumed to be equal. The ratio between the same levels should therefore scale with $\sqrt{\mu_{D_2}/\mu_{H_2}} \approx 1.41$. In fact, the distance between the lowest

vibrational levels of $X\ ^1\Sigma_g^+$, where the potential is the least anharmonic, decreases by approximately 1.39 when moving from H_2 to D_2. A more appropriate model to account for this anharmonicity is a Morse potential as defined in (2.17), which is well suited to model most potential energy curves. With its eigenvalues $\tilde{E}_v = E_v - E_v^2/4D_e$ in relation to the quantum harmonic oscillator, the ratio of vibrational levels becomes:

$$\frac{\tilde{E}_v^{(H_2)}}{\tilde{E}_v^{(D_2)}} = \sqrt{\frac{\mu_{D_2}}{\mu_{H_2}}} \cdot \frac{D_e^{(D_2)}}{D_e^{(H_2)}} \cdot \frac{E_v^{(H_2)} - 4D_e^{(H_2)}}{E_v^{(D_2)} - 4D_e^{(H_2)}} \approx \sqrt{\frac{\mu_{D_2}}{\mu_{H_2}}} \cdot \frac{E_v^{(H_2)} - 4D_e}{E_v^{(D_2)} - 4D_e} \tag{6.6}$$

In the last step, the Morse constants except for the masses have been assumed to be identical again, e.g. the well depth $D_e^{H_2} \approx D_e^{D_2}$. The additional factor in the ratio introduced by the Morse potential is positive and always smaller than one, as $E_v < 4D_e$ applies to all vibrational levels and those of H_2 have generally a higher energy at the same v. It becomes smaller for increasing v, when the difference to $4D_e$ is reduced and the ratio in total approaches unity. This value as defined in (6.6) is shown in the right plot of Figure 6.17 for the $X\ ^1\Sigma_g^+$ and $B\ ^1\Sigma_u^+$ states of molecular hydrogen and deuterium. Both trends exhibit the harmonic oscillator limit for low vibrational levels v and then decrease as discussed above.
Because the potential energy curve of each electronic state may be considered equal on this order of magnitude as mentioned earlier, the lower energetic difference fits considerably more eigenstates into the same potential well. In numbers, the ground state $X\ ^1\Sigma_g^+$ of molecular deuterium possesses 22 bound vibrational levels compared to the 15 in the hydrogen molecule. The deep $B\ ^1\Sigma_u^+$ state changes from 39 to 52. This contraction of the rovibrational structure causes the population of higher rotational levels in the ground state at room temperature, too.

Apart from this fundamental difference of the amount of vibrational levels, the general structure of the bound emissions, that is the region between the elastic scattering line and the dissociation line, remains the same between the isotopologues. Depending upon its potential energy curve and analog to the descriptions in the previous Section 6.1, each electronic state forms at least one half of a Condon parabola converging against an atomic emission line after dissociation.
For the 2pλ states $B\ ^1\Sigma_u^+$ ($\lambda = 0$) and $C\ ^1\Pi_u$ ($\lambda = 1$), the intensity distributions correlate particularly well for bound transitions, as these states are still well below the dissociation threshold for H(2l) + H(1s) of 14.76 eV which they actually converge towards in the end,

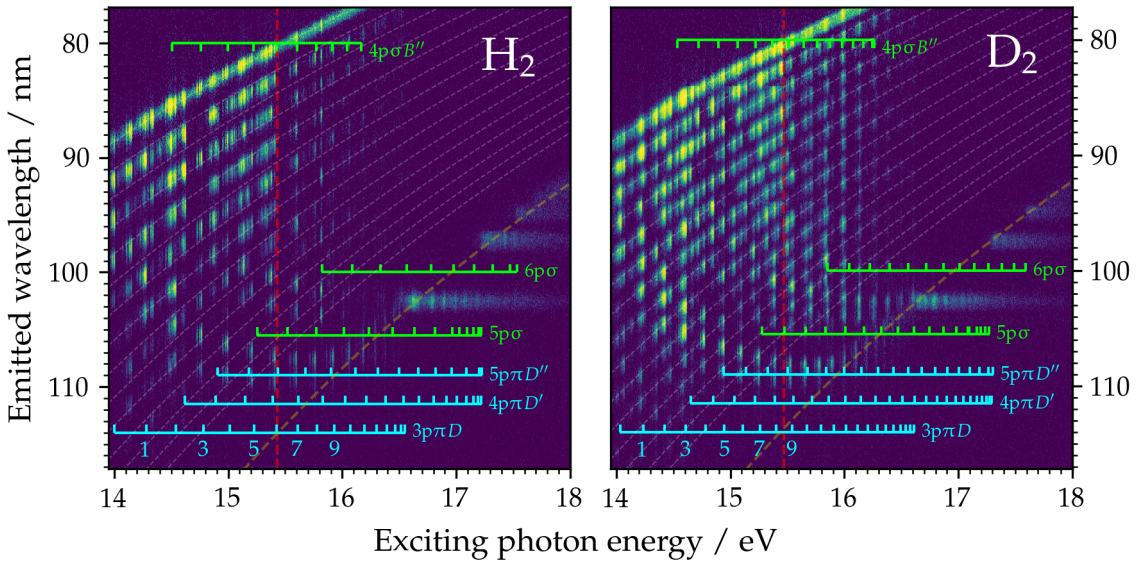

Fig. 6.18: *The partial emission maps from experimental data in the region of higher npλ states of molecular hydrogen (left) and deuterium (right). Analog to Figure 6.10, the vibrational levels of several* $^1\Sigma_u^+$ *npσ states (green) by their R(1) and* $^1\Pi_u$ *npπ states (blue) by their Q(1) branches are annotated along with the ground state levels in emission (grey dashed), the dissociation line (yellow dashed) and the ionization threshold (red dashed)*

and the ionization threshold for D_2^+ of 15.47 eV. The same applies to the continuum emissions following below the dissociation line. The mass influence on the wavefunctions in the vibrational continuum manifests here through the horizontal trends of maximal intensity developing along the excitation axis, which were discussed for H_2 in detail in Section 6.1.1. The individual peaks for D_2 are condensed spectrally, because the frequency and phase of these wavefunctions vary more quickly with the continuum levels $E_{k''}$. The included continuum wavefunctions in the potential energy diagram in the left plot of Figure 6.17 demonstrate the higher frequency of deuterium's continuum states when compared to hydrogen at the same total energy. The larger number of intensity maxima at any given excitation energy is a result of the compressed vibrational structure though, which causes the respective bound wavefunction to provide more antinodes.
A significant difference arises for the higher $np\lambda$ states with $n \geq 3$. Introduced in Section 6.1.5, these states are referred to as superexcited (of the first kind) due to their energetic position around or above the ionization threshold. The ensuing competition between molecular fluorescence, autoionization and predissociation (as they are also above the 2p dissociation limit) alters the band structure on the emission map, as

any given upper vibrational level may be found in different positions or not at all in the case of ionization. The vastly heavier deuterium atoms now slow down any dissiociation or vibrational autoionization processes, which allows fluorescence to be more competitive in these situations [GMVJ16]. This outcome is immediately visible on the emission map by the significantly increased count of bound features in the region of these superexcited states, which is shown for molecular deuterium side-by-side with hydrogen in Figure 6.18. The previous depiction for only H_2 in Figure 6.10 left most vibrational levels without any emissions once the ionization threshold is crossed and only few beyond the H(2p) dissociation threshold. This changes significantly in D_2 with a wider array of band structure still remaining both between the dissociation and ionization threshold as well as beyond. Specific and quantative investigations into these altered decay pathways can be found in recent literature [GMVJ15, GMJD16, GMVJ16], which, amongst other things, show additional influences to these processes by local pertubations between the many vibrational levels.
In contrast, the direct dissociation channel behaves in line with expectations and is slightly reduced compared to molecular hydrogen [LSJ12a]. This reflects on the emission map by the dominant contribution of predissociation to the Lyman-α line in particular.

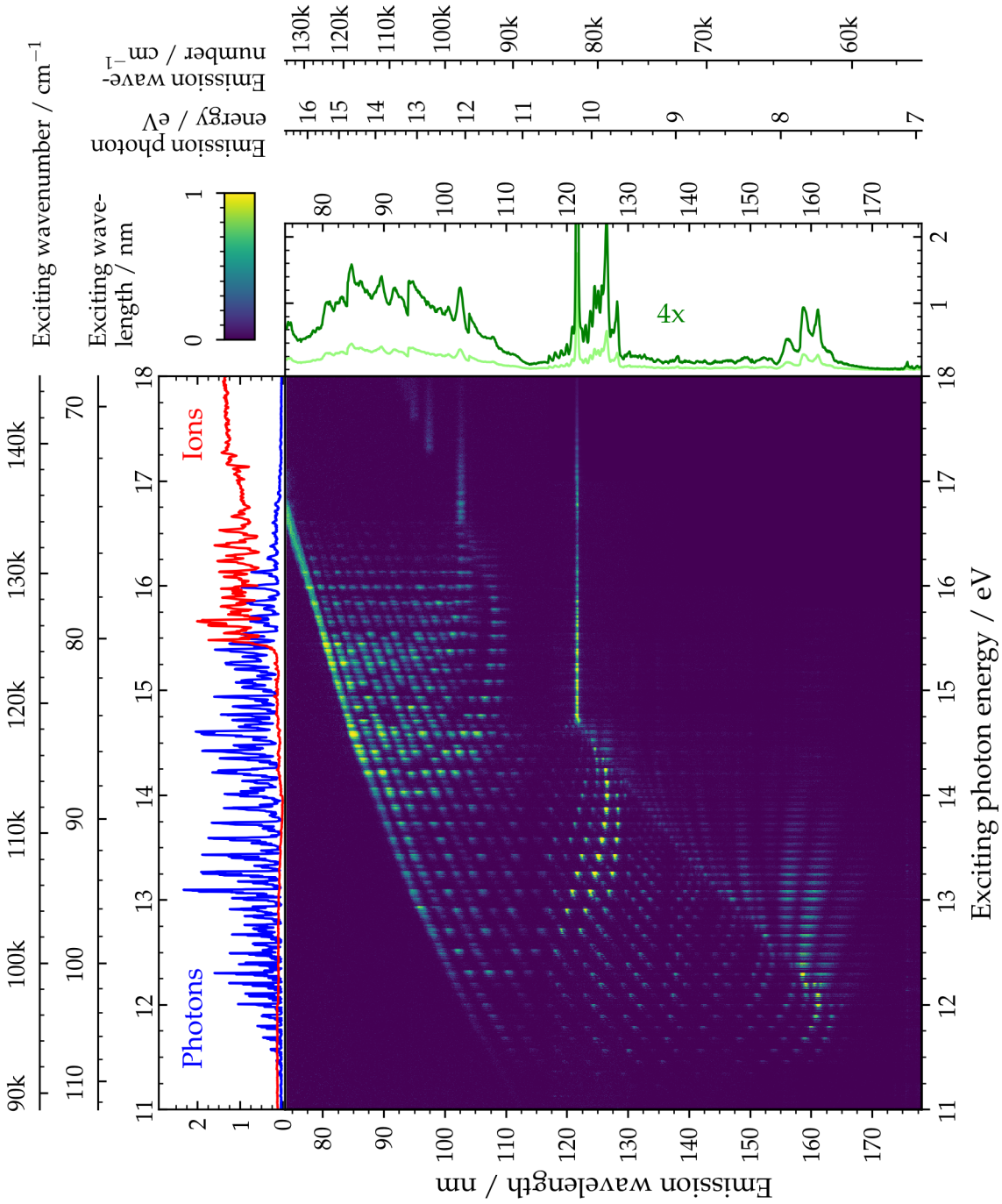

Fig. 6.19: *The complete rovibronic emission map of molecular deuterium in the regime of singly excited electronic states. The excitation function for photon emission as a sum in vertical direction in blue, for ionization in red as well as the integrated emission spectrum in green is shown. A non-linear intensity scaling with* $a = 15$ *is used as defined in* (3.3).

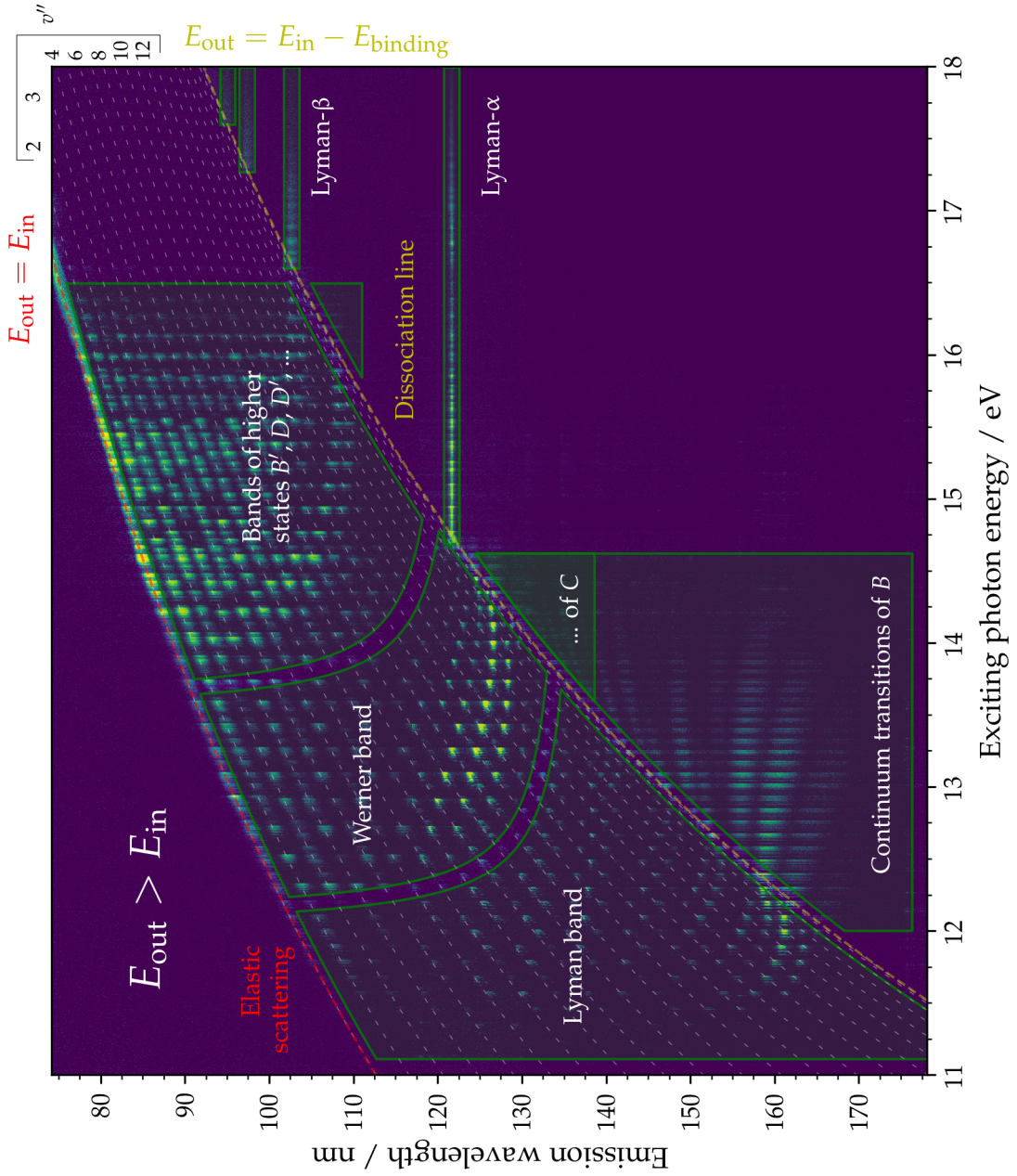

Fig. 6.20: *The complete rovibronic emission map of molecular deuterium in the regime of singly excited electronic states. The most relevant visible features are summarized categorically, such as different regions of bound transitions or unbound transitions as well emission after dissociation. The same presentation is used as in Figure 6.19.*

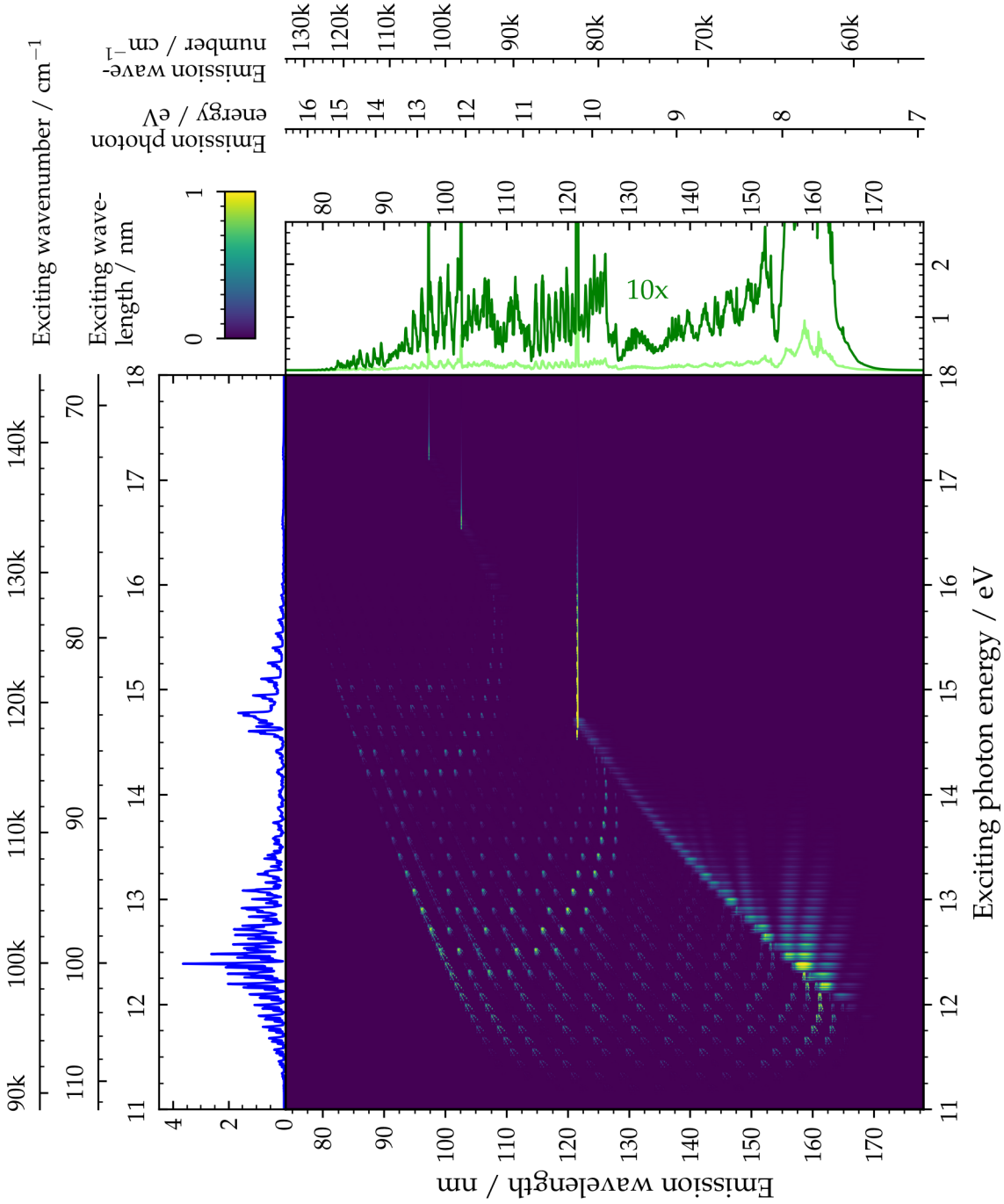

Fig. 6.21: *The complete rovibronic emission map of molecular deuterium in the regime of singly excited states based on the simulation with a comparable resolution to Figure 6.19. The excitation function for photon emission as a sum in vertical direction in blue as well as the integrated emission spectrum in green is shown. A non-linear intensity scaling with $a = 45$ is used as defined in* (3.3).

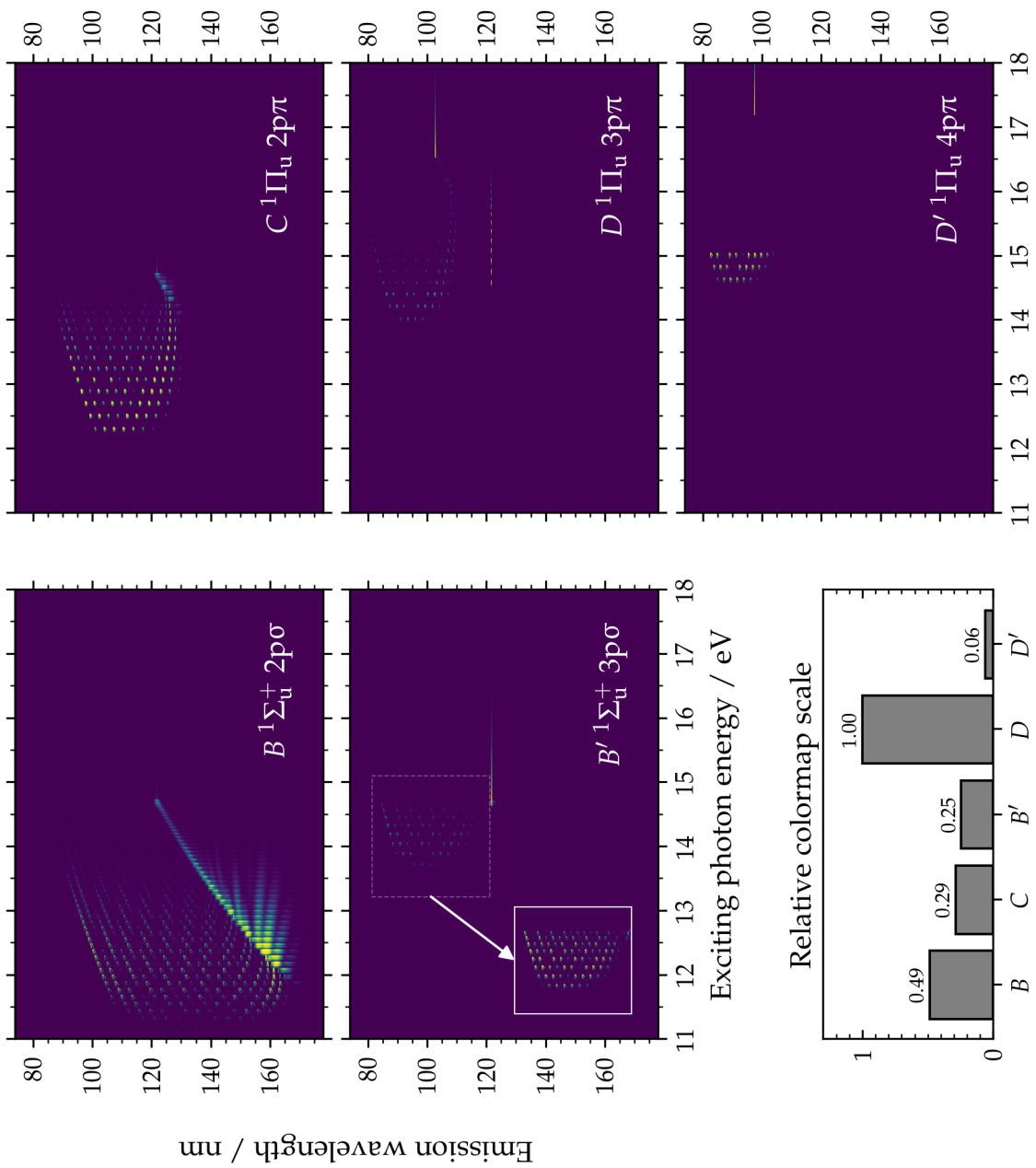

Fig. 6.22: *The separated emission maps of molecular deuterium based on the simulation for each of the major states involved. Each state is scaled individually to maximize its contrast with* $a = 35$ *as defined in* (3.3)*. The relation between the colormaps is shown in the lower left plot. In addition, the inset for the* $B'\,{}^1\Sigma_u^+$ *state adds the bound transitions again scaled individually, which is around fifteen times weaker.*

6.3 Molecular tritium

The tritium molecule T_2 consists of two tritons, the nuclei of the third and heaviest naturally occuring isotope of hydrogen. It is no longer stable and undergoes a β^--decay with a half-life of 12.3 years, transmuting it to ^{3}He. As such, it appears only in trace amounts, usually as a result of cosmic ray interaction or the byproduct of artifical nuclear reactions. It sports an additional neutron over the deuteron and is thus composed of one proton and two neutrons, three times the mass of the single proton of hydrogen. Therefore, it exhibits an even stronger isotopic effect.
The spectroscopy of molecular tritium is restricted severly by its radioactive properties, however. Recently, some work is motivated by its use as a possible fuel for sustainable nuclear fusion reactions, e.g. to employ spectroscopic detection methods for storage and handling [GKM17, MBB17]. On a fundamental level, a few studies take advantage of the large isotopic shift to test advanced quantum electrodynamical calculations and other kinds of precision measurements via Raman scattering [VR87, UKE16, TSU18]. But, there is no literature on the general electronic structure via photon absorption or emission spectroscopy of its electronically excited states. Nevertheless, it has been included occassionaly in theoretical calculations in this regard, e.g. [SR87].
Due to the experimental difficulties, this species could not be investigated experimentally. Furthermore, the observation of selectively excited rovibronic transition would be complicated by the intense radioluminescence of this species due to its own radioactive decay [Sch82]. At a target density similar to the experiments performed in this work, it results in emissions over a wide spectral range covering the majority of states, including those not accessible via dipole transitions from the ground state. The computational model introduced in Chapter 4, however, can be applied to envision the emission map of molecular tritium without the obstacles mentioned above. Its results are shown in Figure 6.23 as a composited matrix and in Figure 6.24 with the emissions separated by state. The adaption of the model is analog to molecular deuterium via corrections for the nuclear mass and fundamental constants:

$$\mu_{T_2} = 1.512\,\mathrm{u} \qquad\qquad R_{T_2} = 13.603\,\mathrm{eV}$$

The resulting shift in potential energy is up to 0.12 eV. The thermal population of rotational levels in the ground state at room temperature based on (4.24) is further increased

to include levels up to $J \leq 6$. It amounts to $0.1, 0.23, 0.26, 0.21, 0.12, 0.06, 0.02$ for each level starting at $J = 0$, respectively.
In contrast to the emission maps simulated for molecular hydrogen and deuterium, there were no assumptions made for the predissociation ratios of the superexcited states of molecular tritium due to a lack of theoretical or experimental data on this subject. Only the dissociation by direct excitation into the vibrational continuum of a state is included. It should be emphasized at this point once more, that while this theoretical model predicts reliably the structure of emissions, the preceding comparions with the experimental data show various deviations in the intensities for individual features. The underlying model has no concept of coupling between states, which are like the just mentioned predissociation added empirically afterwards. These emission maps of molecular tritium, as with all other purely simulated ones in this work, are shown as an estimate on what to expect.
The increase in the number and density of rovibrational levels already discussed for molecular deuterium is even more pronouced for T_2, of course. Where D_2 contracted the rovibrational structure by about 30% to 40%, it amounts here to 50% to 60%. The ground state $X\ ^1\Sigma_g^+$ sports 25 and the particularly wide $B\ ^1\Sigma_u^+$ state 52 bound vibrational levels. Nevertheless, the general structure of the bound emission is preserved and for each electronic state, the intensity develops along Condon parabolae. The dissociative continuum emissions gain additional oscillations along the vertical axis, as the higher mass again increases the frequency of these states for the same $E_{k''}$. The direct excitation into the vibrational continuum of the electronic states is again comparable, but overemphasized due to the lack of bright peaks following predissociation. While this decay channel is completely ignored in these calculations as mentioned above, it can be expected to diminish as a continuation of the trend in molecular deuterium.

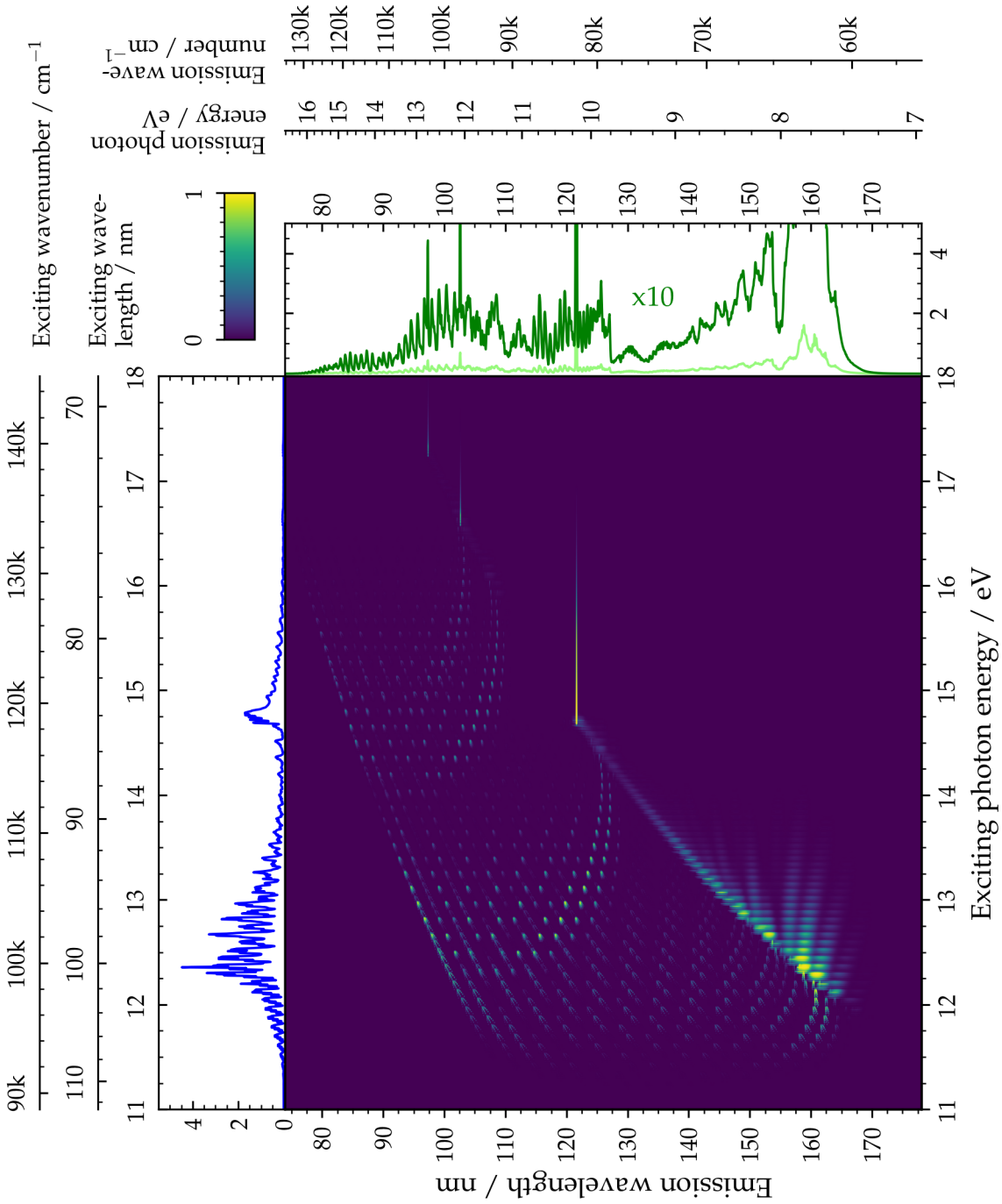

Fig. 6.23: *The complete rovibronic emission map of molecular tritium in the regime of singly excited states based on a simulation. The excitation function for photon emission as a sum in vertical direction in blue as well as the integrated emission spectrum in green is shown. A non-linear intensity scaling with* $a = 15$ *is used as defined in* (3.3).

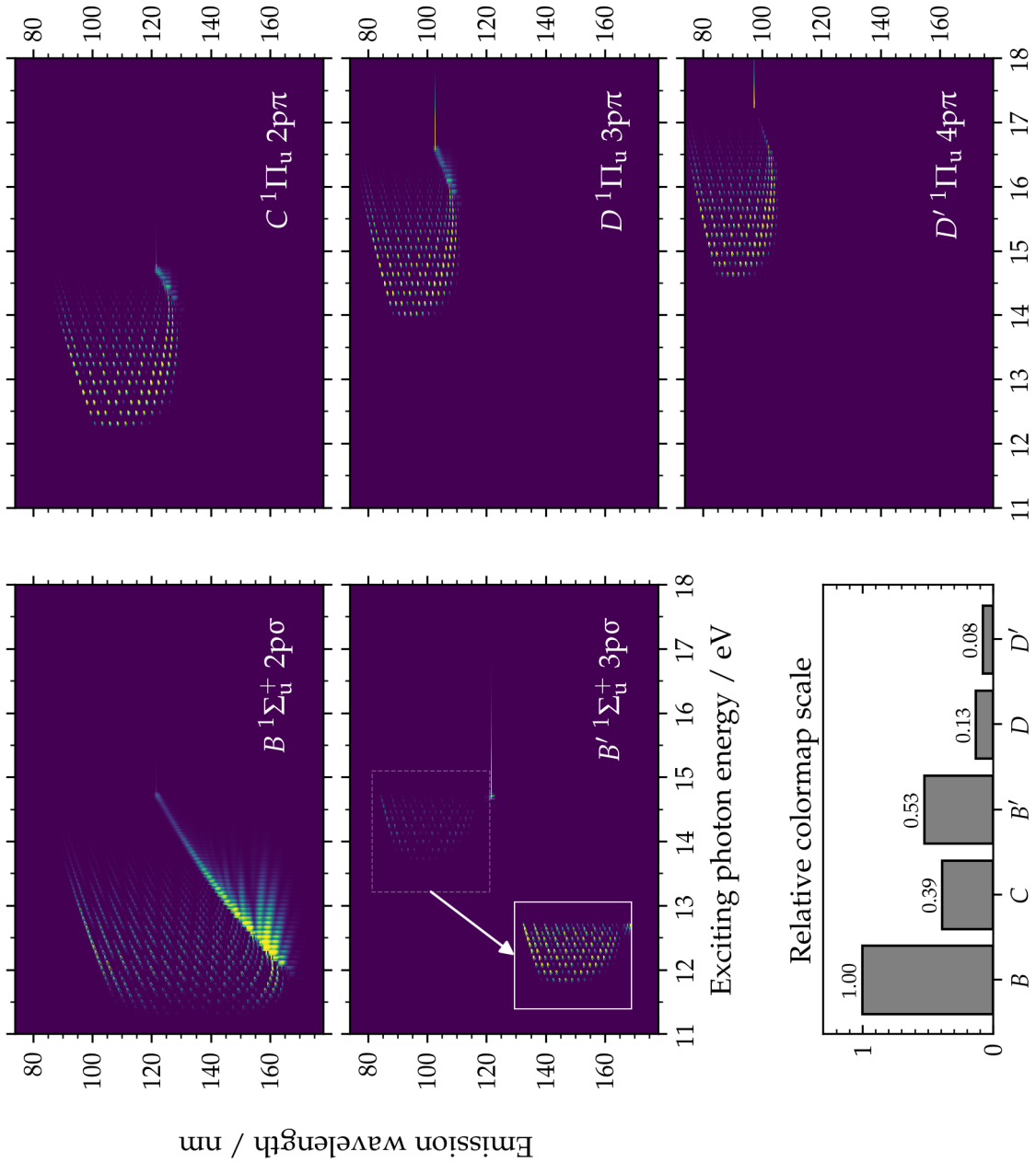

Fig. 6.24: *The separated emission maps of molecular tritium based on the simulation for each of the major states involved. Each state is scaled individually to maximize its contrast with* $a = 35$ *as defined in* (3.3)*. The relation between the colormaps is shown in the lower left plot. In addition, the inset for the* $B'\ ^1\Sigma_u^+$ *state adds the bound transitions again scaled individually, which is around fifteen times weaker.*

6.4 Hydrogen deuteride

The hydrogen deuteride molecule HD is a singly deuterated hydrogen molecule, thus consisting of two different hydrogen isotopes in the form of a proton and a deuteron. While still homopolar, it is the lightest of the isotopically asymmetrical variants of hydrogen and thus not strictly homonuclear. This prevents the nuclear dipole moment in (2.44) from vanishing completely and enables rovibrational transitions in the dipole approximation at least in principle.
It was indeed measured for the first time by Herzberg in 1950 [Her50b] and became quickly the focus of theoretical works until today [TCK85a, TCK85b, GHH88, PK08, BLS09], as its correct treatment and precise prediction serves as a test for the numerical limits of the Born-Oppenheimer approximation and non-adiabatic methods. At the same time, the experimental methods developed further to observe these weak features [NT82, RJM82, VR87] in both pure rotational transitions as well as the fundamental rovibrational bands.
Today, it is particularly convenient for testing predictions in quantum electrodynamics. These appear only as very small corrections and are hence observed in rovibrational transitions [CDS18]. While hydrogen still serves as the fundamental prototype system in these calculations, the features are significantly easier to measure in HD. The symmetrical isotopologues are still restricted to weaker quadrupole transitions.
This intensity ratio is also used in astrophysical studies to estimate the isotopic ratio between hydrogen and deuterium in interstellar media such as clouds [BS75] or planetary atmospheres [BGM86]. While scarcer than the D_2 molecule itself, its brighter transitions makes it comparable to the abundant H_2 isotopologues. Finally, the selection rule (2.47) regarding the inversion in homonuclear molecules is diminished in HD. It allows dipole-forbidden lines between states of equal inversion symmetry to appear. A recent review of related works can be found in [DRU10].

For this molecule, no experimental data is available. As with molecular tritium, the developed computational model can still be applied. Its results are shown in Figure 6.25 as a composited matrix and in Figure 6.26 with the emissions separated by state. The required corrections to H_2 are much smaller than for the other symmetrical isotopologues with a reduced mass of $\mu_{\mathrm{HD}} = 0.672\,\mathrm{u}$. The thermal population of rotational levels at room temperature based on (4.24) extends slightly to $J \leq 4$ and amounts to

$0.20, 0.39, 0.27, 0.10, 0.023$ for each level starting at $J = 0$, respectively. No empirical predissociation ratios were used to account for this decay channel similar to T_2. While the selection rule (2.47) regarding the inversion symmetry in homonuclear molecules should be weakened as mentioned above, these effects are comparably small and hence not incorporated. Furthermore, all fragment emissions are attributed to hydrogen rather than deuterium, as the difference between these lines amounts to 3 meV or 0.03 nm.

With only the mass difference taken into account, the result exhibits only the isotopic effects already discussed for the symmetric isotopologues. The magnitude of these lie between molecular hydrogen and deuterium in line with its reduced mass value. The interesting effects that may be found in this species require significantly more sophisticated theoretical models and experimental results to compare against. The simulated emission map presented here may therefore serve as an initial benchmark to analyze these emerging discrepancies to a common homonuclear molecule without isotopic asymmetry.

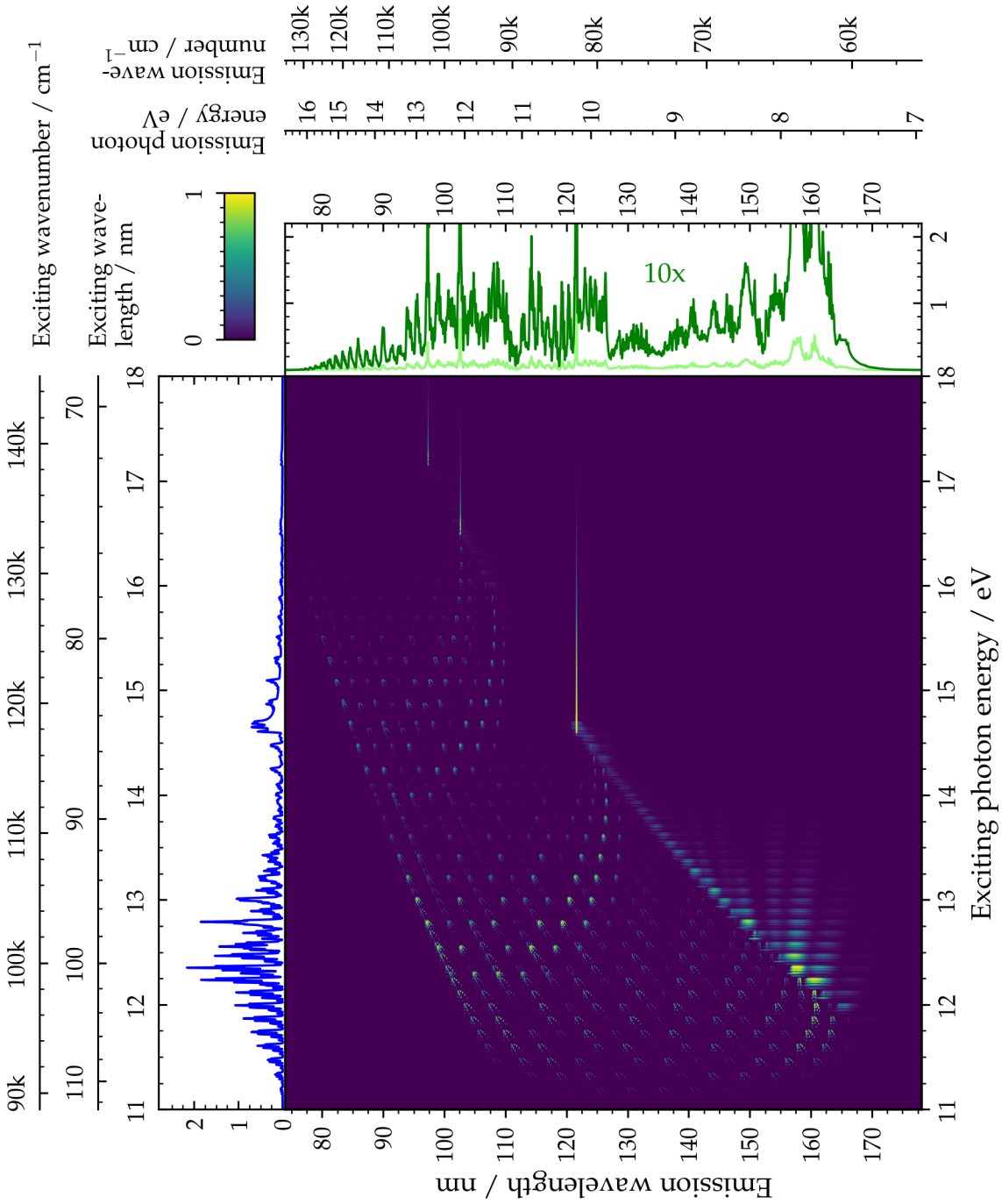

Fig. 6.25: *The complete rovibronic emission map of hydrogen deuteride in the regime of singly excited states based on a simulation. The excitation function for photon emission as a sum in vertical direction in blue as well as the integrated emission spectrum in green is shown. A non-linear intensity scaling with* $a = 45$ *is used as defined in* (3.3).

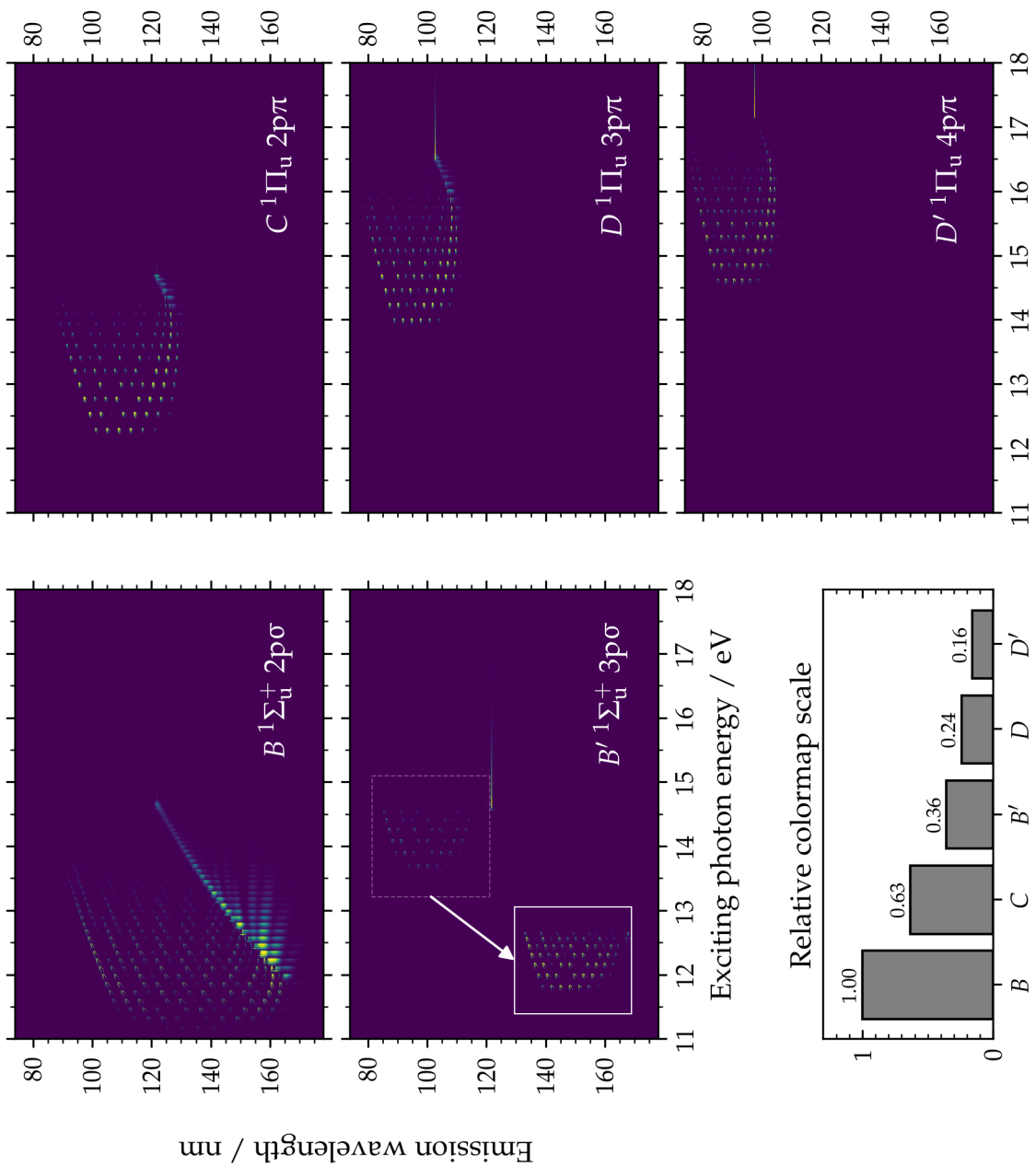

Fig. 6.26: *The separated emission maps of hydrogen deuteride based on the simulation for each of the major states involved. Each state is scaled individually to maximize its contrast with* $a = 25$ *as defined in* (3.3)*. The relation between the colormaps is shown in the lower left plot. In addition, the inset for the* $B'\ ^1\Sigma_u^+$ *state adds the bound transitions increased two hundred times in their intensity.*

6.5 Carbon Monoxide

The carbon monoxide molecule CO is a compound consisting of a single carbon and a single oxygen atom. It occurs typically as a product of incomplete combustion processes of carbohydrates and other carbon-containing compounds, but is also part of the mammal metabolism in trace amounts as a signal molecule [WW05]. Furthermore, it is the second most abundant molecule in the interstellar medium after H_2 with a relative fraction of approximately 10^{-4} [UB02]. It emits significantly brighter lines in the radio and infrared spectral ranges however, as its purely rotational and rovibrational transitions are no longer dipole-forbidden due to the heteronuclear asymmetry. Combined with a low variation of the CO ratio to H_2 across different regions in the universe, it is used to determine the molecular hydrogen distribution indirectly as a tracer [NGU98].

Its astrophysical significance continuously spawned a number of spectroscopic studies to improve upon earlier works [Bir26, TS72, ERF87] with modern techniques, e.g. Fourier transform absorption spectroscopy, in the investigation of its rovibrational structure in general [SLG99, Bak05, NSZ13] and details of the isotopologues [HNF16, NHT16, THH17, HNF17]. At the same time, the importance of carbon monoxide in this context was reinforced by its observation in comets, cool dwarfs, quasars, supernova remnants as well as the atmosphere of transiting exoplanets [WFA11, KBM13].
A different field of research are this molecule's superexcited states, the bound neutral states beyond the lowest ionization threshold of 14.01 eV [EKRK93]. As with with the higher lying electronically excited states H_2 (e.g. in Section 6.1.5) and its isotopologues, these usually feature a complicated competition between different decay channels. In molecules that are heavier than hydrogen in particular, this includes a wide array of fragments with different charge and excitation states after dissociation. As these may be neutral, they are often detected by their subsequent photon emissions as a function of the photon energy of exciting synchrotron radiation, e.g. in [EMU95, EMU96, EMU97]. This is analog to the concept of emission maps presented in this work, albeit on a smaller scale and focussed on a particular process. A corresponding shaded matrix representation of VUV fluorescence of atomic fragments for a continuous range of excitation energies is actually found in [EMU95].

An emission map of this species was recorded experimentally as an outlook to heavier as well as heteronuclear molecules. It covers those electronic states which feature bound

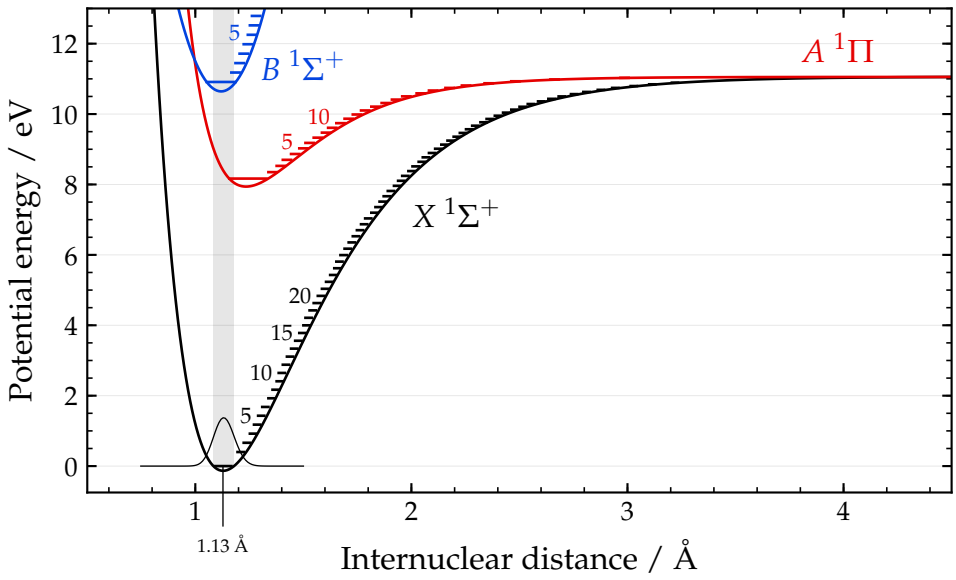

Fig. 6.27: *The Born-Oppenheimer potential energy curves of carbon monoxide were used to simulate its emission map. The ground state $X\ ^1\Sigma^+$ (black) is included alongside the electronically excited states $A\ ^1\Pi$ (blue) and $B\ ^1\Sigma^+$ (red), which are optically accessible from $X\ ^1\Sigma^+$. For each state, the vibrational levels are annotated. The curves are constructed from Morse parameters [DHWTJF13] and directly from [LJS11].*

transitions between the ground state and their upper rovibrational levels by absorption and emission of photons, namely $A\ ^1\Pi$ and $B\ ^1\Sigma^+$. The measured result is shown in Figure 6.28 with an accompanying summary of relevant features by category in Figure 6.29. Due to the lower excitation energies, the data contains several contaminations of higher orders of the synchrotron radiation, in particular from the bending magnets around the insertion devices of the utilized beamline. These may pass the primary monochromator at multiples of the intended energy and hence cause features to appear, which belong to different processes. In this case, this applies to a set of faint emission from ionic fragments that seemingly appear already below the lowest energy required for any ionization of 14.01 eV [EKRK93]. Furthermore, the lower signal-to-noise ratio of these measurements causes stray light to appear as a roughly constant background on a whole vertical column when exciting into upper vibrational levels of $A\ ^1\Pi$. These erroneous features are annotated explicitely in the summary of Figure 6.29 in cyan.
As in the preceding sections of this chapter, a simulated map with the model introduced in Chapter 4 was performed as well and the corresponding composited emission map is

found in Figure 6.30. The emissions are not separated by state for this species, because the two involved states are always fully isolated. For the required potential energy curves, precise calculations with non-adiabatic corrections similar to molecular hydrogen cannot be found in recent literature. They are instead constructed from Morse parameters from [DHWTJF13] for the electronically excited states $A\ ^1\Pi$, $B\ ^1\Sigma^+$ and obtained by adiabatic calculations for the ground state $X\ ^1\Sigma^+$ [LJS11]. A plot of this potential energy landscape is given in Figure 6.27 for these three relevant states. The thermal population of rotational levels at room temperature based on (4.24) includes contributions from up to $J = 23$, at which point less than 1% remains for $J > 23$.
Several other emission bands in the visible spectral region, such as the so called Ångstrom band system between $B\ ^1\Sigma^+$ and $A\ ^1\Pi$, the Herzberg band system between $C\ ^1\Sigma^+$ and $A\ ^1\Pi$ or others, have been investigated as well, e.g. both in earlier works [PBR84, PRSW85, ARV86] as well as recently with very high resolution on rare isotopologues [HSZ12]. Further references can be found cited in these publications. Similar to the band system between $E, F\ ^1\Sigma_g^+$ and $X\ ^1\Sigma_g^+$ in hydrogen, this spectral range has not been investigated in this work.

The emission map in the chosen range of exciting and emitted photon energy is dominated by the molecular bands of $A\ ^1\Pi$, the lowest electronically excited state that is optically accessible. In contrast to the typical case for homonuclear molecules such as hydrogen in the preceding sections, this state in carbon monoxide has a comparable equilibrium distance to the ground state. Therefore, its Frank-Condon factors for transitions between the two develop differently and favor transitions with lower changes in the vibrational level. The excitation into $v' = 0$ is therefore the strongest and emissions fall off significantly for larger differences of v', v''. Even though the ground state $X\ ^1\Sigma^+$ of CO is extraordinary deep and actually converges towards the same limit as $A\ ^1\Pi$ while its zero-point energy is about 8 eV lower, any features with $v' \geq 10$ vanish completely. This relation between the internuclear distances of electronic states is more common for heteronuclear diatomic molecules, particularly for greater mass differences between the atoms [Dem05]. It is very pronounced on the simulated emission map of carbon monoxide by a single diagonal trend for the bound emissions of maximum intensity rather than a Condon parabola. It begins for $v' = 0$ at a small v_0'' and then develops along $v'' - v' \approx v_0''$. In the experimental data, some intensity remains for transitions to low v'' even when exciting into higher v', which can be attributed to deviations introduced by

the Condon approximation (a constant electronic transition moment for all R) applied in the simulation.
The $B\ ^1\Sigma^+$ state contributes bound photon emissions only from its two lowest vibrational levels $v' = 0, 1$. Its higher levels $v' \geq 2$ are known to completely predissociate and are hence just seen in absorption [BTBJ95]. Its equilibrium distance is almost identical to the ground state and therefore strongly favors excitations into $v' = 0$. The subsequent emissions, apart from $v'' = 0$, form a diffuse band which can no longer be attributed to specific lower vibrational levels v''. This may be caused by the strong interaction with the $D'\ ^1\Sigma^+$ state, which is suspected to actually form a double well state with $B\ ^1\Sigma^+$. However, it is not accessible directly by the ground state in $v = 0$, but may be populated through rotational coupling from the excited level and then fluoresce [TBJR92]. Furthermore, the intensity increases on the line position of atomic emissions of carbon fragments to suggest significant predissociation also for the $v = 0$ level of $B\ ^1\Sigma^+$.
Starting at excitation energies of around 10 eV and thus after the decline of bound emissions from $A\ ^1\Pi$, several lines of fundamental transitions in atomic carbon appear. They are part of the complicated photodissociation processes in carbon monoxide and have been studied spectrally dispersed in the past as a function of excitation energy, e.g. in the form of emission maps in [EMU95] as mentioned above. The emission map presented here is therefore the first extension using this technique to carbon monoxide's molecular bands.

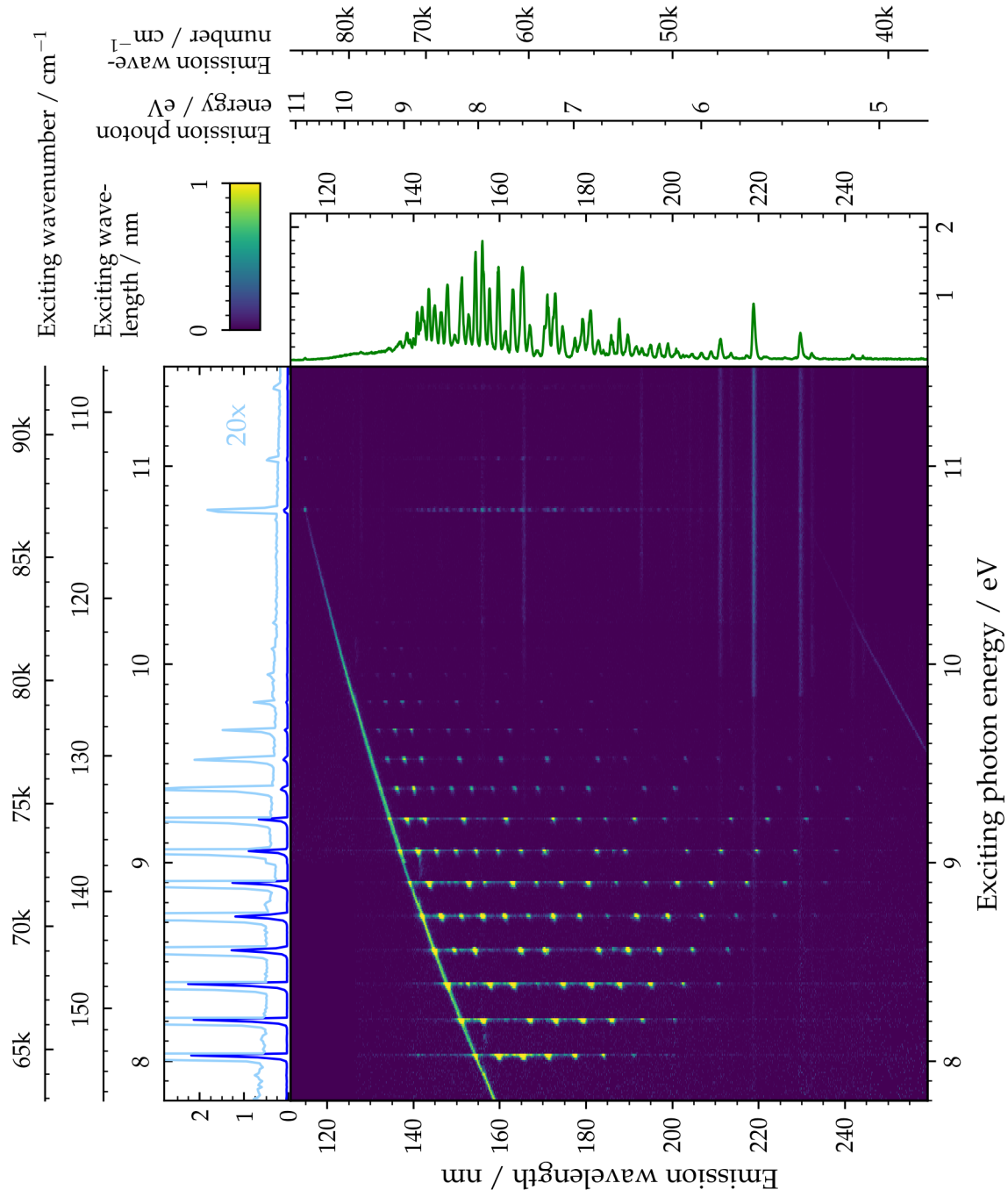

Fig. 6.28: *A rovibronic emission map of carbon monoxide covering the majority of bound molecular emissions and the beginning of various fragmentation channels. The excitation function for photon emission as a sum in vertical direction in blue as well as the integrated emission spectrum in green is shown. A non-linear intensity scaling with $a = 60$ is used as defined in* (3.3).

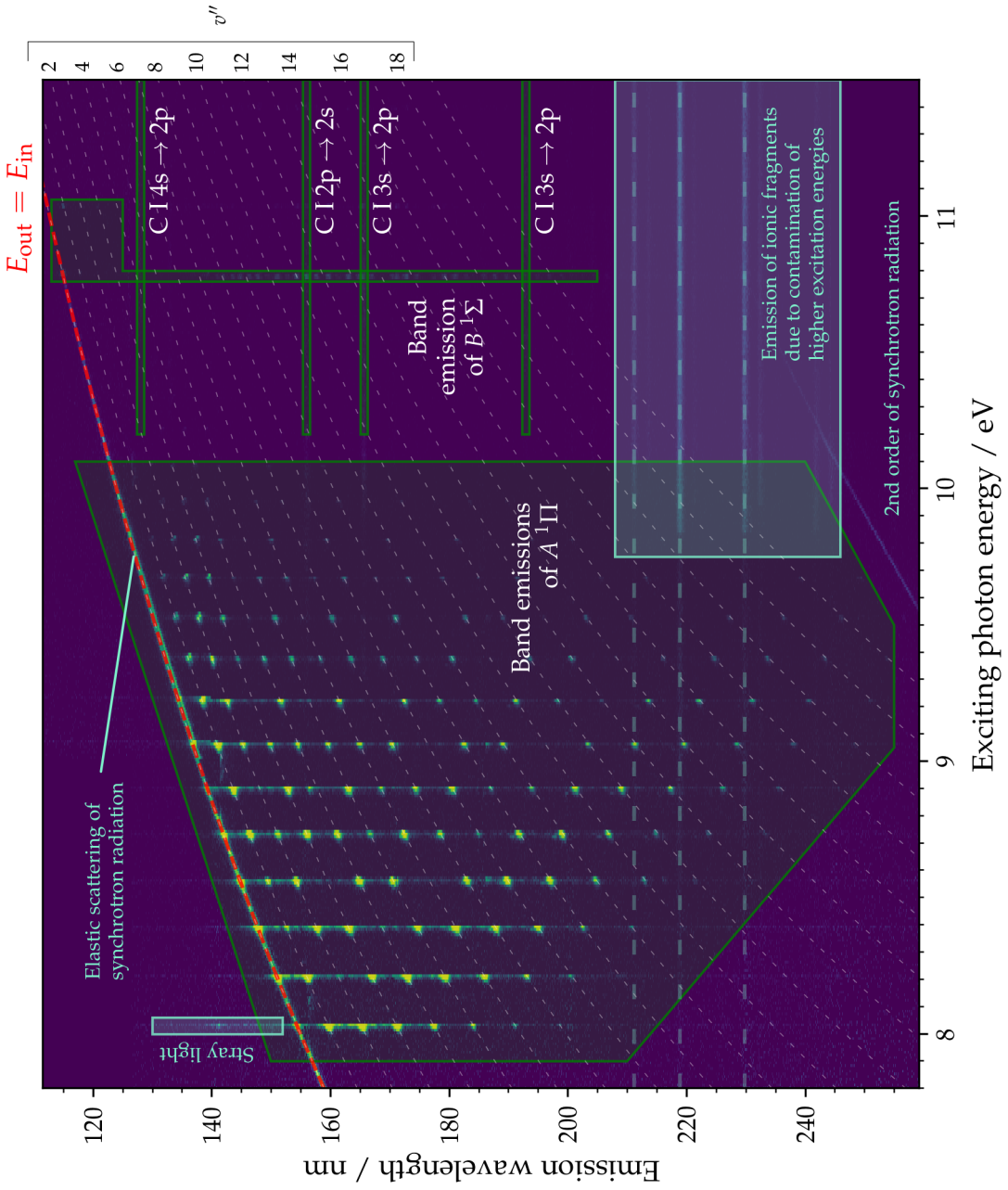

Fig. 6.29: *A rovibronic emission map of carbon monoxide covering the majority of bound molecular emissions and the beginning of various fragmentation channels. The most relevant visible features are summarized in green, while erroneous emissions due to stray light or higher orders of the beamline are annotated in cyan. The same presentation is used as in Figure 6.28.*

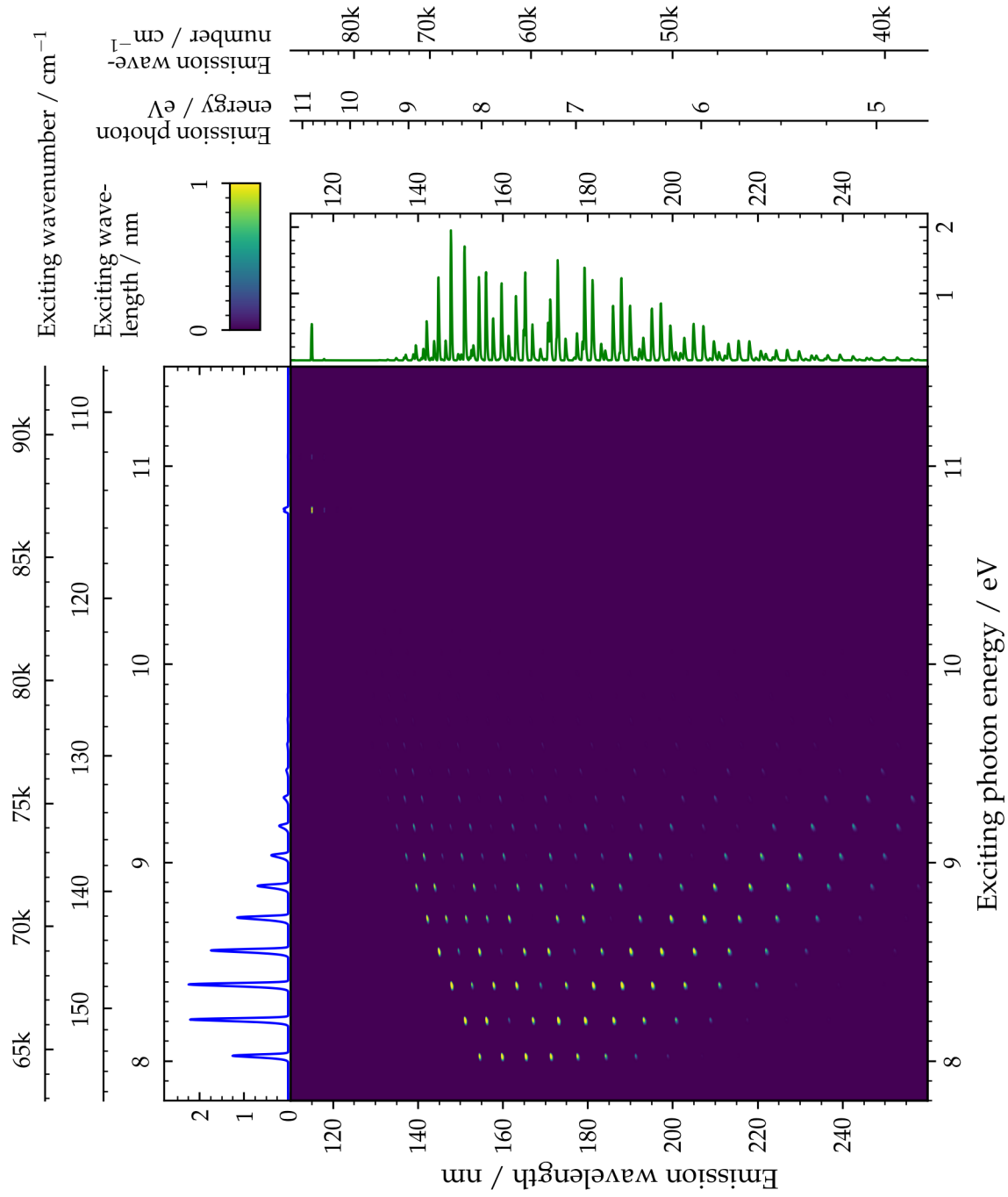

Fig. 6.30: *A rovibronic emission map of carbon monoxide covering the majority of bound molecular emissions based on the simulation with a comparable resolution to Figure 6.28. The excitation function for photon emission as a sum in vertical direction in blue as well as the integrated emission spectrum in green is shown. A non-linear intensity scaling with $a = 35$ is used as defined in* (3.3).

Chapter 7

Conclusion

The electronic structure of even the smallest molecule causes a rich absorption and emission structure. Their nature has been a focus of spectroscopic investigations since its early beginnings and is thought to be generally well unterstood as a case for textbooks. However, plenty of systems still exhibit transitions, that require extensive theoretical treatment to disentagle and identify their intertwined system of lines.
A way to unravel these features is the separation into distinct excited states and their corresponding decay channels. This work aimed to apply such a method to luminescence spectroscopy of several small molecular systems. The small bandwidth and wide tunability of synchrotron radiation facilities was used to select singular excitation features over a large part of the accessible rovibronic states. The dispersed photon emission spectra for each of these features by itself then contain only its respective deexcitation processes. This data was presented on two-dimensional maps depicting the emission intensity as a function of both exciting and emitted photon energy, which were termed rovibronic emission maps.
For the experimental part of this work, an established set-up for dispersed luminescence spectroscopy on gaseous species after excitation by synchrotron radiation was enhanced to accomplish such a scope of measurements within the limited time available at synchrotron radiation facilities. A new differentially pumped static pressure cell enabled a large and stable target density while still maintaining high vacuum conditions. In conjunction with an optimized optical and electronical configuration, the required fluence and resolution was achieved. Finally, a new software framework was developed to

control the experimental environment and record data with a high degree of automation. An accompanying computational method based on numerical solutions of the stationary Schrödinger equation in the Born-Oppenheimer approximation allowed the simulation of emission maps and gave a theoretical groundwork on a qualitative level. With its help, the visual features to expect on rovibronic emission maps could be explored on their own to understand the underlying systematics. In addition, it assisted throughout the analysis of the experimentally obtained results.

The investigated molecular species were hydrogen, its isotopologue deuterium and carbon monoxide with both experimental and theoretical results. Furthermore, the hydrogen isotopologues tritium and hydrogen deuteride were included with only simulations based on the developed computational method.

Hydrogen demonstrated a particular abundance of emission features in the regime of single excited states at excitation energies between 11 and 18 eV and corresponding emissions down to 7 eV. The molecular bands for several electronically excited $n\mathrm{p}\lambda$ states of the $^1\Sigma_u^+$ and $^1\Pi_u$ series could be identified and their appearances on the emission map correlated with their electronic structure. Particularly the $B\ ^1\Sigma_u^+$ $2\mathrm{p}\sigma$ state reaveled a large amount of dissociative continuum transitions, which so far have been investigated only sparsely. They are of great interest in astrophysics as a primary photodestruction mechanism of hydrogen in the universe and also visualize the relationship between bound and unbound states. The atomic emissions lines from hydrogen fragments were used to explore both direct dissociation as well as predissociation processes, which become more prominent above the first ionization threshold. Here, the competition between the deexcitation channels of hydrogen's superexcited Rydberg states could be disentangled especially well by the emission map technique.

Deuterium as well as the simulated results for tritium and hydrogen deuteride were used to analyze the isotopic sensitivity of this method. The influence of the nuclear mass could be illustrated due to its large difference for these species. Apart from its general consequences on energetic levels and their build-up, it vastly changed the competition of decay channels in the region of superexcited Rydberg states again. While not included in the computational method, the asymmetrical hydrogen deuteride was suggested to have the additional potential of exhibiting transitions which are normally dipole forbidden for homopolar molecules.

As an outlook for heavier and fully heteronuclear diatomic molecules, a partial emission map was measured and simulated for carbon monoxide at excitation energies between

7.8 and 11.5 eV and corresponding emissions down to 5 eV. Several discrepancies arising from the differences to the smaller hydrogen were found for the molecular band structure and the onset of its numberous fragmentation channels. This data complements earlier works [EMU95], which already applied a mapping technique to the dissociation of this molecule's superexcited states.

The holistic approach for rovibronic emission maps presented in this work enables a visualization of the electronic structure of a small molecule, as the individual path it takes in each transition can be traced. This includes many processes already known from textbooks and elementary lectures as well as the still not fully explored interactions of superexcited states beyond the Born-Oppenheimer approximation and dissociative continuum transitions. On one hand, it may therefore be used as an instrument for teaching fundamental concepts of molecular physics. On the other hand, its separation of individual excitations can reveal details that remain hidden otherwise.

Metro measuring environment

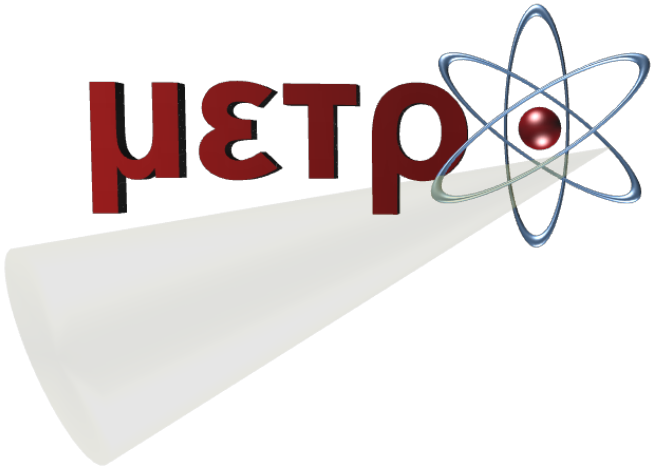

The method of Photon Induced Fluorescence Spectroscopy features a wide range of different targets, detection schemes and excitation methods. In each invididual experiment, the apparatus can consist of a unique combination of devices. Furthermore, it often requires integration into the local infrastructure of large research facilities such as synchrotron radiation sources with minimal effort in order to use the allocated time there as efficient as possible. The computer based control system is therefore a vital component to achieve the full potential of the employed equipment.
Over the course of this work, a new software framework called μετρό (from greek "measure", romanized "Metro") has been developed to allow the control of arbitrary laboratory equipment and recording of measured data in a flexible manner. This chapter describes the design goals, the fundamental concepts and abstractions used to reach those and gives an introduction into its extensibility to develop additional features.

Design goals

The previously used software solution had been developed with *LabVIEW*, which is geared towards rapid development of data acquisition and instrument control programs for a specific piece of equipment. But its low barrier of entry is quickly lost when using abstractions to accomodate flexible configurations of the experimetal set-up. At the same time, the dataflow driven programming paradigm can easily introduces race conditions on parallel measurement tasks, which have to be properly synchronized in an experiment involving multiple detection systems. On the basis of these prior experiences, two primary design goals were defined:

- **Ease of extensibility**
  The often occuring changes to experimental details require frequent additions to the computer interface as well. To integrate with any experimental set-ups, every aspect of the measuring process is to be customizable. The abstractions should be constructed in such a way as to minimize the amount of time and code required to add such new functionality. This is especially important to require the least amount of training and experience in order to successfully modify and extend the software.

- **Confidence in recorded data**
  It is essential for a measurement program to ensure that data is read out in its entirety and safely stored. For the application with PIFS, a set of data is usually characterized by the recording time, which has to kept as constant as possible for several devices at once. The interface with external hardware is often accompanied by long latencies which have to be taken into account. In the event of some malfunction, either in hard- oder in software, the least amount of data possible should be lost or corrupted.

In addition, a set of secondary goals and technical requirements served as guidelines during the development:

- **Performance**
  In general, extensibility takes priority over performance optimization. The rate of data acquisition should not be limited by software capabilities though for the same reason of available time at facilities. A properly defined threading model allows

the interface to be responsive at all times while managing a number experimental devices in parallel.

- **Online presentation of measured data**
  The limited time available at large research sites to perform a proposed experiment necessitates careful planning of the measurement parameters. Preliminary analysis and realtime presentation of recorded data is able to support this decision process to use the time as efficient as possible. In compliance with the extensibility goal, a set of provided display tools should adapt quickly to any added component.

- **(Re-)Configurability**
  Apart from the customization options in terms of the functionality itself, experimental equipment usually involves sets of varying parameters that require configuration, which may include parameters related to hardware addressing or operating mode. The display and analysis tools in software mentioned above then add additional runtime settings. Once the application then is properly set up for the current purpose, this state should be quickly restorable at any point in the future.

Python was chosen as the implementation language. It is an interpreted language available on a wide range of platforms with an emphasis on code readibility and expressiveness [vRWC01]. Since its inception in 1990, it has been applied to a wide array of scientific computing problems and became one of the most popular languages to all its branches [Oli07, MA11]. In the field of experimental physics and in particular accelerated related research, it is already used extensively for control, acquisition and analysis purposes [CER06]. As such, there is a vast repository of science-related frameworks and libraries such as *numpy* [Oli06], *scipy* [JOP01], Matplotlib [Hun07] or *h5py* [Col08], bindings for commonly used hardware and software solutions like *EPICS* and *TANGO* and it offers excellent support to integrate native code via *ctypes* [Pytb] and *cython* [BBC11] for performance as well as hardware access. Finally, it is widely considered an excellent language for beginners, which strenghtens the design goal of easy extensibility [Tol15]. The *Qt* toolkit and its *Python* binding *PyQt5* [Riv13] is used for the graphical user interface and further services such as timing and synchronization of events. This framework maintains the ability to run on many hard- and software platforms while still allowing full integration and performance like a native application. In addition, it features a set of visual tools to ease the creation of complex user interfaces similar to the interface design

provided by *LabVIEW*. The binding to Python in particular uses code introspection to reduce the amount of required glue code for user interaction to a minimum.

Overview

Both from a user's point of view as well as a developer's perspective, the *Metro* software package is separated into generic components that control the application and measuring process as a whole and specific components for the actual functionality of experimental equipment, data analysis and more. This separation allows an arbitrary combination of the specific components, called *devices*, to accomodate any configuration of an experimental set-up while leaving the core functions unchanged. This is realized through the following *Python* package hierarchy:

- `metro`
  - `metro.services`
  - `metro.frontend`
  - `metro.interfaces`
  - `metro.external`
- `devices`
- `scripts`

The generic parts are most visibly represented by the controller window shown in Figure A.1, the first point of interaction after starting the software. It is part of the frontend component (found in `metro.frontend`) that provides the user interface for general tasks such as indicating the current program status and configuration of the measuring process or data storage. In addition, it is the starting point for the creation of devices, which each encapsulate the implementation and interface for a specific task such as the control and readout of experimental equipment, analysis and display of recorded data and more. The majority of devices are located in the `devices` package, but may also be loaded from any external location. The *device* abstraction is described in more detail further below as the main entry point for extensibility. Behind both of these components, the backend provides the logic for the core functionality of measurement control and

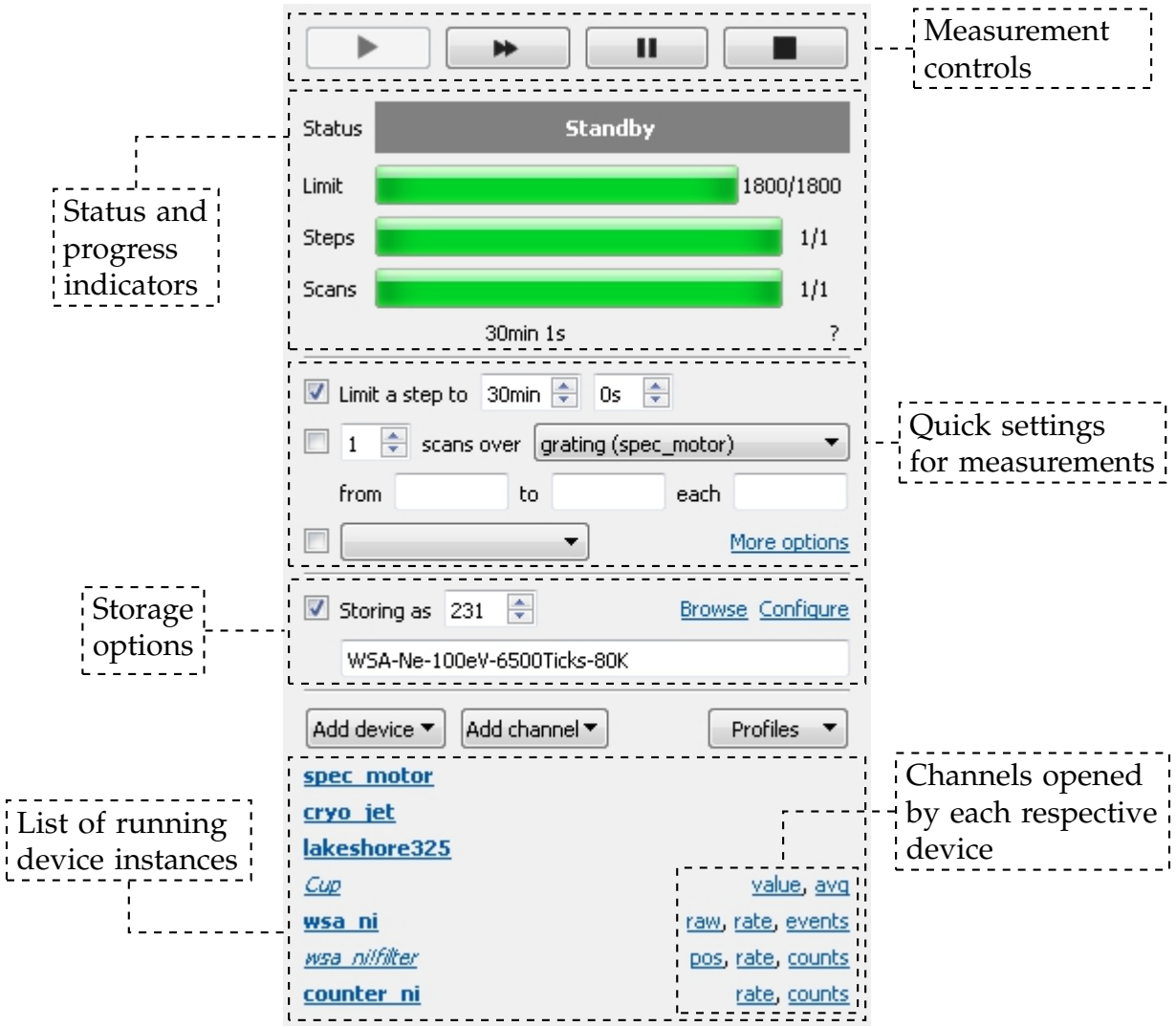

Fig. A.1: *The controller interface of* Metro *running on* Windows 7. *This window is the initial starting point after lauching the software and allows interaction with the* Metro *core that coordinates the measurement process, data storage as well as devices and channel created by the user.*

```
import serial
import metro
from metro.interfaces import serial_aux

class Device(metro.WidgetDevice):
    arguments = {
        'port': serial_aux.SerialPortArgument(),
        'baudrate': [9600, 1200, 4800, 192000],
        'timeout': 0.5
    }
    descriptions = {
        '__main__': 'Periodic readout of serial port.',
        'port': 'Serial port to use.',
        'baudrate': 'Baudrate', 'timeout': 'Read timeout'
    }

    def prepare(self, state, args):
        self.port = serial.Serial(**args)
        self.channel = metro.StreamChannel('value')

        timer = metro.QTimer(self)
        timer.setInterval(1000)
        timer.timeout.connect(self.on_timer_timeout)
        self.editPause.valueChanged.connect(timer.setInterval)
        self.measure_connect(timer.start, timer.stop)

        if state is not None:
            self.editInterval.setValue(state)

    def finalize(self):
        self.port.close()
        self.channel.close()

    def serialize(self):
        return self.editPause.value()

    @metro.QSlot()
    def on_timer_timeout(self):
        self.channel.addData(float(self.port.read(64)))
```

Listing A.1: *Sample device showcasing the typical interaction with the Metro core*

data management in `metro.services`, hardware drivers in `metro.interfaces` as well as packaged external libraries in `metro.external`. The most commonly used parts of the interface between the experiment-agnostic frontend and backend and the specific devices in use are provided in the package `metro` itself.
The frontend as depicted in Figure A.1 is the default interface used. But the underlying framework is designed in such a way, that it may be simply hidden (so called kiosk mode) or completely replaced by a custom implementation tailored for a more specfic use case. As long as the required interface is provided, this may be used as a drop-in replacement and work with any properly written device.
In Listing A.1, a typical device implementation is shown that showcases the interaction with the most important *Metro* components *device*, *channel* and *measurement* in a basic manner. It will be used in the following sections as an illustration while describing each of these concepts individually. The terminology used for data types and language constructs follows the official *Python* documentation [Pyta]. Whenever applicable, type annotations according to the `typing` module as defined in PEP 484 [vRLL14] are used in code listings. The device itself enables the periodic readout of a number sent over a serial port during a measurement.

Devices

As an analog to a singular electronic device as part of a complete apparatus, a device in *Metro* represents a self-contained piece of logic and optionally user interface to perform a specific task. An application programming interface (API) is provided to each device to interact with the core of *Metro* along with abstract implementations for a wide array of tasks in order to require as least code as possible to implement the designated function. As only the most basic conceptual features of a a measuring system is provided by the frontend and framework itself, all actual functionality is implemented as a device. In its current state, some examples included in the `devices` package are:

- `measure.position.dld_rd`
  Configures a Roentdek TDC8HP to operate a delay line detector.
- `measure.generic.counter_ol`
  Reads out the digital counter of a measurement device compatible with the *OpenLayers* API.

- `filter.dld`
  Calculates the position of hits on a delay line anode from its raw timings and applies an optinal linear transformation.

- `control.commercial.iseg_nhq2xx`
  Enables remote control of iseg high voltage sources such as the NHQ226L.

- `control.facility.damc`
  Enables remote control of various beamline parameters at the BESSY II facility.

- `display.waveform`
  Displays the value of a scalar signal varying as a function of time.

- `display.hist2d`
  Displays a two-dimensional histogram of individual points, e.g. hits on a photon detector.

- `analyze.scan_matrix`
  Puts together individual spectra as columns acquired by another device to a matrix representation.

- `util.ui_web_proxy`
  Provides a web interface to access any graphical *Metro* device in the browser.

- `evac`
  An Model-view-controller framework to monitor and control vacuum chambers and equipment on embeddable systems.

A device is defined by an importable Python module containing a class called `Device` that controls its lifecycle and interfaces with the *Metro* core. This class is expected to inherit at least from the abstract class `metro.GenericDevice`, but generally a more concrete implementation with further functionality is used. These range from support for a user interface to mostly implemented devices for customizable complex flow schemes. The most commonly used base class is `metro.WidgetDevice` that provides a Qt top-level widget for this device with the respective integration into the frontend and the expected behaviour coming along with it. An alternative without any prepared user interface is `metro.FunctionalDevice`, which fills the interaction-related abstract

methods of `GenericDevice` with stubs. The `devices.abstract` package contains incomplete device templates for specific purposes to share common code not specific to a particular device. For example, `devices.abstract.parallel_event_source` implements all the machinery and synchronization required for data acquisition in a separate interpreter process with the inheriting device then only complementing the actual readout code.

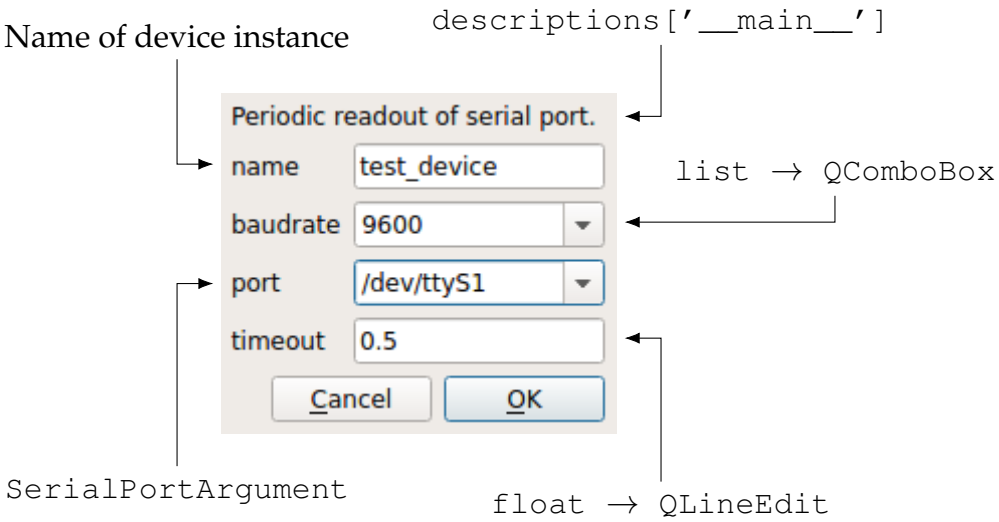

Fig. A.2: *The new device dialog running on GNOME 3 for the sample device in Listing A.1. In addition to the device name, each argument is presented and may be manipulated by interface elements. The built-in types like `list` and `float` are implemented internally, while the custom argument type `SerialPortArgument` may render any widgets, here a `QComboBox` populated with all available serial ports on the system.*

The typical interactions of a device as shown in the example in Listing A.1 concern the device meta-informations, the lifecycle, channels and measuring. The latter two are described in their respective sections below.

For meta-information about the device across all its instances, the `Device` class may define a number of static properties with the two most common ones found around lines 6 and 11 in the example:

- `arguments: dict[str, Any]`
  A dictionary [Pytc] with configuration options to be determined at creation time of each device instance. This is useful for settings known in advance, which usually stay constant over the lifetime of the device or are complex to change during runtime such as hardware addresses. When the device is created through the controller,

a dialog is created with suitable Qt interface elements depending on the type of its value to modify it. In addition, complex arguments for items such as other devices, channels or hardware devices can be defined via `metro.AbstractArgument` that allow convenient selction by the user and are converted into the respective object.

This dialog appearing for the sample device is shown in Figure A.2. Its first argument is based on a custom `metro.AbstractArgument` and offers a `QComboBox` [Qt a] with all serial ports found on the system while returning it as a `str` to the device. The second tuple argument allows selection of one of its `int` elements by a `QComboBox` and the third a `float` number by `QLineEdit` [Qt b], both types which are built-in and handled internally.

- `descriptions: dict[str, str]`
  A dictionary to describe the configuration options specified in `arguments`, which will be used as tooltips in the device creation dialog. In addition, a summary for the device itself can be given via the special key `__main__`.

- `ui_file: Optional[str]`
  While `metro.WidgetDevice` tries to find a suitable .ui file defining the interface automatically (used in Listing A.1), this behaviour may be overwritten by this `str` value. If the interface is created programmatically, this may be set to `None`.

Each instance of a device exists within a defined lifecycle summarized in Figure A.3. It should always be written in such a way that multiple instances of the same device can live at the same time. The `Device` class may overwrite one of these abstract methods to take part in the lifecylce:

- `prepare(args: dict[str, Any], state: Any) -> None`
  Called upon creation of this device instance. The `args` dictionary contains the evaluated values of `Device.arguments`. The `state` object may either be `None` if none exists or the return value of a previous call to `serialize`.

- `finalize() -> None`
  Called upon destruction of this device instance to release any used resources.

- `serialize() -> None`
  Called upon saving a profile to serialize the current state of this device. The return value will be passed to `prepare` when this profile is loaded in the future.

These methods can be found in Listing A.1 on lines 17, 30 and 34, respectively. In the example, `prepare` is used to initialize the hardware connection by the serial port, create a *Metro* channel to publish the acquired data, create a timer for periodic readout and restore the user interface to a saved state if provided. The `finalize` method closes both the hardware connection and the registered channel. In `serialize`, the current value of the relevant user interface element is returned.

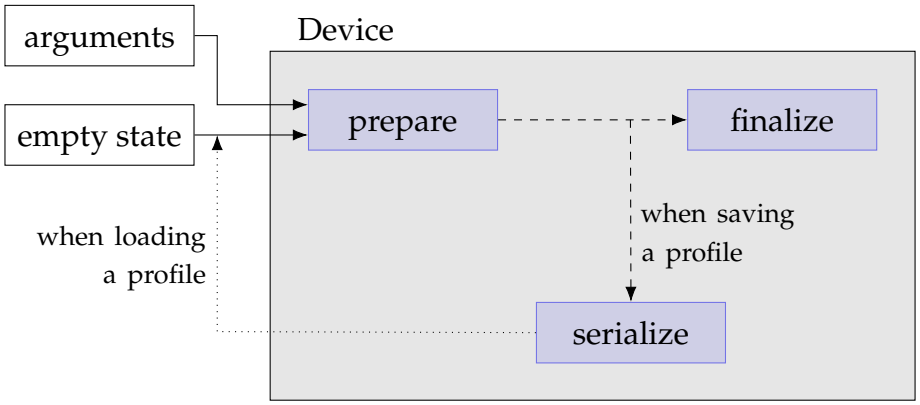

Fig. A.3: *The basic lifecycle of a* Metro *device and the relevant abstract methods (blue). Upon first creation, the* `prepare` *method is called with the device arguments and an empty state. When a profile is saved during the lifetime of a device, the* `serialize` *method is called to return the current state in order replace the the empty state later on. The* `finalize` *method allows cleanup of resources when the device is meant to be destroyed (e.g. by closing its window for* `metro.WidgetDevice`*).*

The `serialize` method is part of the profiles system, which aims to fulfill the capability for rapid reconfigurability in *Metro*. When a profile is saved, the state of all components created by the user, which are primarily the loaded devices, is serialized and saved in a JSON [ECM17] file. In addition to generic meta informations such as name, path and the passed arguments, this state contains the return value of `serialize`. This value is a means to save the custom state only relevant for this device. Upon loading a profile, all saved components are recreated as if created manually by the user in the first place.
The synchronization with the measurement system of *Metro* is performed by registering the `QTimer` [Qt c] slots on line 25. A device may register any number of slots to any of the signals emitted during a measurement. These are explained in detail further below.

Channels

The exchange of data in *Metro* is handled by channels. Once created by a producer of data, these represent an unidirectional flow of data from this provider to any number of consumers, which subscribe to a particular channel in order to receive the data. Both ends are often a device, but channels may also obtain their data from external sources or compute it at at runtime from other channels. In addition, channels may transparently store the data added to them to persistent storage if configured to do so. This abstraction therefore acts both as a sink and source of all data handled by devices.

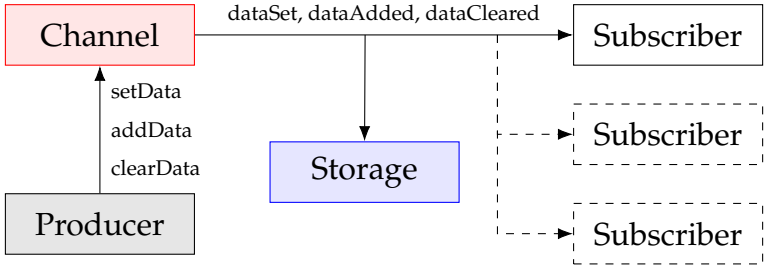

Fig. A.4: *Channels allow data recorded or generated during runtime to flow from producers to any number of subscribers or some kind of storage. This interface is defined by the three actions* set *to replace all currently stored data,* add *to extend the set and* clear.

A channel consists of a single object inheriting from `metro.AbstractChannel`, which defines the functionality common to all channels such as subscriptions and channel modes. While it has no expectation about the type and layout of data handled, it is assumed to be contained in *numpy* arrays. The `metro` package then contains several implementations of this abstract class with different properties. The two most commonly used are:

- `StreamChannel`
  This class is optimized for continuous data sets where the size along one dimension is constant (as a parameter called `shape`) and arbitrary along another. A typical example are event-based measurements which may occur at random times within the measurement window, such as the hits on an anode-based photon detector. This channel type aggregates this data whenever it is accessed to appear as a singular set. As such, it can be significantly more expensive than a `DatagramChannel`.

- `DatagramChannel`
  Here the data sets taken at a time must be fixed in size and are handled individually.

This is the case for cameras, for example, which take singular images in known intervals. It is capable of very high data rates and data sizes through the use of optimization flags that minimize its memory usage and processing.

It is also possible to create a custom subclass of `metro.AbstractChannel` (or its stub implementation `metro.ChannelAdapter`) for more specialized scenarios. This is used by some detector devices to export the raw binary data stream read out from the hardware, for example.
In the sample device in Listing A.1, a typical interaction of devices providing data through a channel is shown. A scalar `StreamChannel` (`shape` $= 0$) is created on line 19 and after each read from the serial port, the sample is simply added to this channel on line 39. This data manipulation constitutes the primary interface of a channel through two data manipulation methods:

- `addData(data: Any) -> None`
  Add data to existing data already saved in the current context in this channel.

- `setData(data: Any) -> None`
  Replace all existing data in the current context of this channel.

The meaning of channel context, as well as the actual argument types, depends on the specific implementation and its properties set during creation, but usually equates to the current measurement step. Properties common to all channels by being defined in *metro.AbstractChannel* are *mode*, *frequency* and *hint*. The *mode* describes how data is generated:

- *direct*
  Samples are generated directly by manual calls of the provider to the respective methods such as `setData` and `addData`.

- *computing*
  The channel computes samples by using those emitted by one or more other channels, once per sample emitted. A *Python* callable must be provided that consumes the argument channel and returns a value for this channel to use.

- *integrating*
  Similar to computing mode, but here all samples generated by the argument

channels during a measuring step are passed to the callable to return a single result. As such, a channel operating in this mode always uses *step* frequency (see below).

The *frequency* property specifies at what times data is generated. This may change the data structure returned and the semantics of some methods. The division of measurements into scans and steps is described in its respective section below.

- *continuous*
  Samples are generated at arbitrary intervals and are grouped in steps. For several scans, the samples are appended to the same step each time.

- *step*
  There is always exactly one sample at the end of each step for all scans. This mode is commonly used for statistics over one step like the number of counts on average and all channels in integration mode are forced to this frequency. If it is used by a direct channel, the sample should be generated during the *stopped* signal.

- *scheduled*
  This mode ignores any scan or step boundaries and emits samples at some fixed interval such as for logging purposes.

A suitable presentation for the content of a channel can be suggested by the *hint* property. It is especially useful to allow *Metro* to automatically pick the proper device to display the contained data. In addition to the default *unknown* hint, which gives no further information, the possible values are:

- *arbitrary*
  The channel does not necessarily contain any interpretable numeric data and therefore no attempt should be done to display it with any generic display device.

- *indicator*
  Only the most recent sample is relevant and should be displayed at a time. This hint is useful when complete data sets are added to the channel each time instead of point-by-point, such as images.

- *waveform*
  The probed variables varies over time and should be presented value by value as a function over time.

- *histogram*
  Not the individual values are relevant but their distribution or number of occurences. A typical example here are spectral measurements with MCP-based detectors, where a histogram of either time or position is required.

Measurement

Metro defines a measurement as a sequence of a number of scans with each scan comprised of a number of steps. Each step represents a certain configuration of the measuring environment, such as the value of an experimental parameter being scanned over; this may be the excitation energy at a synchrotron radiation facility or the grating position of a spectrometer, for instance.

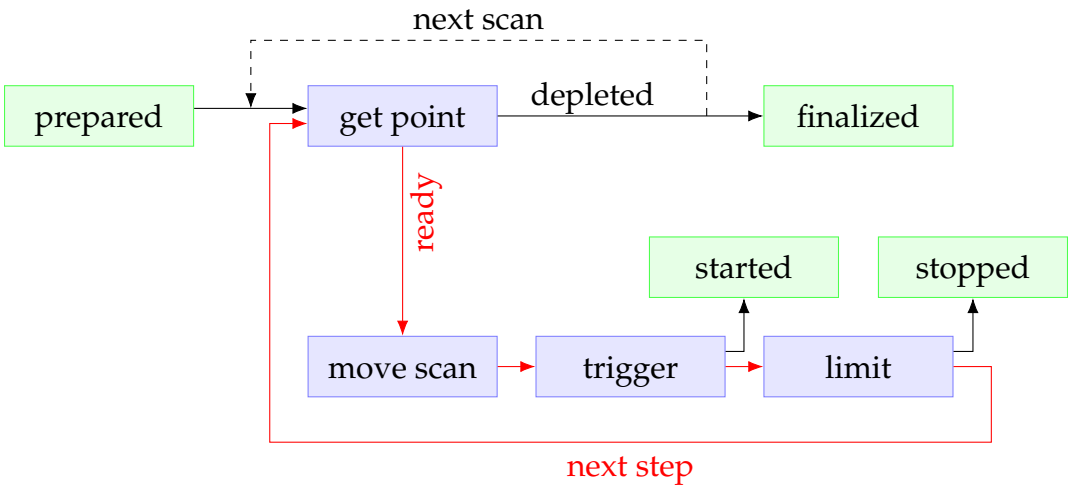

Fig. A.5: *Schematic overview of a measurement sequence with the emitted signals (green) and execution of measuring operators (blue). After preparation, the first step of the first scan is entered. In each step, the point operator decides whether to continue the current scan. In this case, the step sequence (red) is executed with the started/stopped signal signifying the actual measurement window. If no further points are available for a scan, the measurement is either finalized or proceeds to the next scan.*

A measurement is managed and controlled by an instance of `metro.Measurement`. It is usually created by the controller upon starting a measurement, but a device may override this authority and create it instead. This object's main function is to synchronize the participants of a measurement passed to it: *nodes*, *channels* and *measuring operators*. *Nodes* are objects implementing the `metro.measure.Node` interface to be able to listen

to the signals emitted during a measurement that occur at the beginning and end of the complete process as well as each step. These and options to influence their progression are described further below. The `metro.AbstractDevice` class and in turn every device implements this interface. A data acquisition device may use these signals to begin and end the readout of data, for example. Usually, all opened *channels* will participate in a measurement and will prepare their internal data structures accordingly to separate data into scans and steps. The most common exception are static channels created from loading data from disk. *Measuring operators* are objects to control a specific piece of the measurement process. There are five different types of these operators and each measurement will require exactly one of each:

- *Point operators* choose the parameter set or step value for the next step. Most commonly this is the next entry of a predefined list of values to scan over, but the point operator may also calculate this in an arbitrary way. If there are no more points, the current scan concludes.
- *Scan operators* provide a mechanism to adjust the scanned parameter to the value returned by the *Point Operator*. This may be a device connected to a motor driving the grating mechanics of a luminescence spectrometer.
- *Trigger operators* decide when to begin the actual recording of data for a given step. The default operator used returns immediately, but a custom implementation may wait for a hardware trigger or any other event to happen.
- *Limit operators* determine when the data recording started by the trigger operator comes to an end. In many cases, this is done manually or after a fixed amount of time has passed.
- *Status operators* convey the current status of the measurement process to the user and the transitions through its stages. By default, the controller acts as a status operator.

The `metro.measure` module implements a number of basic measuring operators used implicitely when starting measurement with the controller interface, but devices may provide more advanced or customized versions of all operator types through respective APIs in `AbstractDevice`. In addition, it is possible to enhance the functionality of the measurement process, e.g. to multi-dimensional scans via the `metro.ScansetProxy`

object that implements both a *Point Operator* and a *Scan Operator* and takes sets of each operator type in turn to execute them in an interweaved manner.
The complete sequence for a measurement is outlined in Figure A.5 showing the relation between signals and operators. Nodes, which are usually devices, may block the progression during the *prepared*, *stopped* or *finalized* signal by acquiring the so called *step block*. In addition, the start of a measurement as a whole may be blocked through the use of the *run block*. These are available as `metro.StepBlock` and `metro.RunBlock` respectively and are accessed using their methods:

- `acquire() -> None`
- `release() -> None`

While the *run block* is typically used during the initialization of hardware when its controlling device is created, the *step block* may ensure that all data is properly read out before the next step begins.
The sample device in Listing A.1 uses a very common pattern by connecting its `QTimer` [Qt c] directly to the measurement signal, namely *started* and *stopped*, through the use of

```
AbstractDevice.measure_connect(
    started_slot: QtCore.pyqtSlot = None,
    stopped_slot: QtCore.pyqtSlot = None,
    prepared_slot: QtCore.pyqtSlot = None,
    finalized_slot: QtCore.pyqtSlot = None
) -> None
```

Here the timer will only run during the measurement window of each step and trigger its timeout slot which performs the recording. A device may call `measure_connect` repeatedly to register any number of slots in any combination.

Current implementation status

At the time of this writing in July 2018, the master branch (the default source code configuration, revision `79d9956`) as developed in the AG Ehresmann since December 2013 contains a total of 28283 lines in 185 files of Python source code with smaller contributions of Cython, QML and Bash. From this single codebase, the use cases encountered

with PIFS in terms of supported hardware and interface to external facilities can be managed. This has allowed its deployment for all stationary spectroscopy experiments and over the course of 28 beamtimes so far, both to run the measurement process as well as to monitor and control the vacuum systems. In addition, it has been expanded to other experiments performed in collaborations with other groups through the use of custom devices tailored for these external set-ups:

- **Cookiebox ARPES** [HHH18]
  This angle resolved spectrometer is capable of simultanous acquisition of electrons for all angles of a given plane. The device `measure.custom.cookiebox` configures and reads out a set of Roentdek TDC8HPs as well as performs several live analysis algorithms to obtain angular distributions and electron spectra.

- **X-ray Streak Camera at Free-electron lasers**
  An X-ray streak camera, which is described as part of a characterization scheme for FEL bunch trains in Chapter 7, may be controlled and interfaced with the local facility infrastructure through the use of several devices in `measure.streak`.

- **Spectral Sensing of the Madeira compound eye**
  The circadian clock of the Rhyparobia maderae cockroach is investigated by long-term electroretinogram recordings with respect to its spectral sensitivity. The device `control.homebrew.madeira_sense` implements a custom measuring scheme to perform these investigations autonomously for several days at a time, while configuring the optical components for the time of day and other parameters through a number of additional devices.

The minimum *Python* version required is currently 3.3 with a small list of essential dependencies: `PyQt5`, `numpy`, `scipy`, `h5py` and `typing` (included in the standard library for $\geq$ 3.5). Depending on the employed hardware and use of optional optimizations, `cython`, `pyopengl`, `pyserial`, `pyvisa` or `pyepics` can be used additionally.

Spectral characterization of SASE bunch trains at free-electron lasers

The recent availability of free-electron lasers (FELs) at shorter wavelengths enabled the investigations of the nonlinear response of matter in the X-ray wavelength regime, i.e. at photon energies where the dominant interaction involves the strongly bound core electrons in all but the lightest of elements. The temporal coherence and intensity properties of such devices extends the applications of previous light sources, from the femtosecond laser in the visible regime to the hard X-rays generated by storage rings, across many areas of science. In atomic and molecular physics in particular, it allows to monitor the flow of charge and energy in highly correlated systems and scale diffraction techniques down to a single particle [MT10].
This chapter introduces a characterization method for the spectral properties of FEL radiation using an X-ray streak camera, which is able to cope with the exceptionally high repetition rates at facilities such as FLASH or the upcoming European XFEL. Along with a short introduction into the fundamental background of FELs and this detector device, a motivation for the spectral characterization and first results obtained at FLASH are included.

X-ray free electron laser

The principle underlying these machines begins with the same process as in a synchrotron radiation source introduced in Section 3.1. A relativistic electron beam passes along an undulator causing the electrons to emit electromagnetic radiation as shown in Figure B.1. Through feedback of the generated radiation field on the position of the electrons, they

are forced into phase with each other and thus emit with much greater coherence. Because this process uses a single-pass amplifier without the need for optical resonator elements and a configurable gain profile through the initial synchrotron radiation, it is well applicable to the X-ray spectral range and thus so far the only method to achieve coherent radiation with very high intensities and ultrashort pulses there.

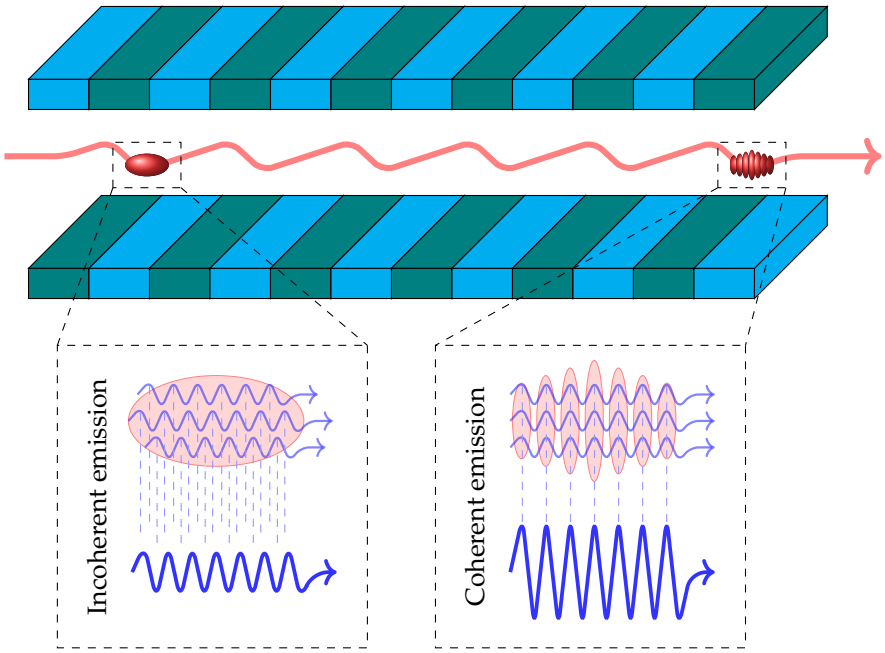

Fig. B.1: *In the beginning of traversing an undulator structure, the synchrotron radiation emitted by the electrons is incoherent due to their random phases. Through a sufficiently long interaction with the radiation field, small coherent fluctuations can be amplified and bunch the electrons at the resonant wavelength. In saturation at the end of the undulator, they emit coherently.*

Due to the non-uniform charge density and finite pulse length of the electron beam in the undulator, it contains a large range of fundamental wavelengths. Random fluctuations in the beam parameters cause different radiation-electron interactions across these modes, that can be the seed for amplification and lasing. The resulting FEL pulses are both temporally and spectrally noisy and possess a reduced spatial and temporal coherence. This is similar to amplified spontaneous emission in conventional lasers and thus referred to as self amplified spontaneous emission (SASE).
In addition to the SASE principle, a number of techniques exist and are in development to improve upon the coherence properties up to full temporal and transverse coherence. Most prominently among them, the FERMI@Elettra facility in Trieste, Italy uses a con-

ventional laser to seed the fluctuations in the electron beam [AAB12]. If the seed power dominates the initial SASE power, its coherence is maintained during the amplification process. While this method is being used very successfully, the limited availability of suitable seeding lasers at low wavelengths restricts it currently to $\lambda \geq 10\,\mathrm{nm}$.

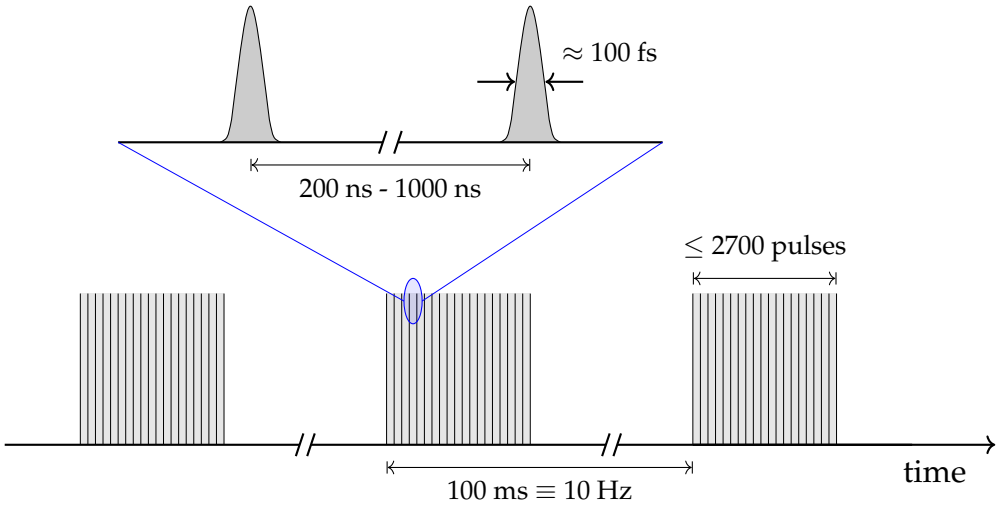

Fig. B.2: *The time structure of the upcoming European XFEL facility consisting of bunch trains with up to 2700 individual pulses at a repetition rate of 10 Hz. Within one train, the spacing between bunches is in the order of several hundred nanoseconds, while each bunch by itself has a length of around 100 fs. [ABC07]*

The randomness in some of an FEL's properties requires the development of diagnostic techniques that work on an individual shot-by-shot basis. While machines built with normal conducting cavities operating at room temperature are limited to repetition rates below 120 Hz, the use of superconducting cavities at FLASH and the European XFEL in Hamburg, Germany increases this well above 1 kHz [Sch10]. This is achieved by accelerating long trains of electron bunches at 10 Hz with up to 2700 individual bunches each spaced around 1 µs apart as illustrated in Figure B.2. The small time gaps between the respective pulses pose a significant challenge to the individual characterization by the need for correspondingly high acquisition rates.

X-ray streak camera

Streak camera-type detectors measure the temporal structure of electromagnetic radiation by *streaking* it along a spatial axis, thus obtaining a projection of the original time axis. For wavelengths in the visible regime and lower, this is achieved by deflection in a rapidly changing electric field after conversion of the light into photoelectrons. This technique is ideally suited for the bunch trains employed by FELs such as FLASH or the European XFEL shown in Figure B.2, whose internal structure is tightly spaced but separated by long intervals from each other. Every train can be streaked separately to reveal its inner composition of bunches. Through the use of a dispersive grating, the spectral information is additionally projected along the perpendicular spatial axis. The resulting streak image therefore contains time on one axis and wavelength on the other as illustrated in Figure B.3.

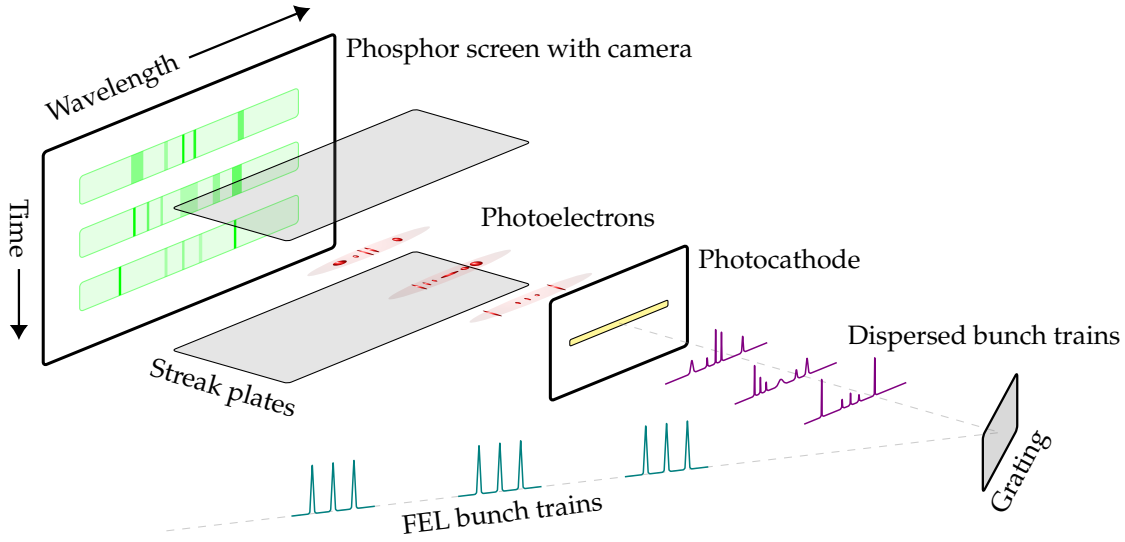

Fig. B.3: *In the proposed characterization scheme, the incoming FEL bunch trains are dispersed on a grating and converted to photoelectrons with an identical time and intensity structure by the x-ray streak camera's photocathode. The streak tube behind deflects those electrons in dependence of their arrival time on a luminescent screen, thereby projecting the original time information onto a spatial axis perpendicular to the dispersion axis.*

A commercially available streak camera *Hamamatsu C7700-31* has been used as the detector device. In contrast to common streak cameras operating in the visible spectral range which are completely sealed, this device uses a detachable photocathode mounted on a small disk in front of the open streak tube to operate in vacuum as shown in

C7700-31	
Spectral response	10 eV - 10 keV
Time resolution	$\geq$ 10 ps
Cathode size	80 µm x 17.3 mm
Sweep time	1 ns - 1 ms
Sweep frequency	$\leq$ 100 Hz
Dynamic range	1000 : 1

C11440-22CU	
Sensor	sCMOS FL-400
Pixel number	2048 x 2048
Pixel size	6.5 µm x 6.5 µm
Average noise	$\leq$ 1.3 electrons
Dynamic range	23000 : 1

Tab. B.1: *Technical specifications of the* Hamamatsu C7700-31 *streak camera (left) [Ham14] and* Hamamatsu C11440-22CU *CMOS camera (right) as reported by the manufacturer.*

Figure B.4. The slit-shaped cathode consists of a 100 nm Parylene-N substrate on which 30 nm gold have been deposited for a high quantum efficieny of the photoelectric effect at photon energies beyond 10 eV. The vertical cathode size is parallel to the streak direction and influences significantly the time resolution with sizes of 80 µm and 200 µm available for the initial experiments. Behind the streak tube, a phosphor screen converts the streaked electrons back into visible light which subsequently gets amplified by an image intensifier *Hamamatsu V7669*. A *Hamamatsu A2098* relay lens demagnifies the amplified picture in the ratio 2:1 onto a *Hamamatsu C11440-22CU* CMOS camera. It is usually operated in a 2x2 binning mode to match the spatial resolution of the phosphor screen coming before. The technical specifications as given by the manufacturer can be found in Table B.1.

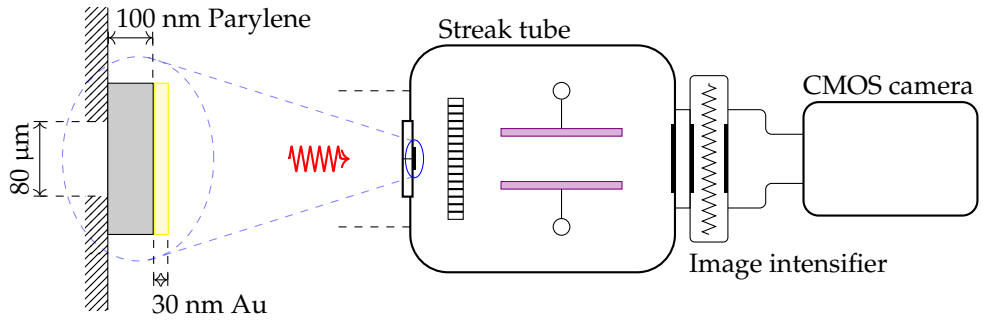

Fig. B.4: *The complete* Hamamatsu C7700-31 *streak camera system consists of the actual streak tube with a replaceable photocathode mounted in the front followed by an acceleration mesh. The streaking plates (purple) deflect the created electrons perpendicular to the slit cathode. After conversion by a luminescent screen into visible light and an image intensifier, an optical system focuses the streaked image onto a* Hamamatsu C11440-22CU *CMOS camera.*

First results at FLASH

In preparation for operation at the upcoming European XFEL, the general principle shown in Figure B.3 was first demonstrated during regular user operation at FLASH. Following a description of the experimental set-up, the first results are shown with a discussion of the achievable temporal and spectral resolution.
The FLASH facility at DESY was the first free-electron laser to operate in the vacuum ultraviolet regime at photons energies between 50 and 290 eV or wavelengths between 4.2 and 51 nm [AAA07]. Its superconducting accelerator reaches a maximum of 1.25 GeV electron energy resulting in typical pulse energies in the order of 100 µJ and lengths around 100 fs. As discussed above, it is capable of achieving high repetition rates through the use of bunch trains in place of the regular single bunches at a fundamental frequency of 10 Hz. At this machine, these trains consist of up 500 individual bunches at spacings between 1 and 10 µs.

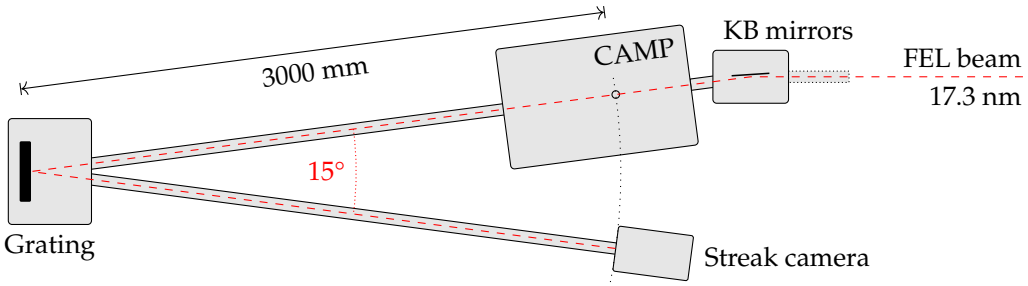

Fig. B.5: *In the experiment performed at FLASH's BL1, the transparent interaction chamber called CAMP allowed the FEL beam to pass through. The spherical grating was positioned in such a way that its focus coincided with the FEL focus created by the KB mirrors. At the focus distance of the other arm, the streak camera's photocathode was mounted to obtain a accurate projection of the dispersed spectrum.*

In the context of an experiment performed at BL1 there, a 3m normal incidence spectrometer was mounted behind the transparent interaction chamber CAMP to disperse the transmitted FEL radiation using its rotatable platinum-coated spherical grating at a line density of 2400 mm^{-1} as shown in Figure B.5. The streak camera was installed at its exit arm with both the camera and the focus created by the beamline's KB mirrors on the grating's rowland circle. The free-electron laser operated in this case at a photon energy of 71.6 eV or wavelength of 17.3nm in 30 bunches per train each 1 µs apart at a bunch train repetition rate of 10 Hz. In order to obtain a single one of these trains per streak

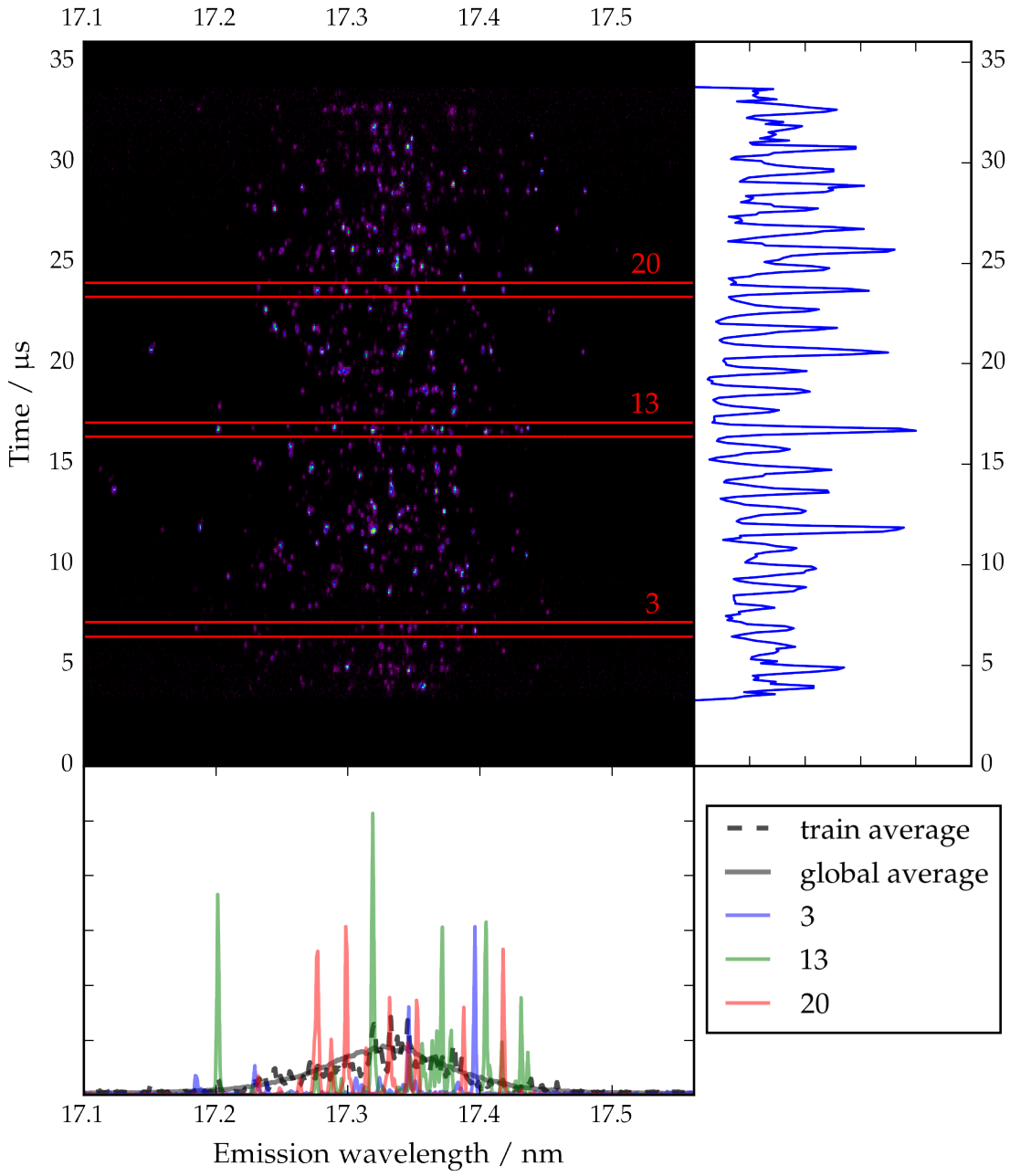

Fig. B.6: *The streak image in operating mode separates each bunch in the train of 30 bunches at FLASH on the vertical time axis, while the spectral information through dispersion in the spectrometer in 4th order is on the horizontal axis. The selected single-shot spectra (bottom plot) exhibit the noisy and spiky structure generated by SASE, while the averages approximate a gaussian shape. Within one train, the individual bunch intensities (right plot) fluctuate significantly as well.*

image, the duration of one such streak was set to 50 µs and at the same rate of 10 Hz to capture all FEL pulses during the acquisition window.
Figure B.6 shows an exemplary single streak image of a bunch train from this result set measured in 4th order of the spectrometer. Along the vertical time axis, the streak axis, each individual bunch of the train is clearly separated by 1 µs when streaked over 50 µs in total. The horizontal axis is aligned along the grating's dispersion axis and hence contains the spectral information. The influence of SASE can be seen in the the noisy and spiky spectral structure as well as the fluctuations of the individual bunches' total intensity over time (with the actual and much smaller temporal structure, which also consists of scattered spikes, not resolvable by this device). In contrast, the wavelength spectrum averaged over 16000 bunches appears Gaussian, while the average taken over the displayed train only approximates it with singular, strong spikes still appearing.

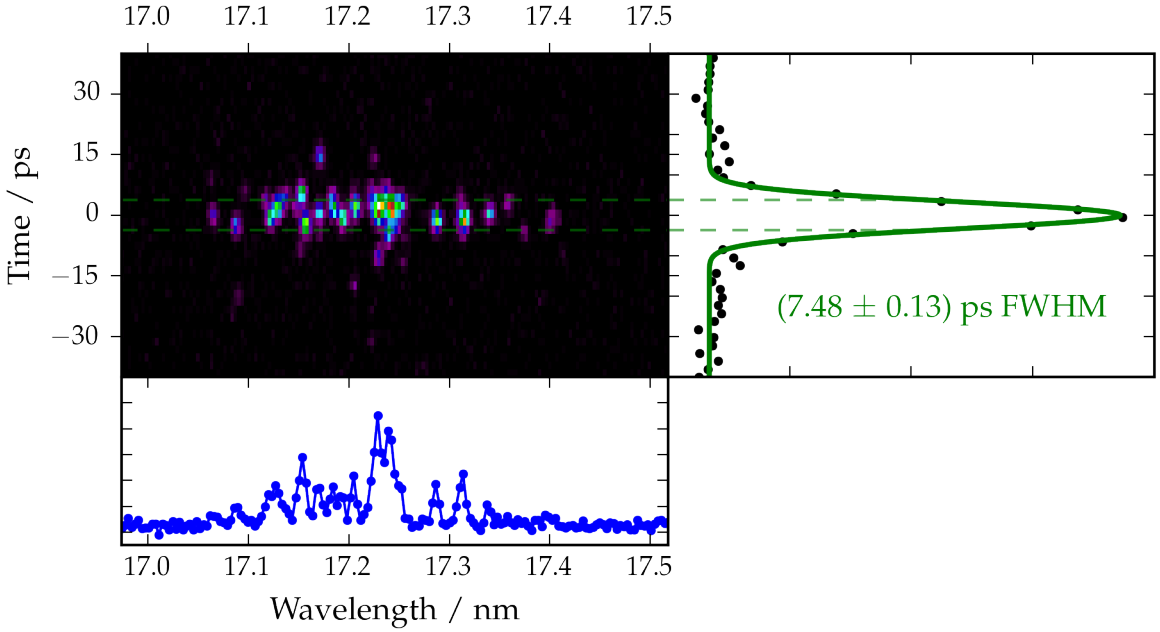

Fig. B.7: *A singular bunch in 1st order of the spectrometer streaked over the smallest possible time range of* $\tau = 1\,\text{ns}$ *allows an estimation of the achievable time resolution of the* Hamamatsu C7700-13 *streak camera given the actual pulse length is much shorter on the order of 100 fs. The FWHM (green dashed line) in the time profile (right plot) obtained by gaussian fit (green line) yields a time resolution of* $\Delta\tau = (7.48 \pm 0.13)\,\text{ps}$ *or* $\tau/\Delta\tau = 135 \pm 2$.

The opposite perspective of a single bunch is shown in Figure B.7 by streaking over the smallest accessible time range of 1 ns. In addition, the spectrometer was operating in

1st rather than 4th order to increase the single shot statistics at a reduced wavelength dispersion.
The spectral resolution of this set-up is estimated by the FWHM of Gaussian fits to spectral emission lines of individual bunches and yields in the 4th order of the spectrometer as shown in Figure B.6 for the narrowest lines:

$$\Delta\lambda = (1.433 \pm 0.005)\,\mathrm{pm} \qquad \lambda/\Delta\lambda = 12140 \pm 40$$

In physical units of the camera sensor, this is equivalent to $\Delta\lambda \equiv 1.68\,\mathrm{Pixel}$ in 2x2 binning mode, which in turn results in a physical spot size on the camera sensor of 22 µm and 44 µm on the photocathode.
For the temporal resolution, the FEL pulses' time profiles are also fitted by Gaussians. Since the length of these pulses is actually in the order of 100 fs and hence much smaller than measured, the complete width can be attributed to the apparatus itself. The result depends on the streak range τ and yields for 50 µs (shown in Figure B.6) and 1 ns (shown in Figure B.7) respectively:

$$\Delta\tau_{50\,\mu\mathrm{s}} = (299 \pm 2)\,\mathrm{ns} \qquad 50\,\mu\mathrm{s}/\Delta\tau_{50\,\mu\mathrm{s}} = 175 \pm 1$$
$$\Delta\tau_{1\,\mathrm{ns}} = (7.48 \pm 0.13)\,\mathrm{ps} \qquad 1\,\mathrm{ns}/\Delta\tau_{1\,\mathrm{ns}} = 135 \pm 2$$

The contributions to the time spread and hence the time resolution limit according to the manufacturer [Ham14] are:

- **Initial velocity distribution of photoelectrons**
  Based on literature on the characterization of transparent metal cathodes [HKP81], this material-dependent value can be calculated to $\Delta t_\mathrm{v} \approx 2.9\,\mathrm{ps}$.

- **Travel time spread by deflecting electric field**
  This quantity only depends on the streak tube's internal operating parameters and is given with $\Delta t_\mathrm{E} = 2.3\,\mathrm{ps}$ [Ham14].

- **Spatial spread by photocathode**
  The finite size of the photocathode spreads the image on the phosphor screen, which depends on the cathode size w (80 µm in this experiment) and the streak range τ in relation to the visible phosphor screen length of 18.7 mm [Ham14]. In

general this leads to $\Delta t_S = w\,\tau \cdot 57.8\,\mathrm{mm}^{-1}$ or in practive for the considered ranges $\Delta t_{S,50\,\mu s} = 225\,\mathrm{ns}$ and $\Delta t_{S,1\,ns} = 4.5\,\mathrm{ps}$.

Since each of these components cause a Gaussian broadening of the time profile, the total time spread as a convolution of the individual terms can be estimated by the root of quadratic sums. For longer time ranges such as $\tau = 50\,\mu s$ as used in the present experiment, only the spatial spread is considered due to $\Delta t_S \gg \Delta t_v + \Delta t_E$:

$$\Delta t = \sqrt{\Delta t_v^2 + \Delta t_E^2 + \Delta t_S^2}$$

$$\Delta t_{50\,\mu s} = 225\,\mathrm{ns} \qquad\qquad \Delta t_{1\,ns} = 5.9\,\mathrm{ps}$$

The obtained values $\Delta\tau$ from the experimental data are each about 30% higher than the calculated time spreads Δt. All of these values (in terms of spatial resolution on the sensor) are significantly higher than the spatial resolution limit reached on the dispersion axis. It may therefore be assumed that this common deviation was mostly caused by external experimental factors such as suboptimal focus conditions on the photocathode, that apply to all streak ranges in the same manner. The best attainable time resolution $\Delta\tau$ can be narrowed down in this case to the range $\Delta t \leq \Delta\tau \leq 1.3\Delta t$.

Spatial (spectral) resolution limit

The horizontal detector axis perpendicular to the streak direction, which was used for wavelength dispersion in the FLASH experiment, is only limited by the optical projection throughout the streak camera, consisting of:

- Spot size on the photocathode
- Corn size of one or all of the phosphor screens behind the streak rube and in the image intensifier
- Individual pixel size of the camera sensor

The wavelength resolution obtained from the experiment amounts to $\Delta s = 1.7$ Pixel on the CMOS camera, which equates with 2x2 binning used in this experiment and the 2:1 demagnification lens to an actual size of

$$\Delta s_{CMOS} = 22\,\mu m \qquad\qquad \Delta s_{Cathode} = 44\,\mu m$$

on the CMOS sensor and photocathode, respectively. Given an individual pixel size of 13 µm, this component can be neglected and it is recommendable to continue operating in 2x2 binning mode for an improved signal-to-noise ratio. Hence, the limiting factor is either the focus condition achieved in the experiment or the corn size of the phosphor screens at an upper value of $\Delta s = 44\,\mu\text{m}$.

Characterization limit of FEL bunch trains

In this configuration of streaking over ranges in the order of 100 µs, the relative time resolution directly defines an upper limit on the number of bunches that can be resolved individually. The slit width w of the photocathode could be identified as the main contribution in this case with a direct inverse relationship, while all other contributions can be neglected:

$$\left(\frac{t}{\Delta t}\right)_{\text{Diag}} = \frac{17.8\,\mu\text{m}}{w} \propto \frac{1}{w}$$

This relation is valid until the (upper) spatial resolution limit is reached at $\Delta s = 1.7\,\text{Pixel}$, which equates to a maximal relative time resolution of $(t/\Delta t)_{\text{Diag,max}} \approx 300$ and a reasonable minimal slit size of $w_{\text{min}} \approx 55\,\mu\text{m}$.

Time resolution limit for physical processes

When operating at smaller streak intervals to investigate fast physical interactions, a significant constant time spread emerges due to instrinsic properties of the electron acceleration and focusing in addition to the slit dependent value as discussed above. With an infinitely small photocathode slit size, this value defines a lower bound for the absolute time resolution:

$$\Delta t_{\text{min}} = \Delta t_{\text{v}} + \Delta t_{\text{E}} \approx 5.2\,\text{ps}$$

In this case, this value is already higher than the limit imposed by the (upper) spatial resolution limit of $\Delta t_{\text{Screen}} \approx 3.3\,\text{ps}$.

Bibliography

[AAA07] Ackermann, W., G. Asova, V. Ayvazyan, A. Azima, N. Baboi, J. Bähr, V. Balandin, B. Beutner, A. Brandt, A. Bolzmann et al.. *Operation of a free-electron laser from the extreme ultraviolet to the water window*. Nature Photonics, 1, 336 (2007).

[AAB12] Allaria, E., R. Appio, L. Badano, W. Barletta, S. Bassanese, S. Biedron, A. Borga, E. Busetto, D. Castronovo, P. Cinquegrana et al.. *Highly coherent and stable pulses from the FERMI seeded free-electron laser in the extreme ultraviolet*. Nature Photonics, 6, 699 (2012).

[ABB99] Anderson, E., Z. Bai, C. Bischof, S. Blackford, J. Demmel, J. Dongarra, J. Du Croz, A. Greenbaum, S. Hammarling, A. McKenney and D. Sorensen. *LAPACK Users' Guide*. Society for Industrial and Applied Mathematics, third edition (1999).

[ABC07] Altarelli, M., R. Brinkmann and M. Chergui. *The European X-ray Free-Electron Laser: Technical design report*. Technical Report, DESY XFEL Project Group, Germany (2007). DESY–2006-097.

[ÁEK04] Álvarez Ruiz, J., P. Erman, A. Kivimäki, E. Melero Garcia, E. Rachlew and M. Stankiewicz. *Selective excitation of the* $n\mathrm{p}\sigma\ ^1\Sigma_u^+$ *and* $n\mathrm{p}\pi^1\Pi_u$ *to* $E, F\ ^1\Sigma_g^+$ *emission systems in molecular hydrogen using synchrotron radiation*. Chemical Physics Letters, 388(1-3), 31 (2004).

[AL15] Astashkevich, S. A. and B. P. Lavrov. *Lifetimes of Vibro-Rotational Levels in Excited Electronic States of Diatomic Hydrogen Isotopologues*. Journal of Physical and Chemical Reference Data, 44(2), 023105 (2015).

[ARL93] Abgrall, H., E. Roueff, F. Launay, J.-Y. Roncin and J.-L. Subtil. *The Lyman and Werner Band Systems of Molecular Hydrogen*. Journal of Molecular Spectroscopy, 157, 512 (1993).

[ARL97] Abgrall, H., E. Roueff, X. Liu and D. E. Shemansky. *The emission continuum of electron-excited molecular hydrogen*. The Astrophysical Journal, 481, 557 (1997).

[ARV86] Amiot, C., J. Y. Roncin and J. Verges. *First observation of the CO* $E\ ^1\Pi$ *to* $B\ ^1\Sigma^+$ *and* $C\ ^1\Sigma^+$ *to* $B\ ^1\Sigma^+$ *band systems. Predissociation in the* $E^1\Pi(v = 0)$ *level*. Journal of Physics B: Atomic and Molecular Physics, 19(1), L19 (1986).

[ASK84] Ajello, J. M., D. E. Shemansky, T. L. Kwok and Y. L. Yung. *Studies of extreme-ultraviolet emission from Rydberg series of H2 by electron impact*. Physical Review A, 29(2), 636 (1984).

[ASY82] Ajello, J. M., S. K. Srivastava and Y. L. Yung. *Laboratory studies of uv emissions of H2 by electron impact. the Werner- and Lyman-band systems*. Physical Review A, 25(5), 2485 (1982).

[Bak05] Baker, J. *The diffuse $v = 4$ and 5 vibrational levels of the $B\,^1\Sigma^+$ Rydberg state of carbon monoxide*. Chemical Physics Letters, 408(4), 312 (2005).

[BBC11] Behnel, S., R. Bradshaw, C. Citro, L. Dalcin, D. S. Seljebotn and K. Smith. *Cython: The Best of Both Worlds*. Computing in Science & Engineering, 13(2), 31 (2011).

[BDJ35] Beutler, H., A. Deubner and H. O. Jünger. *Über das Absorptionsspektrum des Wasserstoffs. II*. Zeitschrift für Physik, 98(3), 181 (1935).

[BFG01] Bahrdt, J., W. Frentrup, A. Gaupp, M. Scheer, W. Gudat, G. Ingold and S. Sasaki. *A quasi-periodic hybrid undulator at BESSY II*. Nuclear Instruments and Methods in Physics Research Section A: Accelerators, Spectrometers, Detectors and Associated Equipment, 467, 130 (2001).

[BGGM80] Breton, J., P. M. Guyon and M. Glass-Maujean. *Radiative emission from singlet superexcited levels of H_2*. Physical Review A, 21(6), 1909 (1980).

[BGM86] Bezard, B., D. Gautier and A. Marten. *Detectability of HD and non-equilibrium species in the upper atmospheres of the giant planets from their submillimeter spectrum*. Astronomy and Astrophysics, 161, 387 (1986).

[Bir26] Birge, R. T. *The Band Spectra of Carbon Monoxide*. Phys. Rev., 28, 1157 (1926).

[BJ06] Brandsen, B. H. and C. J. Joachain. *Physics of Atoms and Molecules*. Dorling Kindersley, second edition (2006).

[BLS09] Bubin, S., F. Leonarski, M. Stanke and L. Adamowicz. *Charge asymmetry in pure vibrational states of the HD molecule*. The Journal of Chemical Physics, 130(12), 124120 (2009).

[BO27] Born, M. and R. Oppenheimer. *Zur Quantentheorie der Molekeln*. Annalen der Physik, 84, 457 (1927).

[BS75] Bussoletti, E. and G. Stasińska. *H2 and HD Infrared Lines Expected from Dense Interstellar Objects*. Astronomy and Astrophysics, 39, 177 (1975).

[BTBJ95] Baker, J., W.-Ü. L. Tchang-Brillet and P. S. Julienne. *First observation of the $v = 3$ level of the $B\,^1\Sigma^+$ Rydberg state of CO*. The Journal of Chemical Physics, 102(10), 3956 (1995).

[CDS18] Cozijn, F. M. J., P. Dupré, E. J. Salumbides, K. S. E. Eikema and W. Ubachs. *Sub-Doppler Frequency Metrology in HD for Tests of Fundamental Physics*. Phys. Rev. Lett., 120, 153002 (2018).

[CER06] CERN. *Python: The Holy Grail of Programming*. CERN Bulletin, 11/2006 (2006).

[Col08] Collette, A. *HDF5 for Python* (2008). URL `https://www.h5py.org/`.

[Con26] Condon, E. *A Theory of Intensity Distribution in Band Systems*. Phys. Rev., 28, 1182 (1926).

[Con28] Condon, E. U. *Nuclear Motions Associated with Electron Transitions in Diatomic Molecules*. Phys. Rev., 32, 858 (1928).

[CSLHXL17] Chun-Sheng, J., Z. Lie-Hui and P. Xiao-Long. *Improved Pöschl–Teller potential energy model for diatomic molecules*. International Journal of Quantum Chemistry, 117(14), e25383 (2017).

[Dem05] Demtröder, W. *Molecular Physics: Theoretical Principles and Experimental Methods*. Wiley-VCH (2005).

[Dem06] Demtröder, W. *Atoms, Molecules and Photons*. Springer (2006).

[DHS70] Dalgarno, A., G. Herzberg and T. L. Stephens. *A new continuous emission spectrum of the hydrogen molecule*. The Astrophysical Journal, 162, L49 (1970).

[DHWTJF13] De-Heng, S., L. Wen-Tao, S. Jin-Feng and Z. Zun-Lue. *Theoretical study of spectroscopic and molecular properties of several low-lying electronic states of CO molecule*. International Journal of Quantum Chemistry, 113(7), 934 (2013).

[DIU11] Dickenson, G., T. Ivanov, W. Ubachs, M. Roudjane, N. de Oliveira, D. Joyeux, L. Nahon, W.-Ü. Tchang-Brillet, M. Glass-Maujean, H. Schmoranzer, A. Knie, S. Kübler and A. Ehresmann. *VUV Spectroscopic Study of the $D^1\Pi_u$ State of Molecular Deuterium*. Molecular Physics, 109(22), 2693 (2011).

[dLDS12] de Lange, A., G. D. Dickenson, E. J. Salumbides, W. Ubachs, N. de Oliveira, D. Joyeux and L. Nahon. *VUV Fourier-transform absorption study of the Lyman and Werner bands in D_2*. The Journal of Chemical Physics, 136(23), 234310 (2012).

[DRU10] De Lange, A., E. Reinhold and W. Ubachs. *Phenomena of g-u symmetry-breakdown of HD*. International Reviews in Physical Chemistry, 21, 257 (2010).

[ECM17] ECMA International. *ECMA-404: The JSON Data Interchange Syntax*. ECMA International (2017).

[EGL47] Elder, F. R., A. M. Gurewitsch, R. V. Langmuir and H. C. Pollock. *Radiation from Electrons in a Synchrotron*. Phys. Rev., 71, 829 (1947).

[EKRK93] Erman, P., A. Karawajczyk, E. Rachlew-Källne, C. Strömholm, J. Larsson, A. Persson and R. Zerne. *Direct determination of the ionization potential of CO by resonantly enhanced multiphoton ionization mass spectroscopy*. Chemical Physics Letters, 215(1), 173 (1993).

[EMU95] Ehresmann, A., S. Machida, M. Ukai, K. Kameta, M. Kitajima, N. Kouchi, Y. Hatano, K. Ito and T. Hayaishi. *Threshold behaviour of neutral photodissociation with excitation of CO probed by dispersed fragment VUV fluorescence*. Journal of Physics B: Atomic, Molecular and Optical Physics, 28(24), 5283 (1995).

[EMU96] Ehresmann, A., S. Machida, M. Ukai, K. Kameta, M. Kitajima, N. Kouchi, Y. Hatano, K. Ito and T. Hayaishi. *Photodissociation of CO: partial cross sections for neutral dissociative excitation*. Journal of Physics B: Atomic, Molecular and Optical Physics, 29(16), 3629 (1996).

[EMU97] Ehresmann, A., S. Machida, M. Ukai, K. Kameta, M. Kitajima, N. Kouchio, Y. Hatano, K. Ito and T. Hayaishi. *CO Rydberg series converging to the CO^+ D and C states observed by VUV-fluorescence spectroscopy*. Journal of Physics B: Atomic, Molecular and Optical Physics, 30(8), 1907 (1997).

[ERF87] Eidelsberg, M., J.-Y. Roncin, A. L. Floch, F. Launay, C. Letzelter and J. Rostas. *Reinvestigation of the vacuum ultraviolet spectrum of CO and isotopic species: The B* $^1\Sigma^+ \leftrightarrow X\ ^1\Sigma^+$ *transition*. Journal of Molecular Spectroscopy, 121(2), 309 (1987).

[FLS65] Feynman, R. P., R. B. Leighton and M. Sands. *The Feynman Lectures on Physics, Vol. 3: Quantum Mechanics*. Addison Wesley (1965).

[Foc35] Fock, V. *Zur Theorie des Wasserstoffatoms*. Zeitschrift für Physik, 98(3–4), 145 (1935).

[FSC85] Freund, R. S., J. A. Schiavone and H. M. Crosswhite. *The Electronic Spectrum and Energy Levels of the Deuterium Molecule*. Journal of Physical and Chemical Reference Data, 14(1), 235 (1985).

[GAP12] Gay, C. D., N. P. Abel, R. L. Porter, P. C. Stancil and G. J. Ferland. *Rovibrationally resolved direct photodissociation through the Lyman and Werner transitions of* H_2 *for FUV/X-ray irradiated environments*. The Astrophysical Journal, 746(1), 78 (2012).

[GBGM79] Guyon, P. M., J. Breton and M. Glass-Maujean. *Predissociation of the* $^1\Pi_u^+$ *states of* H_2*: Measurement of the various dissociation yields*. Chemical Physics Letters, 68(6), 314 (1979).

[GG97] Gates, K. and W. Gragg. *Notes on TQR algorithms*. Journal of Computational and Applied Mathematics, 86(1), 195 (1997).

[GHH88] Grayce, C. J., R. A. Harris and E. L. Hahn. *The nuclear-quadrupole-induced dipole moment of HD*. Chemical Physics Letters, 147(5), 443 (1988).

[GKM17] Grösle, R., A. Kraus, S. Mirz and S. Wozniewski. *First Calibration of an IR Absorption Spectroscopy System for the Measurement of* H_2*,* D_2*, and HD Concentration in the Liquid Phase*. Fusion Science and Technology, 71(3), 369 (2017).

[GMBG79] Glass-Maujean, M., J. Breton and P. Guyon. *A fano-profile study of the predissociation of the* $3p\pi$ *D* $^1\Pi_u^+$ *state of* H_2. Chemical Physics Letters, 63(3), 591 (1979).

[GMJD16] Glass-Maujean, M., C. Jungen, G. Dickenson, N. de Oliveira and W. Ubachs. *The excited* $J = 0\ ^1\Sigma_u^+$ *levels of* D_2*: Measurements and ab initio quantum defect study*. Journal of Molecular Spectroscopy, 320, 33 (2016).

[GMJR10] Glass-Maujean, M., C. Jungen, G. Reichardt, A. Balzer, H. Schmoranzer, A. Ehresmann, I. Haar and P. Reiss. *Competing decay-channel fluorescence, dissociation, and ionization in superexcited levels of H2*. Physical Review A, 82(6), 062511 (2010).

[GMJS10] Glass-Maujean, M., C. Jungen, H. Schmoranzer, A. Knie, I. Haar, R. Hentges, W. Kielich, K. Jänkälä and A. Ehresmann. H_2 *Superexcited States: Experimental and Theoretical Characterization of their Competing Decay-Channel Fluorescence, Dissociation, and Ionization*. Phys. Rev. Lett., 104, 183002 (2010).

[GMJS13a] Glass-Maujean, M., C. Jungen, H. Schmoranzer, I. Tulin, A. Knie, P. Reiss and A. Ehresmann. *Experimental and theoretical studies of excited states of* H_2 *observed in the absorption spectrum: II. The* $6p\pi$ *and* $7p\pi$ $1\Pi_u$ *states*. Journal of Molecular Spectroscopy, 293-294, 11 (2013).

[GMJS13b] Glass-Maujean, M., C. Jungen, H. Schmoranzer, I. Tulin, A. Knie, P. Reiss and A. Ehresmann. *Experimental and theoretical studies of excited states of H_2 observed in the absorption spectrum: III. The 5pσ, 6pσ and 7pσ $^1\Sigma_u^+$ states*. Journal of Molecular Spectroscopy, 293, 19 (2013).

[GMJS13c] Glass-Maujean, M., C. Jungen, A. Spielfiedel, H. Schmoranzer, I. Tulin, A. Knie, P. Reiss and A. Ehresmann. *Experimental and theoretical studies of excited states of H_2 observed in the absorption spectrum: I. The 5pπD" $1\Pi_u$ state*. Journal of Molecular Spectroscopy, 293-294, 1 (2013).

[GMJV17] Glass-Maujean, M., C. Jungen, A. Vasserot, H. Schmoranzer, A. Knie, S. Kübler, A. Ehresmann and W. Ubachs. *Experimental and theoretical studies of the npσ $^1\Sigma_u^+$ and npπ $^1\Pi_u^+$ ($n \geq 4$,N'=1–6) states of D_2: Energies, natural widths, absorption line intensities, and dynamics*. Journal of Molecular Spectroscopy, 338, 22 (2017).

[GMKW07a] Glass-Maujean, M., S. Klumpp, L. Werner, A. Ehresmann and H. Schmoranzer. *Observation of the oscillating absorption spectrum of a double-well state: the state of H_2*. Journal of Physics B: Atomic, Molecular and Optical Physics, 40(2), F19 (2007).

[GMKW07b] Glass-Maujean, M., S. Klumpp, L. Werner, A. Ehresmann and H. Schmoranzer. *Study of the $B''\bar{B}\ ^1\Sigma_u^+$+ state of H_2: Transition probabilities from the ground state, dissociative widths, and Fano parameters*. The Journal of Chemical Physics, 126(14), 144303 (2007).

[GMSJ12] Glass-Maujean, M., H. Schmoranzer, C. Jungen, I. Haar, A. Knie, P. Reiss and A. Ehresmann. *Ab initio nonadiabatic study of the 3p π D $1\Pi u$+ state of H2 and D2*. Physical Review A, 86(5), 052507 (2012).

[GMVJ15] Glass-Maujean, M., A.-M. Vasserot, C. Jungen, H. Schmoranzer, A. Knie, S. Kübler and A. Ehresmann. *Experimental and theoretical study of the npπ $^1\Pi_u^-$ ($n \geq 4$) excited states of D_2: Absolute absorption cross sections and branching ratios for ionization, dissociation and fluorescence*. Journal of Molecular Spectroscopy, 315, 155 (2015). Spectroscopy with Synchrotron Radiation.

[GMVJ16] Glass-Maujean, M., A.-M. Vasserot, C. Jungen, H. Schmoranzer, A. Knie, S. Kübler and A. Ehresmann. *Experimental and theoretical study of the npσ $^1\Sigma_u^+$ ($n \geq 4$) $N = 0$ excited states of D_2: Absolute absorption cross sections and branching ratios for ionization, dissociation and fluorescence*. Journal of Molecular Spectroscopy, 320, 25 (2016).

[Ham14] Hamamatsu. *High Dynamic Range X-Ray Streak Camera C7700-31 Instruction Manual*. Hamamatsu (2014).

[Han18] Hans, A. *Fluoreszenzspektroskopie an Clustern & Flüssigkeiten - Untersuchung interatomarer und intermolekularer Prozesse in dichten Medien*. Dissertation, Universität Kassel (2018).

[Hel16] Helmholtz-Zentrum Berlin für Materialien und Energie. *The U125-2 NIM beamline at BESSY II*. Journal of large-scale research facilities, 2, A53 (2016).

[Her44] Herzberg, G. *Atomic Spectra and Atomic Structure*. Dover Publications, second edition (1944).

[Her50a] Herzberg, G. *Molecular Spectra and Molecular Structure I: Spectra of Diatomic Molecules*. Krieger Publishing Company, second edition (1950).

[Her50b] Herzberg, G. *Rotation-Vibration Spectrum of the HD Molecule*. Nature, 166, 563 (1950).

[HHH18] Hartmann, N., G. Hartmann, R. Heider, M. S. Wagner, M. Ilchen, J. Buck, A. O. Lindahl, C. Benko, J. Grünert, J. Krzywinski et al.. *Attosecond time–energy structure of X-ray free-electron laser pulses*. Nature Photonics, 12, 215 (2018).

[HKP81] Henke, B., J. Knauer and K. Premaratne. *The characterization of x-ray photocathodes in the 0.1-10 keV photon energy region*. Journal of Applied Physics, 52(3), 1509 (1981).

[HKS15] Hans, A., A. Knie, P. Schmidt, L. Ben Ltaief, C. Ozga, P. Reiß, H. Huckfeldt, M. Förstel, U. Hergenhahn and A. Ehresmann. *Lyman-series emission after valence and core excitation of water vapor*. Phys. Rev. A, 92, 032511 (2015).

[HLF17] Hans, A., L. B. Ltaief, M. Förstel, P. Schmidt, C. Ozga, P. Reiß, X. Holzapfel, C. Küstner-Wetekam, F. Wiegandt, F. Trinter et al.. *Fluorescence cascades evoked by resonant interatomic Coulombic decay of inner-valence excited neon clusters*. Chemical Physics, 482, 165 (2017). Electrons and nuclei in motion - correlation and dynamics in molecules (on the occasion of the 70th birthday of Lorenz S. Cederbaum).

[HNF16] Hakalla, R., M. L. Niu, R. W. Field, E. J. Salumbides, A. N. Heays, G. Stark, J. R. Lyons, M. Eidelsberg, J. L. Lemaire, S. R. Federman et al.. *VIS and VUV spectroscopy of* $^{12}C^{17}O$ *and deperturbation analysis of the* $A\ ^1\Pi$, $v = 1 - 5$ *levels*. RSC Advances, 6, 31588 (2016).

[HNF17] Hakalla, R., M. Niu, R. Field, A. Heays, E. Salumbides, G. Stark, J. Lyons, M. Eidelsberg, J. Lemaire, S. Federman, N. de Oliveira and W. Ubachs. *Fourier-transform spectroscopy of* $^{13}C^{17}O$ *and deperturbation analysis of the* $A\ ^1\Pi$ *(*$v = 0 - 3$*) levels*. Journal of Quantitative Spectroscopy and Radiative Transfer, 189, 312 (2017).

[HOS17] Hans, A., C. Ozga, R. Seidel, P. Schmidt, T. Ueltzhöffer, X. Holzapfel, P. Wenzel, P. Reiß, M. N. Pohl, I. Unger, E. F. Aziz, A. Ehresmann, P. Slavíček, B. Winter and A. Knie. *Optical Fluorescence Detected from X-ray Irradiated Liquid Water*. The Journal of Physical Chemistry B, 121(10), 2326 (2017).

[HS15a] Hertel, I. V. and C.-P. Schulz. *Atoms, Molecules and Optical Physics 1: Atoms and Spectroscopy*. Springer (2015).

[HS15b] Hertel, I. V. and C.-P. Schulz. *Atoms, Molecules and Optical Physics 2: Molecules and Photons, Spectroscopy and Collisions*. Springer (2015).

[HSH18] Hans, A., V. Stumpf, X. Holzapfel, F. Wiegandt, P. Schmidt, C. Ozga, P. Reiß, L. B. Ltaief, C. Küstner-Wetekam, T. Jahnke, A. Ehresmann, P. V. Demekhin, K. Gokhberg and A. Knie. *Direct evidence for radiative charge transfer after inner-shell excitation and ionization of large clusters*. New Journal of Physics, 20(1), 012001 (2018).

[HSO18] Hans, A., P. Schmidt, C. Ozga, G. Hartmann, X. Holzapfel, A. Ehresmann and A. Knie. *Extreme Ultraviolet to Visible Dispersed Single Photon Detection for Highly Sensitive Sensing of Fundamental Processes in Diverse Samples*. Materials, 11(6), 869 (2018).

[HSZ12] Hakalla, R., W. Szajna and M. Zachwieja. *Extended analysis of the Ångström band system ($B\ ^1\Sigma^+$ - $A\ ^1\Pi$) in the rare $^{12}C^{17}O$ isotopologue*. Journal of Physics B: Atomic, Molecular and Optical Physics, 45(21), 215102 (2012).

[Hun07] Hunter, J. D. *Matplotlib: A 2D Graphics Environment*. Computing in Science & Engineering, 9(3), 90 (2007).

[HW04] Haken, H. and H. C. Wolf. *The Physics of Atoms and Quanta*. Springer, seventh edition (2004).

[JAP98] James, G. K., J. M. Ajello and W. R. Pryor. *The middle ultraviolet-visible spectrum of H_2 excited by electron impact*. Journal of Geophysical Research, 103(E9), 20113 (1998).

[JOP01] Jones, E., T. Oliphant, P. Peterson et al.. *SciPy: Open source scientific tools for Python* (2001). URL `http://www.scipy.org/`.

[KBM13] Konopacky, Q. M., T. S. Barman, B. A. Macintosh and C. Marois. *Detection of Carbon Monoxide and Water Absorption Lines in an Exoplant Atmosphere*. Science, 339, 1398 (2013).

[KdLU03] Koelemeij, J., A. de Lange and W. Ubachs. *Search for outer-well states above the ionization potential in H_2*. Chemical Physics, 287(3), 349 (2003).

[LJS11] Liu, Y. F., Y. Jia, D. H. Shi and J. F. Sun. *Accurate ab initio potential of $CO(X\ ^1\Sigma^+)$ at low cost via correlation scaling and extrapolation method*. Journal of Quantitative Spectroscopy & Radiative Transfer, 112, 2296 (2011).

[LL81] Landau, L. D. and L. M. Lifshitz. *Quantum Mechanics Volume 3: Non-Relativistic Theory*. Butterworth-Heinermann, third edition (1981).

[LSJ12a] Liu, X., D. E. Shemansky, P. V. Johnson, C. P. Malone and M. A. Khakoo. *Electron and photon dissociation cross sections of the D_2 singlet ungerade continua*. Journal of Physics B: Atomic, Molecular and Optical Physics, 45(10), 105203 (2012).

[LSJ12b] Liu, X., D. E. Shemansky, P. V. Johnson, C. P. Malone, M. A. Khakoo and I. Kanik. *Electron and photon dissociation cross sections of the H_2 singlet ungerade continua*. Journal of Physics B: Atomic, Molecular and Optical Physics, 45(1), 015201 (2012).

[MA11] Millman, K. J. and M. Aivazis. *Python for Scientists and Engineers*. Computing in Science & Engineering, 13(2), 9 (2011).

[MBB17] Mirz, S., U. Besserer, B. Bornschein, R. Grösle, B. Krasch and S. Welte. *Design of a Spectroscopy Experiment for All Hydrogen Isotopologues in the Gaseous, Liquid, and Solid Phase*. Fusion Science and Technology, 71(3), 375 (2017).

[MBK89] Marston, C. C. and G. G. Balint-Kurti. *The Fourier grid Hamiltonian method for bound state eigenvalues and eigenfunctions*. The Journal of Chemical Physics, 91(6), 3571 (1989).

[MMR88] Macías, A., F. Martín, A. Riera and M. Yáñez. *A Pratical Solution to the "Unknown Normalization" Problem*. International Journal of Quantum Chemistry, 33, 279 (1988).

[MT10] McNeil, B. W. J. and N. R. Thompson. *X-ray free-electron lasers*. Nature Photonics, 4(12), 814 (2010).

[NGU98] Neininger, N., M. Guelin, H. Ungerechts, R. Lucas and R. Wielebinski. *Carbon monoxide emission as a precise tracer of molecular gas in the Andromeda galaxy*. Nature, 395, 871 (1998).

[NHT16] Niu, M. L., R. Hakalla, T. M. Trivikram, A. N. Heays, N. de Oliveira, E. J. Salumbides and W. Ubachs. *Spectroscopy and perturbation analysis of the A* $^1\Pi$ *(*$v = 0$*) state of* $^{13}C^{16}O$. Molecular Physics, 114(19), 2857 (2016).

[NS87] Noll, T. and H. Schmoranzer. *Fluorescent dissociation of selectively excited rotationa-vibrational states of* H_2 *(B, C) molecules*. Physics Scripta, 36, 129 (1987).

[NSZ13] Niu, M. L., E. J. Salumbides, D. Zhao, N. de Oliveira, D. Joyeux, L. Nahon, R. W. Field and W. Ubachs. *High resolution spectroscopy and perturbation analysis of the CO A* $^1\Pi$ *-* $X\ ^1\Sigma^+$ *(0,0) and (1,0) bands*. Molecular Physics, 111(14-15), 2163 (2013).

[NT82] Nelson, J. B. and G. C. Tabisz. *New Spectroscopic Determination of the Dipole Moment of HD in the Ground Vibrational State*. Phys. Rev. Lett., 48, 1393 (1982).

[OJS16] Ozga, C., K. Jänkälä, P. Schmidt, A. Hans, P. Reiß, A. Ehresmann and A. Knie. *X-ray absorption spectroscopy of the chiral molecules fenchone,* α*-pinene, limonene and carvone in the C1s excitation region*. Journal of Electron Spectroscopy and Related Phenomena, 207, 34 (2016).

[Oli06] Oliphant, T. E. *A guide to NumPy*. Trelgol Publishing (2006).

[Oli07] Oliphant, T. E. *Python for Scientific Computing*. Computing in Science & Engineering, 9(3), 10 (2007).

[ORK15] Ozga, C., P. Reiß, W. Kielich, S. Klumpp, A. Knie and A. Ehresmann. *Fluorescence cascades after excitation of XeII 5p 4 6p satellite states by synchrotron radiation*. Journal of Physics B: Atomic, Molecular and Optical Physics, 48(1), 015004 (2015).

[OSW99] Orlikowski, T., G. Staszewska and L. Wolniewczy. *Long range adiabatic potentials and scattering lengths for the EF, e and h states of the hydrogen molecule*. Molecular Physics, 96(10), 1445 (1999).

[Pau26] Pauli, W. *Über das Wasserstoffspektrum vom Standpunkt der neuen Quantenmechanik*. Zeitschrift für Physik, 36(5), 336 (1926).

[PBR84] Prasad, C., G. Bhale and S. P. Reddy. *The Ångström (B* $^1\Sigma^+$ *-* $A\ ^1\Pi$*) band system of* $^{13}C^{18}O$. Journal of Molecular Spectroscopy, 104(1), 165 (1984).

[PK08] Pachucki, K. and J. Komasa. *Electric dipole rovibrational transitions in the HD molecule*. Phys. Rev. A, 78, 052503 (2008).

[Pla62] Platzman, R. L. *Superexcited States of Molecules*. Radiation Research, 17(3), 419 (1962).

[PRSW85] Prasad, C., S. Reddy and M. Sandys-Wunsch. *The Herzberg ($C\ ^1\Sigma^+$ - $A\ ^1\Pi$) band system of $^{13}C^{18}O$*. Journal of Molecular Spectroscopy, 114(2), 436 (1985).

[Pyta] Python Software Foundation. *Built-in Types*. URL `https://docs.python.org/3/library/stdtypes.html`.

[Pytb] Python Software Foundation. *ctypes: A foreign function library for Python*. URL `https://docs.python.org/3/library/ctypes.html`.

[Pytc] Python Software Foundation. *Mapping types: dict*. URL `https://docs.python.org/3/library/stdtypes.html?highlight=dict#mapping-types-dict`.

[Qt a] Qt Company Ltd. *QComboBox Class*. URL `http://doc.qt.io/qt-5/qcombobox.html`.

[Qt b] Qt Company Ltd. *QLineEdit Class*. URL `http://doc.qt.io/qt-5/qlineedit.html`.

[Qt c] Qt Company Ltd. *QTimer Class*. URL `http://doc.qt.io/qt-5/qtimer.html`.

[RA17] Rau, A. R. and G. Alber. *Shared symmetries of the hydrogen atom and the two-bit system*. Journal of Physics B: Atomic, Molecular and Optical Physics, 50(24), 242001 (2017).

[RBS01] Reichardt, G., J. Bahrdt, J.-S. Schmidt, W. Gudat, A. Ehresmann, R. Müller-Albrecht, H. Molter, H. Schmoranzer, M. Martins, N. Schwentner and S. Sasaki. *A 10m-normal incidence monochromator at the quasi-periodic undulator U125-2 at BESSY II*. Nuclear Instruments and Methods in Physics Research Section A: Accelerators, Spectrometers, Detectors and Associated Equipment, 467, 462 (2001).

[Riv13] Riverbank Computing. *PyQt5* (2013). URL `https://riverbankcomputing.com/software/pyqt`.

[RJM82] Rich, N., J. Johns and A. McKellar. *Frequency and intensity measurements in the fundamental infrared band of HD*. Journal of Molecular Spectroscopy, 95(2), 432 (1982).

[SC72] Smith, W. H. and R. Chevalier. *Radiative-lifetime studies of the emission continua of the hydrogen and deuterium molecules*. The Astrophysical Journal, 177, 835 (1972).

[Sch49] Schwinger, J. *On the Classical Radiation of Accelerated Electrons*. Phys. Rev., 75, 1912 (1949).

[Sch82] Schmieder, R. W. *Optical emission spectrum of tritium gas*. Journal of the Optical Society of America, 72(5), 593 (1982).

[Sch10] Schneider, J. R. *FLASH — from accelerator test facility to the first single-pass soft x-ray free-electron laser*. Journal of Physics B: Atomic, Molecular and Optical Physics, 43(19), 194001 (2010).

[SD72] Stephens, T. L. and A. Dalgarno. *Spontaneous radiative dissociation in molecular hydrogen*. Journal of Quantitative Spectroscopy and Radiative Transfer, 12, 569 (1972).

[SLG99] Stark, G., B. R. Lewis, S. T. Gibson and J. P. England. *High-Resolution Oscillator Strength Measurements of the CO B $^1\Sigma^+$ - X $^1\Sigma^+$ (0,0) and (1,0) Vibrational Bands*. The Astrophysical Journal, 520(2), 732 (1999).

[SNR90] Schmoranzer, H., T. Noll, E. Roueff, H. Abgrall and R. J. Bieniek. *Rotational effects in the continuous vacuum-ultraviolet fluorescence spectrum of H2 associated with spontaneous dissociation*. Physical Review A, 42(3), 1835 (1990).

[SR87] Schwartz, C. and R. J. L. Roy. *Nonadiabatic eigenvalues and adiabatic matrix elements for all isotopes of diatomic hydrogen*. Journal of Molecular Spectroscopy, 121(2), 420 (1987).

[SvdW15] Smith, N. and S. van der Walt. *A Better Default Colormap for Matplotlib* (2015). URL `https://www.youtube.com/watch?v=xAoljeRJ3lU`. Talk presented at SciPy 2015.

[SW67] Stecher, T. P. and D. A. Williams. *Photodestruction of hydrogen molecules in H I regions.* Astrophysical Journal Letters, 149, 29 (1967).

[SW02] Staszewska, G. and L. Wolniewicz. *Adiabatic Energies of Excited $^1\Sigma_u$ States of the Hydrogen Molecule*. Journal of Molecular Spectroscopy, 212(2), 208 (2002).

[SZ78] Schmoranzer, H. and R. Zietz. *Observation of selectively excited continuous vacuum ultraviolet emission in molecular hydrogen*. Physical Review A, 18, 1472 (1978).

[TBJR92] Tchang-Brillet, W.-Ü. L., P. S. Julienne, J.-M. Robbe, C. Letzelter and F. Rostas. *A model of the B $^1\Sigma^+$ - D′ $^1\Sigma^+$ Rydberg-valence predissociating interaction in the CO molecule*. The Journal of Chemical Physics, 96(9), 6735 (1992).

[TCK85a] Thorson, W. R., J. H. Choi and S. K. Knudson. *Novel theory of the HD dipole moment. I. Theory*. Phys. Rev. A, 31, 22 (1985).

[TCK85b] Thorson, W. R., J. H. Choi and S. K. Knudson. *Novel theory of the HD dipole moment. II. Computations*. Phys. Rev. A, 31, 34 (1985).

[THH17] Trivikram, T. M., R. Hakalla, A. N. Heays, M. L. Niu, S. Scheidegger, E. J. Salumbides, N. de Oliveira, R. W. Field and W. Ubachs. *Perturbations in the A $^1\Pi$, $v = 0$ state of $^{12}C^{18}O$ investigated via complementary spectroscopic techniques*. Molecular Physics, 115(24), 3178 (2017).

[Tol15] Tollervey, N. H. *Python in Education*. O'Reilly (2015).

[TS72] Tilford, S. G. and J. D. Simmons. *Atlas of the Observed Absorption Spectrum of Carbon Monoxide Between 1060 and 1900* Å. Journal of Physical and Chemical Reference Data, 1(1), 147 (1972).

[TSU18] Trivikram, T. M., M. Schlösser, W. Ubachs and E. J. Salumbides. *Relativistic and QED Effects in the Fundamental Vibration of T_2*. Phys. Rev. Lett., 120, 163002 (2018).

[UB02] Unsöld, A. and B. Baschek. *The New Cosmos: An Introduction to Astronomy and Astrophysics*. Springer (2002).

[UKE16] Ubachs, W., J. Koelemeij, K. Eikema and E. Salumbides. *Physics beyond the Standard Model from hydrogen spectroscopy*. Journal of Molecular Spectroscopy, 320, 1 (2016).

[VR87] Veirs, D. and G. M. Rosenblatt. *Raman line positions in molecular hydrogen: H_2, HD, HT, D_2, DT, and T_2*. Journal of Molecular Spectroscopy, 121(2), 401 (1987).

[vRLL14] van Rossum, G., J. Lehtosalo and L. Langa. *PEP 484: Type Hints* (2014). URL `https://www.python.org/dev/peps/pep-0484/`.

[vRWC01] van Rossum, G., B. Warsaw and N. Coghlan. *PEP 8: Style Guide for Python Code* (2001). URL `https://www.python.org/dev/peps/pep-0008/`.

[WFA11] Weaver, H. A., P. D. Feldman, M. F. A'Hearn, N. D. Russo and S. A. Stern. *The Carbon Monoxide Abundance in Comet 103P/Hartley 2 During the EPOXI Flyby*. The Astrophysical Journal Letters, 734(1), L5 (2011).

[WFF09] Weinhardt, L., O. Fuchs, A. Fleszar, M. Bär, M. Blum, M. Weigand, J. D. Denlinger, W. Yang, W. Hanke, E. Umbach and C. Heske. *Resonant inelastic soft x-ray scattering of CdS: A two-dimensional electronic structure map approach*. Phys. Rev. B, 79, 165305 (2009).

[WKB11] Wang, J., K. S. Kim and E. J. Baerends. *Electron pair density in the lowest $^1\Sigma_u^+$ and $^1\Sigma_g^+$ states of H_2*. The Journal of Chemical Physics, 135(7), 074111 (2011).

[Wol93] Wolniewicz, L. *Relativistic energies of the ground state of the hydrogen molecule*. The Journal of Chemical Physics, 99(3), 1851 (1993).

[WOS06] Wolniewicz, L., T. Orlikowski and G. Staszewska. *$^1\Sigma_u$ and $^1\Pi_u$ states of the hydrogen molecule: Nonadiabatic couplings and vibrational levels*. Journal of Molecular Spectroscopy, 238(1), 118 (2006).

[WS03a] Wolniewicz, L. and G. Staszewska. *$^1\Sigma_u^+ \rightarrow X\,^1\Sigma_g^+$ transition moments for the hydrogen molecule*. Journal of Molecular Spectroscopy, 217(2), 181 (2003).

[WS03b] Wolniewicz, L. and G. Staszewska. *Excited $^1\Pi_u$ states and the $^1\Pi_u \rightarrow X\,^1\Sigma_g^+$ transition moments of the hydrogen molecule*. Journal of Molecular Spectroscopy, 220(1), 45 (2003).

[WW05] Wu, L. and R. Wang. *Carbon Monoxide: Endogenous Production, Physiological Functions, and Pharmacological Applications*. Pharmacological Reviews, 57(4), 585 (2005).

Publications by the author

Journal Papers

M. Pitzer, Ph. Schmidt, C. Ozga, A. Hans, P. Reiß, I.D. Petrov, A.N. Artemyev, A. Ehresmann, A. Knie, Ph.V. Demekhin: *Circular Dichroism in Fluorescence Emission Following the C 1s $\rightarrow \pi^*$ Excitation and Resonant Auger Decay of Carbon Monoxide*, Molecules **23**, 1534 (2018)

A. Hans, Ph. Schmidt, C. Ozga, G. Hartmann, X. Holzapfel, A. Ehresmann, A. Knie: *Extreme Ultraviolet to Visible Dispersed Single Photon Detection for Highly Sensitive Sensing of Fundamental Processes in Diverse Samples*, Materials **11**, 869 (2018)

L. Ben Ltaief, A. Hans, Ph. Schmidt, X. Holzapfel, F. Wiegandt, P. Reiß, C. Küstner-Wetekam, T. Jahnke, R. Dörner, A. Knie, A. Ehresmann: *VUV photon emission from Ne clusters of varying size following photon and photoelectron excitations*, J. Phys. B.: At. Mol. Opt. Phys. **51**, 065002 (2018)

A. Hans, V. Stumpf, X. Holzapfel, F. Wiegandt, Ph. Schmidt, C. Ozga, P. Reiß, L. Ben Ltaief, C. Küstner-Wetekam, T. Jahnke, A. Ehresmann, Ph.V. Demekhin, K. Gokhberg, A. Knie: *Direct evidence for radiative charge transfer after innershell excitation and ionization of large clusters*, New J. Phys. **20**, 012001 (2018)

M. Ilchen, G. Hartmann, P. Rupprecht, A.N. Artemyev, R.N. Coffee, Z. Li, H. Ohldag, H. Ogasawara, T. Osipov, D. Ray, Ph. Schmidt, T.J.A. Wolf, A. Ehresmann, S. Moeller, A. Knie, Ph.V. Demekhin: *Emitter-site-selective photoelectron circular dichroism of triflouromethyloxirane*, Phys. Rev. A **95**, 053423 (2017)

A. Hans, C. Ozga, R. Seidel, Ph. Schmidt, T. Ueltzhöffer, X. Holzapfel, P. Wenzel, P. Reiß, M.N. Pohl, I. Unger, E.F. Aziz, A. Ehresmann, P. Slavicek, B. Winter and A. Ehresmann: *Optical fluorescence detected from X-ray irradiated water*, J. Phys. Chem. B **121**, 2326 (2017)

A. Hans, L. Ben Ltaief, M. Förstel, Ph. Schmidt, C. Ozga, P. Reiß, X. Holzapfel, C. Küstner- Wetekam, F. Wiegandt, F. Trinter, U. Hergenhahn, T. Jahnke, R. Dörner, A. Ehresmann, Ph.V. Demekhin, A. Knie: *Fluorescence cascades evoked by resonant interatomic Coulombi decay of inner-valence excited neon clusters*, Chem. Phys. **482**, 165 (2017)

A. Hans, A. Knie, M. Förstel, Ph. Schmidt, P. Reiß, C. Ozga, U. Hergenhahn, A. Ehresmann: *Determination of absolute cross sections for cluster-specific decays*, J. Phys. B: At. Mol. Opt. Phys. **49**, 105101 (2016)

C. Ozga, K. Jänkälä, Ph. Schmidt, A. Hans, P. Reiß, A. Ehresmann, A. Knie: *X-ray absorption spectroscopy of the chiral molecules fenchone, α-pinene, limonene and carvone in the C1s excitation region*, J. Electron Spectrosc. Relat. Phenom. **207**, 34 (2016)

P. Reiss, Ph. Schmidt, C. Ozga, A. Knie, A. Ehresmann: *Dispersed fluorescence spectrometry from the VIS to VUV spectral range for experiments at heavy-ion storage facilities*, Phys. Scripta **2015**, T166 (2015)

P. Reiss, Ph. Schmidt, I. Tulin, A. Knie, R. Hentges, A. Ehresmann: *Photon-photon coincidence apparatus with position sensitive detectors*, Nucl. Instrum. Methods Phys. Res. Sect. A **776**, 57 (2015)

A. Hans, A. Knie, Ph. Schmidt, L. Ben Ltaief, C. Ozga, P. Reiß, H. Huckfeldt, M. Förstel, U. Hergenbahn, A. Ehresmann: *Lyman-series emission after valence and core excitation of water vapor*, Phys. Rev. A **92**, 032511 (2015)

A. Knie, A. Hans, M. Förstel, U. Hergenhahn, Ph. Schmidt, P. Reiß, C. Ozga, B. Kambs, F. Trinter, J. Voigtsberger, D. Metz, T. Jahnke, R. Dörner, A.I. Kuleff, L.S. Cederbaum, Ph.V. Demekhin, A. Ehresmann: *Detecting ultrafast interatomic electronic processes in media by fluorescence*, New J. Phys. **16**, 102002 (2014)

A. Knie, M. Ilchen, Ph. Schmidt, P. Reiß, C. Ozga, B. Kambs, A. Hans, N. Müglich, S.A. Galitskiy, L. Glaser, P. Walter, J. Viefhaus, A. Ehresmann, Ph.V. Demekhin: *Angle-resolved study of resonant Auger decay and fluorescence emission processes after core excitations of the terminal and central nitrogen atoms in N_2O*, Phys. Rev. A **90**, 13416 (2014)

A. Knie, N. Burbank, Ph. Schmidt, C. Ozga, A. Ehresmann: *Electron-impact induced fluorescence for EUV spectrometer-detector calibration*, J. Electron Spectrosc. Relat. Phenom. **185**, 492 (2012)

Conference Contributions

Ph. Schmidt, A. Hans, C. Ozga, A. Ehresmann, A. Knie: *Tracing the molecular potential energy landscape on rovibronic emission maps of molecular hydrogen*, DPG Frühjahrstagung der Sektion AMOP, Erlangen (2018)

Ph. Schmidt, A. Hans, C. Ozga, M. Glass-Maujean, A. Ehresmann, A. Knie: *Mapping the entirety of optical transitions in the singly excited regime of hydrogen and its isotopes with rotational resolution*, International Conference on Photonic, Electronic and Atomic Collisions, Cairns, Australia (2017)

Ph. Schmidt, P. Reiß, G. Hartmann, C. Ozga, M. Wilke, A. Knie, A. Ehresmann: *Applications of X-ray streak detectors for spectroscopy, characterization and diagnostics at SASE Free-Electron Lasers*, DPG Frühjahrstagung der Sektion AMOP, Mainz (2017)

Ph. Schmidt, M. Wilke, A. Knie, A. Ehresmann: *Spectral characterization of SASE bunch trains*, European Conference on Atoms, Molecules and Photons, Frankfurt (2016)

Ph. Schmidt, A. Hans, C. Ozga, P. Reiß, L. Ben Ltaief, A. Ehresmann, M. Glass-Maujean, A. Knie: *Complete characterization of the Lyman band continuum emissions of molecular hydrogen and deuterium by photon-induced fluorescence spectrometry*, DPG Frühjahrstagung der Sektion AMOP, Hannover (2016)

Ph. Schmidt, A. Hans, C. Ozga, P. Reiß, L. Ben Ltaief, K. Hosaka, M. Kitajima, N. Kouchi, A. Knie, A. Ehresmann: *Excitation-energy resolved fluorescence spectra of hydrogen molecules in the regime of singly excited molecular states*, International Conference on Photonic, Electronic and Atomic Collisions, Toledo, Spain (2015)

Ph. Schmidt, M. Wilke, A. Knie, A. Ehresmann: *XUV streak camera for spectral characterization of SASE bunch trains*, Intense Field, Short Wavelength Atomic and Molecular Processes, Hamburg (2015)

Ph. Schmidt, C. Ozga, P. Reiß, A. Hans, L. Ben Ltaief, A. Knie, A. Ehresmann, K. Hosaka, M. Kitajima, N. Kouchi: *Excitation energy resolved photon-induced fluorescence spectrum of hydrogen molecules in the regime of singly excited molecular states*, DPG Frühjahrstagung der Sektion AMOP, Heidelberg (2015)

Ph. Schmidt, P. Reiß, A. Knie, A. Ehresmann, K. Hosaka, Y. Nakanishi, K. Shiino, N. Kouchi: *Photon-photon coincidence in the EUV regime for very large gas pressures after dissociation of hydrogen molecules in superexcited states intro neutral fragments*, DPG Frühjahrstagung der Sektion AMOP, Berlin (2014)

Ph. Schmidt, P. Reiß, B. Kambs, A. Knie, Arno Ehresmann: *Ly-α coincidence after dissociation of hydrogen molecules in superexcited states intro neutral fragments*, DPG Frühjahrstagung der Sektion AMOP, Hannover (2013)

Erklärung

Hiermit versichere ich, dass ich die vorliegende Dissertation selbständig, ohne unerlaubte Hilfe Dritter angefertigt und andere als die in der Dissertation angegebenen Hilfsmittel nicht benutzt habe. Alle Stellen, die wörtlich oder sinngemäß aus veröffentlichten oder unveröffentlichten Schriften entnommen sind, habe ich als solche kenntlich gemacht. Dritte waren an der inhaltlichen Erstellung der Dissertation nicht beteiligt; insbesondere habe ich nicht die Hilfe eines kommerziellen Promotionsberaters in Anspruch genommen. Kein Teil dieser Arbeit ist in einem anderen Promotions- oder Habilitationsverfahren durch mich verwendet worden.

Kassel, _____ _____